



Department of Naval Architecture, Ocean and Marine
Engineering

University of Strathclyde

**Numerical Investigation into Bio-inspired Flow
Control for Renewable Turbine**

Wendi LIU

A thesis presented in fulfilment of the requirements for the
degree of Doctor of Philosophy

November 2015

©Wendi Liu

Drinking Vis-à-vis the Bending River (No. 1) (Zhao, 2012)

Du Fu (Tang Dynasty, China)

The beauty of spring fades as whirling blossoms fly;

The countless petals in the wind make me repine.

Do enjoy the flitting blooms while they pass the eye;

Mind not whether you may be drunk, just drink your wine;

In the tower riverside the kingfishers nest.

By the Park unicorns line the way to the grave mound;

Nature reveals that of life we should make the best;

Why should we by the vanity of fame be bound?

I would like to dedicate this thesis to my loving parents and grandparents

Declaration

I hereby declare that this thesis and all material contained herein is a record of work carried out in the Department of Naval Architecture, Ocean and Marine Engineering of Engineering Faculty, University of Strathclyde during the period from October 2011 to November 2015. This thesis is the result of the author's original research except where otherwise indicated. It has been composed by the author and has not been previously submitted for examination, which has led to the award of a degree.

The copyright of this thesis belongs to the author under the terms of the United Kingdom Copyright Acts as qualified by University of Strathclyde Regulation 3.50. Due acknowledgement must always be made of the use of any material contained in, or derived from, this thesis.

Signed:

Date:

Acknowledgements

“If I can see farther it is only because I stand on the shoulders of giants”

--Issac Newton (1642-1727)

I would like to express my deepest appreciation to my primary supervisor, Dr. Qing Xiao, whose encouragement, supervision and expertise from the start enabled me to develop an understanding of the subject. It changed my life! I would also like to give my deepest thanks to my secondary supervisor, Prof. Atilla Incecik, for his valuable support and help during my studies.

I am grateful for the supervision from Prof. Sandy Day and Mr. David Clelland for the project of *TLPWIND UK: “Driving down the cost of offshore wind in UK waters”* during the last year of my Ph.D. study. I am also grateful to my colleague Ms. Elif Oguz for her cooperation and help during this project.

I am grateful to the technical support from Dr. Ke Sun and Harbin Engineering University at the beginning of this research. The financial support from Dr. Fai Cheng and Lloyd’s Register Limited for the research of *Bio-inspired Active Flow Control for Oscillating Foil Turbine by Blade Flexibility* was really helpful. The technical guidance and support for the research of *Passive Flow Control for Oscillating Foil Turbine by Flexible Material* from Dr. Qiang Zhu, Professor of University of California, is much appreciated. I also thank Dr. Narakorn Srinil for his technical support with the research of *Passive Investigation on Vertical Axis Turbine with Flexible Blade*.

I would like to take this opportunity to express my gratitude to my group colleagues Ms. Jianxin Hu, Ms. Xue Wang, Mr. Saishuai Dai, Mr. Enhao Wang, Mr. Yuanchuan

Liu, Dr. Wei Jin, Dr. Wei Shao, Dr. Yue Deng and Dr. Laibing Jia, for their kind guidance and support during my Ph.D. study.

I would also like to thank the Faculty of Engineering, University of Strathclyde for provision of the USE-HPC and ARCHIE-WeST high performance computing facilities. The results contained in the present research were obtained using the USE-HPC and the EPSRC funded ARCHIE-WeSt High Performance Computer (www.archie-west.ac.uk). EPSRC grant no. EP/K000586/1.

Also, I would like to thank Prof. Peilin Zhou for providing me with the opportunity to study at the University of Strathclyde. It has enlarged my horizon. I would like to thank Mrs. Thelma Will, the department's research secretary, for her kind assistance and support on both an academic and private life.

I would like to thank my external examiner, Prof. Longbin Tao, and my internal examiner, Dr. Mahdi Khorasanchi, on their time and effort to review my thesis since the submission of the soft bound copy on 16th July 2015. Special thanks to the convener of my VIVA, Prof. Nigel Barltrop and Prof. Osman Turan, on their help of my VIVA exam on 5th November 2015.

I would like to express my appreciation to Ms. Xu Xue for her understanding and support during my studies.

And finally, I would like to thank my parents for their financial support, encouragement and trust. I would like to remember my grandfather who passed away during my Ph.D. studies. I hope he knows of my achievements.

It is not easy to complete doctoral studies, but I did it. My journey of discovery the wonderful word is just starting!

Publications

The following papers have been either published, or accepted for publication, in scientific journals and conferences during my Ph.D. study. Four of the journal articles (J1, J2, J4 and J5), four of the conference papers (C1, C2, C5 and C6) have been drawn from this thesis.

Journal articles

- J1. **Wendi Liu**, Qing Xiao and Qiang Zhu. "A coupled fluid-structure study of the passive flexibility effect on oscillating foil energy harvester" AIAA Journal (In Press).
- J2. **Wendi Liu** and Qing Xiao. "Investigation on Darrieus Type Straight Blade Vertical Axis Wind Turbine with Flexible Blade" Ocean Engineering 110 A (2015): pp 339-356.
- J3. Sun, Quan, Yinghong Li, Bangqin Cheng, Wei Cui, **Wendi Liu**, and Qing Xiao. "The characteristics of surface arc plasma and its control effect on supersonic flow." Physics Letters A 378, no. 36 (2014): pp 2672-2682.
- J4. **Wendi Liu**, Qing Xiao and Fai Cheng. "A bio-inspired study on tidal energy extraction with flexible flapping wings" Bio-inspiration & Bio-mimetics 8, no. 036011 (2013): pp 1-16.
- J5. Qing Xiao, **Wendi Liu** and Atilla Incecik. "Flow control for VATT by fixed and oscillating flap." Renewable Energy 51 (2013): pp 141-152.

Conference papers

- C1. **Wendi Liu** and Qing Xiao. "Bend and Twist Effect for Large-Scale Vertical Axis Turbine" 11th European Wave and Tidal Energy Conference Series (EWTEC), September 6th – 11th September 2015, Nantes, France, #607.
- C2. **Wendi Liu** and Qing Xiao. "A study on oscillating foil energy harvester with a passive flexible foil." Grand Renewable Energy (GRE) International Conference and Exhibition, 27th July – 1st August 2014, Tokyo, Japan.
- C3. Enhao Wang, Qing Xiao and **Wendi Liu**. "Numerical Simulation of Multi-Modal Vortex-Induced Vibration of a 3D Flexible Circular Cylinder." International Conference on Marine Technology (ICMT) 2014, 7th – 9th July 2014, Glasgow, UK, Session 6-1.
- C4. Enhao Wang, Qing Xiao and **Wendi Liu**. "System Damping Effect on VIV Energy Extraction Device." The 8th International Workshop on Ship Hydrodynamics (IWSH), 23rd – 25th September 2013, Seoul, Korea.
- C5. **Wendi Liu** and Qing Xiao. "Energy extraction by flexible flapping twin wing." 32nd International Conference on Ocean, Offshore and Arctic Engineering (OMAE), 9th–14th June 2013, Nantes, France, 2013-10233.
- C6. **Wendi Liu** and Qing Xiao. "Flow control for VATT by fixed and oscillating flap." 22nd International Offshore and Polar Engineering Conference (ISOPE) 17th–22nd June 2012, Rhodes, Greece, 1098-6189.

Abstract

There are several methods for enhancing the efficiency of the Vertical Axis Turbine (VAT) and Oscillating Foil Turbine (OFT), such as the variable pitch method for the VAT blade and the non-sinusoidal pitch method for the OFT. However, all of them are not bio-inspired methods. The main objective of the present research is to develop innovative methods to enhance the efficiency of a renewable turbine by using bio-inspired flow controls. In the present research, bio-inspired methods are used to modify the traditional rigid turbine blade such as the active and passive flow controlled flaps for VAT which are inspired by the fishtail motion and the active and passive blade flexibility for OFT which is inspired by butterfly wings. Simulations are carried out by solving 2D/3D Navier-Stokes equations either by themselves or fully coupled with a finite element structure solver at both laminar and turbulent flow conditions. The results show energy extraction efficiency enhancement effects by using bio-inspired flow controlled methods for both VAT and OFT under certain conditions. The mechanics of bio-inspired flow control, such as vortex control for VAT using an active or passive oscillating flap, force enhancement and phase shift effects of active flow controlled OFT and LEV control for passive flow controlled OFT, are also studied. Previous research studies on the HAT show a blade stress reduction effect and longer life cycles by using composite material or Morphing Blade (MB). However, not much is known about the performance and function of the composite material regarding VAT. The present study on the passive flow controlled spanwise flexible blade of VAT shows the blade structural characteristics associated with bending and twist deflection as sinusoidal functions. The blade external

unsteady loads and the power performance of VAT are first studied, which have been further extended to a blade stress analysis.

Nomenclature

Roman symbols

\bar{c}	=	turbine chord-radius ratio which defined as $\bar{c} = c/R$
A	=	sweep area (m ²)
AR	=	aspect ratio
c	=	blade chord length (m)
c_c	=	centrifugal force coefficient
c_d	=	drag coefficient
c_{eff}	=	effective chord length of flexible material (m)
c_f	=	total fluid force coefficient
c_{ft}	=	total force coefficient
c_l	=	lift coefficient
c_m	=	moment coefficient of VAT
c_n	=	normal force coefficient
c_{op}	=	power coefficient
c_{pit}	=	pitching centre measured from leading edge (m)
c_{pr}	=	pressure coefficient
c_{sf}	=	length of metal stiffener (m)
c_{st}	=	stress coefficient
c_t	=	thrust coefficient
D_{is}	=	blade displacement (m)
DR	=	density ratio
E	=	Young's modulus (Pa)

- E_c = Young's modulus coefficient
- f^* = reduced frequency
- f_0 = frequency of flapping wing (Hz)
- $f_{0.18}$ = frequency of flapping wing with $f^*=0.18$ (Hz)
- $f_{5.5}$ = turbine rotational frequency with tip speed ratio of 5.5 (Hz)
- F_b = body force (N)
- F_c = centrifugal force (N)
- F_f = total fluid force (N)
- F_{ft} = total force (N)
- F_n = normal force (N)
- f_n = natural frequency of selected material (Hz)
- f_r = turbine blade natural frequency at each mode (Hz)
- FR = natural frequency ratio which is defined as $FR = f_n/f_{0.18}$
- F_t = thrust force (N)
- g = gravitational acceleration (m/s^2)
- H = blade span length (m)
- $h(t)$ = instantaneous heaving position (m)
- h_0 = amplitude of heaving motion (m)
- L = lift force (N)
- l_{st} = length from blade strut to its nearest blade tip (m)
- M = blade moment relative to the turbine centre (Nm)
- $M_z(t)$ = instantaneous moment coefficient of the OFT
- n = flexible coefficient
- N = number of turbine blades

n_t = revolution ratio between turbine and flap for oscillating flap turbine

p = local pressure (Pa)

p_∞ = incoming flow pressure (Pa)

p_o = instantaneous power (W)

R = turbine radius (m)

Re = turbine Reynold's number based on blade or foil chord

St = Strouhal number of foil oscillating

t = instant time (s)

T_{flap} = flap revolution period (s)

T_{m1} = blade 1st bending mode period of regions a and c (s)

T_{m2} = blade 1st bending mode period of region b (s)

T_{m3} = blade 1st torsion mode period of regions a and c (s)

T_{m4} = blade 1st torsion mode period of region b (s)

T_{m5} = blade 1st bending mode period of tip strut condition (s)

T_{m6} = blade 1st torsion mode period of tip strut condition (s)

T_{m7} = blade 2nd bending mode period of regions a and c (s)

T_{sf} = thickness of metal stiffener (m)

T_{turb} = turbine revolution period (s)

U = incoming flow velocity (m/s)

V_i = instantaneous induced velocity (m/s)

$V_t(t)$ = instantaneous resultant velocity (m/s)

$x_l o_l y_l$ = local body fitted coordinate

Greek symbols

- $\alpha(t)$ = blade instantaneous angle of attack (deg)
- β = angle between the flap centre line and the main part centre line for oscillating flap turbine (deg)
- β_0 = instantaneous angle (deg)
- β_{0_amp} = angle amplitude (deg)
- η = energy extraction efficiency
- $\theta(t)$ = instantaneous pitching angle (deg)
- θ_0 = amplitude of pitching motion (deg)
- θ_t = turbine azimuthal angle (deg)
- λ = tip speed ratio
- μ = dynamic viscosity (Pa·s)
- ν = Poisson's ratio
- Π = effective stiffness
- Π_r = blade natural frequency ratio in each mode which is defined as $\Pi_r = f_r/f_{5.5}$
- ρ_f = fluid density (kg/m³)
- ρ_s = density of structure (kg/m³)
- σ = structure principal stress (Pa)
- σ_s = turbine solidity
- φ = phase difference between heave and pitch motion (rad)
- ω = turbine angular velocity (rad/s)
- ω_f = rotational angular velocity of oscillating flap for oscillating flap turbine (rad/s)

Abbreviations

<i>AOA</i>	Angle of Attack
<i>AUV</i>	Autonomous Underwater Vehicles
<i>BEM</i>	Boundary Element Method
<i>CFD</i>	Computational Fluid Dynamics
<i>CVT</i>	Constant-Volume Tetrahedron
<i>DBD</i>	Dielectric Barrier Discharge
<i>DOF</i>	Degree of Freedom
<i>FEM</i>	Finite Element Method
<i>FSI</i>	Fluid Structure Interaction
<i>HAT</i>	Horizontal Axis Turbine
<i>LE</i>	Leading Edge
<i>LEC</i>	Leading Edge Control
<i>LES</i>	Leading Edge Suction
<i>LEV</i>	Leading Edge Vortex
<i>MAV</i>	Micro Aerial Vehicle
<i>MB</i>	Morphing Blade
<i>OFT</i>	Oscillating Foil Turbine
<i>PBC</i>	Periodic Boundary Condition
<i>PDMS</i>	Polydimethylsiloxane
<i>SBC</i>	Symmetry Boundary Condition
<i>TEC</i>	Trailing Edge Control
<i>TFI</i>	Trans-Finite Interpolation
<i>UDF</i>	User Defined Function

URANS Unsteady Reynolds-Averaged Navier–Stokes equations

VAT Vertical Axis Turbine

WBC Wall Boundary Condition

Contents

Declaration	i
Acknowledgements	iii
Publications	vii
Journal articles	vii
Conference papers.....	viii
Abstract	x
Nomenclature	xiii
Roman symbols.....	xiii
Greek symbols	xvi
Abbreviations.....	xvii
Contents	xx
List of Figures	xxiv
List of Tables.....	xxxvi
PART I: Introduction, Literature Review and Methodology	1
Chapter 1: Introduction	2
1.1 Introduction.....	2
1.2 Working principle of renewable turbine	8
1.2.1 Working principle of VAT	8
1.2.2 Working principle of OFT.....	11
1.2.3 Comparison among different turbines under body fitted coordinate	14
1.3 Objectives of this thesis	17
1.4 Structure of this thesis.....	19
Chapter 2: Literature Review	21
2.1 Review of the research on straight blade VAT.....	21

2.1.1 Research method for VAT	21
2.1.2 Parameter studies for straight blade VAT	31
2.2 Review of the research on OFT	40
2.2.1 OFT with forced pitching and heaving motions.....	42
2.2.2 OFT with semi-activated systems	49
2.2.3 OFT with self-sustained systems.....	51
2.3 Review of the research on blade stress estimation and reduction for renewable turbine.....	54
2.4 Review of bio-inspired research and its application in the aerodynamics or marine industry	56
2.5 Summary.....	61
Chapter 3: Mathematical Formulations and Numerical Algorithm.....	63
3.1 Introduction.....	63
3.2 FLUENT	63
3.2.1 Governing equations	63
3.2.2 Model validation	65
3.2.3 Computational domain	69
3.3 In-house FSI code	70
3.3.1 Fluid dynamics	72
3.3.2 Structure dynamics	75
3.3.3 Fluid-structure coupling	78
3.3.4 In-house code validation	83
3.3.5 Computational domain and verification	105
3.4 Stress calculation in Section 6.2	110
PART II: Bio-inspired Active Flow Control for Renewable Turbine.....	112

Chapter 4: Bio-inspired Active Flow Control for Vertical Axis Turbine by Oscillating Flap	113
4.1 Introduction.....	113
4.2 Description of problem	114
4.3 Results and di scussions.....	116
4.3.1 Mechanism of flow control by oscillating flap	116
4.3.2 Oscillating flap parameters.....	120
4.4. Summary	126
Chapter 5: Bio-inspired Active Flow Control for Oscillating Foil Turbine by Flexible Blade	127
5.1 Introduction.....	127
5.2 Description of problem	128
5.3 Results and discussions.....	137
5.3.1 Mechanism of various bio-inspired flexible shapes for a single wing	137
5.3.2 Parametric study	146
5.4. Summary	157
PART III: Bio-inspired Passive Flow Control for Renewable Turbine.....	160
Chapter 6: Bio-inspired Passive Flow Control for Vertical Axis Turbine by Oscillating Flap and Passive Flexible Blade.....	161
6.1 Bio-inspired Passive Flow Control for VAT by Oscillating Flap	161
6.1.1 Introduction	161
6.1.2 Description of problem.....	161
6.1.3 Results and discussions	163
6.1.4 Summary of Section 6.1	168
6.2 Investigation of VAT with Passive Flexible Blade	168
6.2.1 Introduction	168

6.2.2 Description of problem.....	169
6.2.3 Results and discussions	177
6.2.4 Summary of Section 6.2	206
Chapter 7: Bio-inspired Passive Flow Control for Oscillating Foil Turbines by Flexible Material	208
7.1 Introduction.....	208
7.2 Description of problem	208
7.2.1 Benchmark model	208
7.2.2 Structural design of flexible foils	209
7.3 Results and discussions.....	212
7.3.1 Energy harvesting performance with stiffeners of real materials.....	212
7.3.2 Young’s modulus effect	220
7.3.3 Density ratio effect	224
7.4 Summary	232
PART IV: Conclusions and Recommendations	235
Chapter 8: Conclusions and Recommendations	236
8.1 Conclusions.....	236
8.2 Recommendations for future research	239
References	242
Appendix I: MathCAD Calculation Process for Structural Parameters of 2D Free Oscillating Cylinder	265
Appendix II: MathCAD Calculation Process for Structural Parameters of 2D Free Oscillating Isogai Airfoil.....	266
Appendix III: MathCAD Calculation Process for Structural Parameters of 3D AGARD Wing.....	267
Appendix IV: Curriculum Vitae.....	280

List of Figures

Figure 1. 1 Three different types of turbine for tidal/wind energy with (a) HAT (Brøndsted et al., 2005), (b) VAT (Gretton, 2009) and (c) OFT (Kinsey et al., 2011).	2
Figure 1. 2 Comparison of efficiency among different types of (a) HAT and VAT (Hau and Von Renouard, 2013) and (b) OFT (Kinsey Dumas, 2008).	3
Figure 1. 3 The diagram of a vertical axis turbine under a tip speed ratio of 3.0 with instantaneous velocities and forces. Blue arrow: induced velocity; Green arrow: free stream velocity; Red arrow: resultant velocity; Cyan arrow represents lift force and magenta arrow is drag force (Gretton, 2009).	8
Figure 1. 4 The configuration of an oscillating foil turbine (Kinsey and Dumas, 2008).	11
Figure 1. 5 Sketch of turbine blade forces, resultant velocity and angle of attack under body fitted coordinate $x_l o_l y_l$.	15
Figure 1. 6 The instantaneous resultant velocity and blade angle of attack for the (a) HAT, (b) VAT and (c) OFT with body fitted coordinate $x_l o_l y_l$.	17
Figure 2. 1 Schematic of single stream tube model (Wang, 2005).	23
Figure 2. 2 Schematic of vortex model for a single blade (Islam, 2008).	26
Figure 2. 3 Schematic of cascade model (Islam, 2008).	27
Figure 2. 4 Geometry of Airfoils for Sensitivity Analysis by Islam et al. (2007b).	33
Figure 2. 5 Power curves for the three analysed rotors (just the $\lambda=2.33$ value of cambered NACA0021 was calculated) (Castelli et al., 2012a).	33
Figure 2. 6 Schematic diagram of the variable-pitch blade mechanism utilizing four-bar linkage (Kiwata et al., 2010).	36
Figure 2. 7 Sketch of spring variable-pitch design concept (Sun et al., 2009).	36

Figure 2. 8 Sketch of the flow direction and augmentation channel concept (Khan et al., 2009).	37
Figure 2. 9 Schematic representation of the VAT showing the main components (left) and schematic of the blade leading-edge region showing the attachment of the DBD plasma actuator (right) (Greenblatt et al., 2012).	39
Figure 2. 10 Top view of a rotor assembly illustrating the adjustments of blade ailerons relative to a prevailing wind with the variable flap method (Haar, 2011). ..	40
Figure 2. 11 Schematics of (a) a system with forced heaving and pitching motions, (b) a semi-activated system with forced pitching but induced heaving motions (modified from Zhu and Peng (2009)), and (c) a self-sustained system with induced heaving and pitching motions (modified from Peng and Zhu (2009)) (Xiao and Zhu, 2014).	41
Figure 2. 12 Side view (left) and photograph (right) of the flutter engine (Jones et al., 1999).	43
Figure 2. 13 The influence of non-sinusoidal pitching profiles on oscillating wing power efficiency: (a) Profile of pitching and heaving with an adjustable constant β ; (b) efficiency variation with β at various oscillating non-dimensionalized frequency St . (reproduced from Xiao et al., 2012).	46
Figure 2. 14 Schematic of the flapping-foil energy harvester used in Zhu et al. (2009).	50
Figure 2. 15 Schematic of the fully passive flapping wing turbine used in Young et al. (2013).	53
Figure 2. 16 Drawings of forewings from insects, arranged on the phylogenetic tree used to calculate independent contrasts (Combes and Daniel, 2003a).	57
Figure 2. 17 Schematic representation of the fin kinematics calculated by Shoele and Zhu (2012).	59

Figure 3. 1 Schematic diagram for unsteady time marching. 65

Figure 3. 2 Time-averaged power coefficient variation with tip speed ratio 67

Figure 3. 3 Time-averaged power coefficient variation with tip speed ratio 68

Figure 3. 4 Instantaneous blade moment coefficient variations with instantaneous time (grid dependence test with 159,163 cells of coarse grid, 357,159 cells of medium grid and 746,152 cells of fine grid). 69

Figure 3. 5 Computational domain and mesh distribution for the simulations in Chapter 4 and Section 6.1. 70

Figure 3. 6 Configuration for the CVT method. 80

Figure 3. 7 Sketch of validation cases of the flow passes stationary cylinder (Helen, 2008). 83

Figure 3. 8 Flow pass stationary cylinder validation of (a) S_t results and (b) c_l results 84

Figure 3. 9 Flexible model validation of (a) time-averaged drag coefficient (c_d) variation with f_λ , (b) instantaneous vorticity contour at $f_\lambda = 0.5$ and $t/T_{turb}=1/8$ 86

Figure 3. 10 Validation on a rigid oscillating foil as an energy extraction device with $Re=5\times 10^5$; $h_0/c=1.0$; $c_{pit}/c=1/3$; $\theta_0=75^\circ$ and $\varphi=-\pi/2$ – compared with Kinsey and Dumas (2012a; 2012b). 88

Figure 3. 11 Validation results of a 3D rigid flapping foil with $AR=3.0$.
 ▲ Experiment at $Re=1\times 10^4$ (Heathcote et al., 2008); × Experiment at $Re=2\times 10^4$ (Heathcote et al., 2008); * Experiment at $Re=3\times 10^4$ (Heathcote et al., 2008); + Panel method (Heathcote et al., 2008); ● N-S numerical method at $Re=2\times 10^4$ (Young, 2005); — (Orange) Analytical method at $Re=2\times 10^4$ (Garrick, 1937); ■ Present 2D CFD method at $Re=2\times 10^4$ (achieved with a 3D method using Symmetry Boundary Condition (SBC) boundary conditions at the tips) and the black dashed line represents the present 3D CFD method at $Re=2\times 10^4$ 91

Figure 3. 12 Validation results for a rigid blade turbine - comparison with towing tank data (Exp.) by Strickland et al. (1980), Free Vortex Model (VDART) by Strickland et al. (1979) and vortex method combined with finite element analysis (FEVDTM) by Ponta and Jacovkis (2001). 93

Figure 3. 13 Validation results of 2D free oscillating cylinder with (a) non-dimensionalized displacement amplitude and (b) non-dimensionalized displacement frequency against Re 95

Figure 3. 14 Validation results of 2D inviscid flutter of a sweptback wing case for the flutter speed index v_f under Mach number of 0.75..... 97

Figure 3. 15 Dimensions of AGARD 445.6 wing. (From Akgun et al., 2005)..... 98

Figure 3. 16 Validation results of the AGARD wing flutter case for the first mode generalized displacement against with time compared with Yang et al. (2004)..... 100

Figure 3. 17 Validation results of the AGARD wing flutter case for the pressure coefficient comparison between the BEM method (black dashed line based on Sadeghi, 2004) and the CVT method (red dash dotted line computed by the present study)..... 101

Figure 3. 18 Validation on a flexible 3D plunging wing in water flow with $Re=3\times 10^4$; $AR=3.0$; $h_0=1.75\times 10^{-2}$ m; $f_0=1.74$ Hz; $\Pi=2.14\times 10^2$; $E=210$ GPa and Density Ratio (DR)=7.8 – compared with Heathcote et al. (2008) and Gordnier et al. (2010). 103

Figure 3. 19 Validation results of wing lift coefficient on a flexible 3D plunging wing ($Re=3.0\times 10^4$) $AR=3.0$; $h_0=1.75\times 10^{-2}$ m; $f_0= 1.74$ Hz; $\Pi=4.07\times 10^1$; $E=70$ GPa and Density Ratio (DR)=2.7 – compared with Heathcote et al. (2008) and Gordnier et al. (2010). 103

Figure 3. 20 Validation results of wing tip edge displacement on a flexible 3D plunging wing ($Re=3.0\times 10^4$) $AR=3.0$; $h_0=1.75\times 10^{-2}$ m; $f_0= 1.74$ Hz; $\Pi=4.07\times 10^1$; $E=70$ GPa and Density Ratio (DR)=2.7 – compared with Heathcote et al. (2008) and Gordnier et al. (2010). 104

Figure 3. 21 Boundary conditions test for the tip boundaries comparison with a present 2D CFD method (achieved with a 3D method using Symmetry Boundary Condition (SBC) boundary conditions at the tips for a rigid oscillating foil at $f^*=0.18$ and $\theta_0 = 60^\circ$). 106

Figure 3. 22 Flow chart, Computational domain and mesh movement for vertical axis turbine case: (a) flow chart of the present FSI solver, (b) 3D mesh topology, (c) 3D fluid (cyan, yellow, blue and green represent different blocks) and structure (red colour) meshes and corresponding CVT mapping example, (d) 2D Fluid mesh and (e) ~ (h) mesh movement during one turbine revolution (red circle represents the mesh rotation centre; green represents turbine blade). 109

Figure 3. 23 Tests for the sensitivity of time step size. 110

Figure 3. 24 Diagrammatic sketch of external loads (red arrow) and constrains (cyan arrow) conditions at each cell for ANSYS structural solver. 111

Figure 4. 1 The active oscillating turbine blade in the present study. 113

Figure 4. 2 Schematic diagram of flow configuration. 115

Figure 4. 3 Comparison of instantaneous blade moment coefficient against time for two different blade turbines ($\lambda=1.572$). For oscillating blade, $\beta_0=30^\circ$; $n_t=3.0$ 117

Figure 4. 4 Comparison of instantaneous blade lift coefficient against time for two different blade turbines ($\lambda=1.572$). For oscillating blade, $\beta_0=30^\circ$; $n_t=3.0$ 117

Figure 4. 5 Comparison of vortex contour within one revolution for fixed and oscillating flap turbine at $\lambda=1.572$. (a) $t/T_{turb}=5/12$, fixed flap; (b) $t/T_{turb}=6/12$ fixed flap (c) $t/T_{turb}=7/12$, fixed flap; (d) $t/T_{turb}=5/12$, oscillating flap; (e) $t/T_{turb}=6/12$, oscillating flap; (f) $t/T_{turb}=7/12$, oscillating flap. For oscillating flap, $\beta_0=30^\circ$; $n_t=3.0$. 119

Figure 4. 6 Oscillating flap amplitude effect on the instantaneous blade momentum coefficient and time-averaged power coefficient. ($n_t=3$) (a) Instantaneous blade moment coefficient against time; (b) Time-averaged power coefficient against tip speed ratio. 122

Figure 4. 7 Comparison of vortex contour for an oscillating flap blade with oscillating amplitude of $\beta_0=15^\circ$ and $\beta_0=30^\circ$ ($\lambda=2.2$; $n_t=3$) (a) $t/T_{turb}=4/12$ and $\beta_0=15^\circ$; (b) $t/T_{turb}=5/12$ and $\beta_0=15^\circ$; (c) $t/T_{turb}=6/12$ and $\beta_0=15^\circ$; (d) $t/T_{turb}=4/12$ and $\beta_0=30^\circ$; (e) $t/T_{turb}=5/12$ and $\beta_0=30^\circ$; (f) $t/T_{turb}=6/12$ and $\beta_0=30^\circ$ 123

Figure 4. 8 Oscillating flap frequency effect on the instantaneous blade momentum coefficient and time-averaged power coefficient. ($\beta_0=15^\circ$) (a) Instantaneous blade moment coefficient against time; (b) Time-averaged power coefficient against tip speed ratio. 125

Figure 5. 1 Schematic diagram for (a) oscillating energy device (b) upstroke (c) downstroke. 129

Figure 5. 2 Structure of (a) rainbow trout fin, (b) hawkmoth wing, (c) two-dimensional model of leading edge control model (top view from Fig. 2 (a)), (d) two-dimensional model of trailing edge control model (right view from Fig. 2 (b)), (e) Schematic illustrating fish swimming in group, (f) Two-dimensional twin-wing parallel configuration. 131

Figure 5. 3 Snapshots for four models over one flapping cycle..... 134

Figure 5. 4 Comparison of (a) power coefficient and (b) efficiency among various flexible/rigid modes with nominal effective AOA of 10° . ($h_0/c=0.5$ ■: rigid, ▲: LEC, ▼: TEC and ►: Integrated) and ($h_0/c=1.0$ □: rigid, Δ: LEC, ▽: TEC and ▷: Integrated); $\alpha_f=30^\circ$ (LEC) and $d_b/c=0.15$ (TEC) and $\alpha_f=30^\circ$ plus $d_b/c=0.15$ (integrated model). 138

Figure 5. 5 Instantaneous vortex contours over half a cycle for various flexible/rigid wings $h_0/c=1.0$; $f^*=0.2$; nominal effective AOA of 10° ; $\alpha_f=30^\circ$ (LEC) and $d_b/c=0.15$ (TEC) and $\alpha_f=30^\circ$ plus $d_b/c=0.15$ (integrated model)..... 140

Figure 5. 6 Instantaneous lift coefficient and moment coefficient (a) lift coefficient, (b) moment coefficient $h_0/c=1.0$; $f^*=0.2$; nominal effective AOA of 10° ; $\alpha_f=30^\circ$ (LEC) and $d_b/c=0.15$ (TEC) and $\alpha_f=30^\circ$ plus $d_b/c=0.15$ (integrated model). In (b), solid line:

rigid c_m , dashed line: LEC c_m , dash dot line: TEC c_m , dash double dot line: integrated c_m , ■: rigid $d\theta/dt$, Δ : LEC $d\theta/dt$, ∇ : TEC $d\theta/dt$ and \triangleright : integrated $d\theta/dt$ 142

Figure 5. 7 Instantaneous power coefficient with nominal effective AOA of 10° and $h_0/c=1.0$; $f^*=0.2$. For a flexible wing $\alpha_f=30^\circ$ (LEC) and $d_b/c =0.15$ (TEC) and $\alpha_f=30^\circ$ plus $d_b/c =0.15$ (integrated model). 143

Figure 5. 8 Foil local AOA along chord-wise direction at $\theta_i(t)=\theta_0$ for different flexible coefficients (n) at nominal effective AOA $\alpha_0=10^\circ$. (a) LEC, $\alpha_f=30^\circ$. (b) TEC, $d_b/c=0.15$. (c) Integrated model $\alpha_f=30^\circ$ and $d_b/c=0.15$ 145

Figure 5. 9 Various LEC parameters' effect on the cycle-mean efficiency at nominal effective AOA $\alpha_0=10^\circ$. (a) Flexible coefficient (n), (b) leading edge local AOA α_f . ($h_0/c=0.5$). 148

Figure 5. 10 Instantaneous c_l , dh/dt , c_m and $d\theta/dt$ (LEC $h_0/c=0.5$; $f^*=0.15$) at nominal effective AOA $\alpha_0=10^\circ$. (a) Flexible coefficient effect and (b) α_f effect. 149

Figure 5. 11 Effect of TEC parameters on the time-mean efficiency at nominal effective AOA $\alpha_0=10^\circ$. (a) Flexible coefficient (n) and (b) trailing edge displacement (d_b/c) ($h_0/c=0.5$). 150

Figure 5. 12 Instantaneous c_l , dh/dt , c_m and $d\theta/dt$ (TEC with $h_0/c=0.5$; $f^*=0.15$) at nominal effective AOA $\alpha_0=10^\circ$. (a) flexible coefficient effect and (b) trailing edge deformation effect. Open square with lines: $d\theta/dt$ 151

Figure 5. 13 Comparison of time-mean efficiency versus f^* between integrated flexible wing and a rigid wing for various α_0 (■: rigid $\alpha_0=10^\circ$, ▲: rigid $\alpha_0=5^\circ$, ▼: rigid $\alpha_0=0^\circ$, □: integrated $\alpha_0=10^\circ$, Δ : integrated $\alpha_0=5^\circ$, ∇ : integrated $\alpha_0=0^\circ$ and \triangleright : integrated $\alpha_0=-10^\circ$) with $h_0/c=0.5$; $\alpha_f=30^\circ$; $d_b/c=0.15$; $n=3$ for leading edge and $n=5$ for trailing edge. 153

Figure 5. 14 Comparison of time-mean efficiency versus f^* under twin rigid foils configuration for different gap ratio with $h_0/c=0.5$ at nominal effective AOA $\alpha_0=10^\circ$. 154

Figure 5. 15 Instantaneous lift coefficient and moment coefficient for rigid single and twin foil at nominal effective AOA $\alpha_0=10^\circ$ with $h_0/c=0.5$ and $f^*=0.2$ 155

Figure 5. 16 Comparison of instantaneous vortex contours at nominal effective AOA $\alpha_0=10^\circ$ for (a) single rigid wing and (b) parallel rigid twin-wings ($S_f = 3$) with $h_0/c=0.5$; $\alpha_0=10^\circ$ and $f^*=0.2$ 156

Figure 5. 17 Comparison of time-mean efficiency versus f^* under twin wing configuration (TEC model ($d_b/c=0.05$) vs. rigid model with $h_0/c=0.5$ and $S_f = 3$). ■: rigid, $\alpha_0=10^\circ$, ▲: rigid, $\alpha_0=5^\circ$, ▼: rigid, $\alpha_0=0^\circ$; □: TEC, $\alpha_0=10^\circ$, Δ: TEC, $\alpha_0=5^\circ$, ∇: TEC, $\alpha_0=0^\circ$ 157

Figure 6. 1 Sketches and principles for (a) and (b) spring controlled blade and spring restoring moment theory (Sun et al., 2009), (c) vertical axis turbine blade with passive oscillation flap. 162

Figure 6. 2 Comparison of time-averaged power coefficient against tip speed ratio for fixed, active oscillating flap and passive oscillating flap turbine. For the active oscillating flap turbine, $\beta_0=15^\circ$ and $n_t=3$ 164

Figure 6. 3 Instantaneous active and passive flap angle during one period for tip speed ratio $\lambda=0.8, 0.99, 1.572$ and 2.2 . For active oscillating flap turbine, $\lambda=2.2$; $\beta_0=15^\circ$ and $n_t=3$ 165

Figure 6. 4 Comparison of instantaneous blade moment coefficient against time for fixed, active oscillating flap and passive oscillating flap turbine with $\lambda=2.2$. For active oscillating flap turbine, $\beta_0=15^\circ$ and $n_t=3$ 166

Figure 6. 5 Comparison of vortex contour within one revolution for active and passive oscillating flap turbines at $\lambda=2.2$. For active oscillating flap turbines, $\beta_0=15^\circ$ $n_t=3$ (a) $t/T_{turb}=4/12$ and active flap; (b) $t/T_{turb}=5/12$ and active flap; (c) $t/T_{turb}=6/12$ and active flap; (d) $t/T_{turb}=4/12$ and passive flap; (e) $t/T_{turb}=5/12$ and passive flap; (f) $t/T_{turb}=6/12$ and passive flap..... 167

Figure 6. 6 3D VAT model for (a) Hameed and Afaq (2013) and (b) in the present simulation..... 170

Figure 6. 7 Sketch of turbine blade forces, resultant velocity and angle of attack under local body fitted coordinate $x_l o_l y_l$ 170

Figure 6. 8 Examples of comparison between blade total force coefficient and blade centrifugal force coefficient with $l_{st}/c=10/3$, $\Pi=3.19 \times 10^3$ 173

Figure 6. 9 VAT blade design for the present simulation. 174

Figure 6. 10 First four mode shapes with $l_{st}/c=10/3$, $\Pi=3.19 \times 10^3$ 178

Figure 6. 11 Time histories of the generalized displacements of the first ten modes with $l_{st}/c=10/3$, $\Pi=3.19 \times 10^3$ and $\lambda=5.5$ 179

Figure 6. 12 Power coefficient vs. tip speed ratio for rigid blade turbine and c_{op} value for $\lambda=3.5$, 5.5 and 7.5. 179

Figure 6. 13 Instantaneous non-dimensionalized displacement at (a) and (c) $H/c=0$ and (b) and (d) $H/c=5$ for different tip speed ratios with $l_{st}/c=10/3$, $\Pi=3.19 \times 10^3$. (a) and (b) time is non-dimensionalized by blade mode cycles and (c) and (d) time is non-dimensionalized by turbine revolution. 182

Figure 6. 14 Instantaneous twist angle at (a) $H/c=0$ and (b) $H/c=5$ for different tip speed ratios with $l_{st}/c=10/3$, $\Pi=3.19 \times 10^3$. (a) and (b) time is non-dimensionalized by blade mode cycles and (c) and (d) time is non-dimensionalized by turbine revolution. 184

Figure 6. 15 Non-dimensionalized bending and twist displacement contour with $l_{st}/c=10/3$, $\Pi=3.19 \times 10^3$ and $\lambda=5.5$ viewing from the inner side of the blade. 185

Figure 6. 16 Non-dimensionalized bending and twist displacement contour with $l_{st}/c=10/3$, $\Pi=3.19 \times 10^3$ and $\lambda=7.5$ viewing from the inner side of the blade. 185

Figure 6. 17 Contour of stress distribution over the blade under the largest external load condition for the flexible blade for different tip speed ratios with $l_{st}/c=10/3$ and $\Pi=3.19 \times 10^3$ viewing from the inner side of the blade. 188

Figure 6. 18 Blade bending-twist motion and pressure distribution for different time instants with $l_{st}/c=10/3$, $\Pi=3.19 \times 10^3$ and $\lambda=5.5$ 189

Figure 6. 19 Pressure distribution with $l_{st}/c=10/3$, $\Pi = 3.19 \times 10^3$ and $\lambda=5.5$. (a) $t/T_{turb}=3/8$ and (b) and (c) $t/T_{turb}=5/8$ 191

Figure 6. 20 Pressure coefficient distribution at (a) $t/T_{turb}=3/8$ and (b) $t/T_{turb}=5/8$ with $l_{st}/c=10/3$, $\Pi=3.19 \times 10^3$ and $\lambda=5.5$ 192

Figure 6. 21 Pressure distribution at $t/T_{turb}=5/8$ for different tip speed ratios with $l_{st}/c=10/3$ and $\Pi=3.19 \times 10^3$ 193

Figure 6. 22 Structure characteristics with $l_{st}/c=10/3$, $\Pi=9.37 \times 10^2$ and $\lambda=5.5$. (a) and (b) time is non-dimensionalized by blade mode periods and (c) and (d) time is non-dimensionalized by turbine period. 196

Figure 6. 23 Non-dimensionalized bending and twist displacement contour with $l_{st}/c=10/3$, $\Pi=9.37 \times 10^2$ and $\lambda=5.5$ viewing from the inner side of the blade. 196

Figure 6. 24 Contour of stress distribution over the blade under the largest external load condition of the flexible blade with $l_{st}/c=10/3$, $\Pi=9.37 \times 10^2$ and $\lambda=5.5$ viewing from the inner side of the blade. 197

Figure 6. 25 Blade bending-twist motion and pressure distribution for different time instants with $l_{st}/c=10/3$, $\Pi=9.37 \times 10^2$ and $\lambda=5.5$ 197

Figure 6. 26 Pressure distribution at (a) $t/T_{turb}=1/8$ and (b) $t/T_{turb}=5/8$ with $l_{st}/c=10/3$, $\lambda=5.5$ and $\Pi=9.37 \times 10^2$ compared with $\Pi=3.19 \times 10^3$ 198

Figure 6. 27 Structure characteristics with $l_{st}/c=0$, $\Pi=3.19 \times 10^3$ and $\lambda=5.5$. (a) and (b) time is non-dimensionalized by blade mode periods and (c) and (d) time is non-dimensionalized by turbine revolution..... 201

Figure 6. 28 Non-dimensionalized bending and twist displacement contour with $l_{st}/c=0$, $\Pi=3.19 \times 10^3$ and $\lambda=5.5$ viewing from the inner side of the blade. 201

Figure 6. 29 Contour of stress distribution over the blade under the largest external load condition for the flexible blade turbine with $l_{st}/c=0$, $\Pi=3.19\times 10^3$ and $\lambda=5.5$ viewing from the inner side of the blade..... 202

Figure 6. 30 Blade bending-twist motion and pressure distribution for different time instants with $l_{st}/c=0$, $\Pi=3.19\times 10^3$ and $\lambda=5.5$ 202

Figure 6. 31 Pressure distribution at (a) $t/T_{turb}=1/8$ and (b) $t/T_{turb}=4/8$ with $\lambda=5.5$, $\Pi=3.19\times 10^3$ and $l_{st}/c=0$ compared with $l_{st}/c=10/3$ 203

Figure 6. 32 Instantaneous moment coefficient at $\lambda=5.5$ 204

Figure 6. 33 Vorticity contour at $t/T_{turb}=5/8$ and $\lambda=5.5$ 204

Figure 6. 34 Time averaged power coefficient. 205

Figure 7. 1 Schematic diagram of oscillating energy device. 209

Figure 7. 2 (a) Inner structural design for trailing edge flexible foil and (b) flexible foil displacement. 211

Figure 7. 3 The overall performance of a flexible oscillating foil device with $h_0/c=1.0$. ● Cu $\theta_0=60^\circ$; ▲ WC $\theta_0=60^\circ$; ■ Rigid $\theta_0=60^\circ$; □ Rigid $\theta_0=75^\circ$; △ WC $\theta_0=75^\circ$ 214

Figure 7. 4 Time histories for foils with Cu and WC stiffeners at $f^*=0.18$ and $\theta_0=60^\circ$ 216

Figure 7. 5 Vorticity contours and schematic representation of foil kinematics for rigid and flexible foils at $f^*=0.18$; $\theta_0 =60^\circ$ in half an oscillating period. In the schematic plot, the flexible foil is shown with blue solid lines, and the rigid foil is shown as red dashed lines. 217

Figure 7. 6 Young's modulus effect on the efficiency of a flexible foil at $f^*=0.18$ and $\theta_0 =60^\circ$ 220

Figure 7. 7 Trailing edge deformations of a flexible foil with different Young's modulus coefficient at $f^*=0.18$ and $\theta_0=60^0$	221
Figure 7. 8 Time histories for Young's modulus effect at $f^*=0.18$ and $\theta_0=60^0$	223
Figure 7. 9 Density ratio effect on the efficiency of a flexible foil at $f^*=0.18$ and $\theta_0=60^0$	225
Figure 7. 10 Density ratio effect at $f^*=0.18$ and $\theta_0=60^0$	227
Figure 7. 11 Time histories with low density ratios ($DR=8.9$ and 30) at $f^*=0.18$ and $\theta_0=60^0$	228
Figure 7. 12 Time histories with large density ratios ($DR=700$ and 1200) at $f^*=0.18$ and $\theta_0=60^0$	230
Figure 7. 13 Vorticity contours for density ratio effect at $f^*=0.18$ and $\theta_0=60^0$ in half an oscillating period.	231

List of Tables

Table 3. 1 Main geometry and flow conditions for Darrieus wind turbine.....	66
Table 3. 2 Mesh dependence test.....	67
Table 3. 3 Unsteady time step size and turbulent model test.	68
Table 3. 4 Summary of validation cases for in-house FSI code.....	82
Table 3. 5 Turbulence $k-\omega$ model validation with Kinsey and Dumas (2012a).....	91
Table 3. 6 Validation results for AGARD wing mode frequency prediction by using ANSYS and beam analytical solution compared with published results.	99
Table 4. 1 Operating conditions of WANXIANG II power station (From Sun, 2007).	115
Table 4. 2 Comparison of key performance parameters for two different turbines	118
Table 4. 3 Summary of numerical cases for oscillating flap.	120
Table 5. 1 Various parameters investigated in the present study.	135
Table 7. 1 Case summary for real materials.	211
Table 7. 2 Case summary for virtual materials used to test Young's modulus effect. The Poisson ratio (ν) for all cases is 0.34.	219
Table 7. 3 Case summary for virtual materials used to test density ratio effect. The effective stiffness (II) and Poisson ratio (ν) for all cases are 5.25×10^1 and 0.34 respectively.	223

PART I: Introduction, Literature Review and Methodology

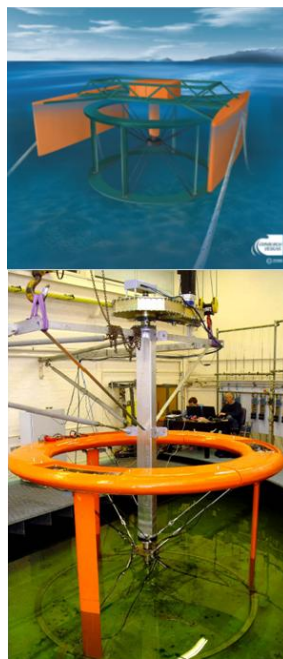
Chapter 1: Introduction

1.1 Introduction

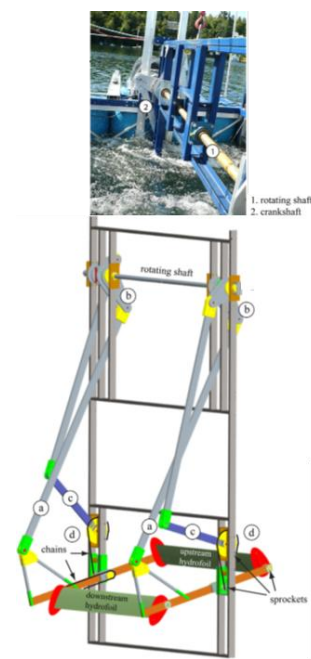
In the past decades, the renewable energy industry has developed rapidly due to the conventional energy resource shortage and less environmental impact (such as no greenhouse gases). Among various ocean and offshore renewable energies, tidal energy and wind energy have their distinct superiorities over other types of renewable energies. They are less sensitive to climate change and are predictable in both space and time domains. Tidal/wind turbines are becoming one of the most efficient devices which transform tidal/wind energy into mechanical power (Nicholls-Lee et al., 2008).



(a) HAT example
(Brøndsted et al., 2005)



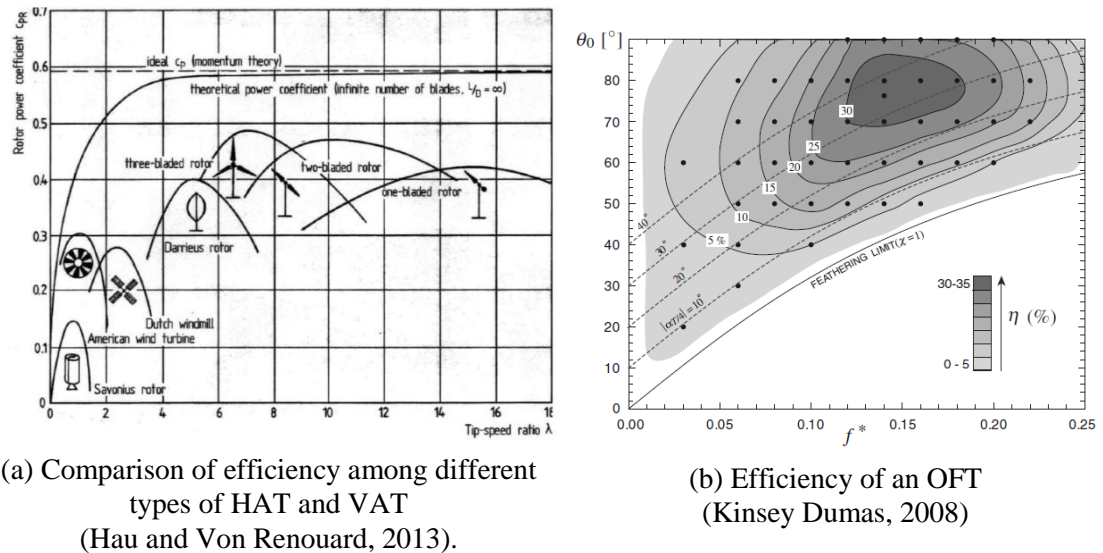
(b) VAT example
(Gretton, 2009)



(c) OFT example
(Kinsey et al., 2011)

Figure 1. 1 Three different types of turbine for tidal/wind energy with (a) HAT (Brøndsted et al., 2005), (b) VAT (Gretton, 2009) and (c) OFT (Kinsey et al., 2011).

Most of the existing tidal/wind renewable energy devices can be classified into three groups, i.e., Horizontal Axis Turbine (HAT), Vertical Axis Turbine (VAT) and Oscillating Foil Turbine (OFT). Examples of these devices are shown in Fig. 1.1 (a)-(c).



(a) Comparison of efficiency among different types of HAT and VAT (Hau and Von Renouard, 2013).

(b) Efficiency of an OFT (Kinsey Dumas, 2008)

Figure 1. 2 Comparison of efficiency among different types of (a) HAT and VAT (Hau and Von Renouard, 2013) and (b) OFT (Kinsey Dumas, 2008).

A HAT is a type of energy turbine where the main rotor shaft is horizontally installed. The blades, shaft and generator must be installed onto a tower and the rotating disk must be towards the fluid flow to gain the maximum extraction efficiency (Drewry and Georgiou, 2007). HAT is commonly used in the modern renewable industry as it has already been well developed. As shown in Fig. 1.2 (a), the working tip speed ratio for HAT is around 6.0 to 18.0 depending on the blade numbers of the HAT. The peak power coefficient could reach 0.48.

In comparison with the HAT, VAT has many advantages, such as its simple blade design, its ability to function in all current flow directions without being pointed in the flow direction and its non-sensitivity to water depth for tidal or water current

usage. Nonetheless, the efficiency of the existing H-shaped VAT is still relatively low compared to the horizontal axis turbine. Therefore, it is necessary and there are huge potential benefits in carrying out further research in order to enhance VAT's efficiency via various mechanical and control methods (Gretton et al., 2009; Gretton, 2009; Scheurich and Brown, 2013; Wenlong et al., 2013; Micallef et al., 2014). As shown in Fig. 1.2 (a), the working tip speed ratio for VAT is smaller than for HAT and the peak power coefficient is also lower than that of HAT.

The use of vertical axis turbines can be dated back to 2000 years ago. The first description on the use of VAT was in a Chinese book in 1219 (Liu, 2011). Savonius invented the first modern drag driven vertical axis turbine in 1929 (Savonius, 1931). In 1931, French engineer Darrieus invented and patented both troposkien and straight blade vertical axis turbines in the U.S (Darrieus, 1931). In the 1970s, Canada and America conducted several investigations into the power prediction using experimental and numerical methods (South and Rangi, 1973; Templin, 1974; Blackwell, 1974; Strickland, 1975). Many improvements have been achieved in the vertical axis turbine by past researchers since then. However, the energy extraction efficiency of VAT has not been sufficiently high until now. Modern VAT can be grouped into two categories based on the source of the rotating moment. One of them is drag driven turbines; the other is lift driven turbines. The drag coefficient of the drag driven turbine blade, which moves towards the turbine wake, should be much larger than that of other blades in the same turbine, so the rotating moment can be generated (Liu, 2011). The drag driven vertical turbine has a good performance at the small tip speed ratio. Its peak efficiency is around 15%. The blade of a lift driven vertical turbine usually has a cross section of airfoil. It can generate a rotational

moment by the lift force of the blade. The working tip speed ratio and the peak efficiency are all higher than that of a drag driven vertical axis turbine. The lift driven turbine contains a curved bladed type (such as a troposkien shape) and a straight bladed type based on the shape of the blade. A straight bladed type is much simpler in terms of manufacturing but has a larger bending stress than that of the curved bladed. In the present research, the straight blade lift driven vertical axis turbine is mainly considered.

The bio-inspired tidal energy harvester, an OFT imitating fish fins or insect wings and utilizing their flapping motions to extract energy from their surrounding fluid, is one of the most novel devices. Compared with the traditional rotating turbine, the oscillating foil turbines presents several distinguishing characteristics, such as its suitability in shallow water, the mitigation of centrifugal force/stress and low noise during its operation (Xiao and Zhu, 2014). Since the initial development of McKinney and DeLaurier (1981), in the past few years oscillating foil turbines have been extensively studied because of the growing interest in biomimetics and the improved knowledge of the unsteady fluid dynamics involved in flying and swimming motions (Young et al., 2014). In the present research, the motions of OFT are prescribed as sinusoidal pitch and plunge motions to simplify the physical model based on the motion of self-sustained OFT. Since the present research is focus on the energy extraction efficiency enhancement of OFT, energy consumption by the active flow control is ignored. Most existing investigations are limited to rigid oscillating foils (Kinsey and Dumas, 2008; 2012a; 2012b; 2012c; Xiao and Liao, 2010; Xiao et al., 2012; Michael et al., 2010). As shown in Fig. 1.2 (b), a typical OFT works on the

reduced frequency of 0.05-0.25 and reaches its best performance around 0.15. The peak efficiency of OFT is up to 35% based on Fig. 1.2 (b).

Present studies are focused on the enhancement of energy extraction efficiency for VAT and OFT because of their lower efficiency compared with HAT. There are several methods to enhance the energy extraction efficiency of VAT and OFT, such as the variable pitch method and the flow channel and duct method for VAT and the non-sinusoidal pitch method for OFT. However, none of these methods focus on bio-inspired or biomimics techniques. Biomimetics is the study of the mechanisms evolved in nature's biological system, and utilising them for various applications. Over the past 10 years, research studies on the aero-/hydro-dynamics of biomimetics have been carried out rapidly due to increasing demands from the aero/marine industry and the defence sector. There are lots of interesting phenomena in the area of fish fin/tail motion, insect or butterfly wing flapping motion, etc. Typical examples include insect wings in hovering mode and subcarangiform fish caudal/tail fins in propelling and manoeuvring mode. The study on the flapping wing aerodynamics/hydrodynamics has already been widely applied in the design of engineering devices, such as Micro Aerial Vehicle (MAV), Autonomous Underwater Vehicles (AUV) and robotic fish (Sfakiotakis et al., 1999; Triantafyllou et al., 2004; Liu, 2005; Fish and Lauder, 2006). The present research aimed to apply biomimetics features such as the fish fin/tail motion and the flexibility of insect wings in renewable devices (VAT and OFT) to determine innovative methods to enhance energy extraction efficiency.

In recent years, to achieve the large power output requirement and to reduce environmental impact, there has been an increasing trend to develop large scale tidal/wind turbines and move them far away to offshore areas (Hansen, 2013 and Lachenal et al., 2013). Compared to the small scale and near shore devices, these large scale turbine blades/rotors may experience a highly unsteady load due to turbulent wind flow in the offshore area, especially in extreme weather conditions. This may lead to the possible deformation of blades which reduces the turbines structural endurance. Several research studies have aimed to estimate and reduce the blade stress for the large scale HAT by using composite materials (Kong et al., 2005; Shokrieh and Rafiee, 2006; Barlas et al., 2008). The external load and blade stress of VAT are much more pronounced than that of HAT, since the VAT blade encounters radial centrifugal force. However, research on the estimation and reduction of the VAT blade stress is still limited. The present research investigated the blade structural deflection characteristics associated with bending and twisting for the VAT. External unsteady loads on the blade surface and the power performance of VAT were first studied, which have been further extended to a blade stress analysis.

All the study methods for the renewable turbine can be classified into three general categories, which are numerical investigation, analytical investigation and experiential investigation. Within the category of analytical investigation for the renewable turbine, there are three main methods, i.e. momentum models, Vortex models and Cascade models. Present studies use the numerical CFD method for all the investigations and tests. The detailed equations and discussions on the CFD method are included in Chapter 3.

1.2 Working principle of renewable turbine

1.2.1 Working principle of VAT

The diagram of a vertical axis turbine is shown in Fig. 1.3 (Gretton, 2009) and the turbine is rotating with an angular velocity ω in the incoming flow. The present research focuses on the steady state of the turbine (i.e. when the VAT reaches and remains at a constant rotational speed). The startup and cutoff stages are ignored. Thus, the angular velocity ω is fixed with time but varies for different working conditions (or calculation cases).

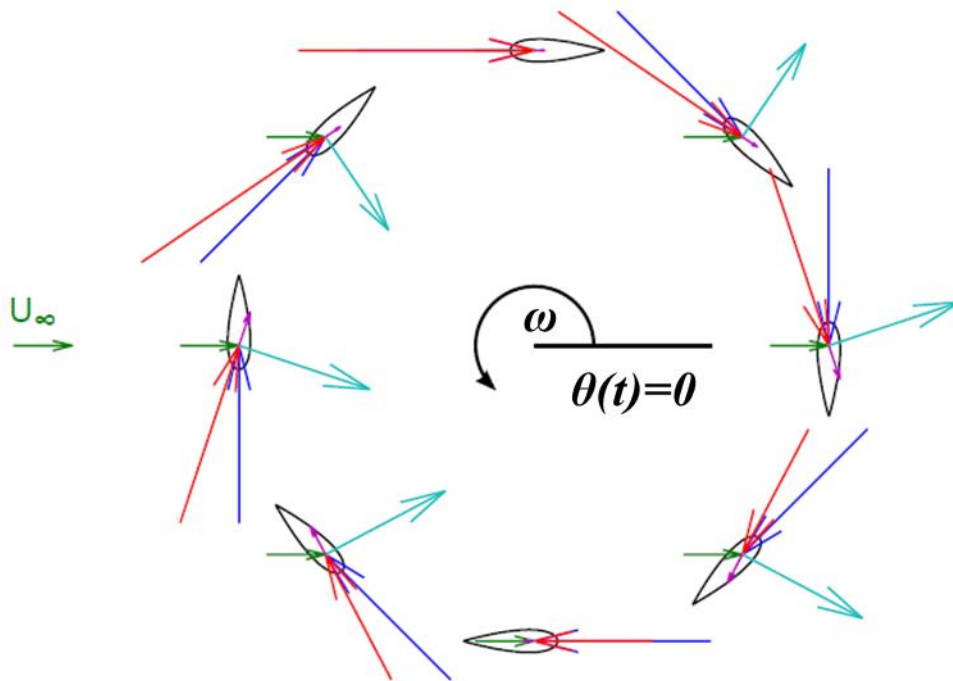


Figure 1. 3 The diagram of a vertical axis turbine under a tip speed ratio of 3.0 with instantaneous velocities and forces. Blue arrow: induced velocity; Green arrow: free stream velocity; Red arrow: resultant velocity; Cyan arrow represents lift force and magenta arrow is drag force (Gretton, 2009).

In order to quantify the rotational speed of the turbine, the non-dimensionalized parameter tip speed ratio λ is defined as follows:

$$\lambda = \frac{\omega R}{U}, \quad (1.1)$$

where R is the turbine radius, U is the velocity of the incoming flow.

Several key parameters which quantify the turbine energy extraction performance are described below.

The blade moment coefficient c_m is defined as:

$$c_m = \frac{M}{\rho_f U^2 R^2 H}, \quad (1.2)$$

where M is the blade moment relative to the turbine pitch centre.

The power coefficient c_{op} is determined by

$$c_{op} = \frac{\sum M \omega}{\rho_f U^3 R H}. \quad (1.3)$$

The blade total fluid force coefficient c_f is defined as:

$$c_f = \frac{F_f}{\frac{1}{2} \rho_f U^2 c H}. \quad (1.4)$$

The blade total force coefficient c_{ft} which contains both the fluid force and centrifuge force is defined as:

$$c_{ft} = \frac{F_{ft}}{\frac{1}{2}\rho_f U^2 cH}. \quad (1.5)$$

The blade lift coefficient c_l and blade drag coefficient c_d are defined as:

$$c_l = \frac{\text{lift force}}{\frac{1}{2}\rho_f U^2 cH}, \quad (1.6)$$

and

$$c_d = \frac{\text{drag force}}{\frac{1}{2}\rho_f U^2 cH}. \quad (1.7)$$

The blade normal force coefficient c_n and thrust force coefficient c_t are defined as:

$$c_n = \frac{F_n}{\frac{1}{2}\rho_f U^2 cH}, \quad (1.8)$$

and

$$c_t = \frac{F_t}{\frac{1}{2}\rho_f U^2 cH}. \quad (1.9)$$

where F_n and F_t are the blade normal force and blade thrust force, respectively.

The Reynolds number for the vertical turbine is defined as:

$$Re = \frac{R\omega c}{\nu}, \quad (1.10)$$

where ν is the kinematic viscosity of fluid flow.

1.2.2 Working principle of OFT

The configuration of the OFT is shown in Fig. 1.4 (Kinsey and Dumas, 2008), where an oscillating NACA0012 foil is immersed in a uniform viscous fluid flow. Practically, the device is forced to pitch/rotate on a fixed axis, so the generated unsteady fluid-dynamic force around the foil and fluid surrounding it activates the foil's up and down heave motion. The kinematic energy of the incoming flow is converted to the mechanical energy associated with the heave motion via a damper, and then transformed into electricity by a generator.

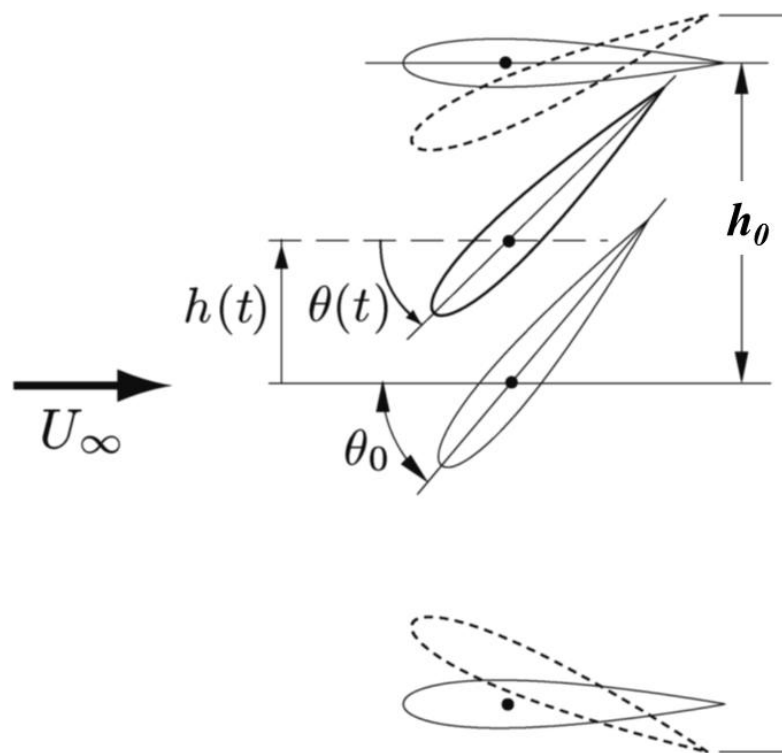


Figure 1. 4 The configuration of an oscillating foil turbine (Kinsey and Dumas, 2008).

To simplify the problem, most existing work assumes that both the pitch and heave motion are predetermined, and thus the power estimated is solely the available hydrodynamic power, ignoring the actuating mechanism in the system (McKinney

and DeLaurier, 1981; Jones and Platzer, 1997; Jones et al., 2003; Kinsey and Dumas, 2008, 2012a, 2012b; Xiao et al., 2012). In this context, the energy extraction is obtained through a foil undergoing a combined pitch and heave motion with the following specified equations:

$$h(t) = h_0 \sin(\omega t), \quad (1.11)$$

$$\theta(t) = \theta_0 \sin(\omega t + \varphi), \quad (1.12)$$

where h_0 and θ_0 are the amplitude of heave and pitch, respectively. φ , which has a fixed value of $-\pi/2$ during the current research, is the phase difference between the heave and pitch motions. The pitch axis is located at one quarter chord length from the leading edge of the foil (the aerodynamic centre).

The flapping reduced frequency f^* is defined as:

$$f^* = \frac{f_0 c}{U}, \quad (1.13)$$

where f_0 is the frequency of the oscillating wing and U is the freestream velocity.

With a flapping wing problem, one of the most important kinematic parameters is the effective Angle of Attack (AOA), which is determined by a blended impact from the wing pitch and heave motion. This is defined with the quasi-steady assumption (ignore the historical and local fluid effects) as:

$$a_{eff}(t) = \theta(t) - \arctan\left(\frac{\dot{h}(t)}{U}\right). \quad (1.14)$$

The maximum effective AOA, which is also sometimes called nominal effective

AOA (α_0), is the maximum pitch angle a wing can reach during each cycle, i.e.

$\theta(t)=\theta_0$, therefore,

$$\alpha_0 = \theta_0 - \arctan\left(\frac{\omega h_0}{U}\right). \quad (1.15)$$

Previous research shows that relying on the sign of α_0 , a flapping wing can either work in an energy consumption regime as a propeller ($\alpha_0 < 0$) or in an energy extraction regime as an oscillating wing energy device ($\alpha_0 > 0$). A mutual stable status is reached when α_0 is equal to zero, which is normally called the feathering state (Anderson et al., 1998; Zhu, 2011; Kinsey and Dumas, 2008). One of the objectives of the current research is to examine whether an oscillating flexible wing could diminish its pitching amplitude in the feathering state (the nominal effective AOA boundary between the propulsion mode and energy extraction mode) relative to a rigid wing. With this success, the energy input to drive the pitching motion can be significantly reduced.

The non-dimensionalized instantaneous power coefficient c_{op} is determined by

$$c_{op} = \frac{p_o}{\frac{1}{2}\rho_f U^3 c} = \frac{1}{U^3} \left[c_l(t) \frac{dh(t)}{dt} + c c_m(t) \frac{d\theta(t)}{dt} \right], \quad (1.16)$$

where $c_l(t)$ and $c_m(t)$ are the instantaneous lift and moment coefficient, respectively, and p_o is the instantaneous power.

The total energy extraction efficiency η is defined as

$$\eta = \frac{\bar{p}_o}{\frac{1}{2}\rho_f U^3 A} = \bar{c}_{op} \frac{c}{A}, \quad (1.17)$$

where A is the sweep area of the oscillating wing.

1.2.3 Comparison among different turbines under body fitted coordinate

The three types of turbine (i.e. HAT, VAT and OFT) can operate based on blade rotating or flapping motions. A body fitted coordinate $x_l o_l y_l$ is established for the turbine blade. The original point of the body fitted coordinate is fixed on the blade centre line and $\frac{1}{4}$ chord length from the turbine blade leading edge. The body fitted coordinate is attached to the turbine blade with corresponding heaving, rotating and/or pitching motions under the global coordinate. The blade body fitted coordinate $x_l o_l y_l$ and corresponding turbine blade forces, resultant velocity and angle of attack of the blade are shown in Fig. 1.5. The mathematical functions of blade angle of attack and blade resultant velocity for HAT, VAT and OFT are as follows:

$$\begin{cases} \alpha(t) = C_1 \\ V_t(t) = C_2 \end{cases} \quad (\text{HAT}), \quad (1.18)$$

$$\begin{cases} \alpha(t) = \arctan \frac{\cos \theta_t}{\lambda + \sin \theta_t} \\ V_t(t) = U \sqrt{\lambda^2 + 2\lambda \sin \theta_t + 1} \end{cases} \quad (\text{VAT}), \quad (1.19)$$

and

$$\begin{cases} \alpha(t) = \arctan \frac{V_i}{U} + \theta(t) \\ V_t(t) = \sqrt{U^2 + V_i^2} \end{cases} \quad (\text{OFT}), \quad (1.20)$$

where, $\alpha(t)$ is the blade angle of attack and $V_t(t)$ is the blade resultant velocity. C_1 and C_2 are constants for different working conditions. θ_t is the azimuthal angle of VAT blade and V_i is the induced velocity of OFT blade.

With the help of the body fitted coordinate and mathematical functions above, the three types of turbine with different configurations and working regime could be compared with each other regarding the blade resultant velocity and blade angle of attack as shown in Fig. 1.6. It is clear that the magnitude of the resultant velocity and blade angle of attack for the HAT do not change during the turbine revolution. The magnitude of the resultant velocity and blade angle of attack for the VAT are varied as sinusoidal functions. There is one cycle for the $V_i(t)$ and $\alpha(t)$ during one turbine revolution and a 90° phase difference between them. For the OFT, there are two sinusoidal cycles for the $V_i(t)$ during one turbine revolution. The $\alpha(t)$ of the OFT has one cycle during one turbine revolution but the wave shape is not a sinusoidal function. The difference in performance of these three types of turbines is due to the different behaviour of the $V_i(t)$ and $\alpha(t)$ of them.

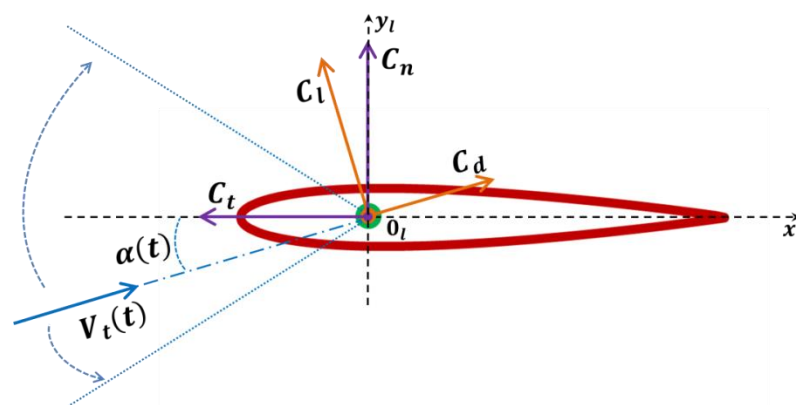
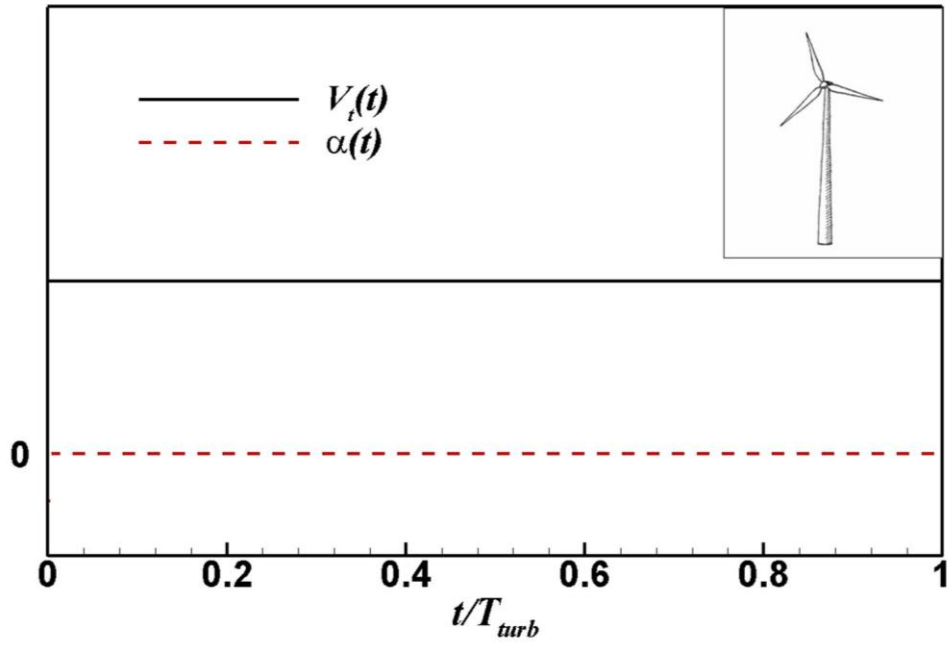
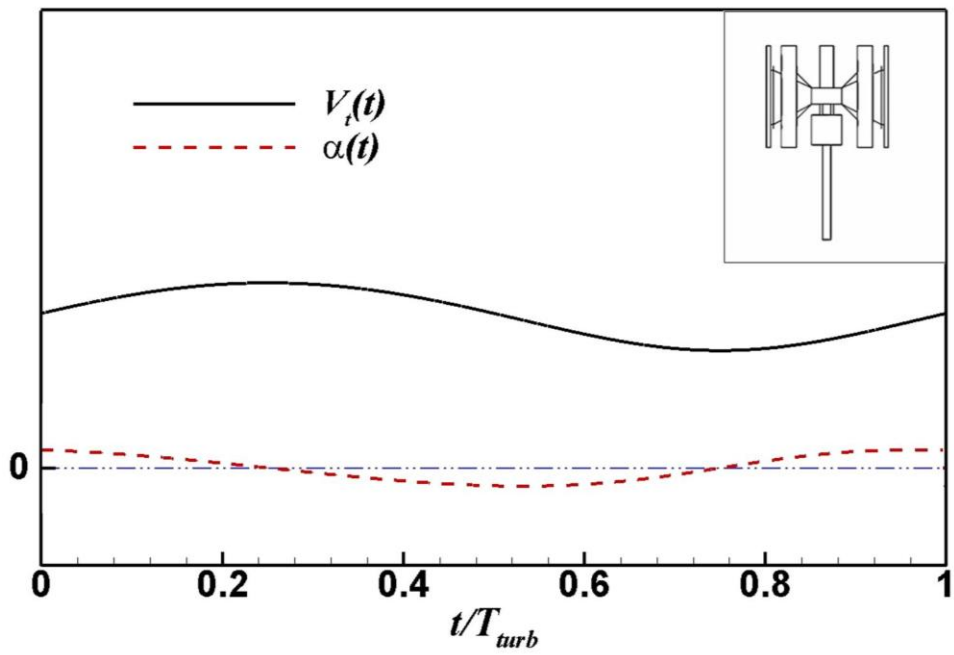


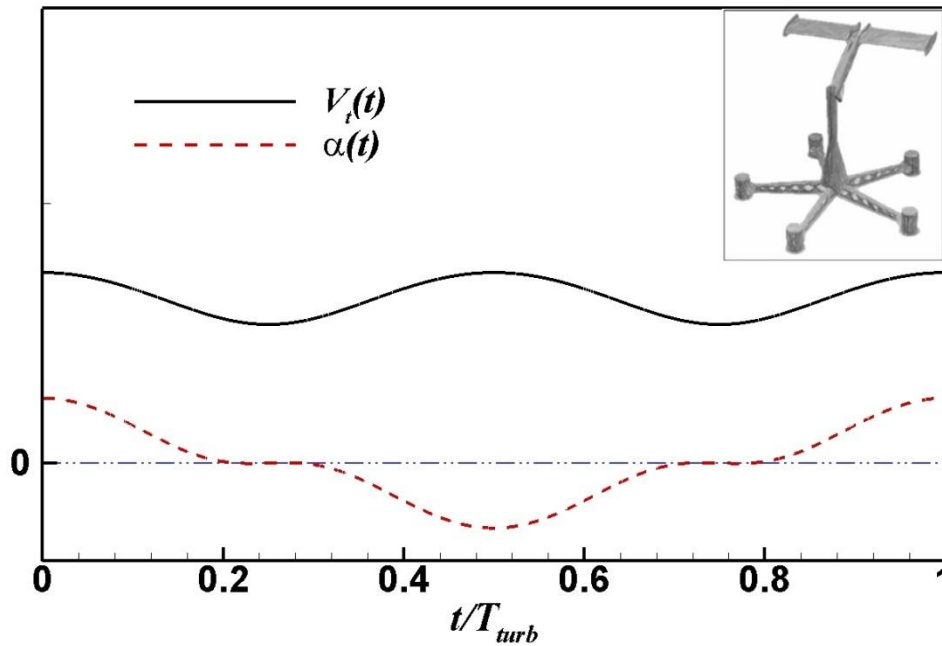
Figure 1. 5 Sketch of turbine blade forces, resultant velocity and angle of attack under body fitted coordinate $x_t o_t y_t$.



(a) HAT



(b) VAT



(c) OFT

Figure 1. 6 The instantaneous resultant velocity and blade angle of attack for the (a) HAT, (b) VAT and (c) OFT with body fitted coordinate x_i, y_i .

1.3 Objectives of this thesis

The main objective of the present research is to develop new methods to enhance the efficiency of renewable turbines by using bio-inspired flow control. The bio-inspired method of blade stress estimation and reduction is also analysed. Present studies select the straight blade Vertical Axis Turbine and the Oscillating Foil Turbine as the renewable turbine models for their low efficiency compared with the well-developed Horizontal Axis Turbine. Bio-inspired methods such as the fish tail active motion and the passive flexibility of butterfly wings are used to modify the traditional rigid turbine blade. The bio-inspired flow control method falls into two categories, i.e. active flow control and passive flow control. In nature, most animals benefit from passive flow control rather than active flow control, such as the passive deformation

of insect wings, etc. However, the active flow control method is widely accepted for industrial application, since it has high reliability and is easy to adapt to different working conditions. There are big differences in the mechanism and simulation method between the active flow controls and the passive flow controls. In industrial application, the motion of the active flow control is governed by gears and conveyor belts or an external signal source and is usually maintained by an external power supply, but the motion of the passive flow control is governed by the interaction between external forces and the material. Thus, the active flow control needs extra control systems compared with the passive flow control. During the simulation, the active motions are pre-determined by the sinusoidal motion functions and not influenced by external fluid field as long as the fluid force does not exceed the upper limit of the operation system, but a Fluid Structure Interaction (FSI) solver which solves fluid field, structure behaviour and the interaction between them is necessary for the simulation of passive flow control cases. The active motions are prescribed based on the flapping motion in nature animals (for bio-inspired studies) or based on the device performance (for optimization purpose). The rigid active motions can be achieved by using linkage, flywheel, spring, etc. The flexible active motions can be achieved by using internal air balloon and blowing-suction machine. The energy consumption by the active flow control is ignored and the energy extraction efficiency enhancement of OFT is mainly focused on by present research. It is more difficult to simulate passive flow control cases compared with the simulation of active flow control cases. Both the bio-inspired active flow control method and the bio-inspired passive flow control method are tested in the present research.

The specific targets of present studies are to test the potential energy extraction efficiency enhancement ability of:

- using an active flow controlled flap which is inspired by the fish tail motion on the VAT;
- using active flow controlled blade chordwise flexibility which is inspired by the flexibility of fish fins and insect wings on the OFT;
- using a passive flow controlled flap which is inspired by the flexibility of fish fins and tails on the VAT;
- using a passive flow controlled spanwise flexible blade which is inspired by the flexibility of animal bodies on the VAT. The blade stress characteristics of using a spanwise flexible blade VAT is carried out and the energy extraction ability of the turbine is investigated in this study.
- using a passive flow controlled chordwise flexible blade which is inspired by the flexibility of fish fins and insect wings on the OFT;

A number of case studies and parameter studies will be provided in the following chapters.

1.4 Structure of this thesis

This thesis includes four parts, PART I provides the introduction to this study, the literature review of the research on vertical axis turbines, oscillating foil turbines, blade stress estimation and reduction for renewable turbines and the review on the bio-inspired application of the marine industry and the methodology used in the present research in Chapters 1, 2 and 3, respectively. PART II and PART III are the main body of this thesis which contain different case studies and results. PART II

includes the studies of bio-inspired active flow control for renewable turbines. It includes active flow control for vertical axis turbines by the bio-inspired oscillating flap in Chapter 4 and active flow control for oscillating foil turbines by the bio-inspired flexible flapping motion in Chapter 5. PART III is the studies of bio-inspired passive flow control for renewable turbines. It contains passive flow control for vertical axis turbines by a bio-inspired oscillating flap and flexible structure blade in Chapter 6 and passive flow control for oscillating foil turbines by a chord wise flexible structure in Chapter 7. The conclusions and recommendations for future work are included in PART IV. The references and appendices used in present studies are also provided at the end of this thesis.

Chapter 2: Literature Review

This chapter presents the overview of past published research studies which are relevant to the present studies. As mentioned in Section 1.1, straight blade VAT and OFT are the turbine models investigated in the present research. Thus, the review on the research of straight blade VAT including different research methods for VAT, the parameter studies of straight blade VAT and the review of the research of OFT including OFT with a forced oscillating, semi-activated and self-sustained system will be presented first. The blade stress characteristics are one of the research aims of the present studies. Moreover, a review of the research on blade stress estimation and reduction for turbines will be conducted. The bio-inspired research and its application in the aerodynamics and marine industry will be reviewed. A summary of the literature review and gaps found from these critical reviews will be listed at last.

2.1 Review of the research on straight blade VAT

It has taken more than 2000 years for mankind to use VAT to generate power. In recent years, research on VAT has become much more popular since the energy extraction efficiency is still low compared with HAT. Different research methods are used for the VAT study and different energy extraction efficiency enhancement methods have been implemented.

2.1.1 Research method for VAT

The research method for VAT can be classified into three general categories, i.e. analytical method, numerical method and experimental test. The analytical solution is to use classic theories and methods to solve the forces acting on the VAT blade or

the fluid field variables. Three different mathematical models are used in the scientific and industrial fields based on different theories such as the stream tube model based on the momentum theory, the Vortex model based on the potential flow theory and the Cascade model that uses Bernoulli's equation. Numerical solution is to solve the governing equations of fluid flow by using numerical methods. Experiential test is also widely used for the VAT research as a validation or confirmation of the analytical or numerical results. Detailed discussions and a review of these methods are provided in the following paragraphs.

2.1.1.1 Analytical solution

Stream tube model (momentum theory)

The stream tube method is based on the momentum theory (or the Newton second law). The forces acting on the turbine blade are equal to the rate of change of the momentum of the fluid flow. Based on this equation, the forces acting on the blade and the overall power coefficient could be solved by the momentum difference of the fluid flow between the upstream and downstream regions. Additional functions such as Bernoulli's equation are needed (Wang, 2005; Islam et al., 2008). The turbine blades are usually replaced by the actuator disk. A stream tube is selected which can cover the entire actuator disk. The cross-section area of the stream tube in the upstream region is smaller than the actuator disk, while the cross-section area of the stream tube in the downstream region is larger than the actuator disk. A schematic plot of the stream tube model is shown in Fig. 2.1.

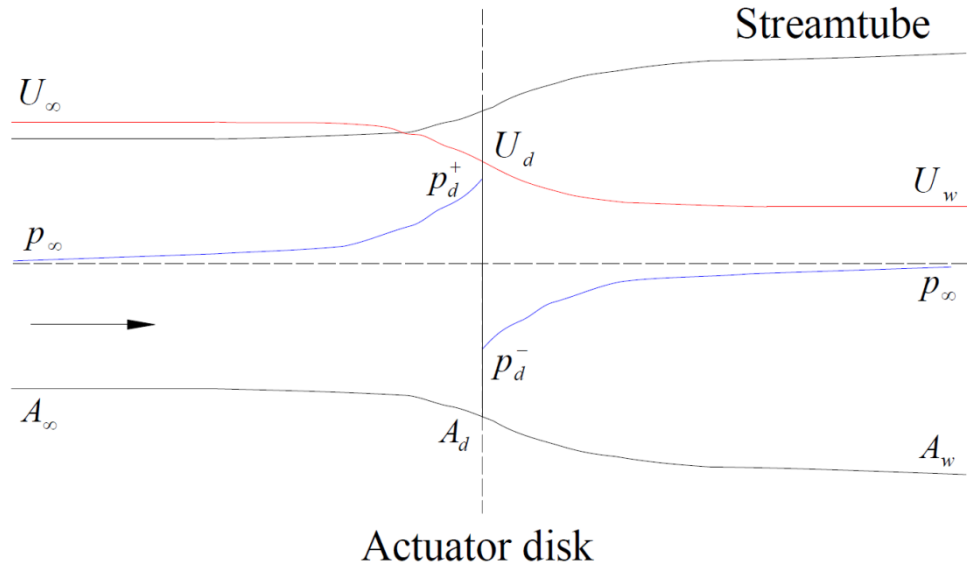


Figure 2. 1 Schematic of single stream tube model (Wang, 2005).

The following equations could be derived based on the momentum theory (Wang, 2005):

$$\begin{cases} c_t = \frac{F_t}{\frac{1}{2}\rho_f U^2 A_d} = 4a(1 - a) \\ c_{op} = \frac{p_o}{\frac{1}{2}\rho_f U^3 A_d} = 4a(1 - a)^2 \end{cases}, \quad (2.1)$$

where A_d is the cross-section area of the stream tube in the downstream region, a is the coefficient of induced velocity. It is clear that the thrust coefficient of the turbine blade reaches its maximum value of 1.0 when a is 0.5. When $a=1/3$, the power coefficient c_{op} reaches its maximum value of 16/27 (i.e. 0.593). This is the upper limit of the kinetic renewable turbine (Betz limit).

There are three different categories for the stream tube method based on different treatments on the stream tube. They are the single stream tube method (Templin, 1974; Camporeale and Magi, 2000), the multiple stream tube method (Read and Sharpe, 1980; Paraschivoiu, 1988) and the double multiple stream tube model (Beri

and Yao, 2011b). The single stream tube method is a method which contains only one stream tube to cover the entire actuator disk. The multiple stream tube method can divide the actuator disk into several isolated stream tubes and apply the momentum theory to each of them. This method can consider the influence of the blade position on the induced velocity. The double multiple stream tube model further divides the stream tubes of the multiple stream tube method into an upstream region and downstream region. The wake flow of the upstream region is the incoming flow of the downstream region in each stream tube. This method can consider the influence of the upstream blades on the downstream blades. Thus, higher accuracy could be achieved.

The stream tube method is widely used in the industrial field because of the simplicity of the mathematical formula and its good accuracy at low tip speed ratio and small solidity (Paraschivoiu, 1988; Camporeale and Magi, 2000; Beri and Yao, 2011b). However, the accuracy will reduce when applying this method to a high solidity or high tip speed ratio condition. The calculation could be diverse if the tip speed ratio is very large (Sun, 2007). This method cannot solve all the variables of the fluid field.

Templin (1974) used the stream tube model to predict the power coefficient of the vertical axis turbine. In his study, the single stream tube model was used which applies one stream tube for the whole turbine actuator disk. The induced velocity was assumed to be constant throughout the actuator disk. The curved blade shape and the dynamic stall effect were taken into account. Different parameters such as cross section shape, solidity and the turbine height diameter ratio were studied.

Camporeale and Magi (2000) compared the stream tube results with the experimental results of the vertical axis turbine model. The turbine blades were pitching about the pivotal axis through the Voith-Schneider system. A single actuator disk with the single stream tube method was used. Good agreement between stream tube results and the experiment results was achieved which provided the possibility of using the single stream tube method to predict the power coefficient and the energy extraction efficiency of a variable pitch vertical axis turbine system.

Vortex model (potential flow theory)

The vortex method is based on the potential flow theory to solve the unsteady fluid field with rotating turbine blades (Larsen, 1975; Holme, 1977; Wilson 1978, Strickland et al., 1979; 1980; Cardona, 1984; Ponta and Jacovkis, 2001). It begins with establishing the mathematical formulas of the unsteady potential flow method, and then solves these formulas based on Boundary Element Method (BEM). Sources and sinks are assigned to the blade surface. Discrete vortices are arranged on the blade surface and the blade wake. The wake vortices move with the fluid particles and ignore the influence from the dissipation, free-surface and wave. It assumes an incompressible fluid field and irrotational field except for the blade surface and wake vortices. All the discrete vortices follow the vorticity conservation law. The vorticity magnitude is calculated by the Kutta condition. The forces acting on the turbine blade and the overall power coefficient could be solved with the correction for the viscous effect (Wang, 2005). Compared with the stream tube method, the vortex method is able to calculate the blade vortex interaction, the blade pressure distribution, the unsteady effect and the instantaneous forces of the blade. However, the calculation time is much more than that of the stream tube method and it has a

worse accuracy than the stream tube method on the blade force calculation with a low tip speed ratio because of the large angle of attack of the blade and dynamic stall (Sun, 2007). A schematic plot of the vortex model is shown in Fig. 2.2.

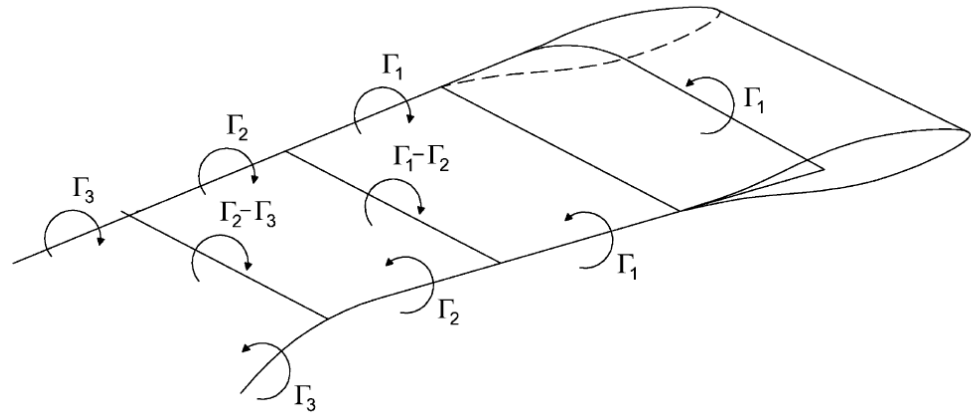


Figure 2. 2 Schematic of vortex model for a single blade (Islam, 2008).

As early as 1978, Wilson (1978) used this model to predict the performance of the Giromill straight blade vertical axis wind turbine. He found that the vertical axis turbine and the horizontal axis turbine have the same limit of the power coefficient and inline force coefficient. The cross wise force decreases with the increases of the tip speed ratio of the vertical axis turbine.

Wang et al. (2007) designed a two dimensional vortex panel method to calculate the unsteady straight blade vertical axis turbine with variable blades. Their results showed good agreement with the experimental data. They also found that their two dimensional vortex panel method has better accuracy than the classic free vortex model and was simpler than the vortex method combined with finite element analysis.

Cascade model

Cascade is defined as the arrangement of turbine blades with equal distance from one to its neighbour. It is the fundamental physical phenomenon of the turbine machine

(Hirsch and Mandal, 1987; Islam, 2008). The cascade model is used to assume the turbine blades are lying in a straight line. The interval between the blades in the cascade model is equal to the circumferential distance of them in the original configuration. Bernoulli's equation is used to set up the mathematical relationship between the incoming flow velocity and the downstream velocity. Semi-empirical expressions are necessary to determine the induced velocity through the downstream velocity.

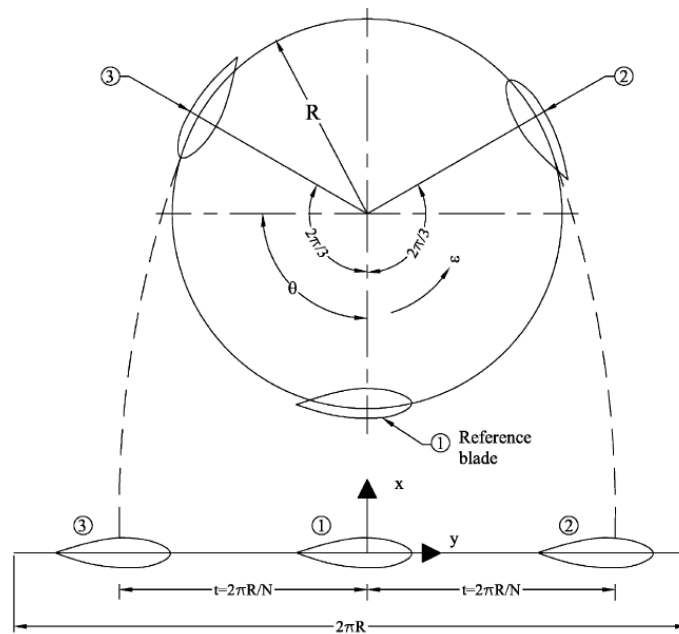


Figure 2. 3 Schematic of cascade model (Islam, 2008).

The cascade model is workable for both high and low solidity and both large and small tip speed ratios of the vertical axis turbine. The instantaneous forces can also be solved by this model. Different effects such as turbine blade Re changes for different time instants, the aspect ratio effect and the flow curvature effect can be taken into account during the cascade model calculation (Islam, 2008). A schematic plot of the vortex model is shown in Fig. 2.3.

Hirsch and Mandal (1987) first used the cascade model for the calculation of the vertical axis wind turbine. Mandal and Burton (1994) also applied this method to study the turbine dynamic stall effect for the vertical axis wind turbine.

2.1.1.2 Computational Fluid Dynamics (CFD) (numerical method)

The CFD method is used to calculate the entire fluid field by solving the partial differential fluid governing equations (Navier-Stokes equations for viscous flow or Euler equations for inviscid flow). Using the CFD method to solve the renewable energy turbine problem has become more and more popular in recent years (Hwang et al., 2006; Wang et al., 2010; Feng et al., 2012; Castelli et al., 2012b; 2013; Mohamed, 2012; 2014; Rossetti and Pavesi, 2013; Almohammadi et al., 2013; Xiao et al., 2013; Danao et al., 2014; Trivellato and Castelli, 2014). The CFD method has many advantages, for example all of the information is available for the calculated fluid field. CFD can also simulate with a full scale model. Because of the characteristics of the vertical axis turbine, a mesh moving method, such as the sliding mesh technique, is necessary for the VAT simulation.

Hwang et al. (2006) simulated the straight blade vertical axis wind turbine using the CFD method. Both the cycloidal blade system and the individual active blade control system are considered in their study. Their results showed that the power output of the turbine with the cycloidal blade system is 30% higher than that with the classic fixed pitch blade. They also found an optimized blade pitch angle variation method for the vertical axis turbine with an individual active blade control system by maximizing the tangential force of the blade to reach the highest power output. They also studied the blade cross-section shape effect using the CFD method through the NACA 4-digit and NACA 6-series. A sensing and actuating system was also

designed to achieve both the cycloidal blade system and the individual active blade control system.

2.1.1.3 Experiment

Experimental testing is one of the most traditional methods for studying the behaviour of renewable energy turbines. There are two general facilities for the VAT experimental test, i.e., the wind tunnel test and the towing tank test. The VAT experiments have two different test methods. One of them is to connect a motor to the VAT shaft and rotate the VAT at a certain angular speed of the motor during the test. This method is used to investigate the VAT in the stable working state only. The other method is to rotate the turbine by the fluid forces. Thus, the rotation speed of the turbine is not a fixed value during the experiment. This method could be used to study the stable working state as well as the start-up and cut off ability.

Strickland et al. (1979) carried out a series of experiment on the vertical axis turbine and repeated the experiment result using the vortex model. The experiment was carried out in a towing tank with the dimension of $10\text{ m} \times 5\text{ m} \times 1.25\text{ m}$. The reason for using a towing tank instead of a wind tunnel to test the vertical axis wind turbine was because the water tank is able to visualize the streak line and the flow structure. They injected dye through the trailing edge of the turbine blade by using a pressurized dye injection system, so the vortices and flow structure could be detected. Strain gauges were used to measure the force of the turbine blade. They were located in the root of the turbine strut. Strain gauge bridges were also used to make sure the strain gauges were only sensitive to the indicated forces. They tested the straight blade vertical axis turbine with one blade, two blades and three blades, respectively. The turbine blade was in a cross section of NACA0012. The span of the turbine

blade is 1.1 m and the chord of the blade is 0.0914 m. The diameter of the turbine is 1.22 m. Three tip speed ratios of the turbine were tested, i.e. 2.5, 5.0 and 7.5 with a fixed Reynold's number of 4×10^4 . A good agreement was achieved between the analytical results (the vortex model) and the experimental results.

Klimas (1982) compared the results from the theoretical conservation of the momentum-based aerodynamic model and the experimental tests for a vertical axis turbine. The turbine rotor radius is 8.5 m with a cross section of NACA0015. He discussed the blade-wake vortex interaction effect, the dynamic stall effect, the apparent mass effect and the circulatory effect of the vertical axis turbine by comparing the analytical and experimental results. He also found a large database for the turbine's performance by using a symmetrical cross section. However, there was a lack of results and research on the performance analysis of the asymmetrical blade turbine at that time. A better agreement has been achieved for the dynamic model than for the Quasi-steady model compared with the experimental results based on his study.

Takamatsu et al. (1985) tested the vertical axis turbine performance on a narrow channel. An open channel with a depth of 1.2 m was used. An orifice-meter was used to measure the mass flow rate of the fluid flow. The shaft of the vertical turbine was connected to a flywheel through a torque sensor. The diameter of the vertical axis turbine rotor is 0.1 m. The chord length of the turbine blade was 0.03 m and the span of the blade was 0.3 m with a cross section of NACA0030. The best performance could be achieved when the double blade vertical axis turbine was located in the narrowest channel. They also predicated the results by using theoretical analysis. However, the theoretical results were not in good agreement with the experimental

results of the instantaneous torque value and the peak energy extraction efficiency.

These disagreements were because the circular motion effect and the unsteady effect of the fluid flow were ignored during the theoretical analysis.

Kiho et al. (1996) tested a straight blade vertical axis tidal turbine. Their experiments were tested at Kurushima straits in Ehime prefecture from 1983 to 1988. The turbine was designed as a three blade Darrieus type turbine. The blades have a cross section of NACA6330018, with a chord length of 0.3 m and a span of 1.6 m. The turbine radius is 0.8 m. A gear box and synchronous generator were designed for this turbine. Different parameters were measured and analysed for the power extraction through the vertical axis tidal turbine in extreme marine conditions. Their results showed that marine kinetic energy could be extracted when the incoming flow is larger than 1.0 m/s. They observed the highest energy extraction efficiency of 56% for their designed tidal turbine at the tip speed ratio of 2.1 (incoming flow of 1.1 m/s).

2.1.2 Parameter studies for straight blade VAT

Since the 1970s, several parameter studies and performance enhancement methods for VAT have been investigated and invented. The most typical ones are listed in the following paragraphs.

2.1.2.1 Solidity and blade profile of VAT

The most effective way to change VAT's performance is to optimize the turbine or blade characteristics. The turbine or blade characteristics include the turbine blade profile, the blade numbers, the diameter of the turbine and the turbine blade chord

length. A non-dimensionalized parameter solidity σ_s is introduced to quantify the main geometrical characteristics of the Darrieus turbine:

$$\sigma_s = \frac{Nc}{R}, \quad (2.2)$$

where N is the number of turbine blades.

Islam et al. (2007a) tested different VAT blade cross-section profiles to improve the small capacity straight blade VAT in its starting and overall performance. Their results show that the classic NACA 4-digit systemic foils are unsuitable for small capacity straight blade VATs. They also suggested a high-lift and low-drag asymmetric foil with camber, high thickness, large leading edge radius and sharp trailing edge as the VAT blade cross section.

Islam et al. (2007b) tested different blade profiles by using several methods as shown in Fig. 2.4. The hydrodynamic performance of LS-0417 was found as the best among different foils under small Re and small λ but the c_{op} was much smaller than that of the classic NACA0015 foil. A new type foil named MI-VAWT1 was designed by them which achieved a higher power coefficient under small Re and small λ and kept the same performance under medium Re .

Beri and Yao (2011a) tested the VAT performance by using a NACA2415 camber foil blade. Their results showed that the NACA2415 camber foil blade has a good start ability but lower energy extraction efficiency.

Castelli et al. (2012a) tested three different blade profiles, which are classic NACA0021, DU 06-w-200 and cambered NACA0021 (which is cambered based on NACA0021 by Castelli et al.). Their results indicated that the best performance was achieved by using the cambered NACA0021 and up to 4% enhancement of the

energy extraction efficiency could be achieved compared with the other two blade profiles at the tip speed ratio of 2.33 as shown in Fig. 2.5.













		
(a) LS(1)-0417 with 1% Camber	(b) LS(1)-0417 with 3% Camber	(c) LS(1)-0417 with 4% Camber
		
(d) LS(1)-0416	(e) LS(1)-0418	(f) LS(1)-0420
		
(g) LS-0417 with 2% Leading Edge Radius	(h) LS-0417 with 4% Leading Edge Radius	(i) LS-0417 with 5% Leading Edge Radius
		
(j) LS-0417 with 0% Leading Edge Thickness	(k) LS-0417 with 2% Leading Edge Thickness	(l) LS-0417 with 3% Leading Edge Thickness

Figure 2. 4 Geometry of Airfoils for Sensitivity Analysis by Islam et al. (2007b).

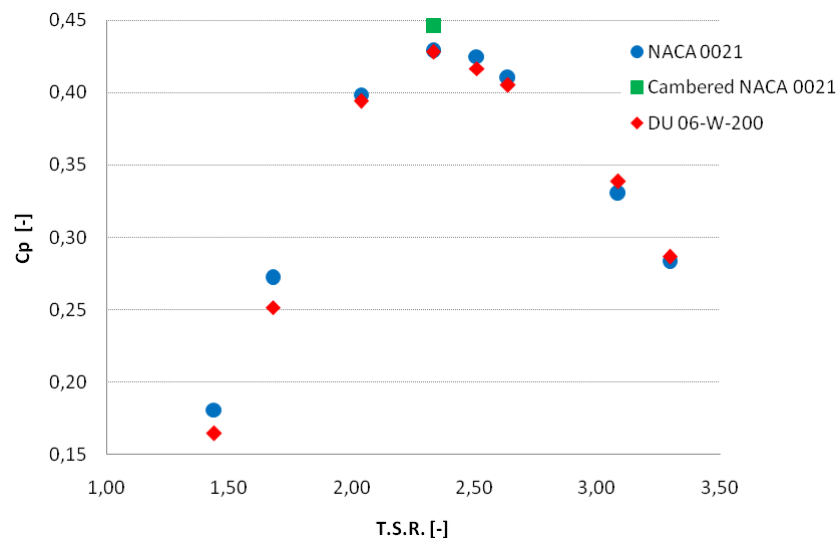


Figure 2. 5 Power curves for the three analysed rotors (just the $\lambda=2.33$ value of cambered NACA0021 was calculated) (Castelli et al., 2012a).

Castelli et al. (2012b) tested the solidity effect by changing the turbine blade numbers. It was found that using a larger σ_s results in the peak c_{op} occurring at smaller λ , but the value of peak c_{op} was reduced. A torque fluctuation and vibration reduction effect was observed by using larger σ_s values. The normal force of the turbine blade was also observed to be reduced by using larger σ_s values.

2.1.2.2 Variable pitch effect for VAT

There are many factors which influence VAT energy conversion efficiency. From the flow point of view, dynamic stall is one of the phenomena which significantly reduce device efficiency. Stall occurs due to flow separation when a turbine blade rotates to a position at a large angle of attack. Once it appears, the blade lift force drops significantly leading to reduced overall energy extraction efficiency. This is very undesirable for the lift force driven VAT and always happens at small tip speed ratios (also known as the self-starting problem). The idea of variable pitch is to improve the self-starting performance of VAT. It is generally accepted that the variable pitch technique could enhance the turbine performance at small λ (Pawsey, 2002).

As early as the 1970s, Drees (1978) and Grylls et al. (1978) tested the VAT performance by using a variable pitch blade which was driven by a central cam. Grylls et al. (1978) carried out experiments on four different pitch amplitudes. A good performance at small λ and better self-start ability were achieved under large blade pitching amplitude. However, the whole turbine system cannot accelerate to a larger λ . By reducing the blade pitching amplitude, better peak c_{op} results could be achieved but the self-start ability of the turbine diminished.

Pawsey and Barratt (1999) modelled the central cam variable pitch VAT by using the momentum theory. A range of pitch amplitudes from 0° to 30° were considered in their work. Corresponding power coefficients were predicted which confirmed the conclusion by Grylls et al. (1978).

Schönborn and Chantzidakis (2007) designed a cyclic pitch control turbine by using both the theoretical and experimental methods. Their results showed an enhancement in the turbine performance at small λ . The cyclic pitch control turbine can actively reduce the blade angle of attack to prevent the cavitation at large turbine rotational speed. By using the hydraulic actuation, the turbine can also have the emergency shutdown configuration.

Hwang et al. (2009) carried out both numerical and experimental research on the cycloidal turbine which is a similar concept with the cyclic pitch control turbine by Schönborn and Chantzidakis (2007). Their results show the turbine has the peak c_{op} value at small λ when σ_s is large. A 25% enhancement of the energy extraction efficiency was also observed by using the individual blade control.

Kiwata et al. (2010) designed a four-bar linkage variable pitch turbine as shown in Fig. 2.6. The pitch amplitude and offset angle are both able to change by using different lengths of the link. By using the four-bar linkage, VAT has the same start-up wind velocity but a higher rotational speed. The peak performance of the VAT energy extraction efficiency has a 12% enhancement compared with classic fixed pitch turbine.

Jing et al. (2014) experimentally tested three different variable pitch control turbines. These are cycloid type, spring-control type and passive variable pitch type turbines. Solidity, eccentric ratio, spring stiffness and other parameters were tested by their

experiment. A positive correlation was found between c_{op} and solidity as well as the eccentric ratio for the cycloid type turbine. A better hydrodynamic performance occurs when using a stronger spring for the spring-controlled turbine. For the passive pitch control turbine, a smaller pitch angle limit has a better energy extraction efficiency performance. Corresponding numerical analysis of the spring-controlled variable pitch VAT, as shown in Fig. 2.7, was also carried out by Sun et al. (2009).

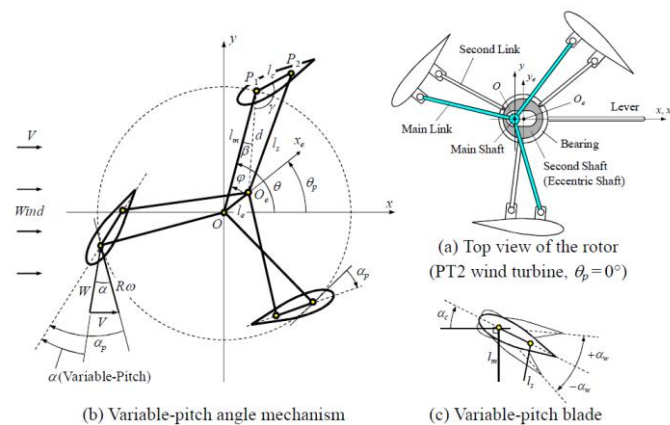


Figure 2. 6 Schematic diagram of the variable-pitch blade mechanism utilizing four-bar linkage (Kiwata et al., 2010).

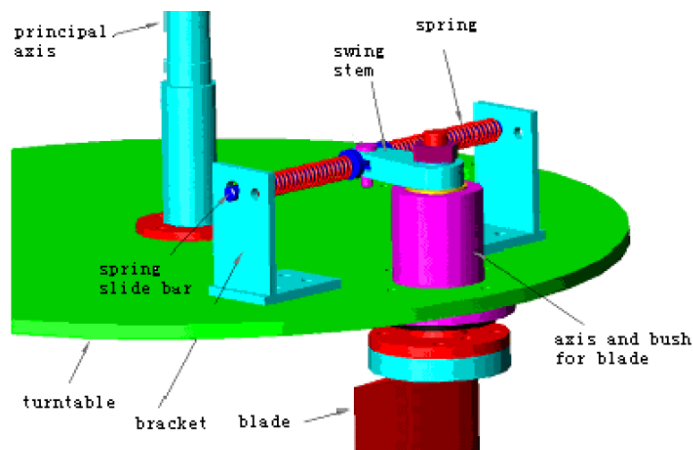


Figure 2. 7 Sketch of spring variable-pitch design concept (Sun et al., 2009).

Pryor (1983), Nemec (2001), Stephens et al. (2009), Stephens and Else (2011) and Paluszek and Bhatta (2012) also invented and patented different methods for the variable pitch vertical axis turbine.

2.1.2.3 Flow directional and augmentation channel effect for VAT

Another way to enhance the VAT performance is to use the flow directional and augmentation channel (or named duct). The idea of the flow direction and augmentation channel for VAT was first introduced by the diffuser augmented of horizontal axis wind turbine (Sun, 2007; Phillips et al., 2002). By using the channel to induce a sub-atmospheric pressure, the flow velocity around the turbine rotor could be increased and then improve the VAT performance (Khan et al., 2006; Khan et al., 2009). A sketch of the flow direction and augmentation channel concept is shown in Fig. 2.8 (Khan et al., 2009).

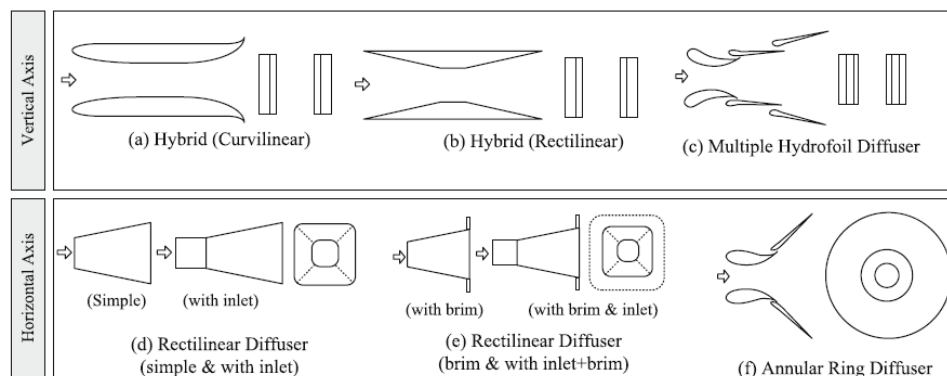


Figure 2. 8 Sketch of the flow direction and augmentation channel concept (Khan et al., 2009).

Faure et al. (1986) first applied a duct on a VAT under river to change the water current direction and speed. After testing, the interaction between the duct and turbine blade was observed which decreased the VAT performance.

Kirke (2006) tested vertical axis turbine into a duct device for its energy extraction efficiency. A triple enhancement of the VAT efficiency was observed by using the duct devices. In addition, the VAT efficiency could exceed the Betz limit, which equals 0.598 and is the upper limit of the efficiency for a kinematic energy absorber.

They also pointed out the advantages of using duct devices, for example that they are environmentally friendly (especially for water animals), minimize turbine size and enhance rotor speed.

Roa et al. (2010) tested two different channel devices, namely EPPLER-420 and NACA11414, for VAT by using experimental and numerical methods. It was observed that the flow was accelerated by using the channelling devices and the turbine blade generated more torque compared with a plain turbine. They could not determine the best configuration with their study and further investigations were suggested.

Gaden and Bibeau (2010) tested a series of channelling devices by using a momentum source turbine model. A 3.1 times enhancement by using the channelling devices was observed compared with the plain turbine and an optimized dimension was also found for the channelling devices.

Castelli et al. (2012c) tested a “C” shape shroud device for the VAT and a 60% enhancement was observed when using it. The “C” shape shroud effect is to let the instantaneous torque of the turbine smoother when applies it onto the upstream of the VAT, while the amplitude of the instantaneous torque of the turbine could increase when applied to the downstream of the VAT.

Georgescu et al. (2013) tested the “S” shape duct devices by using the numerical method. A VAT performance enhancement effect was observed by using this device. A half “S” shape duct device was also suggested to achieve a better performance.

2.1.2.4 Other parameter studies of VAT

Some other parameter studies of VAT are listed below.

Plasma actuators. A research group at the Israel Institute of Technology came up with an idea to control the dynamic stall for the vertical axis wind turbine by using plasma actuators. Greenblatt et al. (2012) carried out experiments on large σ_s small scale VAT by applying Dielectric Barrier Discharge (DBD) actuators on the leading edge of the turbine blade as shown in Fig. 2.9. A series of parameters were studied and a 38% enhancement was observed by using the DBD actuators. Ben-Harav and Greenblatt (2014) used a pulsed DBD actuator to control the dynamic stall on a VAT. Based on their experimental results, they found that the VAT performance was enhanced during the whole working region by using this device and the dynamic stall was also prevented/controlled. Greenblatt et al. (2014) analysed the vortex field of the DBD controlled VAT by using the PIV technology. Their results showed that by using the DBD actuators, the dynamic stall vortices became small and were close to the blade's surface so the dynamic stall effect could be reduced.

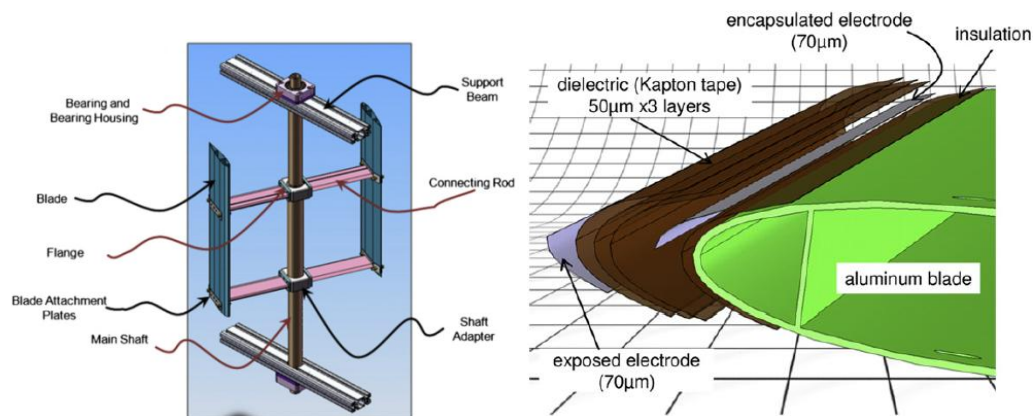


Figure 2. 9 Schematic representation of the VAT showing the main components (left) and schematic of the blade leading-edge region showing the attachment of the DBD plasma actuator (right) (Greenblatt et al., 2012).

Trailing edge (flap) control. Beri and Yao (2011b) studied the VAT performance with the trailing edge modified blade. A positive c_{op} was observed in their study with

this type of blade. Sneeringer (2009), Paluszek and Bhatta (2012) and Haar (2011) all invented and patented the VAT design by using a rotatable trailing edge blade. The top view of a rotor assembly illustrating the adjustments of blade ailerons relative to a prevailing wind with the variable flap method by Haar (2011) is illustrated in Fig. 2.10. Thus the lift force of the turbine blade could be increased and the total performance of the turbine could be enhanced. Haar (2011) also used a blade extension element to achieve the turbine rotational speed control.

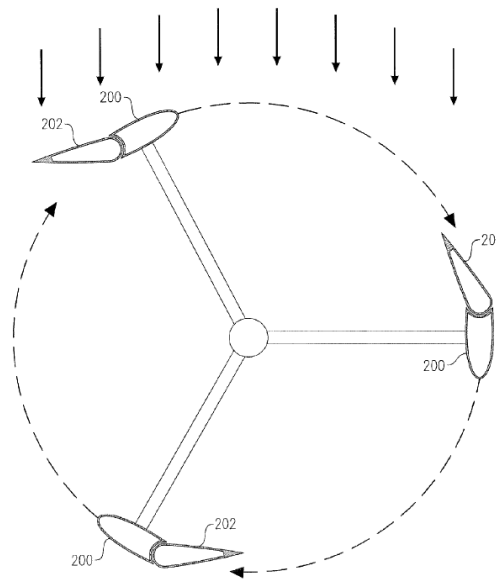


Figure 2. 10 Top view of a rotor assembly illustrating the adjustments of blade ailerons relative to a prevailing wind with the variable flap method (Haar, 2011).

2.2 Review of the research on OFT

In recent years there has been a growing demand to exploit the new types of available ocean renewable devices. As a result, the flapping or oscillating wing has further extended its application from just the propulsion/manoeuvring aspect (energy consumption) to the energy harvesting area (McKinney and DeLaurier, 1981; Jones and Platzer, 1997; Jones et al., 2003; Kinsey and Duman, 2008; 2012a; 2012b; Zhu and Peng, 2009; Zhu et al., 2009; Zhu, 2011; Xiao et al., 2012). Investigations from

relevant research studies show that a flapping motion can vary from its propulsion mode to its energy extraction mode if the wing pitches at an angle exceeding its heave induced Angle of Attack (AOA). The power efficiency generated is comparable to a conventional turbine with rotational blades. The studies on the flapping foil energy harvester fall into three categories: fully activated systems with prescribed motions, semi-activated systems with one degree-of-freedom activated and another one induced by fluid dynamic loads, and fully passive systems in which the motions are completely generated by flow-induced instability (i.e. the flutter phenomenon) as stated in a recent review paper by Xiao and Zhu (2014) and shown in Fig. 2.11.

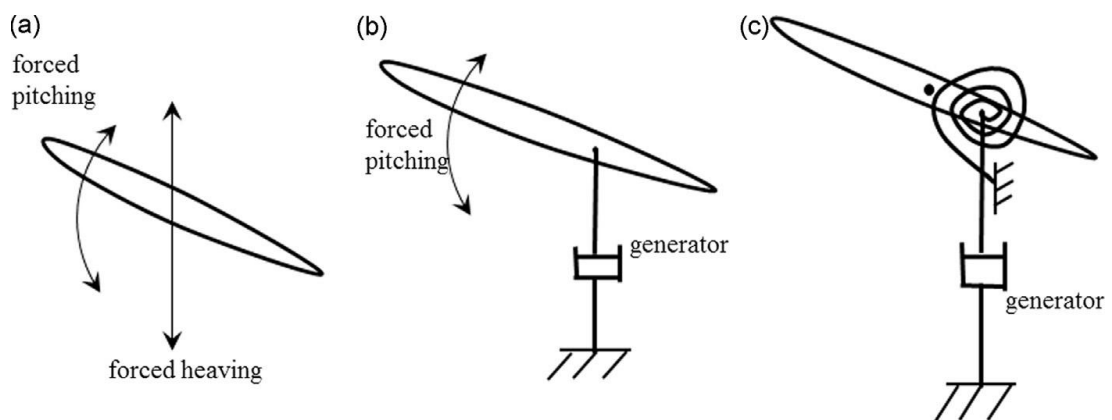


Figure 2. 11 Schematics of (a) a system with forced heaving and pitching motions, (b) a semi-activated system with forced pitching but induced heaving motions (modified from Zhu and Peng (2009)), and (c) a self-sustained system with induced heaving and pitching motions (modified from Peng and Zhu (2009)) (Xiao and Zhu, 2014).

Among these, the fully activated systems are usually used as model systems. By assuming that the foil undergoes certain prescribed motions (in reality these motions can be generated either semi-actively or passively), these model systems are useful in examining the power extraction capacity of the system and the underlying physics.

Since the research about flapping foil energy harvesters is still in the initial stage, most of the existing studies use prescribed foil motions (Xiao and Zhu, 2014).

2.2.1 OFT with forced pitching and heaving motions

The feature of a forced oscillating foil turbine is the prescribed pitch and heave motion. This is an ideal model for OFT which ignores the actuator effect. It is widely accepted and used by most OFT researchers as it is simplified in mathematical formulas but can also provide useful insight into the physical phenomenon as a guideline of the industrial design. In this simplified model, the energy extraction efficiency is calculated based on the sum of the product of lift force and the corresponding plunge velocity and the product of the moment and corresponding pitch angular velocity (Xiao and Zhu, 2014).

McKinney and DeLaurier (1981) first extracted wind energy using the harmonically oscillating foil. They designed a horizontally aligned foil with a symmetrical aerofoil cross-section. With the prescribed combination motion of pitching and plunging, McKinney and DeLaurier (1981) found that the output power and efficiency was accomplishable for both theoretical analyses of unsteady-wing aerodynamics and the wind tunnel experimental test.

Jones and Platzer (1997) systematically studied the unsteady, inviscid, incompressible, two-dimensional fluid flow that passed a moving airfoil or airfoil combinations by using numerical methods. They found that drag force was produced and energy was extracted from the airfoil when the pitch-amplitude of a twin flapping wing increased sufficiently. They believed that this condition would lead to the flutter phenomenon of a free airfoil. They also found that the foil pitch amplitude

must be larger than the induced angle of attack (which is defined in Eq. 1.15 as the nominal effective angle of attack α_0 in Section 1.2.2) and the phase difference between the pitch and plunge motion is restricted to 90° if this phenomenon occurs. Their findings show a potential application of the flapping foil model as an energy extractor.

Jones et al. (1999) carried out both numerical and experimental research on the flutter generator. The flutter engine designed by Jones et al. (1999) is shown in Fig. 2.12. They found that under a fixed nominal effective angle of attack α_0 , there was a reduced optimum plunge frequency and velocity. The optimum plunge velocity was found to increase with the increase of the nominal effective angle of attack α_0 . Their experimental studies for McKinney and DeLaurier's (1981) windmill shows good agreement at a lower angle of attack, but is over-predicted at a high angle of attack.

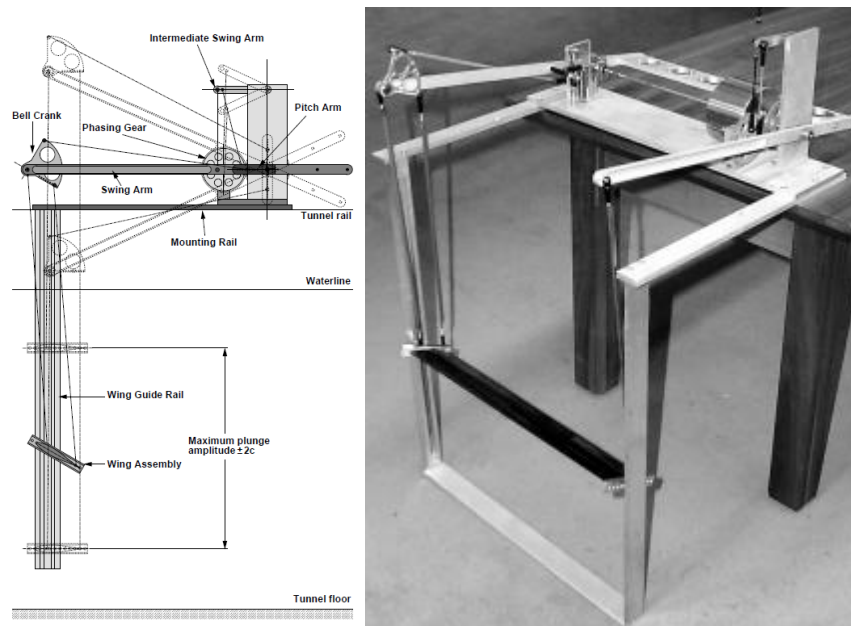


Figure 2. 12 Side view (left) and photograph (right) of the flutter engine (Jones et al., 1999).

Dauids (1999) carried out both numerical and experimental tests for the forced oscillating foil turbine. The unsteady panel method based on the potential flow

theory was used. The numerical results show 30% efficiency of the energy extraction and a power coefficient of 0.52 of the oscillating foil. The optimum value of the plunge amplitude and the reduced frequency were recommended as 0.63 m and 2.0, respectively. This peak value could not be achieved by his experiment because of the high reduced frequency. A large reduced frequency may result in huge stress acting on the oscillating foil generator. In addition, a large reduced frequency results in a high maximum pitch angle of the oscillating foil to maintain the high efficiency which leads to a strong dynamic stall phenomenon. Thus, the experiment stopped at the effective angle of attack to the static stall limit of the oscillating foil. Good agreement had been achieved for small reduced frequency between the unsteady panel results and the experimental results.

Lindsey (2002) tested the oscillating foil turbine with both experimental and numerical methods. Even the power generated by his experiment was limited. The device was recommended by Lindsey (2002) for potential commercial use as a power generator.

Jones et al. (2003) carried out an experiment and numerical test for an oscillating foil turbine device with tandem configuration. A water tank was used for their study and the incoming flow velocity was 16 inches per second. The dimensions of the water tank were 56 inches \times 20 inches \times 15 inches. The dual oscillating foils had a gap of 9.6 chord length. There was a 90 degree phase difference between the upstream foil and the downstream foil. The foil was in a cross section of NACA0014. The chord length of the foil was 2.5 inches and the span of the foil was 13.5 inches. Each foil had two foil sections with a gap of 0.25 inch. The designed dual oscillating foil devices have an ability of 1.4 times the chord length for the plunge amplitude and

90° for the pitch amplitude. A two dimensional panel method and a CFD code were used to repeat the experiment results. Their numerical results were overpredicted compared with the experimental results which may be due to ignoring the mechanical frictions and so on during their numerical calculations which showed potential ability in the energy extraction performance for their designed oscillating foil turbine.

A systematic numerical study by Zhu (2011) presented a novel approach to the energy extraction mode of oscillating turbines. The unstable wake was found in his study. It was also found that a significant vortex shedding occurs at the foil leading edge when the foil has a large AOA which is defined as foil-wake resonance. It was also found that the average energy extraction from the pitch motion is almost zero when the oscillating foil turbine reaches its best performance.

The recent research study of Xiao et al. (2012) also revealed that an appropriately proposed non-sinusoidal pitch trajectory can effectively enhance device efficiency via tuning the instantaneous AOA to a favourable profile. The influence of non-sinusoidal pitching profiles on oscillating wing power efficiency is shown in Fig. 2.13.

Campobasso and Drofelnik (2012) carried out a series of simulations for a foil with forced pitch and heave motion in the air. Compressible Navier-Stokes equations were solved. The *Re* of this study was 1100 and laminar assumption was used. Their simulations confirmed that the efficiency of the oscillating foil turbine is around 35%. A strong dynamic stall was observed at high reduced frequencies.

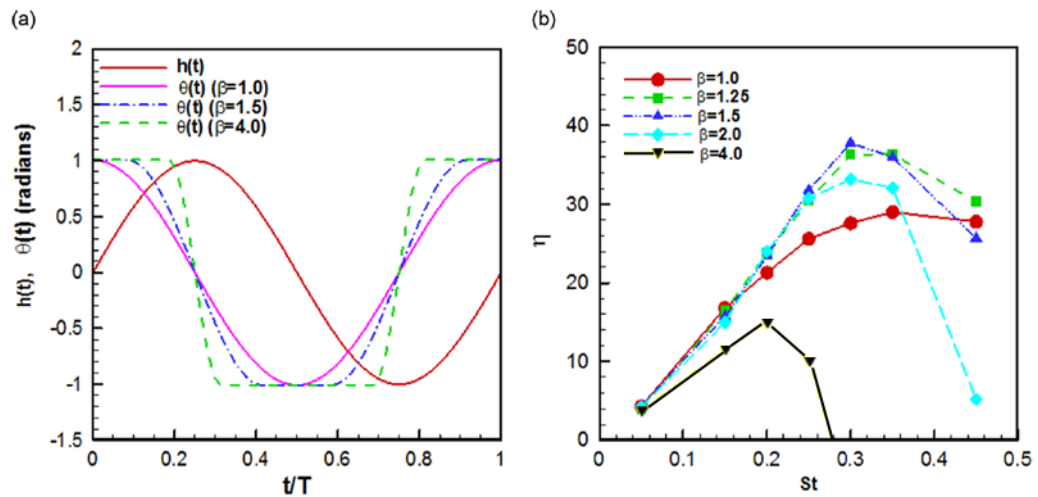


Figure 2.13 The influence of non-sinusoidal pitching profiles on oscillating wing power efficiency: (a) Profile of pitching and heaving with an adjustable constant β ; (b) efficiency variation with β at various oscillating non-dimensionalized frequency St . (reproduced from Xiao et al., 2012).

Le et al. (2013) designed a new shape of oscillating foil inspired by the shape of the scallop and tested the morphological effect by comparing the performance of the scallop shaped foil with that of the classic NACA foils. Different morphological factors such as corrugation and chamber were tested. The two dimensional CFD method was used in their study. Their results show that the performance of a scallop shaped foil at down stroke is better than that at up stroke. They also found that the convex surface is easily formed when the foil supports its pitching centre which affects the formation and development of the Leading Edge Vortex (LEV). Based on their results, the morphology of the foil has the ability to control the phase and location of the near blade vortices so that a better performance can be achieved by optimizing the foil shape. In comparison with the oscillating foil, with the shape of NACA0012, 6% of the energy extraction efficiency enhancement can be achieved by using the scallop shaped foil. Their study showed an alternative foil shape for the oscillating foil turbine for future commercial use.

A series of work has been conducted by Kinsey and Dumas (2008, 2012a, 2012b, 2012c and 2014) on the flapping wing device through experiment and simulation.

Kinsey and Dumas (2008) carried out a detailed analysis of the mechanism of the energy extraction type of oscillating foil. The efficiency map in the parametric space of flapping frequency and pitching amplitude for a NACA0012 at $Re=1100$ by Kinsey and Dumas (2008) is shown in Fig. 1.2 (b). A maximum energy extraction efficiency of 34% was observed with f^* between 0 and 0.25, pitching amplitude θ_0 between 0 degrees and 90 degrees, the heave amplitude of one chord length, $Re=1100$ and an NACA0015 foil shape. It was also observed that the energy extraction efficiency is greater than 20% when pitch amplitude θ_0 is larger than 55 degrees. Their results indicated that the heave amplitude and the oscillation frequency play a more significant role in the energy extraction performance than that of the foil geometry.

Kinsey and Dumas (2012a) carried out a three-dimensional wing test aimed to assess the influence of wing span-length on power generation. With a given aspect ratio AR of 5.0, their prediction was compared to their experimental data. Efforts were also devoted to analysing the dual flapping wing device in a tandem arrangement under the condition of a high incoming Reynolds number at 5×10^5 . An optimized gap (L) between the upstream and downstream foil was found to be at a value of L/c of 5.4 to achieve optimal efficiency.

Kinsey and Dumas (2012b) investigated two dimensional dual oscillating foils with tandem configuration. Both of the foils could share the same flow stream under this arrangement to allow the oscillation foils achieve their highest efficiency. They observed a beneficial effect from the interaction between the downstream vortex and

the downstream foil which led the total system efficiency to 64% under the optimized working condition. However, a harmful effect was also observed from the vortex foil interaction which leads the downstream foil to make a negative contribution to the system energy extraction efficiency. In comparison with the experimental results, the numerical simulations were overpredicted to the peak power coefficient. This may be because of the broken two dimensional coherence of the vortices in the three dimensional experiments.

Kinsey and Dumas (2012c) carried out a three dimensional numerical calculation of the foil oscillating turbine. They found that the hydrodynamic losses of the three dimensional effect could be limited within 10% when endplates' use of the foil tip with the condition of $AR > 10$ was compared with the two dimensional results. A non-horizontal hydro flow which is up to 30 degrees with respect to the foil chord was also considered. They observed that the energy extraction performance is proportional to the projected energy flux.

Kinsey and Dumas (2014) tested a single oscillating foil turbine by using a two dimensional unsteady RANS solver. A maximum efficiency of 43% was found under the Reynolds number of 500,000. Better energy extraction efficiency can be achieved when the effective angle of attack is around 33 degrees based on their results. They also observed that the Leading Edge Vortices are not necessary to occur around the best performance region with high Reynolds number rather than the phenomenon at a low Reynolds number.

2.2.2 OFT with semi-activated systems

The semi-activated OFT system is used to actuate the pitch motion of the foil. The heave motion of the foil is induced by the incoming flow. To achieve this, the power input to actuate the pitch motion is needed. The energy could be extracted from the flow induced heave motion via a damper. The energy extraction efficiency is calculated as the difference between the energy harvest from the heave motion and the energy consumption of the pitch motion. The oscillation foil will only harvest energy when the energy extraction of the foil heave motion is larger than the energy consumption of the pitch motion (Xiao and Zhu, 2014).

Zhu and Peng (2009) created a numerical model which solves the Navier-Stokes equations to investigate the performance of an oscillating foil turbine. The turbine model they used was an activated pitch motion with a passive heave motion. Low Reynolds number flow was considered in their study. They found that the Leading Edge Vortices could recover part of the energy to the oscillating foil through vortex-body interactions to enhance the energy extraction efficiency.

The schematic of the flapping-foil energy harvester used in Zhu et al. (2009) is shown in Fig. 2.14. They prescribed the pitching motion and the plunging motion was calculated from the fluid field which was induced by the pitching motion. Both a 2D thin plate model and a 3D nonlinear boundary-element model were tested. The Fluid Structure Interaction function was also involved in their tests. The optimized system which could achieve the highest energy extraction efficiency was proposed based on their results.

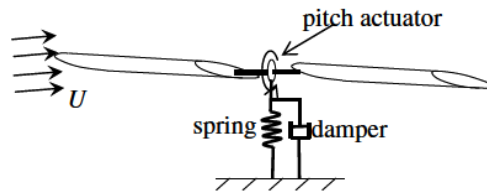


Figure 2. 14 Schematic of the flapping-foil energy harvester used in Zhu et al. (2009).

Abiru and Yoshitake (2011) designed an oscillating foil turbine and experimentally tested its performance. The oscillating foil they designed had a forced pitch motion and a free heave motion. The oscillating foil was supported vertically as a cantilever plate down into the water. An electric motor was designed to achieve the active control of the pitch motion. A magnetic damper was used to collect energy from the heave motion of the oscillating foil. The wing had a symmetrical NACA0015 cross section shape. The chord length of the foil was 0.1 m. The span length of the foil was 0.3 m. The amplitude of the pitching motion of the foil was 50° . The incoming flow velocity was fixed at 1 m/s. Their experiment used a high speed circulating water channel. The size of the channel was $4\text{ m} \times 2\text{ m} \times 1\text{ m}$. The flow velocity could adjust from 0.3 m/s to 3.3 m/s. Their experimental results proved the possibility of using an oscillating foil to extract energy from a fluid flow. The efficiency of the oscillating foil has a positive correlation with the maximum pitch angle up to 50° for the designed oscillating foil turbine. The ratio for the power consumed by the forced pitching to the power generated by the free heaving was found to decrease with the increase of the incoming flow velocity. They also confirmed that the finite span effect will decrease the efficiency of the oscillating foil turbine system. Their designed oscillating foil turbine could achieve 32% to 37% efficiency (which is 3.5 W to 4.4 W in power) with an incoming flow velocity of 1 m/s.

Huxham et al. (2012) designed an oscillating foil energy converter which has a prescribed pitch motion and free translated plunge motion. Experimental tests were carried out for this type of turbine. The oscillating foil was vertically aligned. The material of the turbine foil was aluminium. The foil had a cross section of NACA0012. The chord length of the foil was 0.1 m and the span length was 0.34 m. The oscillating foil was connected with two swing arms to allow the foil to have the pitch and plunge motion. The length of the arm was 0.3 m. The size of the water tunnel was 0.6 m in width and 0.39 m in depth. The dimensionless damping coefficient (which is the damping coefficient non-dimensionalized by fluid density, fluid velocity, blade chord, blade span and the length of lever arm) was fixed at 29.5 during their experimental study. The energy extraction efficiency of the oscillating foil energy turbine could achieve 23.8% with a pitch amplitude of 58° and a reduced frequency of 0.1.

2.2.3 OFT with self-sustained systems

A system with self-sustained motion does not need a power supply at the initial condition. The motion is fully induced by the instabilities of the flow (Xiao and Zhu, 2014). For the self-sustained oscillation foil system, the damper only set up at the foil translation direction. Thus, the energy extraction efficiency of the oscillation foil turbine system is dependent on the product of the lift force and the translation velocity only.

Peng and Zhu (2009) investigated the oscillating wing devices with a self-sustained pitch and heave motion by using a rotational spring and damper. Through a study of the pitch axis location, the stiffness of the rotational spring and so on, they found

four different responses. With the condition of small gaps between the pitch axis and the leading edge as well as strong rotational spring stiffness, the foil remains stable in the initial position. Periodic motion occurs at certain gap between the pitch axis and leading edge. When the oscillating foil changes the pitching angle, the foil undergoes chaotic motion. With the pitch axis close to the trailing edge, the foil flips over. Their results show a potential design guideline for an oscillating foil as an energy harvesting device based on the periodic motion response.

Semler (2010) carried out several experiments on the fully passive oscillating foils in the water tunnel. The oscillating foil model was simplified as a flat plate. Two rail guides were used to allow the flat plate to have a linear back-and-forth motion. The pitch and heave motion of the flat plate were induced by the lift force and moment generated by the fluid flow. A water tunnel with non-uniform flow, a water tunnel with uniform flow and a towing tank were used for the experiment. Dye injection devices were used to visualize the flow structure. The experiment results show that the fully passive flow induced oscillation (the flat plate could change its instantaneous pitch angle automatically at the stroke endpoint without any active control) could be achieved with a selection of the oscillating flat plate parameters, such as flow speed, flat plate size and pitch axis. He found that the energy extraction performance of the oscillating flat plate was sensitive to the pitch axis of the flat plate, the span of the flat plate, the incoming flow velocity and the maximum pitch angle. The best performance could be achieved when the pitch axis was located in 60% to 70% of the chord length from the leading edge with a large incoming flow velocity. With the help of the flow visualization techniques, the flow separation was observed at a large angle of attack which helps to generate the lift of the oscillating flat plate.

Zhu (2012) studied the fully passive oscillating foil system for both the pitch and plunge motion through the two dimensional numerical simulations with the linear shear flow. Zhu's work proved that the oscillating foil turbine is still working with a periodically pitching and heaving motion under the shear flow condition as in the uniform fluid flow condition when the shear rate is small. However, the chaotic condition occurs when the shear rate is large.

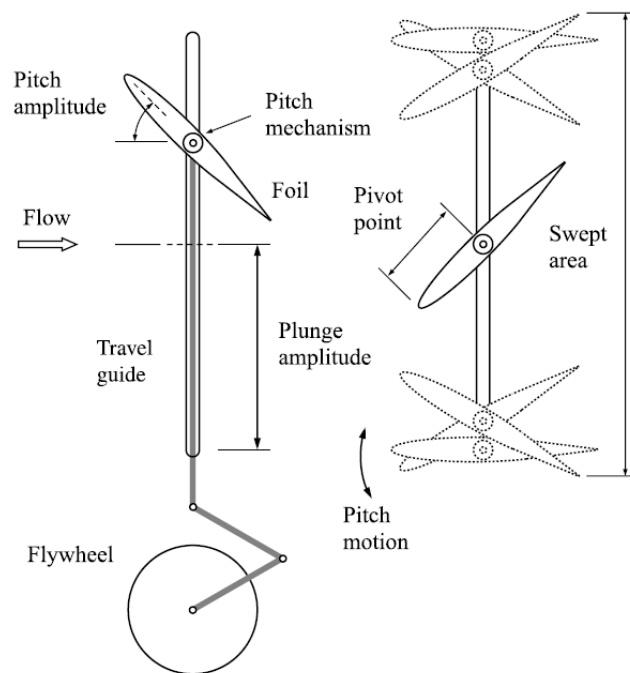


Figure 2. 15 Schematic of the fully passive flapping wing turbine used in Young et al. (2013).

A fully passive flapping foil model, as shown in Fig. 2.15, was designed by Young et al. (2013). The flapping foil turbine is linked to the flywheel for passive control over its pitch and plunge motion. Up to 30% of the power coefficient was found by them under pitch control. The power coefficient could exceed 41% if the oscillating foil turbine uses the angle of attack control. The non-sinusoidal foil pitching motion is also found better in terms of the performance compared with the sinusoidal pitch motion one.

2.3 Review of the research on blade stress estimation and reduction for renewable turbine

To overcome the weakness of the large turbine system which turbine blades experience high stress during operation, new types of composite material have been developed recently. The typical feature of these materials is the ability to deform adaptively to the unsteady loading exerted on it so that more constant and uniform structure stresses on the turbine blades and shaft could be achieved. This could significantly increase the turbine's fatigue endurance, and thus its reliability and sustainability for a long life cycle (Kong et al., 2005; Shokrieh and Rafiee, 2006; Barlas et al., 2008).

Kong et al. (2005) proposed a medium scale blade made of composite material using E-glass/epoxy for a 750 kW horizontal axis wind turbine, which aimed to endure large loads on the blade. Structural analysis with a Finite Element Method (FEM) model confirmed that the proposed blade with the new structure was able to tolerate variable load conditions as well as extreme flow conditions. The full scale static structure experimental test also obtained agreeable conclusions as the analytical results.

Shokrieh and Rafiee (2006) studied the estimation of the fatigue life cycle of a horizontal axis turbine with composite material blades. Their results showed an average life of 22 years of a HAT using composite material blades while the traditional horizontal axis turbine with rigid blades is only 20 years life (Chenna, 2014).

A wind tunnel test was performed by Barlas et al. (2008) for an adaptive HAT blade, of which the trailing edge was designed as a piezoelectric bender. Their results

indicated a significant reduction of blade stress and strain near its root with such a design.

It is worthy to mention that the flexible material has already been used to build up a HAT blade as a so-called “Morphing Blade” (MB). MB has a specific feature to change its shape according to external aerodynamic loadings. It is used as a passive pitch control mechanism to ensure a satisfactory angle of attack for HAT under the off-design wind speed conditions. Recently, the morphing blade has been drawing much attention due to the wind turbine blade design. The idea was introduced from the research on helicopter blades. It has many advantages such as its good aerodynamic performance and being easy to construct and lightweight (Lachenal et al., 2013). Some research has been done to analyse the characteristics of Elastomeric (Peel and Jensen, 2001; Peel et al., 1998), Anisotropic (Daynes and Weaver, 2011; Ge et al., 2010) and Multistable (Daynes et al., 2009) materials for their potential application to the actively controlled morphing blade. The typical feature of these materials is their ability to deform adaptively to the unsteady loading exerted on them so that more constant and uniformed structure stresses on the turbine blades and shaft can be achieved. This could significantly increase the turbine’s fatigue endurance, and thus its reliability and sustainability for a long life cycle. Some preliminary research on the use of morphing blades or composite blades has been done on HAT (Bazilevs et al., 2011; Bir et al., 2011; Deyuan et al., 2003; Harper and Hallett, 2015). Their results show a reduction in the blade stress and an improvement in the fatigue issues by using the morphing or composite turbine HAT blade.

Recently, Hameed and Afaq (2013) designed and studied a straight VAT blade by using both analytical and numerical solutions. The bending deformation in the

spanwise of the blade was allowed, and the structural stress distribution was investigated for blades with different thicknesses under maximum fluid load conditions. In their study, a uniformly distributed external load along the span direction was assumed with its location at one quarter of the leading edge. The centrifugal force was taken into account. Depending on the bending deflection and structure stress, the optimal thickness of the blade was predicted to achieve minimum stress.

More recently, Butbul et al. (2015) carried out a series of experimental tests and FEM analysis on a VAT with a chordwise flexible blade. The study covered a prediction of blade morph direction, magnitude and their effects on power generation. Their results showed that a better performance was observed by using a chordwise flexible morph blade at a low tip speed ratio, which is very helpful for improving the self-starting ability of a VAT compared to a rigid design VAT. However, at a large tip speed ratio, the performance of VAT using a flexible morph blade decreases. It was also observed that the centrifugal force of the blades has a significant impact on large rotational speed which leads to an outward bending motion of the blade, and thus an increased drag force which further reduces turbine energy extraction.

2.4 Review of bio-inspired research and its application in the aerodynamics or marine industry

In nature, insect wings and fish fins are complicated flexible structures that can deform passively, although there are obvious distinctions between them. Previous studies on the flexible role of insect wings, such as those of a butterfly, hawkmoth or bee, conducted on propulsion performance, suggested that some degree of flexibility can achieve a higher level of aerodynamic propulsive thrust by manipulating the

leading edge vortex enhancement/decay mechanism (Nakata and Liu, 2012; Daniel and Combes, 2002).

In particular, the bending and twisting motion of a flexible wing can effectively vary its flying direction and can generate asymmetric forces between the upstroke and downstroke motion, leading to a large cycle-averaged aerodynamic force (Wootton, 1990; Zhu, 2007; Nakata and Liu, 2012; Daniel and Combes, 2002; Yin and Luo 2010).

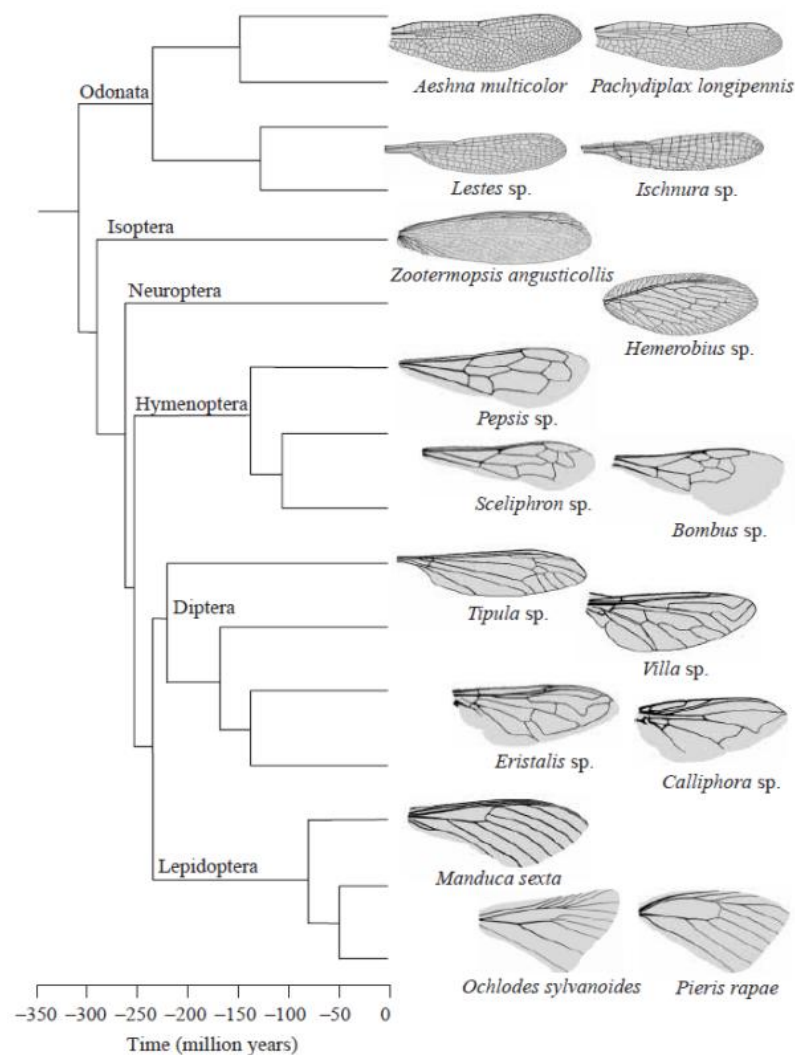


Figure 2. 16 Drawings of forewings from insects, arranged on the phylogenetic tree used to calculate independent contrasts (Combes and Daniel, 2003a).

Combes and Daniel (2003a, 2003b) conducted a relevant study on evaluating the impact of wing stiffness variation in a chord-/span-wise direction of the wing distortion and produced lifting. Their measurements of flexure stiffness and wing venation patterns on the forewings of 16 insect species found that the stiffness in the span-wise direction was approximately one or two orders magnitude higher than that in the chord-wise direction. The drawings of the forewings of insects by Combes and Daniel (2003a) are shown in Fig. 2.16. A sharply decayed flexural stiffness was observed from the wing base to the leading edge. The maximum displacement was less than 0.08 and 0.15 in the span-wise and chord-wise respectively.

Zhu (2007) performed a computational study of a wing with a span-wise and chord-wise distortion, in an attempt to assess the function of wing flexure on propulsion performance in high and low density fluid environments. They found that the inertia of a flexible wing played a major role in wing deformation if the wing was immersed in a low density fluid surrounding, such as air. Both thrust and propulsion efficiency were reduced by increasing the flexure motion. However, within a high density surrounding, like water, the external fluid loading has a primary impact on wing deformation compared with the wing internal inertial force. With their simulation results, the chord-wise flexibility was proved to increase wing propulsion efficiency. These findings highlight the significance of the flexible structure deforms in promoting aerial animals' propulsion movement.

Several researchers investigated the interaction among a school of fish. Liao (2007) found that fish could utilize the vortices induced by upstream fish. Kinsey and Dumas (2012a, 2012b) also focused on the twin foil, especially for tandem

configuration. Their results had showed high power extraction efficiency of up to 64% because of the vortex foil interaction for the downstream foil.

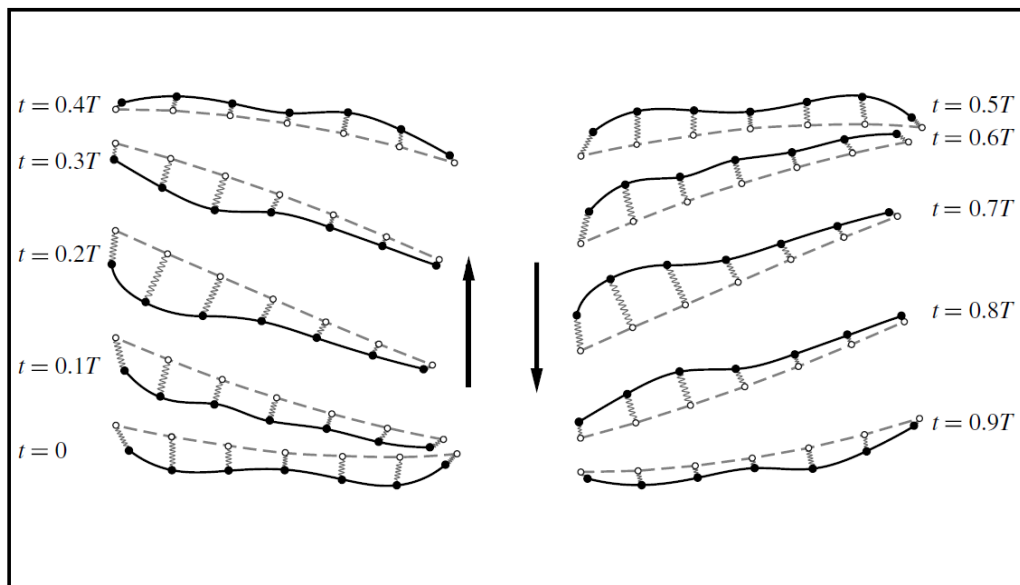


Figure 2. 17 Schematic representation of the fin kinematics calculated by Shoele and Zhu (2012).

It has always been accepted that the biological flexible structure of fish fins plays an important role in fish propulsion and manoeuvring. A recent study by Shoele and Zhu (2012; 2013) addressed the flexibility impact of trout ray fins on trout propelling. With the use of the fully coupled Fluid Structure Interaction (FSI) model, numerical predictions by Shoele and Zhu tested a series of cases to study the relationship between the thrust and fluid field feature. By comparing it with the rigid ray fin model, the flexible models could enhance the thrust significantly. By controlling the leading edge stiffness, i.e., strengthening the leading edge, the propulsion efficiency could reach a higher value. Some degree of domination at the Leading Edge (LE) could effectively increase local AOA, and thus affect the forming and shedding of the Leading Edge Vortex (LEV). An enhanced hydrodynamic force would be generated if the local AOA at the leading edge was around 30° . The schematic

representation of the fin kinematics calculated by Shoele and Zhu (2012) is shown in Fig. 2.17.

Nakata and Liu (2012) studied the three dimensional and flexible effects on the aerodynamic performance of the insect wings. An unsteady fluid structural interaction based analysis was used. The insect model was a hovering hawkmoth (*manduca*). Both flexible and rigid wing models were studied. The aerodynamic forces, power generated by the wing flapping motion and proportion efficiency were studied with passive flexibility as well as the prescribed deformation of the wing. They observed a dynamic wing bending phenomenon of the insect wing. This phenomenon could delay the leading edge vortex breakdown around the wing tip, so that the aerodynamic forces could be enhanced. They found a dynamic change in the bending and twist motion of the insect wing which changes the kinematics of the insect wing around the distal region. This will lead the aerodynamic forces to increase suddenly before the dynamic stall. They also found that the twist motion of the insect wing could increase the proportion efficiency of the hawkmoth. A series of the insect wing rigidity effect of the aerodynamic forces were studied, including Young's modulus of the wing material and the thickness of the insect wing. An optimized result in terms of the propulsion efficiency was suggested by them.

They utilize this flexible feature to achieve high propulsion efficiency and manoeuvring capability. It is widely thought that wing flexibility and deformation would potentially provide new flow mechanisms over completely rigid wings. For example, Heathcote and Gursul (2007) and Heathcote et al. (2008) designed a realistic internal structure for passive flexible flapping wings to test their propulsion

performance by using both experimental and numerical methods. An enhancement of the propulsion efficiency has been observed because of the flexibility.

In contrast to the numerous investigations into the effects of structural deformability on the force-generation performance of flapping foils, the energy harvesting capacity of flexible flapping foils has not been well understood. Le and Ko (2015) investigated the energy extraction performance of an oscillating hydrofoil with both chordwise and spanwise flexibility. A prescribed flexibility motion was used in their study and up to a 30% improvement in the power extraction efficiency was observed. However, despite some recent studies on the flexible wing for propulsion and energy extraction, there is still lack of work on detailed investigations into blade flexibility for vertical axis turbines and oscillating foil turbines.

In a recent work by Tian et al. (2014), a fluid-structure interaction model with an immersed-boundary method was used to study the flow energy extraction with a flexible plate. Four systems were investigated, i.e. rigid plate, flexible plate, flexible leading segment by rigid trailing segment, and rigid plate with active control of leading segment. Their results show an 11.3% enhancement of energy extraction efficiency by applying active control to the leading edge segment. However, for a passively flexible plate, no performance enhancement was observed.

2.5 Summary

In this chapter, relevant literature on the research methods of vertical axis turbines, different methods for the energy extraction performance enhancement of vertical axis turbines, research on the oscillating foil turbine and research on the blade stress prediction and reduction method have been reviewed. An overview of the bio-

inspired research and its application to the aerodynamic or marine industry is also included.

To this end, the following gaps could be identified for relevant research:

- There are many methods to enhance the energy extraction efficiency of a vertical axis turbine, but most of them focus on the design rigid blade pitch motion, designing additional equipment (such as a channel or duct), etc. Some of the researchers patented a vertical axis turbine blade with flaps, but there is a lack of systematic research on the effect of the flap as well as under a bio-inspired active or passive oscillating motion.
- Most existing investigations of the energy extraction performance of the oscillating foil turbine are limited to rigid foils. In contrast to the numerous investigations of the effects of structural deformability on the force generation performance of flapping foils, the energy harvesting capacity of bio-inspired flexible flapping foils has not been well understood.
- Despite the advantage of new material, such as MB, and research on its application for HAT, the investigation of the potential application of bio-inspired composite material to VAT is limited. This is partially because of the even larger variation of unsteady loads applied to a VAT blade during its cyclic rotational motion compared to a HAT.

The main objective of this thesis is to bridge the gap listed above as mentioned in Section 1.3. A new physical phenomenon will be detected and discussed during the study. The results of these studies will also provide a reference or general guidelines for the industrial design of the next generation of renewable turbines.

Chapter 3: Mathematical Formulations and Numerical Algorithm

3.1 Introduction

Two different solvers are used in the present research, one is the commercial software package FLUENT, and the other is the in-house Fluid Structure Interaction (FSI) code used in the CFD and FSI research group at the University of Strathclyde. The commercial software FLUENT is used for the calculations in Chapter 4 and Section 6.1 for the active and passive flow control for the vertical axis turbine by oscillating flap. The in-house FSI solver is used for the rest simulations of the present studies. The detailed governing equations, validations and verifications are listed in the following sections for both solvers.

3.2 FLUENT

3.2.1 Governing equations

The commercial CFD package FLUENT 12.1 is based on solving Unsteady Reynolds-Averaged Navier–Stokes equations (URANS). The governing equations for unsteady incompressible flow associated with mass and moment conservation are as follows

$$\rho_f \frac{\partial \mathbf{U}}{\partial t} = \mathbf{F}_b - \nabla \cdot \mathbf{p}_\infty + \mu \nabla^2 \mathbf{U}, \quad (3.1)$$

and

$$\nabla \cdot \mathbf{U} = 0, \quad (3.2)$$

where ρ_f is the density of the fluid, \mathbf{U} is the vector of velocity, t is the instantaneous time, \mathbf{F}_b is the body force of the fluid, p_∞ is the pressure and μ is the dynamic viscosity.

The modelling in Chapter 4 and Section 6.1 is assumed to be two-dimensional within an isothermal fluid domain. A second order finite volume solver is adopted along with the SIMPLEC algorithm for pressure-velocity coupling. To model the turbulence, various turbulence models are tested and the results indicate that the realizable k - ε turbulent model is the most accurate model for the simulation problems in Chapter 4 and Section 6.1 (shown later). To effectively capture the near wall boundary layer while using reasonable mesh points, the standard wall function is used along with the k - ε turbulent model. The detailed turbulent model is governed by the following two equations as

$$\frac{\partial}{\partial t}(\rho_f k) + \frac{\partial}{\partial x_i}(\rho_f k u_i) = \frac{\partial}{\partial x_i} \left[\left(\mu + \frac{\mu_t}{\sigma_k} \right) \frac{\partial k}{\partial x_j} \right] + G_k + G_b - \rho_f \varepsilon - Y_M + S_K, \quad (3.3)$$

and

$$\frac{\partial}{\partial t}(\rho_f \varepsilon) + \frac{\partial}{\partial x_i}(\rho_f \varepsilon u_i) = \frac{\partial}{\partial x_i} \left[\left(\mu + \frac{\mu_t}{\sigma_\varepsilon} \right) \frac{\partial \varepsilon}{\partial x_j} \right] + C_{1\varepsilon} \frac{\varepsilon}{k} (G_k + C_{3\varepsilon} G_b) - C_{2\varepsilon} \rho_f \frac{\varepsilon^2}{k} + S_\varepsilon, \quad (3.4)$$

where k is the turbulent kinetic energy and ε is the dissipation rate of the kinetic energy. G_k is the generation of turbulent kinetic energy due to the mean velocity gradients; G_b is the generation of turbulent kinetic energy due to the buoyancy; Y_M is the contribution of the fluctuating dilatation in compressible turbulence to the overall dissipation rate; S is the source and σ is the Prandtl number (Manual F., 2009).

The unsteady solution loop within one unsteady time-step is shown in Fig. 3.1. As shown, the macro CG motion along with the User Defined Function (UDF) is adopted to control the sliding mesh for the turbine rotor and oscillating flap motion. Corresponding equations for UDF are shown in Chapter 4 and Section 6.1, respectively. To maintain the mesh twist at a low level, the spring smoothing and re-meshing function is used. The overall flow field problem is solved based on the inertial frame. The instantaneous force and moment of all blades are calculated using UDF and saved at regular time intervals.

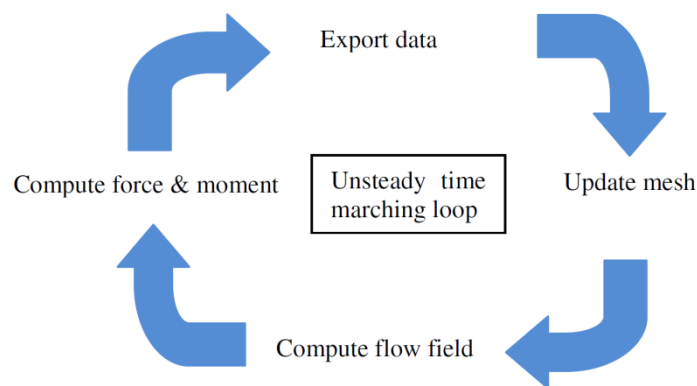


Figure 3. 1 Schematic diagram for unsteady time marching.

3.2.2 Model validation

The computational methodology developed in Chapter 4 and Section 6.1 is verified against a Darrieus wind turbine and a passive pitch control VAT where either the numerical or experimental data are available (Castelli et al., 2011; Sun et al., 2009).

The main geometry and flow conditions for a Darrieus wind turbine are summarized in Table 3.1.

The comparison of the present computed time-mean power coefficient against the tip speed ratio (λ) with Castelli et al.'s (2011) simulation results is shown in Fig. 3.2. The time-averaged value is selected to compare because it can provide the overall level of the simulation accuracy. It can be seen that the predicted power coefficient agrees well with Castell et al.'s results for a tip speed ratio of less than 2.2. However, some differences appear between two results for λ that are larger than 2.4. At these large tip speed ratios, turbulence effect usually strong, simulation becomes more sensitive to the computational mesh and the turbulence model adopted.

Table 3. 1 Main geometry and flow conditions for Darrieus wind turbine

(From Castelli et al., 2011).

Blade profile	NACA 0021	
Rotor diameter	1.03	m
Number of blades	3	-
Blade length	1.4564	m
Blade chord	0.0858	m
Solidity	0.5	-
Stream speed	9	m/s
Reynolds number	7.5×10^5	-

The flow of a passive pitch control VAT (Sun et al., 2009) is also simulated as the second validation case. The main reason for selecting such a relatively complicated case as part of the validation is due to the vast available experimental data and the study for the VAT with the passive oscillating flap in Section 6.1. Successful validation of the developed model with Sun et al.'s (2009) case shows the good capability of the present solver. Fig. 3.3 shows the time-averaged power coefficient variation with the tip speed ratio for the present simulation and the experimental data

from Sun et al. (2009). Good agreement between the present two-dimensional simulation results and their experimental data, based on the blade aspect ratio of 6.0, is clearly seen in Fig. 3.3, indicating the accuracy of the present numerical methods.

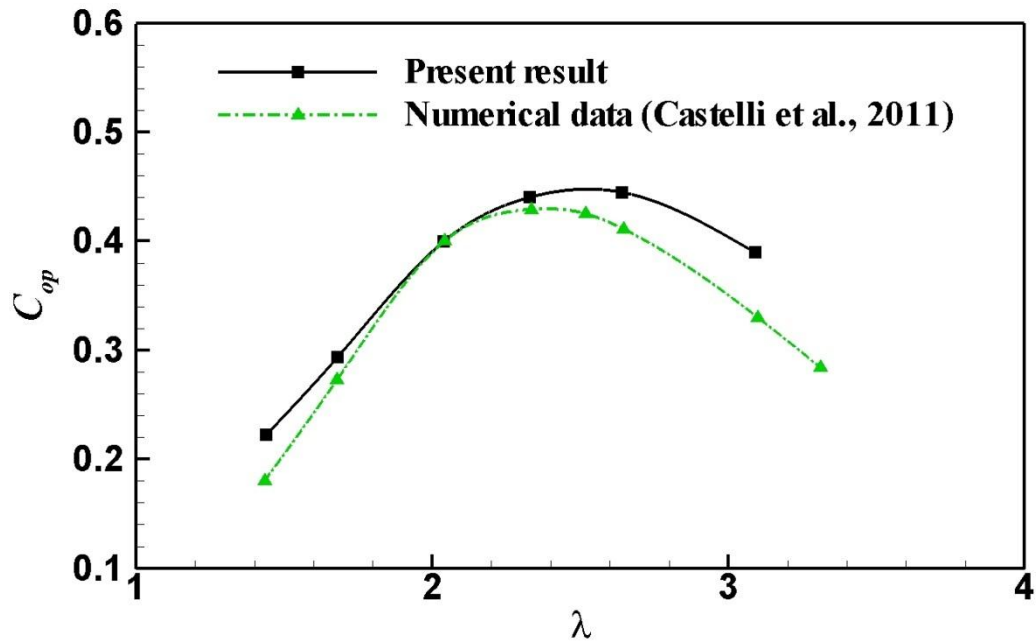


Figure 3. 2 Time-averaged power coefficient variation with tip speed ratio (Comparison with Castelli et al., 2011).

Table 3. 2 Mesh dependence test.

Mesh density	First grid point near wall	Number of cells in the domain	C_{op}
Coarse	0.03	112,626	0.314
Medium	0.01	383,511	0.427
Fine	0.005	785,056	0.446

Apart from the above two validations, the unsteady time-step, mesh independence and turbulence model testing are performed before the detailed investigation. The grid dependence test (the coarse mesh have half grid numbers with medium mesh at each boundaries and the fine mesh have double grid numbers with medium mesh at

each boundaries) is carried out for a full blade turbine at a time-step of 0.5 deg/step with two equation Realizable $k-\varepsilon$ turbulence model at $\lambda=0.99$. The time-mean power coefficient is compared in Table 3.2 along with the detailed mesh information. Fig. 3.4 compares the instantaneous blade moment coefficient (c_m) for three sets of grids. The instantaneous data is selected to compare because it can provide the detail information of the simulation results. Based on these comparisons, there is no significant difference between the medium and fine grid, therefore, all simulations below are computed by the medium grid.

Table 3. 3 Unsteady time step size and turbulent model test.

Turbulent Model	Time-step	c_{op}
Reynolds Stress (5 equations)	0.5°/step	0.411
SST $k-\omega$	0.5°/step	0.329
Realizable $k-\varepsilon$	0.5°/step	0.427
Realizable $k-\varepsilon$	0.2°/step	0.446
Realizable $k-\varepsilon$	0.1°/step	0.454

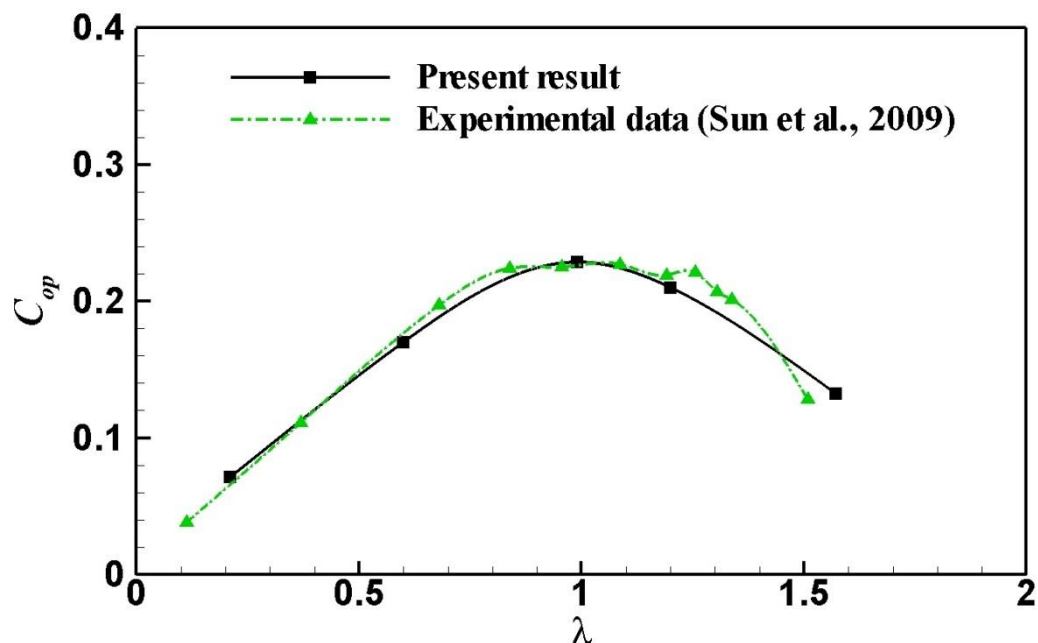


Figure 3. 3 Time-averaged power coefficient variation with tip speed ratio (Comparison with Sun et al., 2009).

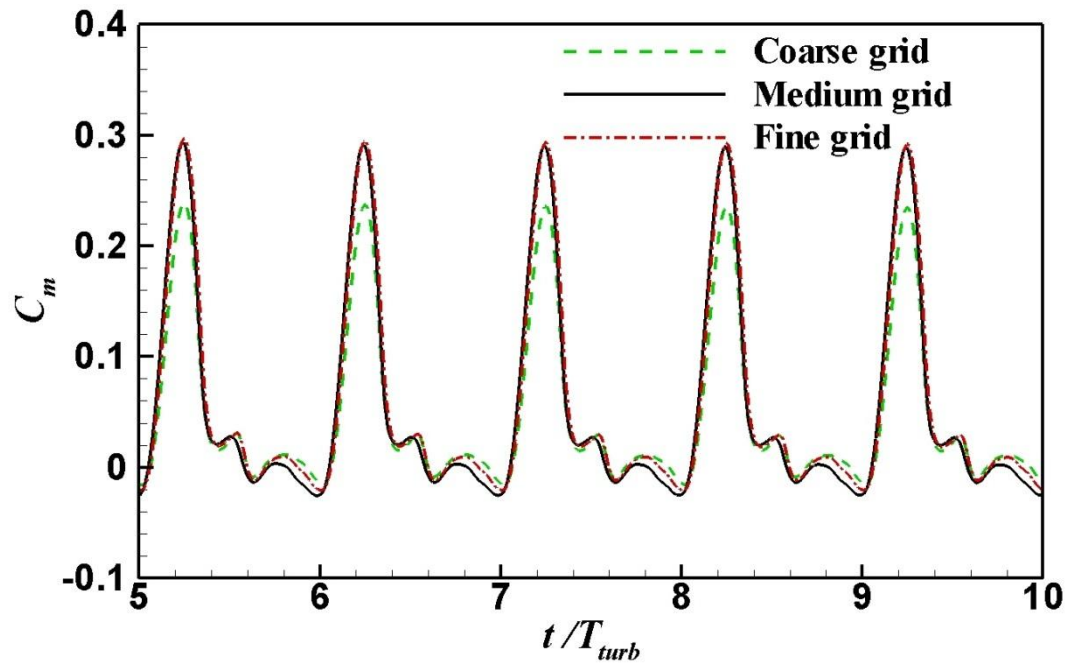


Figure 3. 4 Instantaneous blade moment coefficient variations with instantaneous time (grid dependence test with 159,163 cells of coarse grid, 357,159 cells of medium grid and 746,152 cells of fine grid).

The effects of turbulence modelling and unsteady time-step on the computed results are performed for an oscillating flap blade turbine at $\beta_0=15^\circ$ and $n_t=1.5$. The predicted time-mean c_{op} is listed in Table 3.3. As can be seen from this table, there is no obvious difference in the power coefficient in reducing the time step size. Considering the significantly increased computational time with a small time step, 0.5 deg/step is used in the present simulations. As for the various turbulence models tested, the realizable $k-\varepsilon$ model obtains the closest result in the validated case among the three turbulence models tested.

3.2.3 Computational domain

The computational domain and mesh used in Chapter 4 and Section 6.1 are shown in Fig. 3.5. The turbine is set $9D$ (turbine diameter) away from the inlet boundary and

20D away from the outlet boundary. A uniform constant velocity in the x direction is applied as the incoming flow for the inlet boundary condition as $u=U$, $v=0$ and $\frac{\partial p}{\partial x} = 0$. A pressure outlet with $\frac{\partial p}{\partial n} = 0$ is adopted for the outlet boundary. In order to save time at pre-processing stage, unstructured grids were allocated to both rotational domain and stationary domain. For ease of mesh generation, the dynamic mesh method imbedded in FLUENT which is adopted for handling the oscillating motion of the blade flap, an unstructured grid is constructed within the entire computational domain, while a structured grid is used in the near wall boundary layer around the blade.

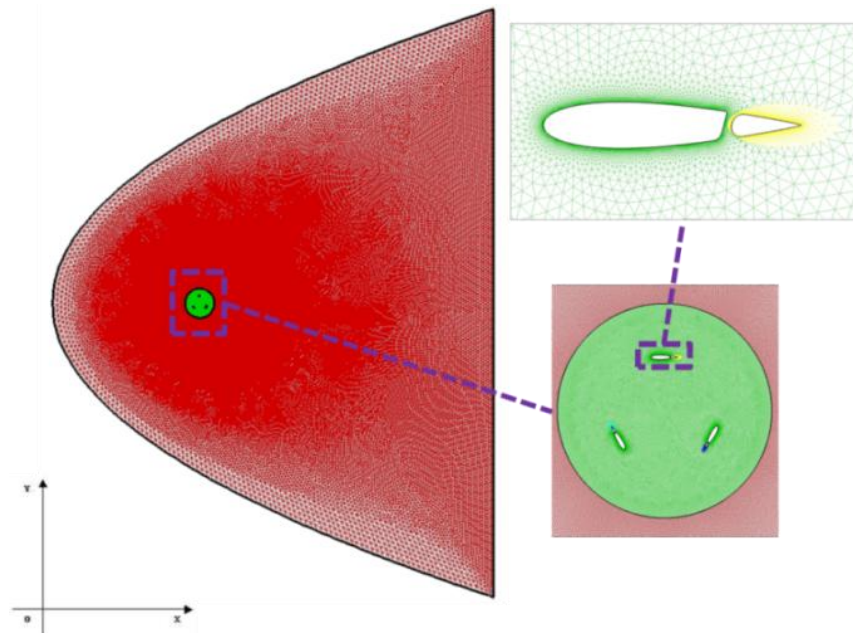


Figure 3. 5 Computational domain and mesh distribution for the simulations in Chapter 4 and Section 6.1.

3.3 In-house FSI code

The in-house code of the University of Strathclyde CFD group which was used in the present studies is written in the FORTRAN programming language. This code was

created by Liu Feng at Princeton University (Liu, 1991) and further developed by researchers at the University of California (Liu and Ji, 1996; Sadeghi et al., 2004) and the University of Strathclyde (Xiao and Liao, 2009; Xiao et al., 2007; 2012; Liu et al., 2013) to enhance the calculation accuracy and enlarge the scope of application.

The present in-house code is a flow solver coupled to a structural solver through the use of a fluid-structure interface method. The time-domain solver for the three-dimensional compressible Favre-Averaged Navier-Stokes equations is coupled to a solver for the linear structural equations. The solution of the nonlinear flow equations is accelerated by using a structured multigrid method and a parallel multiblock approach with the use of MPI. An implicit JST cell centred finite-volume method with second order and fourth order artificial dissipation is used based on Jameson's work (Jameson et al., 1981). Both Jameson's Convective Upwind and Split Pressure (H-CUSP) upwind scheme and second order Roe's Flex Difference Splitting (FDS) upwind scheme are available for present in-house code. The calculation stability is enhanced by using residual smoothing (Papamoschou and Liu, 2008). The second order implicit backward-difference scheme and Jameson's pseudo-time stepping scheme are used for time integration. Both inviscid Euler solver and viscid Navier-Stokes solver are contained in it. Different turbulence models including the Baldwin-Lomax algebraic model and the $k-\omega$ two equation model are available to calculate large Reynolds number flow. Efficiency is achieved through the application of an implicit dual-time multigrid method for the flow, the modal approach for the structure, and by parallel computation. Fluid-structure coupling is achieved by sub-iteration. A grid-deformation algorithm Trans-Finite Interpolation (TFI) is developed to interpolate the deformation of the structural boundaries in the flow grid. The code

is formulated to allow application for general, three-dimensional, complex configurations with multiple independent structures. The code is applicable to general problems of fluid-structure interaction as well as purely fluid dynamic problems in internal and external flows. The detailed equations are listed in the following parts. A flow chart is presented in Fig. 3.22 (a) to show the simulation strategy of present FSI code. The in-house FSI code is used because most of the commercial software cannot solve FSI cases with both rotational turbine or turbomachinery and flexible blade. In addition, all the equations and parameters are controllable with high accuracy by using an in-house code.

3.3.1 Fluid dynamics

The fluid solver is based on the following governing equations of unsteady turbulent flow

$$\frac{\partial}{\partial t} \int_{\Omega} \mathbf{W} d\Omega + \oint_{\partial\Omega} (\mathbf{F} - \mathbf{F}_{\mu}) d\mathbf{S} = 0, \quad (3.5)$$

where, Ω is the control volume and S is the boundary surface. The vector \mathbf{W} contains the conservative variables.

$$\mathbf{W} = \{\rho_f, \rho_f u, \rho_f v, \rho_f w, \rho_f E, \rho_f k, \rho_f \omega\}^T, \quad (3.6)$$

where ρ_f is the fluid density, u , v , and w are the three Cartesian velocity components and the flow specific total energy E is given by

$$E = e + \frac{1}{2}(u^2 + v^2 + w^2), \quad (3.7)$$

where e is the internal energy. k and ω are the turbulent kinetic and specific dissipation rate.

The flux tensors \mathbf{F} and \mathbf{F}_μ represent the inviscid convective fluxes and the diffusive fluxes, respectively. The convective fluxes \mathbf{F} defined in terms of the relative velocity $\mathbf{u} - \mathbf{u}_b$ is

$$\mathbf{F} = \begin{bmatrix} \rho(u - u_b) & \rho(v - v_b) & \rho(w - w_b) \\ \rho u(u - u_b) + p & \rho u(v - v_b) & \rho u(w - w_b) \\ \rho v(u - u_b) & \rho v(v - v_b) + p & \rho v(w - w_b) \\ \rho w(u - u_b) & \rho w(v - v_b) & \rho w(w - w_b) + p \\ \rho \left(E + \frac{p}{\rho}\right)(u - u_b) & \rho \left(E + \frac{p}{\rho}\right)(v - v_b) & \rho \left(E + \frac{p}{\rho}\right)(w - w_b) \\ \rho k(u - u_b) & \rho k(v - v_b) & \rho k(w - w_b) \\ \rho \omega(u - u_b) & \rho \omega(v - v_b) & \rho \omega(w - w_b) \end{bmatrix}, \quad (3.8)$$

where $\mathbf{u}_b = (u_b, v_b, w_b)^T$ is the grid velocity vector. The diffusive fluxes due to the viscous shear stresses, thermal diffusion and turbulence diffusion can be written as

$$\mathbf{F}_\mu = \begin{bmatrix} 0 & 0 & 0 \\ \tau_{xx} & \tau_{xy} & \tau_{xz} \\ \tau_{yx} & \tau_{yy} & \tau_{yz} \\ \tau_{zx} & \tau_{zy} & \tau_{zz} \\ u\tau_{xx} + v\tau_{xy} + w\tau_{xz} - q_x & u\tau_{yx} + v\tau_{yy} + w\tau_{yz} - q_y & u\tau_{zx} + v\tau_{zy} + w\tau_{zz} - q_z \\ \mu^* \frac{\partial k}{\partial x} & \mu^* \frac{\partial k}{\partial y} & \mu^* \frac{\partial k}{\partial z} \\ \mu^* \frac{\partial \omega}{\partial x} & \mu^* \frac{\partial \omega}{\partial y} & \mu^* \frac{\partial \omega}{\partial z} \end{bmatrix}, \quad (3.9)$$

where

$$\mu^* = \mu_L + \sigma^* \mu_T, \quad (3.10)$$

where μ_L is the laminar viscosity, μ_T is the turbulent eddy viscosity, σ^* is the turbulent closure constant equals to 0.5, and $\tau_{\alpha\beta}$ with $\alpha, \beta \in \{x, y, z\}$ is the stress tensor expressed as

$$\tau_{\alpha\beta} = \mu(\partial_\alpha u_\beta + \partial_\beta u_\alpha) - \frac{2}{3} \mu \delta_{\alpha\beta} \partial_\alpha u_\beta, \quad (3.11)$$

and

$$q_\alpha = -k\partial_\alpha\theta. \quad (3.12)$$

In the above equations, μ represents the dynamic viscosity, k the thermal conductivity, and θ the temperature. The stress tensor $\tau_{\alpha\beta}$ is the general form of the shear stresses in f_μ .

The source term S is defined as:

$$S = \left\{ \begin{array}{c} 0 \\ 0 \\ 0 \\ 0 \\ 0 \\ \tau_{\alpha\beta} \frac{\partial u_\alpha}{\partial x_\beta} - b^* \rho \omega k \\ \frac{a\omega}{k} \tau_{\alpha\beta} \frac{\partial u_\alpha}{\partial x_\beta} - b\rho\omega^2 \end{array} \right\}, \quad (3.13)$$

with closure constants of $a=5/9$, $b=0.075$, and $b^*=0.09$.

The fluid governing equations could be discretized into the following semi-discrete form:

$$\frac{d\mathbf{w}}{dt} + \mathbf{R}(\mathbf{w}) = 0. \quad (3.14)$$

By applying the dual-time method with a second order implicit scheme, the above equation could be reformulated into the following forms:

$$\frac{d\mathbf{w}^{n+1}}{dt^*} + \mathbf{R}^*(\mathbf{w}^{n+1}) = 0, \quad (3.15)$$

and

$$R^*(w^{n+1}) = \frac{3w^{n+1} - 4w^n + w^{n-1}}{2\Delta t} + R(w^{n+1}). \quad (3.16)$$

The spatial discretization in the above equations is done based on a finite volume approach. The cell-centred based method is used to calculate gradients. The discretization of the convective fluxes is based on the implicit JST scheme for Navier-Stokes equations. The discretization of the diffusive fluxes is based on a second order and fourth order artificial or matrix dissipation scheme. To cope with the complicated moving mesh cases, a structured multi-block mesh is generated.

3.3.2 Structure dynamics

The structure elastic equations could be discretized in a finite-element model as follows:

$$M\ddot{x}_s + C\dot{x}_s + Kx_s = F, \quad (3.17)$$

where M denotes the symmetric mass matrix, C represents the symmetric structural damping matrix, K is the symmetric stiffness matrix and F is the total fluid dynamic force acting on the object's surface.

By finding the orthogonal mode shape $\tilde{\Phi}$, a relationship equation could be defined as

$$x_s = \tilde{\Phi}q, \quad (3.18)$$

where q is the vector of the generalized displacement in the principal coordinates.

The above equation could be premultiplied by the transpose mode shape $\tilde{\Phi}^T$ as

$$\tilde{\Phi}^T \mathbf{M} \tilde{\Phi} \ddot{\mathbf{q}} + \tilde{\Phi}^T \mathbf{C} \tilde{\Phi} \dot{\mathbf{q}} + \tilde{\Phi}^T \mathbf{K} \tilde{\Phi} \mathbf{q} = \tilde{\Phi}^T \mathbf{F}. \quad (3.19)$$

By assuming a linear combination between the damping matrix and the mass and the stiffness matrices, the above equations could be decoupled and the j th equations are shown below:

$$\ddot{q}_j + 2\zeta_j \omega_j \dot{q}_j + \omega_j^2 q_j = \frac{\tilde{\phi}_j^T}{m_j} \mathbf{F}, \quad (3.20)$$

and

$$\Delta \mathbf{x}_s = \sum_{j=1}^N q_j \tilde{\phi}_j, \quad (3.21)$$

where ζ_j is the modal damping ratio, ω_j is the natural frequency, and m_j is the mass matrix in the j th diagonal element. $\tilde{\phi}_j^T$ is the j th element of mode shape $\tilde{\Phi}^T$ as defined as

$$\tilde{\Phi}^T = [\tilde{\phi}_1, \tilde{\phi}_2, \tilde{\phi}_3, \dots, \tilde{\phi}_N]^T. \quad (3.22)$$

Following Alonso and Jameson (1994), the first-order differential equations are defined as

$$x_{1j} = q_j, \quad (3.23)$$

$$\dot{x}_{1j} = x_{2j}, \quad (3.24)$$

and

$$\dot{x}_{2j} = \frac{\tilde{\phi}_j^T}{m_j} \mathbf{F} - 2\zeta_j \omega_j x_{2j} - \omega_j^2 x_{1j}. \quad (3.25)$$

Thus, the model equation could be rewritten as

$$\dot{\mathbf{X}}_j = \mathbf{A}_j \mathbf{X}_j + \mathbf{F}_j, \quad j = 1 \dots N, \quad (3.26)$$

where,

$$\dot{\mathbf{X}}_j = \begin{bmatrix} \dot{x}_{1j} \\ \dot{x}_{2j} \end{bmatrix}, \quad (3.27)$$

$$\mathbf{A}_j = \begin{bmatrix} 0 & 1 \\ -\omega_j^2 & -2\zeta_j \omega_j \end{bmatrix}, \quad (3.28)$$

and

$$\mathbf{F}_j = \begin{bmatrix} 0 \\ \frac{\tilde{\phi}_j^T}{m_j} \mathbf{F} \end{bmatrix}. \quad (3.29)$$

Then, the model equation could be further discretized by the pseudo-time t^* as

$$\frac{dz_j^{n+1}}{dt^*} + \mathbf{R}_s^*(z_j^{n+1}) = 0, \quad (3.30)$$

and

$$\mathbf{R}_s^*(z_j^{n+1}) = \frac{3z_j^{n+1} - 4z_j^n + z_j^{n-1}}{2\Delta t} + \mathbf{R}_s(z_j^{n+1}), \quad (3.31)$$

where

$$\mathbf{z}_j = \begin{bmatrix} z_{1j} \\ z_{2j} \end{bmatrix}, \quad (3.32)$$

and

$$\frac{dz_{(1,2)j}}{dt^*} = \omega_j \left(-\zeta_j \pm \sqrt{\zeta_j^2 - 1} \right) z_{(1,2)j} + \frac{\sqrt{\zeta_j^2 - 1} \mp \zeta_j}{2\sqrt{\zeta_j^2 - 1}} \frac{\tilde{\phi}_j^T}{m_j} F. \quad (3.33)$$

In the present in-house code, the discretised structural equation (Eq. 3.30) is coupled with the discretised fluid equation (Eq. 3.15). Specifically, the foil displacement data are employed by the fluid residual calculation as the flow boundary condition and the fluid parameters are employed by the structure residual calculation as the hydrodynamic forcing. The detailed fluid-structure coupling algorithm is provided in the following section.

3.3.3 Fluid-structure coupling

Since the fluid domain and the structure domain are calculated independently during the iterations, it is necessary to pass the fluid load from the fluid solver to the structure solver as the boundary conditions to calculate the structural deformation, and to pass the structure displacement from the structure solver to the fluid solver as the boundary conditions to calculate the fluid forces. A linear transformation equation between the fluid domain and the structure domain is used to exchange information between them. The displacement $\Delta \mathbf{x}_f$ of the fluid dynamic grid is expressed in terms of the structural grid displacements $\Delta \mathbf{x}_s$ using a transformation matrix \mathbf{G} as

$$\Delta \mathbf{x}_f = \mathbf{G} \Delta \mathbf{x}_s. \quad (3.34)$$

Since the motion of every node needs to meet the requirements of the conservation of work, both fluid mesh nodes and structure mesh nodes have to obey the following equations:

$$\mathbf{F}_s^T \Delta \mathbf{x}_s = \mathbf{F}_f^T \Delta \mathbf{x}_f = \mathbf{F}_f^T \mathbf{G} \Delta \mathbf{x}_s, \quad (3.35)$$

$$\Delta \mathbf{F}_s = \mathbf{G}^T \Delta \mathbf{F}_f. \quad (3.36)$$

In the transformation equations above, \mathbf{F}_s represents the force vector acting on the structure nodes and \mathbf{F}_f represents the force vector acting on the fluid nodes.

In order to find a proper transformation matrix \mathbf{G} , the Constant-Volume Tetrahedron (CVT) method is used. In this approach each fluid mesh node \mathbf{x}_f is associated with its nearest three structure mesh nodes $\mathbf{x}_{s,1}$, $\mathbf{x}_{s,2}$ and $\mathbf{x}_{s,3}$ as shown in Fig. 3.6. The vectors \mathbf{a} , \mathbf{b} and \mathbf{d} are defined as shown in the following equations (Sadeghi, 2004):

$$\mathbf{a} = \mathbf{x}_{s,2} - \mathbf{x}_{s,1}, \quad (3.37)$$

$$\mathbf{b} = \mathbf{x}_{s,3} - \mathbf{x}_{s,1}, \quad (3.38)$$

and

$$\mathbf{d} = \mathbf{a} \times \mathbf{b}. \quad (3.39)$$

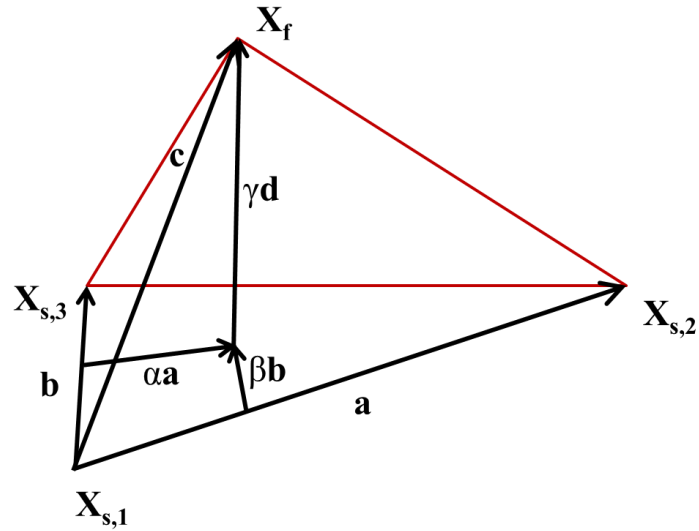


Figure 3. 6 Configuration for the CVT method.

Thus, the position of the fluid mesh node x_f could be calculated by using vector c as below:

$$\mathbf{c} = \mathbf{x}_f - \mathbf{x}_{s,1} = \alpha \mathbf{a} + \beta \mathbf{b} + \gamma \mathbf{d}, \quad (3.40)$$

where the parameters α , β and γ are calculated as

$$\alpha = \frac{(\mathbf{b} \cdot \mathbf{b})(\mathbf{a} \cdot \mathbf{c}) - (\mathbf{a} \cdot \mathbf{b})(\mathbf{b} \cdot \mathbf{c})}{(\mathbf{a} \cdot \mathbf{a})(\mathbf{b} \cdot \mathbf{b}) - (\mathbf{a} \cdot \mathbf{b})(\mathbf{a} \cdot \mathbf{b})}, \quad (3.41)$$

$$\beta = \frac{(\mathbf{a} \cdot \mathbf{a})(\mathbf{b} \cdot \mathbf{c}) - (\mathbf{a} \cdot \mathbf{b})(\mathbf{a} \cdot \mathbf{c})}{(\mathbf{a} \cdot \mathbf{a})(\mathbf{b} \cdot \mathbf{b}) - (\mathbf{a} \cdot \mathbf{b})(\mathbf{a} \cdot \mathbf{b})}, \quad (3.42)$$

and

$$\gamma = \frac{\mathbf{c}_0 \cdot \mathbf{d}_0}{\mathbf{d} \cdot \mathbf{d}}, \quad (3.43)$$

where \mathbf{c}_0 and \mathbf{d}_0 are the initial values of vectors \mathbf{c} and \mathbf{d} . Thus, the following equations could be derived by linearization as

$$\Delta \mathbf{x}_f = \sum_{i=1}^3 [\mathbf{G}]^{(i)} \Delta \mathbf{x}_{s,i}, \quad (3.44)$$

$$\mathbf{G}_{ij}^{(1)} = \delta_{ij} - \mathbf{G}_{ij}^{(2)} - \mathbf{G}_{ij}^{(3)}, \quad (3.45)$$

$$\mathbf{G}_{ij}^{(2)} = \alpha \delta_{ij} - \gamma \mathcal{U} \mathcal{V}(\mathbf{b}), \quad (3.46)$$

$$\mathbf{G}_{ij}^{(3)} = \beta \delta_{ij} + \gamma \mathcal{U} \mathcal{V}(\mathbf{a}), \quad (3.47)$$

where δ_{ij} represents the Kronecker delta. The matrixes \mathcal{U} and $\mathcal{V}(\mathbf{s})$ are given as

$$\mathcal{U} = \delta_{ij} - \frac{2}{d \cdot d} d_i d_j, \quad (3.48)$$

and

$$\mathcal{V}(\mathbf{s}) = \begin{bmatrix} 0 & -Z_3 & Z_2 \\ Z_3 & 0 & -Z_1 \\ -Z_2 & Z_1 & 0 \end{bmatrix}. \quad (3.49)$$

Since the volume of each associated tetrahedron should be a non-zero value and kept as a constant during the structural deformation, the CVT method can only be adopted in three dimensional FSI modelling. Therefore, all two-dimensional cases in Chapter 7 are simulated by using the three dimensional model. The details of the modelling strategies are described in the following sections.

Table 3. 4 Summary of validation cases for in-house FSI code

Validation case ID	Validation case	Validation case type	2D/3D	Inviscid/ Laminar/ Turbulent	Validation purpose	Published data source
1	Flow passes a stationary circular cylinder	Fluid solver validation	2D	Laminar	Basic fluid field calculation ability	Helen (2008), Griffin (1971), Labbe and Wilson (2007), Williamson (1989) and Zheng and Zhang (2008)
2	Active undulating foil	Fluid solver validation	2D	Laminar	Simulation ability for the flexible cases	Deng et al. (2007)
3	OFT	Fluid solver validation	2D	Turbulent	Simulation ability for the OFT cases and turbulence modelling	Kinsey and Dumas (2012a; 2012b)
4	Plunging wing	Fluid solver validation	3D	Turbulent	Simulation ability for 3D cases	Heathcote et al. (2008), Young (2005), and Garrick (1937)
5	VAT	Fluid solver validation	3D	Turbulent	Simulation ability for VAT cases	Strickland et al. (1980), Strickland et al. (1979) and Ponta and Jacovkis (2001)
6	Free transverse oscillating cylinder	Rigid body FSI validation	2D	Turbulent	Simulation ability for 1 DOF rigid FSI cases	Khalak and Williamson (1996; 1999) and Wu (2011)
7	Free oscillating foil	Rigid body FSI validation	2D	Inviscid	Simulation ability for 2 DOF rigid body FSI cases	Zhang et al. (2005), Gao et al. (2005), Bohbot (2001) and Alonso and Jamenson (1994)
8	AGARD 445.6 wing natural frequencies	Modal analysis validation	3D	-	Modal analysis validation	Yates (1988), Akgun et al. (2005), Kolonay (2001) and Li (2002)
9	AGARD 445.6 wing flutter	Fluid structure interface validation	3D	Inviscid	CVT method validation	Yang et al. (2004) and Sadeghi (2004)
10	Flapping wing with spanwise flexibility	FSI solver	3D	Turbulent	Simulation ability for general FSI cases	Heathcote et al. (2008) and Gordnier et al. (2010)

3.3.4 In-house code validation

The numerical methods developed for the present studies have been extensively validated by previous studies (Xiao and Liao, 2010 and Xiao et al., 2012). Further validation cases for the fluid solver, fluid structure interaction for a rigid body, modal analysis for a flexible body, fluid structure interface and fluid structure interaction for a flexible body are presented in the following sections. A summary of the validation cases for the in-house FSI code is listed in Table 3.4.

3.3.4.1 Fluid solver validation cases

Five different validation cases have been used to test the fluid solver of the present FSI code. The details of these validation cases and results are shown in the following sections.

3.3.4.1.1 Flow passes a stationary circular cylinder

The validation of the present calculation code for the fluid solver part starts from the classic case of flow pass a stationary cylinder as shown in Fig. 3.7. The purpose of this validation is to test the basic fluid field calculation ability of the present FSI code.

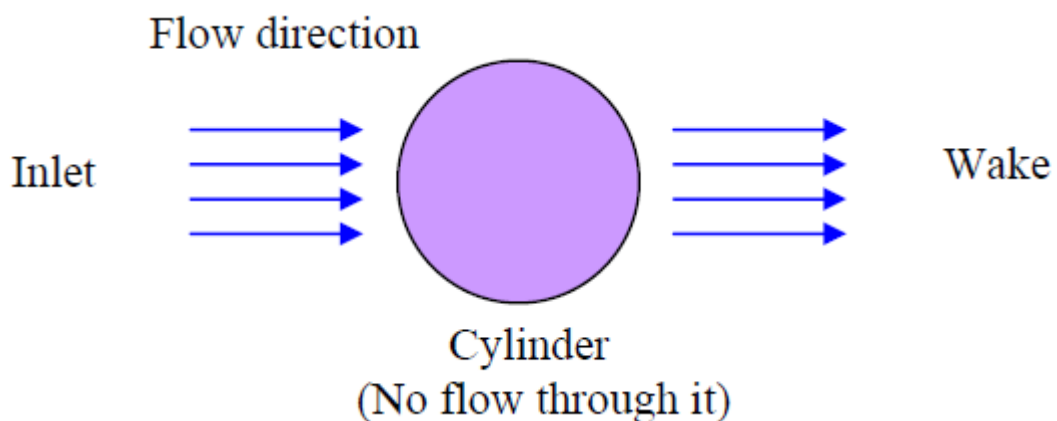
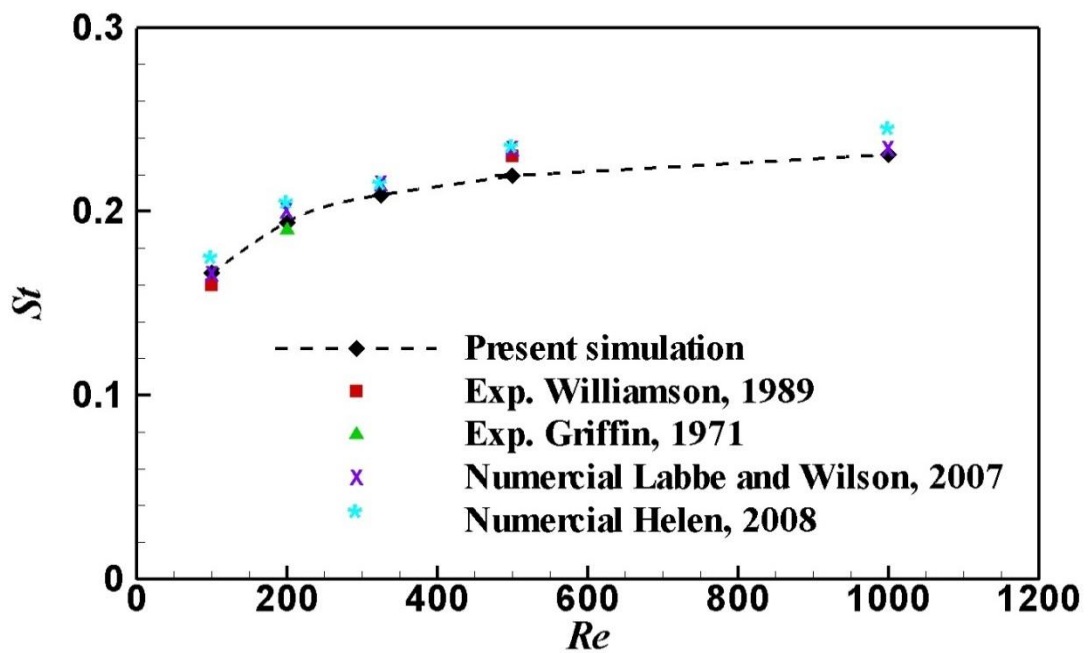
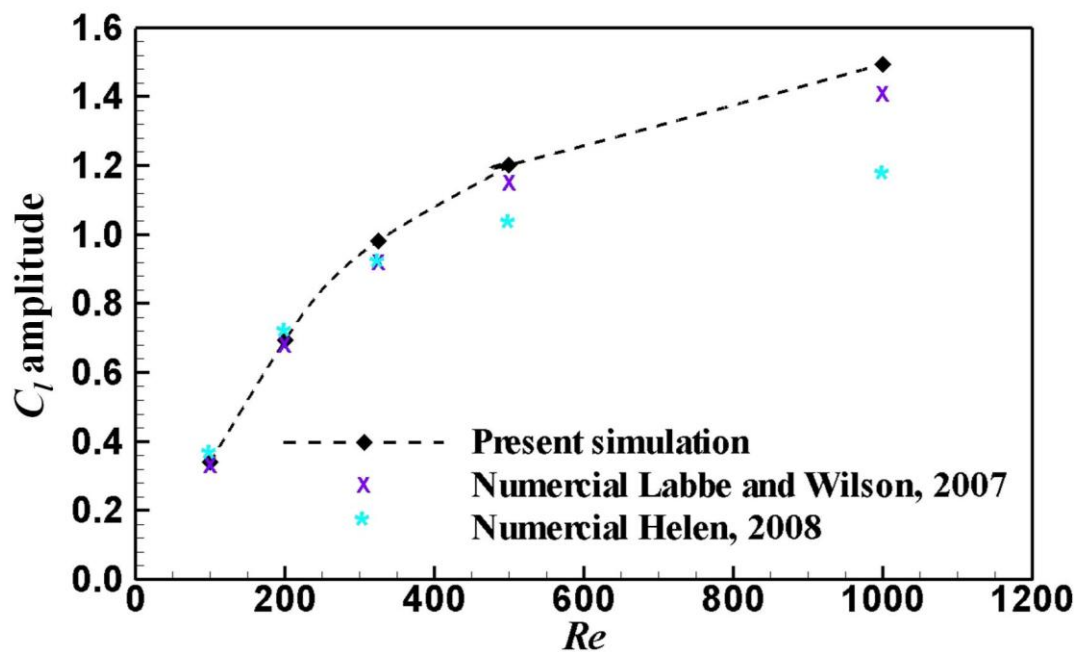


Figure 3.7 Sketch of validation cases of the flow passes stationary cylinder (Helen, 2008).



(a) St results



(b) c_l amplitude results

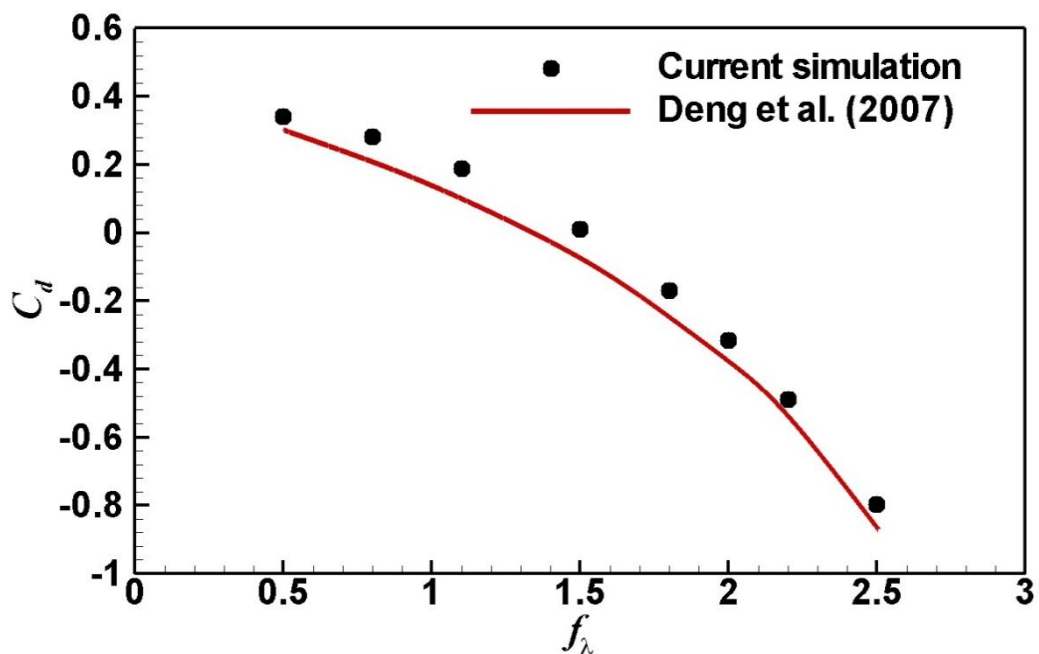
Figure 3. 8 Flow pass stationary cylinder validation of (a) S_t results and (b) c_l results (Comparison with Helen (2008), Griffin (1971), Labbe and Wilson (2007), Williamson (1989) and Zheng and Zhang (2008)).

2D simulation and laminar assumption are used in the present validation case. Five different Re (i.e. 100, 200, 325, 500 and 1000) have been tested. The results compared with Helen (2008), Griffin (1971), Labbe and Wilson (2007), Williamson (1989) and Zheng and Zhang (2008) are shown in Fig. 3.8.

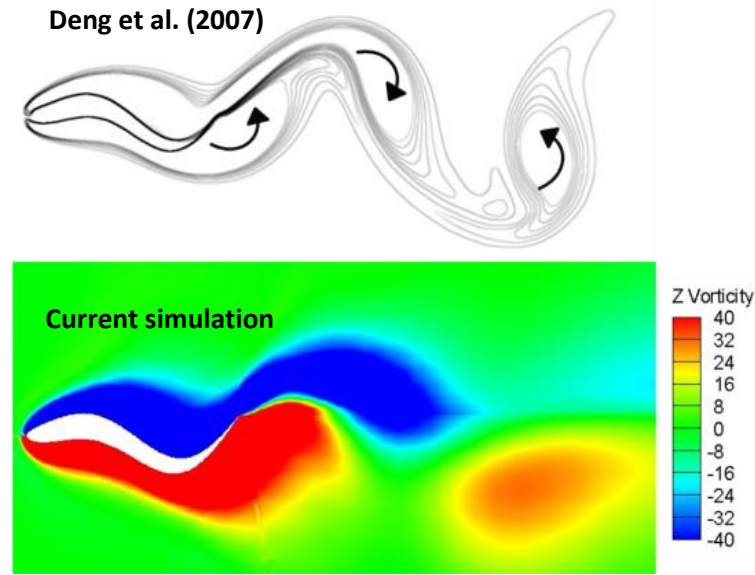
It can be seen that the results have good agreement with the published results at low Re , but some differences exist in Re larger than 400. This may be due to the inaccuracy of the laminar assumption in this Re region.

3.3.4.1.2 Active undulating foil

To validate the capability of the in-house FSI solver to deal with the active flexible models proposed herein, a study on an active undulating fish model is performed in this section and the results are compared with those of CFD work by Deng et al. (2007) in Figs. 3.9 (a) and (b).



(a) Drag coefficient validation



(b) Vorticity contour validation

Figure 3. 9 Flexible model validation of (a) time-averaged drag coefficient (c_d) variation with f_λ , (b) instantaneous vorticity contour at $f_\lambda = 0.5$ and $t/T_{turb}=1/8$ (Comparison with Deng et al., 2007).

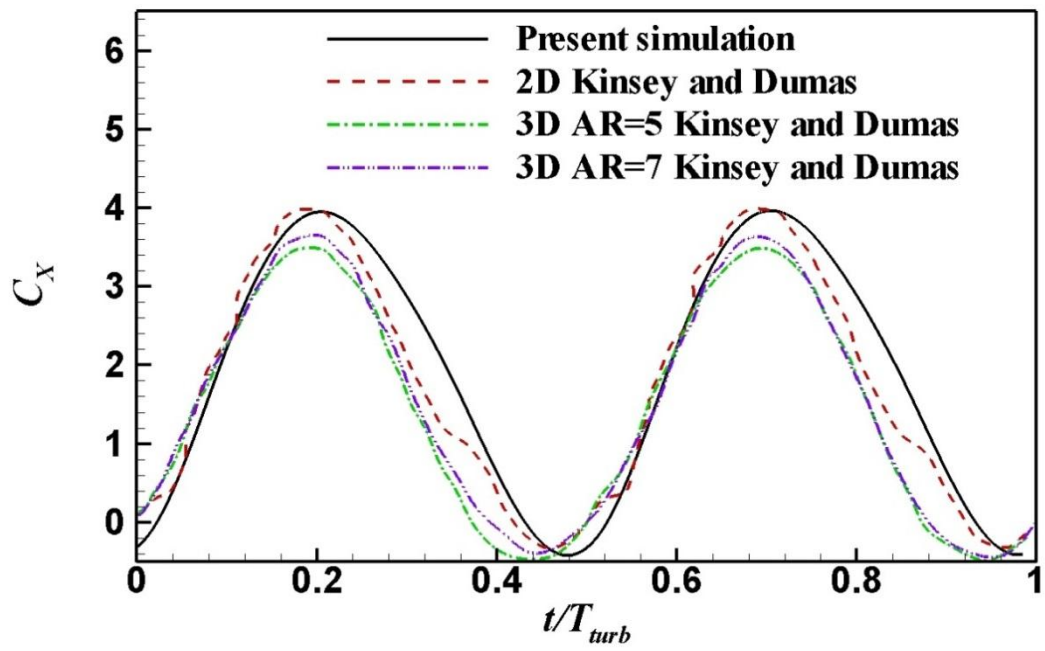
The non-dimensionalized undulating phase speed (f_λ) is defined as:

$$f_\lambda = \frac{2\pi f}{k_\lambda}, \quad (3.50)$$

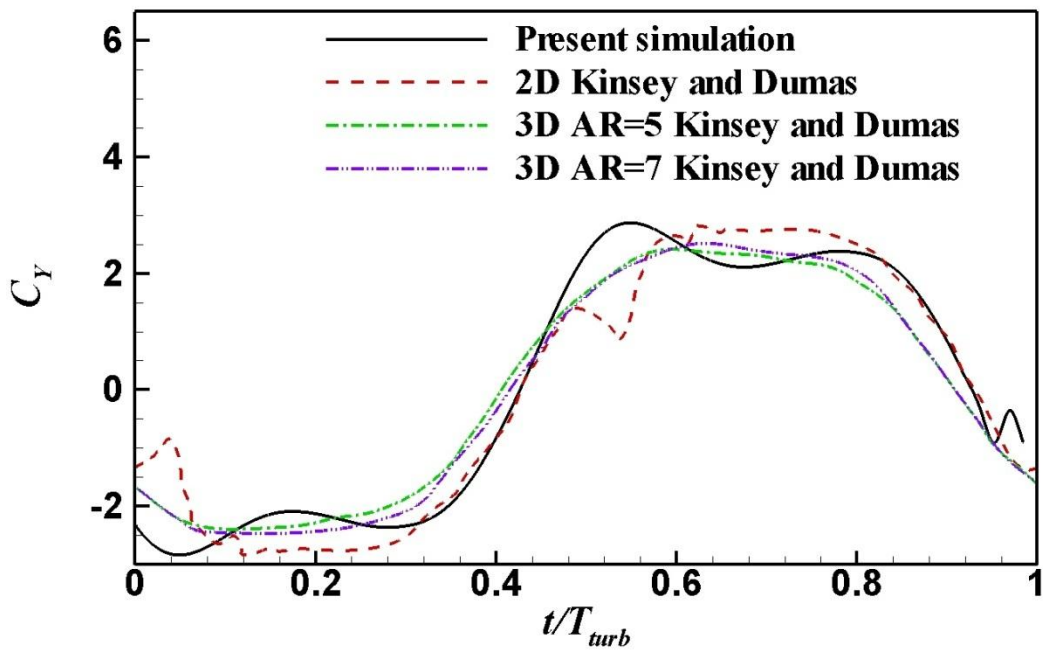
where f is the undulation frequency and k_λ is the non-dimensionalized wave length. “O” shape grid with 50440 nodes is used in this validation case. 10 undulation cycles with 64 time steps per cycle are applied. As can be seen clearly, the predicted results show a good correlation with theirs for both the drag coefficient and fluid fields.

3.3.4.1.3 OFT with the turbulence model

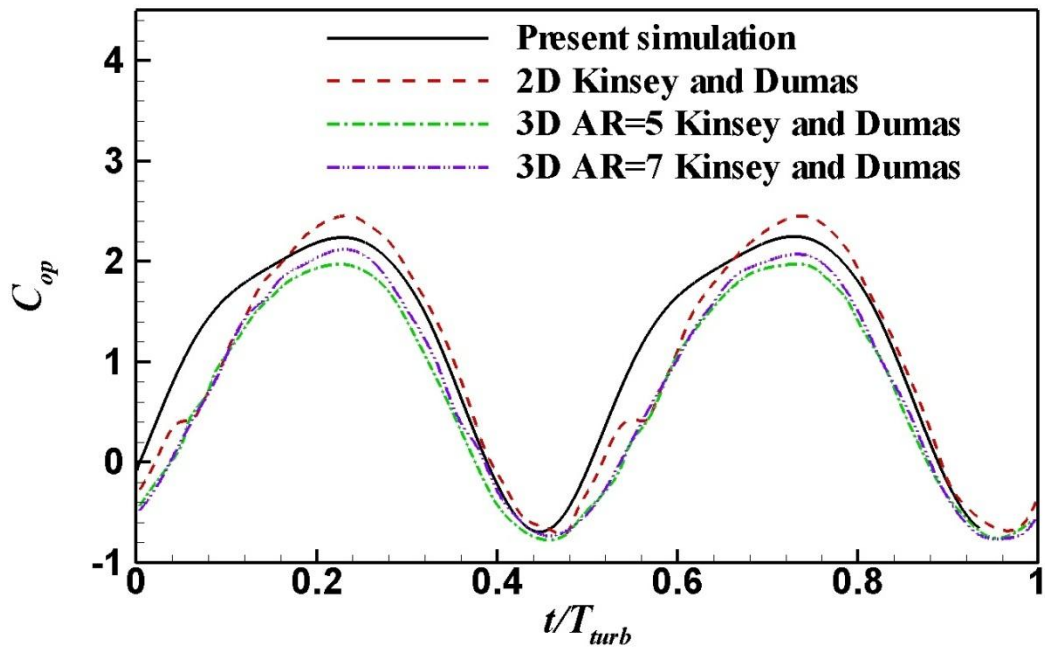
In order to test the accuracy of the model in predicting flow energy harvesting by the oscillating foil turbine, the dynamics and energy harvesting performance of a pitching and heaving wing have been examined.



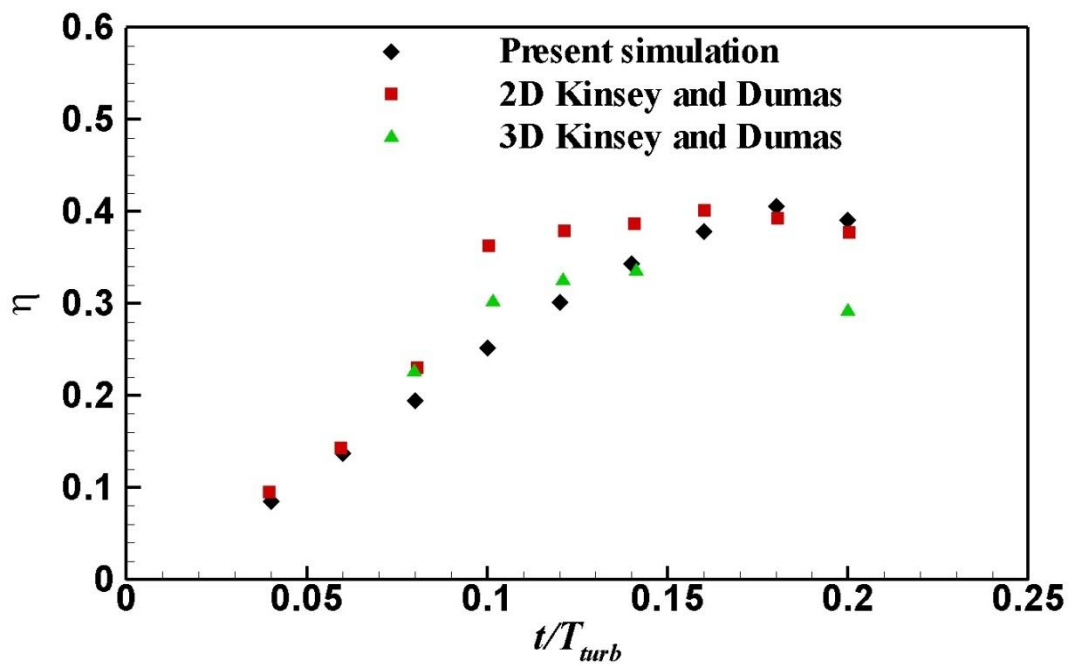
(a) Drag coefficient



(b) Lift coefficient



(c) Power coefficient

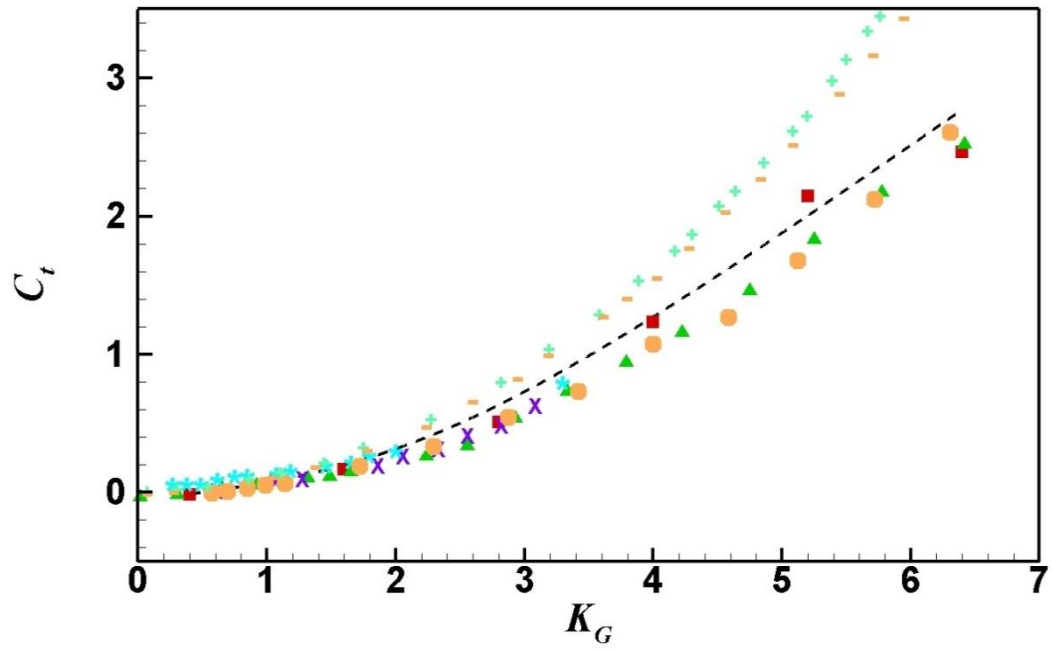


(d) Efficiency

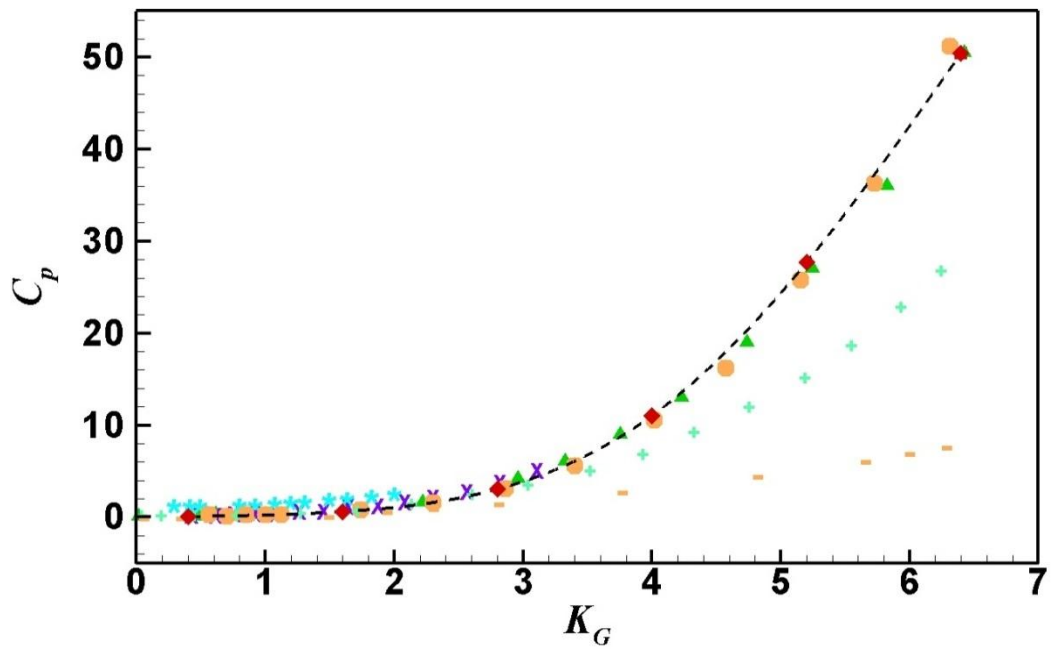
Figure 3. 10 Validation on a rigid oscillating foil as an energy extraction device with $Re=5\times 10^5$; $h_0/c=1.0$; $c_{pit}/c=1/3$; $\theta_0=75^\circ$ and $\varphi=-\pi/2$ – compared with Kinsey and Dumas (2012a; 2012b).

A typical case is a single oscillating foil with an NACA0015 shape flapping at f^* of 0.14. The pitch and heave amplitude are 75° and $1.0c$, and the far-stream Reynolds number is equal to 5×10^5 . The foil pitch at $1/3$ chord length from its leading edge and phase angle between the heave and pitch is $\pi/2$. “O” shape grid with 24960 nodes is used in this validation case. 6 oscillating cycles with 128 time steps per cycle are applied. The time histories of the drag coefficient, lift coefficient and power coefficient at a reduced frequency of 0.14 are shown in Fig. 3.10 (a)-(c) and the dependence of the time-averaged energy extraction efficiency upon the reduced frequency is shown in Fig. 3.10 (d). These results are comparable with the published results of Kinsey and Dumas (2012a; 2012b). Some discrepancies are found between the present simulation and Kinsey and Dumas (2012a; 2012b) at a large flapping frequency. It is believed that this could be attributed to the different flow solvers and turbulence models being used. In the work of Kinsey and Dumas (2012a; 2012b), a commercial CFD solver FLUENT with one equation Spalart-Allmaras turbulence model was used. In the present study, an in-house code with two equation $k-\omega$ models is adopted.

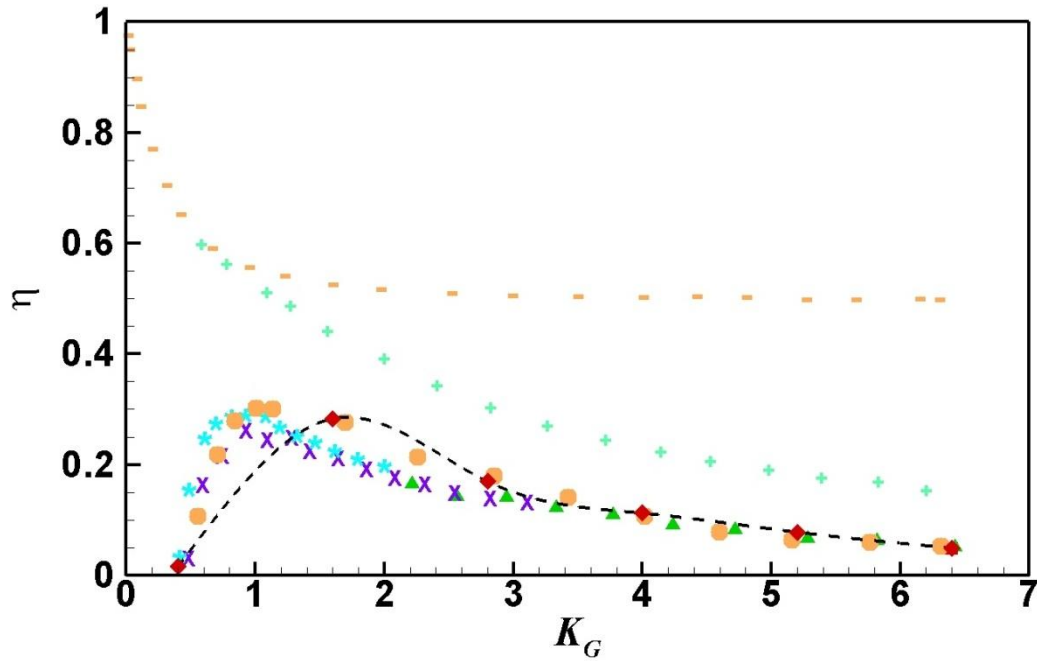
Extensive tests on the two-equation $k-\omega$ turbulence models are performed and the results are summarized in Table 3.5, and compared with those of Kinsey and Dumas (2012a). It is found that the final result is sensitive to a number of parameters related to the CFD solver, i.e. the number of mesh cells, the iteration per time step either in physical time or pseudo time steps as well as the CFL number. Considering the compromise between accuracy and computational time, the medium mesh (51,216 cells) with 128 time steps per cycle, 100 iterations per time step and CFL of 7 is selected for the main simulations in the present studies.



(a) Thrust coefficient



(b) Power coefficient



(c) Efficiency

Figure 3. 11 Validation results of a 3D rigid flapping foil with $AR=3.0$. \blacktriangle Experiment at $Re=1 \times 10^4$ (Heathcote et al., 2008); \times Experiment at $Re=2 \times 10^4$ (Heathcote et al., 2008); * Experiment at $Re=3 \times 10^4$ (Heathcote et al., 2008); + Panel method (Heathcote et al., 2008); \bullet N-S numerical method at $Re=2 \times 10^4$ (Young, 2005); --- (Orange) Analytical method at $Re=2 \times 10^4$ (Garrick, 1937); \blacksquare Present 2D CFD method at $Re=2 \times 10^4$ (achieved with a 3D method using Symmetry Boundary Condition (SBC) boundary conditions at the tips) and the black dashed line represents the present 3D CFD method at $Re=2 \times 10^4$.

Table 3. 5 Turbulence $k-\omega$ model validation with Kinsey and Dumas (2012a).

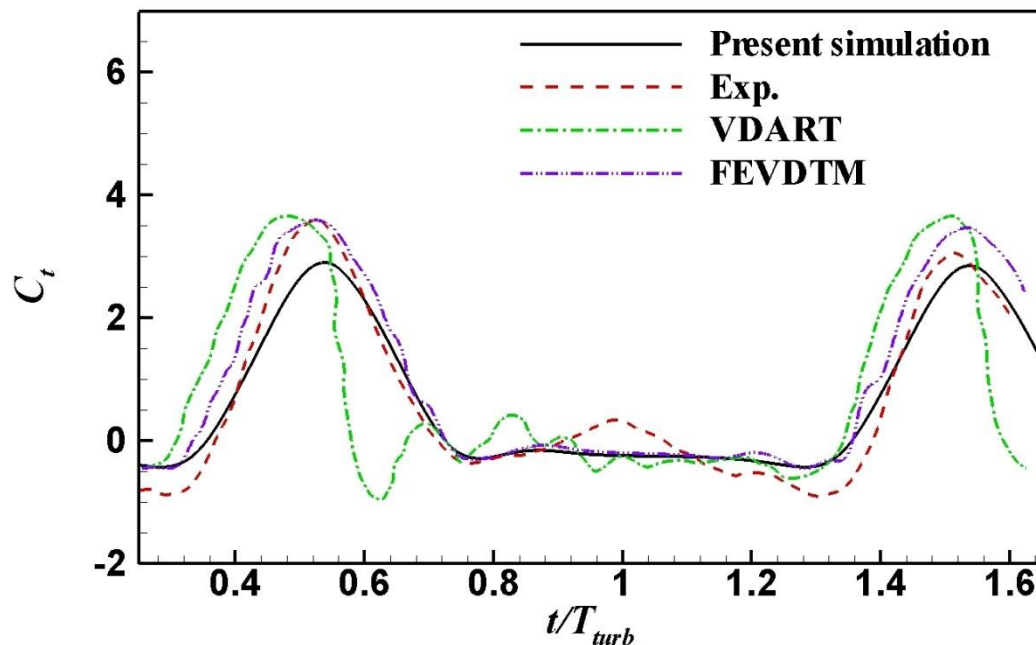
Current $k-\omega$ model validation (comparison with Kinsey and Dumas (2012a), $c_{op}=0.994$)
 NACA0015, $Re=5 \times 10^5$, $f^*=0.14$, pitching amplitude= 75° , pitching axis= $c/3$ and $h_0/c=1$

Mesh	Number of time steps per period	Iterations for one pseudo time step	CFL number	c_{op}
51216	128	100	7	0.96
51216	128	200	3	0.95
51216	64	100	7	0.9
51216	64	200	3	0.89
265740	128	100	7	1.03

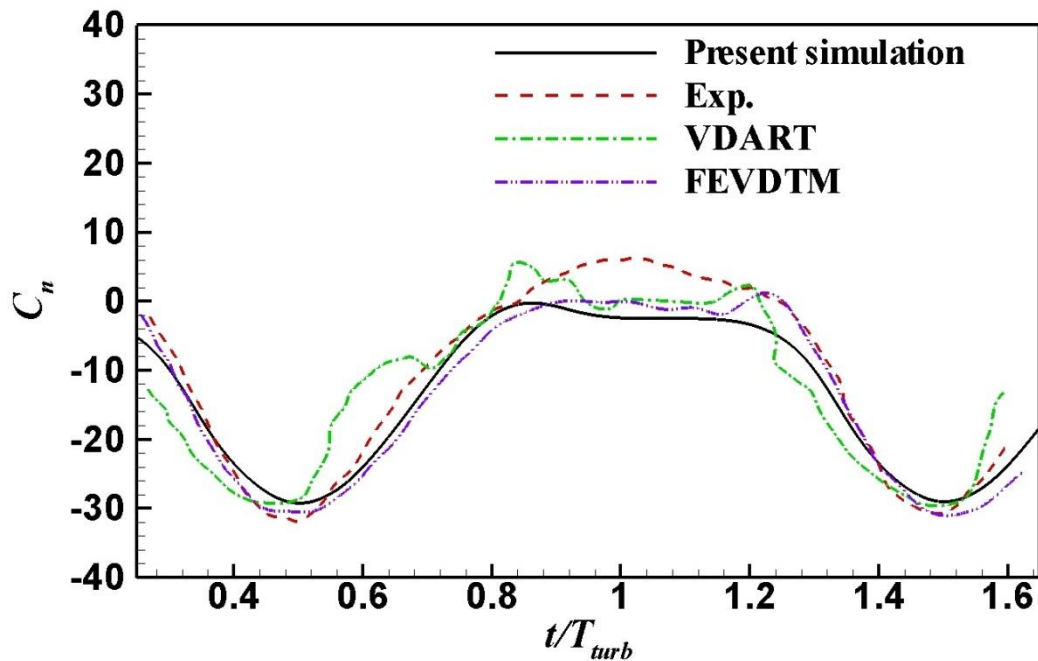
3.3.4.1.4 Three dimensional plunging wing propeller

A further investigation into a three-dimensional plunging-wing case has been conducted to test the calculation ability for three dimensional cases by using the present FSI code. The results predicted by the numerical model at Re of 2×10^4 are compared with the results from Heathcote et al. (2008), Young (2005), and Garrick (1937) in Fig. 3.11, where the non-dimensionalized Garrick frequency (K_G) is defined as $K_G = \pi f_0 c / U$.

Both three-dimensional and two-dimensional (whose mesh has the same topological structure as that in the xy cross-section of the three-dimensional model) simulations using the in-house code have been compared with these results. Good agreement is shown in all cases. Thus, the three dimensional calculation of the present code is reliable.



(a) Instantaneous thrust force coefficient



(b) Instantaneous normal coefficient

Figure 3. 12 Validation results for a rigid blade turbine - comparison with towing tank data (Exp.) by Strickland et al. (1980), Free Vortex Model (VDART) by Strickland et al. (1979) and vortex method combined with finite element analysis (FEVDTM) by Ponta and Jacovkis (2001).

3.3.4.1.5 Three dimensional VAT with the turbulence model

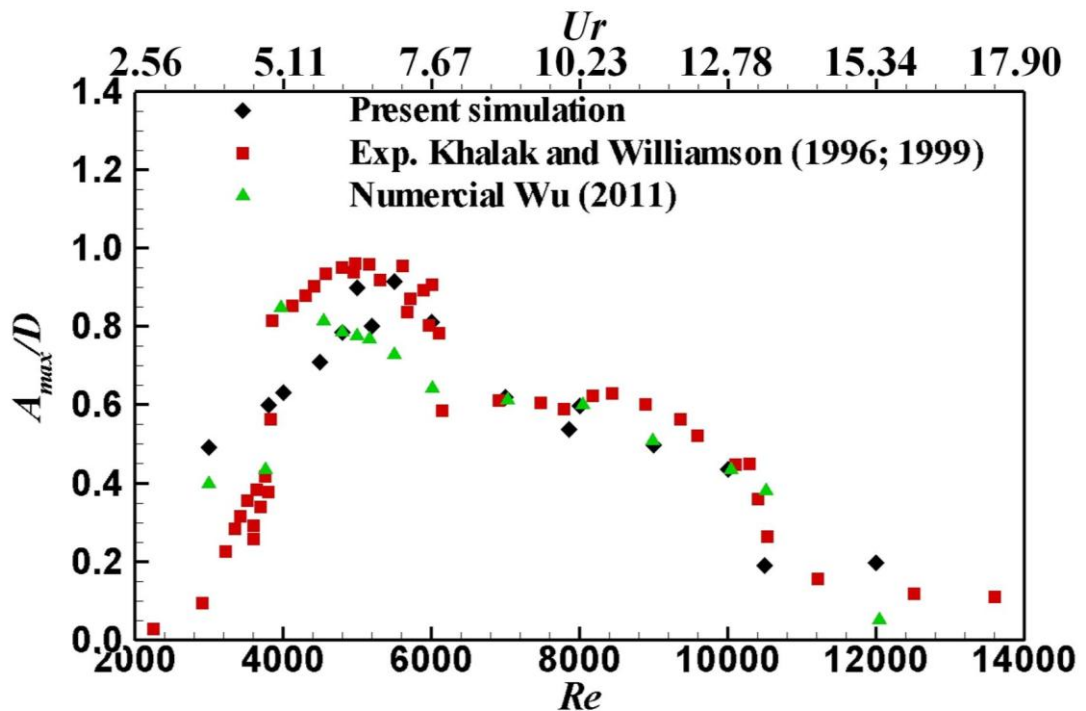
Investigations into a three-dimensional vertical axis turbine with a rigid blade have been conducted in order to simulate the vertical axis turbine cases. The diameter of the turbine is 1.22 m with a chord length of 0.0914 m. The cross-section of the foil is NACA0012. The tip speed ratio is 5.0. The results predicted by the numerical model are compared with the results from Strickland et al. (1980), Strickland et al. (1979) and Ponta and Jacovkis (2001) in Fig. 3.12. Multi-block grid with 1049000 nodes is used in this validation case. 10 turbine revolutions with 72 time steps per revolution are applied. Grid sensitive and time size sensitive tests have been done for this validation test. By double the entire mesh or double the time steps per turbine

revolution, the result difference are all less than 3%. Good agreement is shown in Fig.

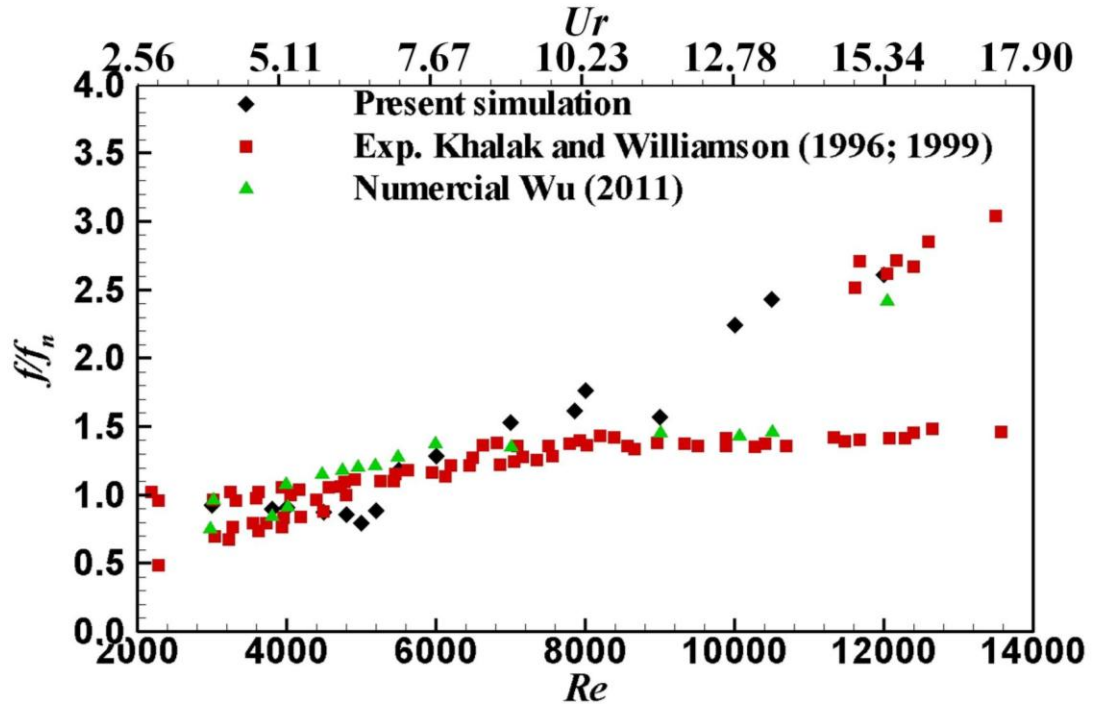
3.12. Thus, the fluid solver of the present FSI code is reliable based on the five validation results above.

3.3.4.2 Fluid structure interaction for rigid body

The fluid structure interaction for rigid body is validated by using the present FSI in-house code. A two dimensional free transverse (one DOF) oscillating cylinder case is calculated. The mass ratio is 2.4, the damping ratio is 0.0054 and the natural frequency of the cylinder in air is 0.7846 Hz. The Re from 3000 to 12000 is tested.



(a) Non-dimensionalized displacement amplitude against Re



(b) Non-dimensionalized displacement frequency against Re

Figure 3. 13 Validation results of 2D free oscillating cylinder with (a) non-dimensionalized displacement amplitude and (b) non-dimensionalized displacement frequency against Re .

The structural governing equation for the cylinder is defined as follows:

$$M\ddot{y} + c_y\dot{y} + k_y y = L, \quad (3.51)$$

where M is the mass of the cylinder, y is the position of the cylinder in the y axis direction, c_y is the damping coefficient, k_y is the spring constant and L is the lift force of the cylinder. This equation could be further transformed into the following form:

$$\ddot{\varepsilon} + 2\xi\dot{\varepsilon} + \varepsilon = \frac{V^{*2}}{\pi} c_l, \quad (3.52)$$

where ε is the non-dimensionalized position of the y axis and ξ is the damping factor.

V^* is the speed index defined as:

$$V^* = \frac{U}{b\omega_n\sqrt{\mu}} \quad (3.53)$$

where b is the radius of the cylinder, ω_n is the natural oscillation frequency of the cylinder and μ is the mass ratio defined as $m/(\rho_f\pi b^2)$.

In order to find out the eigenvectors of the calculated cylinder case, a MathCAD calculation is used. The detailed process of the MathCAD code is provided in Appendix I. “O” type grid with 100152 nodes is used in this validation case. 80 oscillating periods with 128 time steps per revolution are applied. The results calculated by the present code are shown in Fig. 3.13 and compared with Khalak and Williamson (1996; 1999) and Wu (2011). Good agreement has been achieved.

A two dimensional free oscillating foil with pitch and plunge motion (two DOF) is modelled with the inviscid Euler equations. The cross section of the foil is Isogai (1979) NACA64A010 aerofoil. The Mach number of this case is 0.75. The motion governing the equations of this airfoil is as follows:

$$\begin{cases} M\ddot{h} + S_\alpha\ddot{\alpha} + k_h h = -L \\ S_\alpha\ddot{h} + I_\alpha\ddot{\alpha} + k_\alpha\alpha = M' \end{cases} \quad (3.54)$$

where h is the instantaneous heaving position, s_α is the static unbalance of the airfoil, α is the instantaneous pitch angle, k_h is the heaving spring constant, I_α is the rotational moment of inertia, k_α is the pitch spring constant, L and M are the lift force and moment of the foil, respectively. This equation could be further transformed into the following form:

$$\begin{bmatrix} 1 & x_\alpha \\ x_\alpha & r_\alpha^2 \end{bmatrix} \begin{bmatrix} \ddot{\varphi} \\ \ddot{\alpha} \end{bmatrix} + \begin{bmatrix} 0 & 0 \\ 0 & 0 \end{bmatrix} \begin{bmatrix} \dot{\varphi} \\ \dot{\alpha} \end{bmatrix} + \begin{bmatrix} \left(\frac{\omega_h}{\omega_\alpha}\right)^2 & 0 \\ 0 & r_\alpha^2 \end{bmatrix} \begin{bmatrix} \varphi \\ \alpha \end{bmatrix} = \frac{V^{*2}}{\pi} \begin{bmatrix} -C_l \\ 2C_m \end{bmatrix}, \quad (3.55)$$

where x_α is the normalized distance between the rotation centre and the gravity centre of the airfoil, r_α is the normalized radius of gyration, ω_h is the Eigen frequency of heaving, ω_α is the Eigen frequency of rotation and φ is the non-dimensionalized heave position.

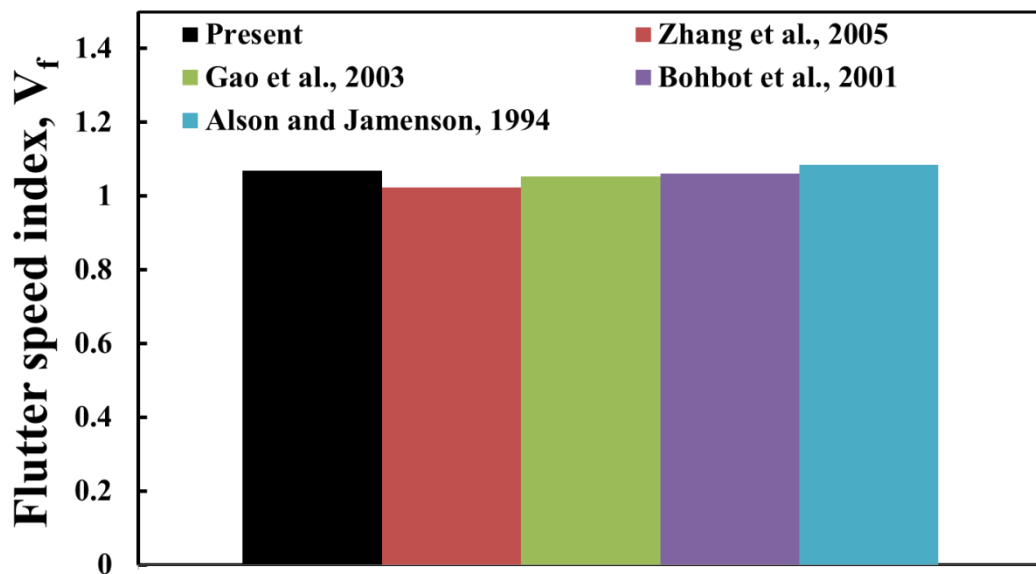


Figure 3. 14 Validation results of 2D inviscid flutter of a sweptback wing case for the flutter speed index v_f under Mach number of 0.75.

The calculation process of airfoil Eigen frequencies by using MathCAD is shown in Appendix II. The results calculated by present code are shown in Fig. 3.14 compared with Zhang et al. (2005) Gao et al. (2005) Bohbot (2001) and Alonso and Jamenson (1994). “O” shape grid with 24960 nodes is used in this validation case. 50 oscillating cycles with 128 time steps per cycle are applied. Good agreement has been achieved. Thus, the calculation ability of fluid structure interaction for rigid bodies of the present code is reliable.

3.3.4.3 Modal analysis for flexible body

As shown in Eq. 3.18 to Eq. 3.22 in Section 3.3.2, present in-house code use modal analysis for the simulation of fluid structure interaction for flexible body. Both MathCAD code and the ANSYS solver calculation are used for the modal analysis of the present FSI solver. An AGARD 445.6 wing case is used for the validation of the modal analysis by using different methods and is compared with the published results. The dimensions of AGARD 445.6 wing are shown in Fig. 3.15 in inches. The wing root is fixed. Young's modulus of the wing is $E=0.47072 \times 10^6$ Psi, density is $\rho_s=0.000123$ slugs/ft³ and Poisson's ratio is $\nu=0.31$.

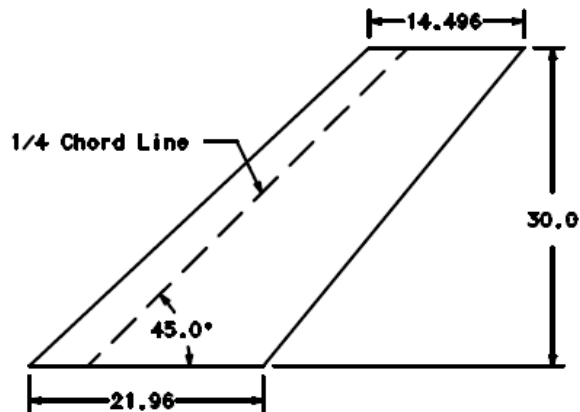


Figure 3. 15 Dimensions of AGARD 445.6 wing. (From Akgun et al., 2005).

The calculation process which uses MathCAD is listed in Appendix III with the beam assumption. The AGARD 445.6 wing model in the ANSYS calculation is SOLID45. The results are listed in Table 3.6. It is clear that the ANSYS calculation has better accuracy for all of the first five modes. The results which use MathCAD with the beam assumption have a good agreement for the 1st mode, but the accuracy for the other four modes is worse. Thus, the ANSYS solver with the SOLID45 model is used for the modal analysis in the present studies.

Table 3. 6 Validation results for AGARD wing mode frequency prediction by using ANSYS and beam analytical solution compared with published results.

Mode	Experiment	Akgun et al. (2005)	Kolonay (2001)	Li (2002)	Present results		Present results	
	Yates (1988)				(ANSYS)		(Beam Analytical)	
	Results	Results	Results	Results	Results	Error	Results	Error
	(Hz)	(Hz)	(Hz)	(Hz)	(Hz)	%	(Hz)	%
1	9.6	9.688	9.63	10.85	8.1098	-15.52	8.871	-7.59
2	38.1	37.854	37.12	44.57	37.824	-0.72	16.216	-57.40
3	50.7	50.998	50.5	56.88	57.842	14.09	23.314	-54.01
4	98.5	92.358	89.94	109.1	97.747	-0.76	26.81	-72.80
5	-	-	-	-	103.94	-	37.551	-

3.3.4.4 Fluid structure interface

The present code uses the CVT method to pass messages between the fluid solver and the structure solver as discussed in Section 3.3.3. In this section, the CVT method is validated with the AGARD wing case by using the ANSYS modal analysis results calculated in Section 3.3.4.3.

The 1st mode generalized displacement q_1 is shown in Fig. 3.16 and is compared with Yang et al. (2004). The comparison of the pressure contour plot between the BEM method (calculated by Sadeghi, 2004) and the CVT method (calculated by the present study) is presented in Fig. 3.17. Good agreements have been achieved. Thus, the CVT method of the present code is reliable.

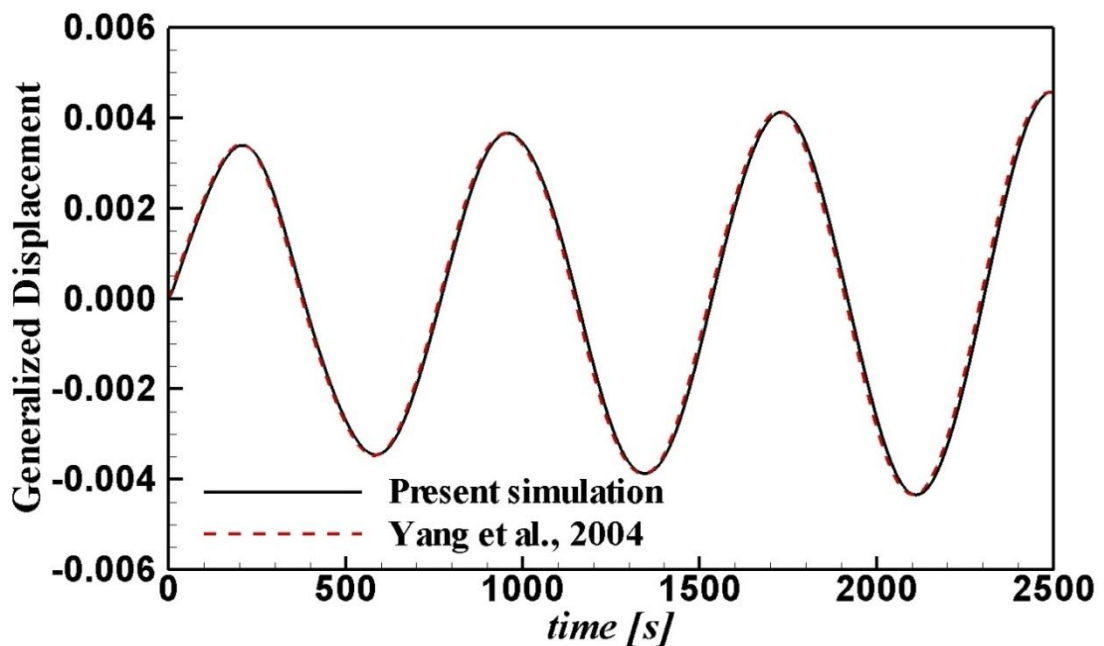


Figure 3. 16 Validation results of the AGARD wing flutter case for the first mode generalized displacement against with time compared with Yang et al. (2004).

3.3.4.5 Fluid structure interaction for flexible body

To validate the capability of this code in solving fluid-structure coupling problems, an additional simulation is performed for a three-dimensional flapping wing with spanwise flexibility and compared with the experimental results from Heathcote et al. (2008) and the numerical results from Gordnier et al. (2010, 2013). Two different types of flexible material, i.e. effective stiffness of 2.14×10^2 and 4.07×10^1 , are studied and the instantaneous plots of some predicted parameters and flow fields are compared with Heathcote et al. (2008) and Gordnier et al. (2010).

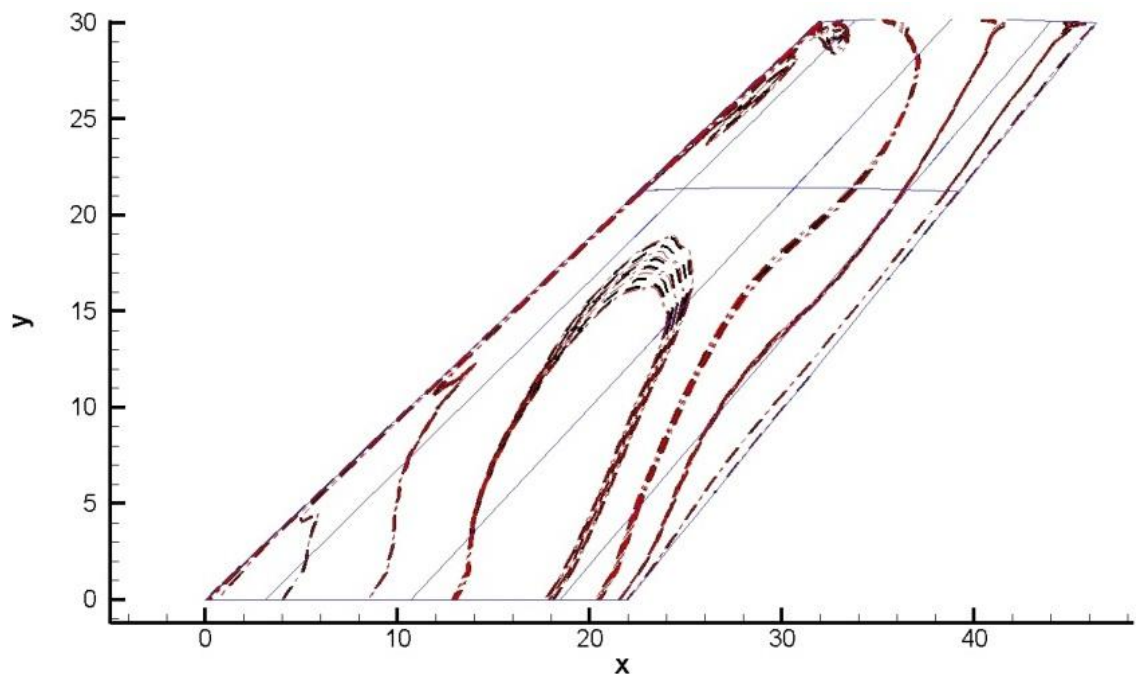
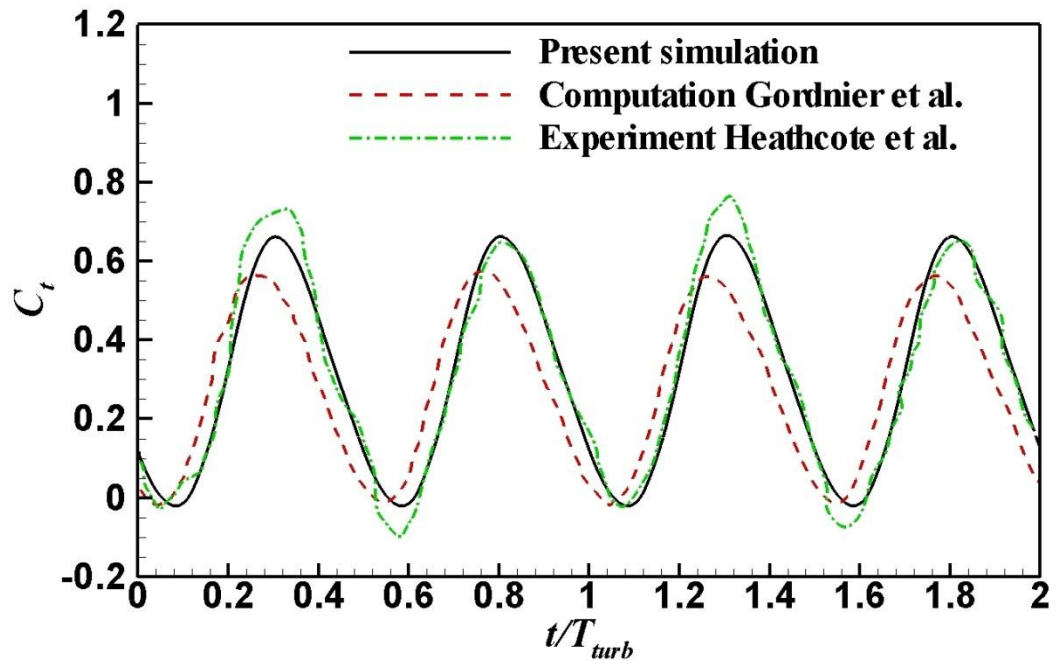
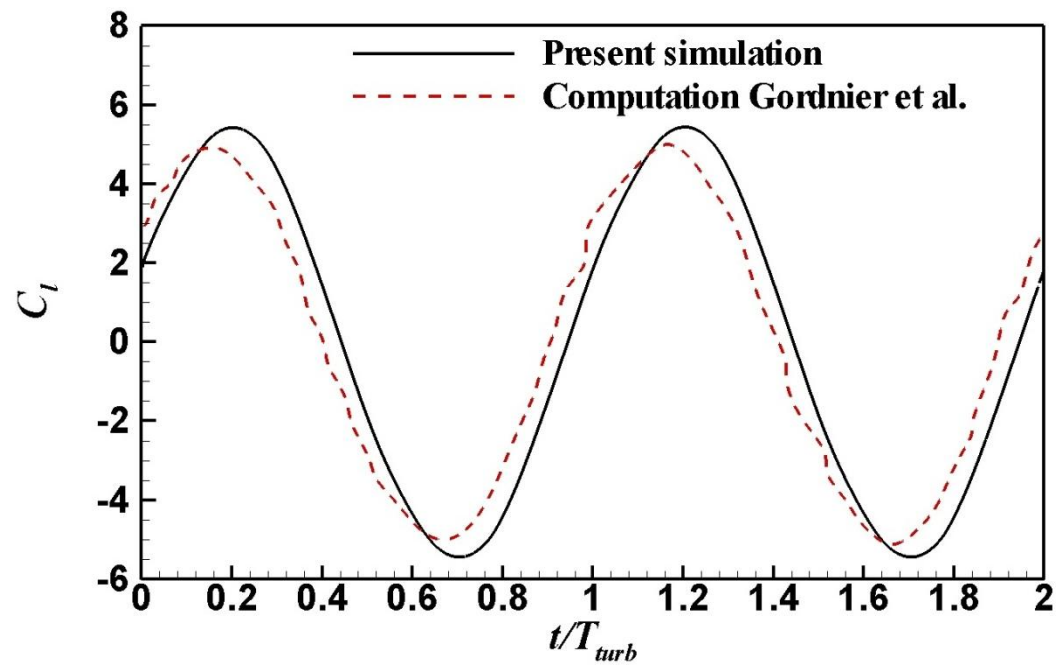


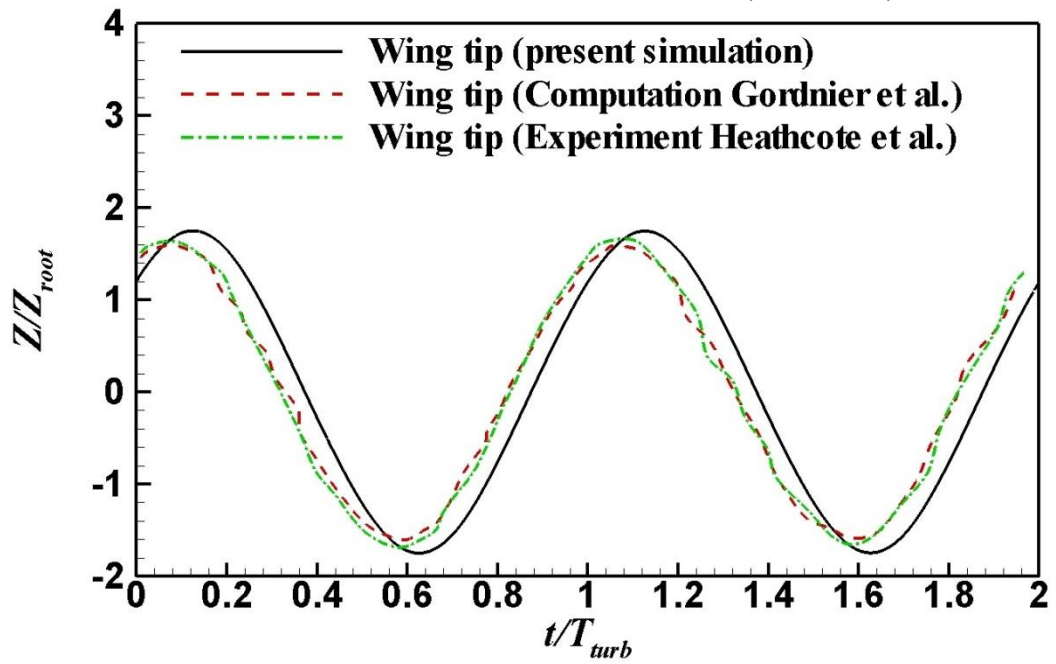
Figure 3. 17 Validation results of the AGARD wing flutter case for the pressure coefficient comparison between the BEM method (black dashed line based on Sadeghi, 2004) and the CVT method (red dash dotted line computed by the present study).



(a) Thrust coefficient



(b) Lift coefficient



(c) Wing tip edge displacement

Figure 3. 18 Validation on a flexible 3D plunging wing in water flow with $Re=3\times 10^4$; $AR=3.0$; $h_0=1.75\times 10^{-2}$ m; $f_0=1.74$ Hz; $\Pi=2.14\times 10^2$; $E=210$ GPa and Density Ratio (DR)=7.8 – compared with Heathcote et al. (2008) and Gordnier et al. (2010).

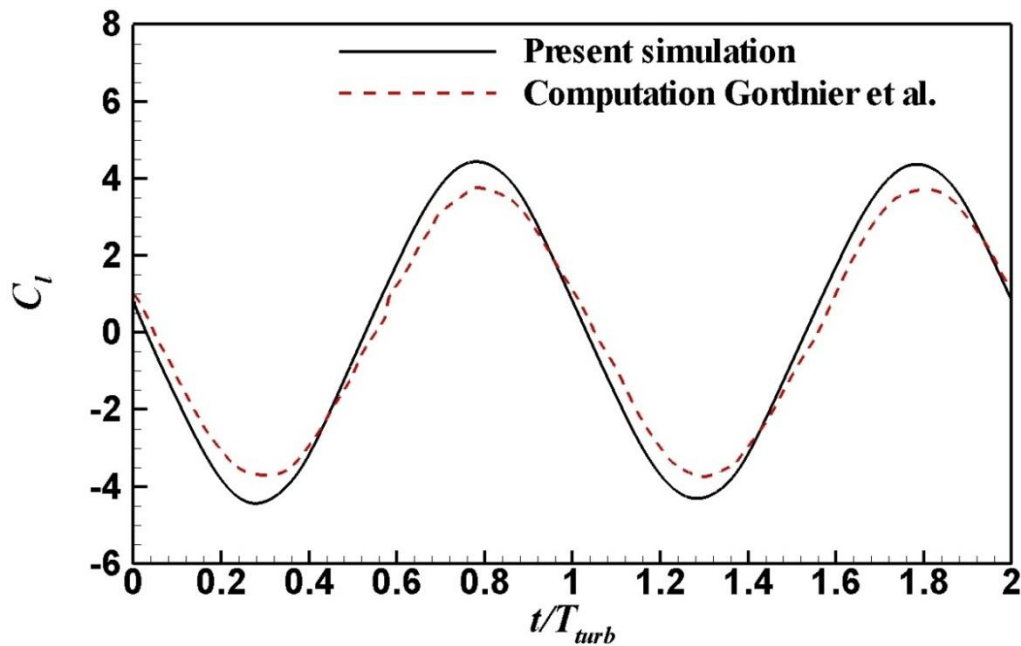


Figure 3. 19 Validation results of wing lift coefficient on a flexible 3D plunging wing ($Re=3.0\times 10^4$) $AR=3.0$; $h_0=1.75\times 10^{-2}$ m; $f_0=1.74$ Hz; $\Pi=4.07\times 10^1$; $E=70$ GPa and Density Ratio (DR)=2.7 – compared with Heathcote et al. (2008) and Gordnier et al. (2010).

The problem addressed is a three-dimensional NACA0012 rectangular wing with a heaving motion in water at Re of 3×10^4 . The chord length is 0.1 m and the span length is 0.3m. The plunging amplitude is 1.75×10^{-2} m with an oscillating frequency of 1.74 Hz. To construct the chordwise flexibility, a thin stiffener along the centre line of the foil is used, which is covered with a PDMS rubber. The thickness of the stiffener is 10^{-2} chord length.

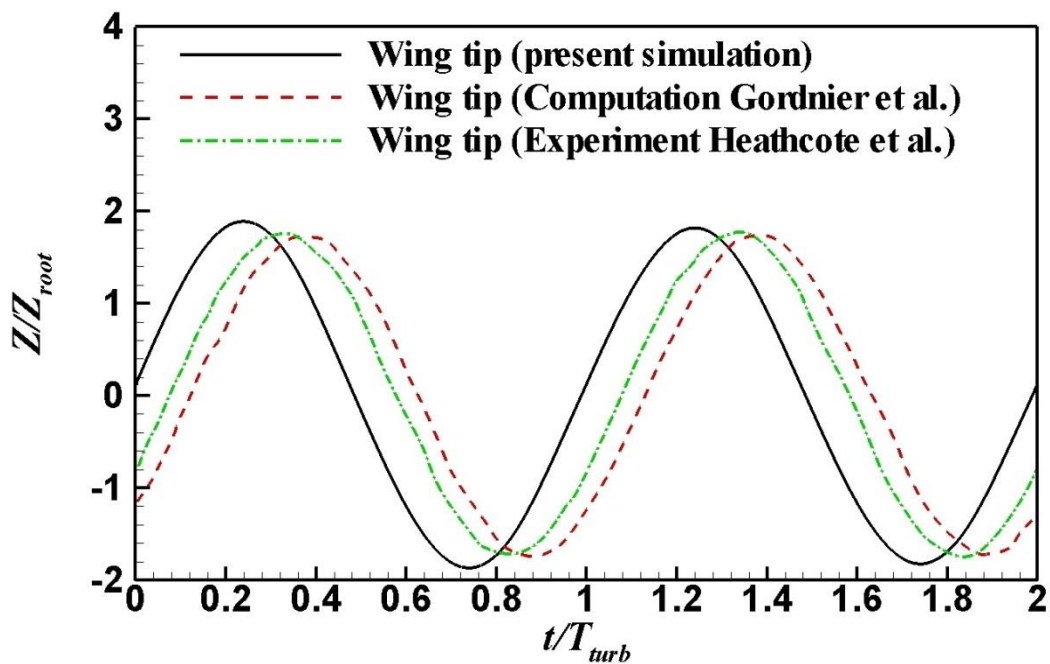


Figure 3. 20 Validation results of wing tip edge displacement on a flexible 3D plunging wing ($Re=3.0 \times 10^4$) $AR=3.0$; $h_0=1.75 \times 10^{-2}$ m; $f_0= 1.74$ Hz; $\Pi=4.07 \times 10^1$; $E=70$ GPa and Density Ratio (DR)= 2.7 – compared with Heathcote et al. (2008) and Gordnier et al. (2010).

In the foil with the effective stiffness of 2.14×10^2 , the material properties of the stiffener are chosen so Young's modulus is 210 GPa and the density ratio is 7.8. The instantaneous thrust, foil tip displacement and lift coefficient are shown in Fig. 3.18 (a)-(c). In the wing with the effective stiffness of 4.07×10^1 , Young's modulus is set as 70 GPa and the density ratio as 2.7 (Gordnier et al., 2013). Multi-block grid with 1600200 nodes is used in this validation case. 10 turbine revolutions with 72 time

steps per revolution are applied. The corresponding results are presented in Fig. 3.19 and Fig. 3.20. It can be observed that a small phase difference occur between the present simulation and the published results. Present Fluid Structure Interaction code uses a linear structure solver with linear coupling strategy between fluid solver and structure solver. Thus, the non-linear structure effect is ignored during the calculation. Blade tip effect of the three-dimensional flapping wing with spanwise flexibility case is also ignored during the calculation which is believed to result the differences in the validation. The instantaneous lift and drag coefficients are comparable with the results of Heathcote et al. (2008) and Gordnier et al. (2013) other than the small phase difference. All of the above results prove the accuracy of the code in coping with fluid-structure interaction problems. Thus, the fluid structure interaction calculation ability for flexible bodies of the present calculation code is reliable.

3.3.5 Computational domain and verification

In Chapter 5, Section 6.2 and Chapter 7, the mesh topologies in the xy plane are the same for the simulations on the oscillating foil turbine and vertical axis turbine cases, but these are different in the z axis direction between the two dimensional and three dimensional meshes. The computational domain and mesh for both the fluid and the structure are shown in Fig. 3.22. The model size in the spanwise direction is one chord length for the cases in Chapter 5 and Chapter 7 and ten chord lengths for the cases in Section 6.2. Two dimensional mesh is used for the simulations in Chapter 5 as shown in Fig. 3.22 (d). The turbine blade is located in the centre of the fluid grid. There is a rotation motion around the rotation centre for the fluid mesh to represent the rotation motion of the turbine blade during the calculation in Section 6.2. The

distance between the turbine blade (mesh centre) and the rotation centre is one turbine radius (R). Fig. 3.22 (e) - (h) shows the mesh movement during one turbine revolution at different time instants.

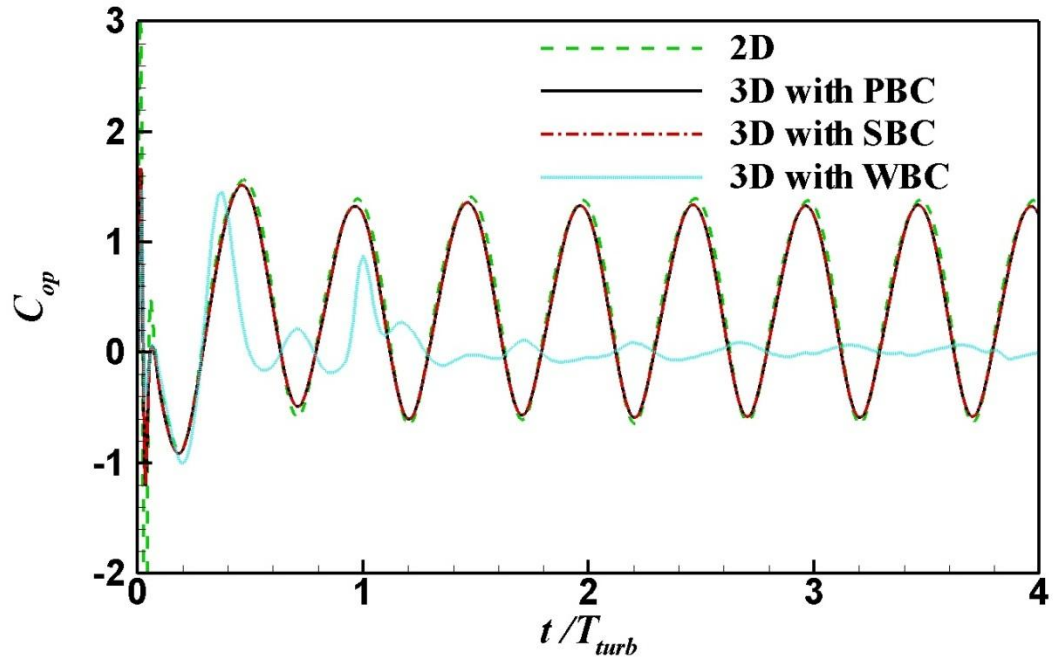
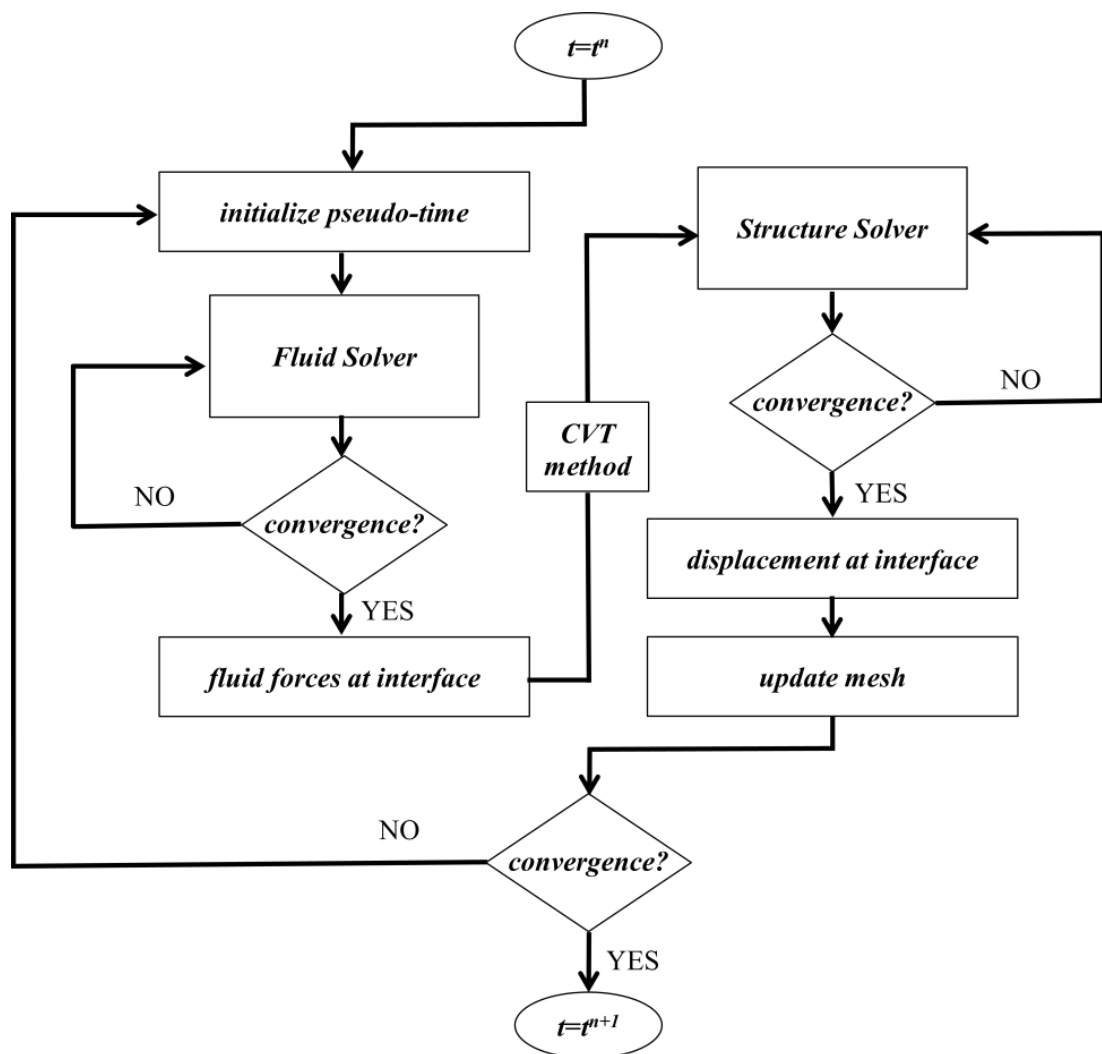


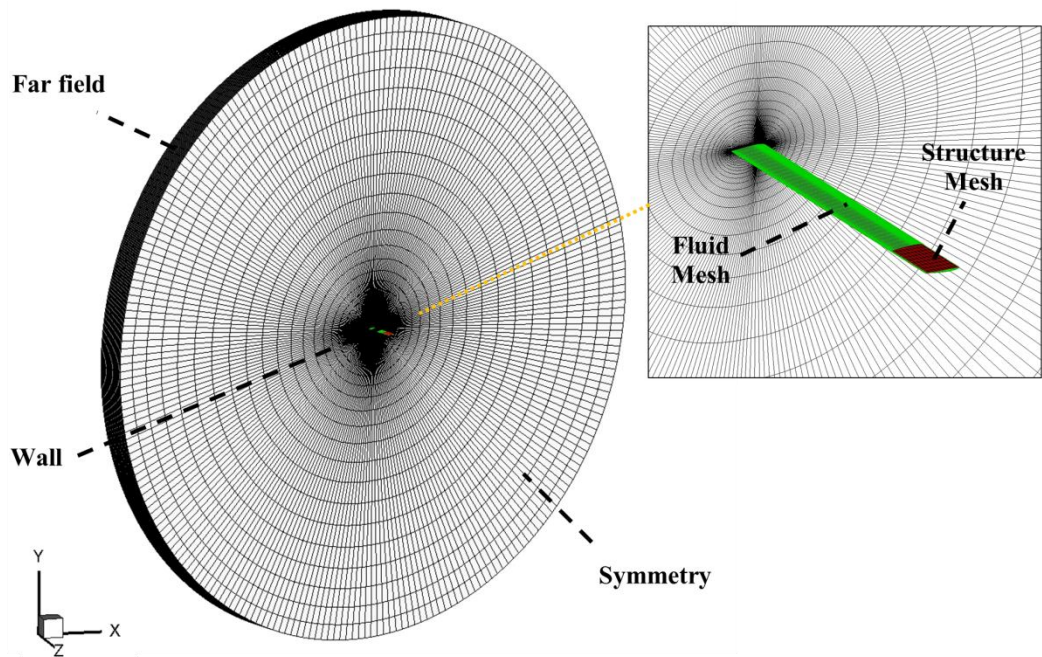
Figure 3. 21 Boundary conditions test for the tip boundaries comparison with a present 2D CFD method (achieved with a 3D method using Symmetry Boundary Condition (SBC) boundary conditions at the tips for a rigid oscillating foil at $f^*=0.18$ and $\theta_0=60^\circ$).

As suggested in the literature from Lifante et al. (2007), Nicolato and Moreira (2009) and Scott et al. (2014), applying the Symmetry Boundary Condition (SBC) at the tips of the foil can effectively mitigate the three-dimensional effects and achieve two-dimensional simulation. The present study has tested SBC, the Periodic Boundary Condition (PBC), and the non-slip Wall Boundary Condition (WBC) with the oscillating foil case. Non-slip WBC is selected for the present test since it has been used by other researchers in their modelling work to replicate some experimental setups. The results are compared with a two-dimensional foil with the same cross section. To do this, a three-dimensional rigid oscillating foil with a reduced

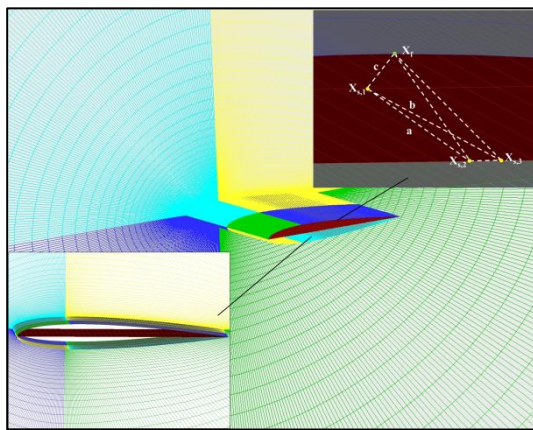
frequency of 0.18 and a pitching amplitude of 60° is modelled with different boundary conditions. A two-dimensional foil model which has the same topological structure as that in the xy cross-section of the three-dimensional model is setup using the same conditions as in the three-dimensional calculations. The time-averaged power coefficient (c_{op}) is shown in Fig. 3.21. It is confirmed that SBC is acceptable for replicating a 2D oscillating foil. It is therefore used in the two-dimensional simulations in Chapter 7.



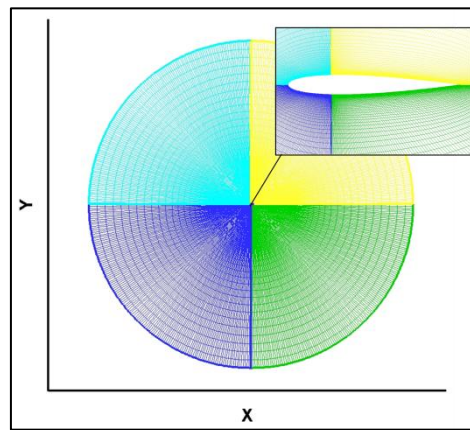
(a) Flow chart of the present FSI solver



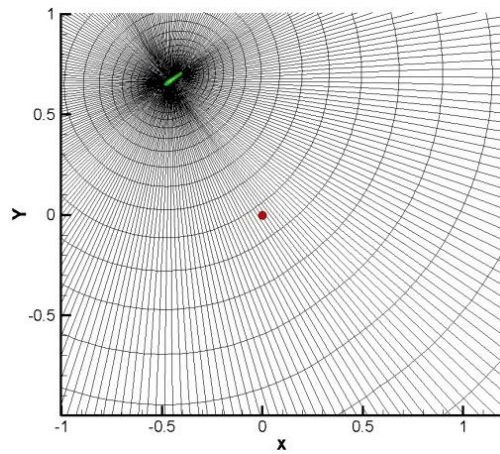
(b) 3D mesh topology



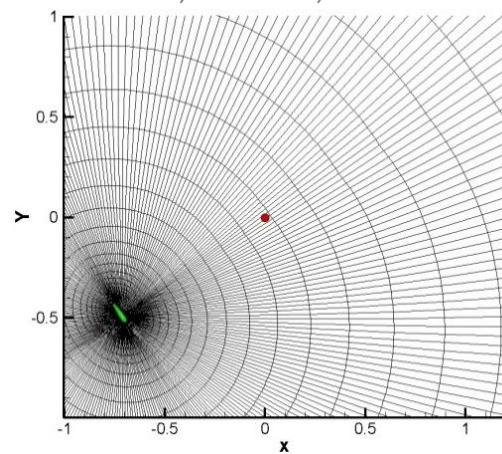
(c) 3D fluid and structure meshes and mapping



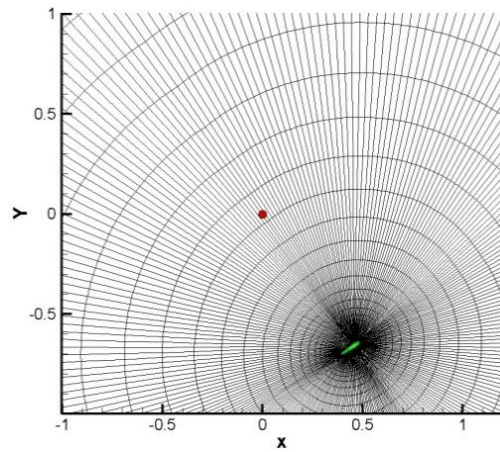
(d) 2D Fluid mesh



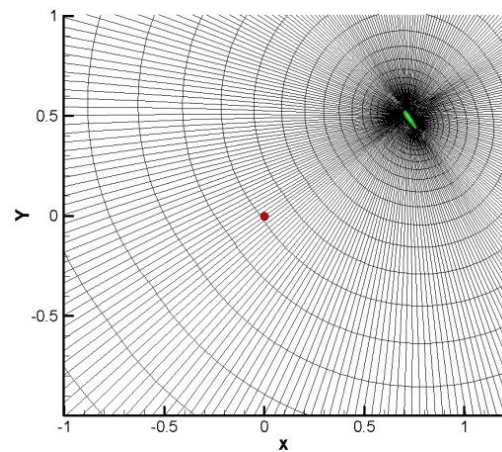
(e) Mesh movement during one turbine revolution at $t/T_{turb}=1/4$



(f) Mesh movement during one turbine revolution at $t/T_{turb}=2/4$



(g) Mesh movement during one turbine revolution at $t/T_{turb}=3/4$



(h) Mesh movement during one turbine revolution at $t/T_{turb}=4/4$

Figure 3. 22 Flow chart, Computational domain and mesh movement for vertical axis turbine case: (a) flow chart of the present FSI solver, (b) 3D mesh topology, (c) 3D fluid (cyan, yellow, blue and green represent different blocks) and structure (red colour) meshes and corresponding CVT mapping example, (d) 2D Fluid mesh and (e) ~ (h) mesh movement during one turbine revolution (red circle represents the mesh rotation centre; green represents turbine blade).

The 3D mesh with $10c$ of span is shown in Fig. 3.22 (b). The structure nodes are applied as an in-line mesh along the foil centreline shown in the lower left corner of Fig. 3.22 (c). An example of the CVT association between the fluid node and

structure nodes is displayed in the top right corner of Fig. 3.22 (c). The far field boundary condition is applied to the inlet and outlet boundaries with uniform constant velocity in the x axis direction for all the meshes. The foil, using the Non-slip wall boundary condition, is set to be $50c$ (chord length) away from the incoming flow and outflow boundaries.

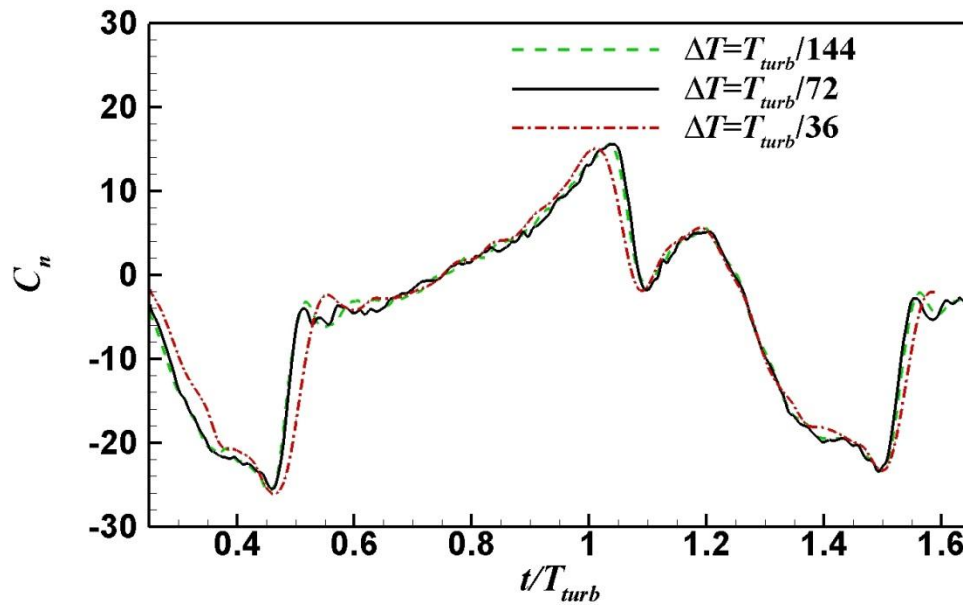


Figure 3. 23 Tests for the sensitivity of time step size.

The sensitivity study of time step size for the vertical axis turbine model is performed at the tip speed ratio $\lambda=3.5$ of the calculation in Section 6.2 and the predicted results are shown in Fig. 3.23. It is seen that there is no significant difference between the time step size of $T_{turb}/144$ and $T_{turb}/72$. Considering a reasonable calculation time, $T_{turb}/72$ is selected for the following calculations.

3.4 Stress calculation in Section 6.2

Apart from the coupled fluid structure interaction modelling, the study in Section 6.2 also adopts further calculations to validate the blade displacement results from the

FSI code and to estimate the blade stress. Structural solver ANSYS has been used to achieve this.

Commercial software ANSYS 15.0 is used as a structural solver to validate the maximum displacement and to analyse the stress distribution under the largest external load conditions. A diagrammatic sketch of the force application in the ANSYS structural solver is shown in Fig. 3.24. The element type of SOLID45 is used and uniform external loads have been applied to each structural cell. A convergence test for the ANSYS Finite Element Analysis has also been carried out for the case of $\lambda=5.5$, $\Pi=3.19, 10^3$ and $l_{st}/c=10/3$. By doubling the calculation element numbers, the difference of maximum deflection and stress between fewer elements and more elements results are all smaller than 0.15%, which passes the FEA convergence criteria.

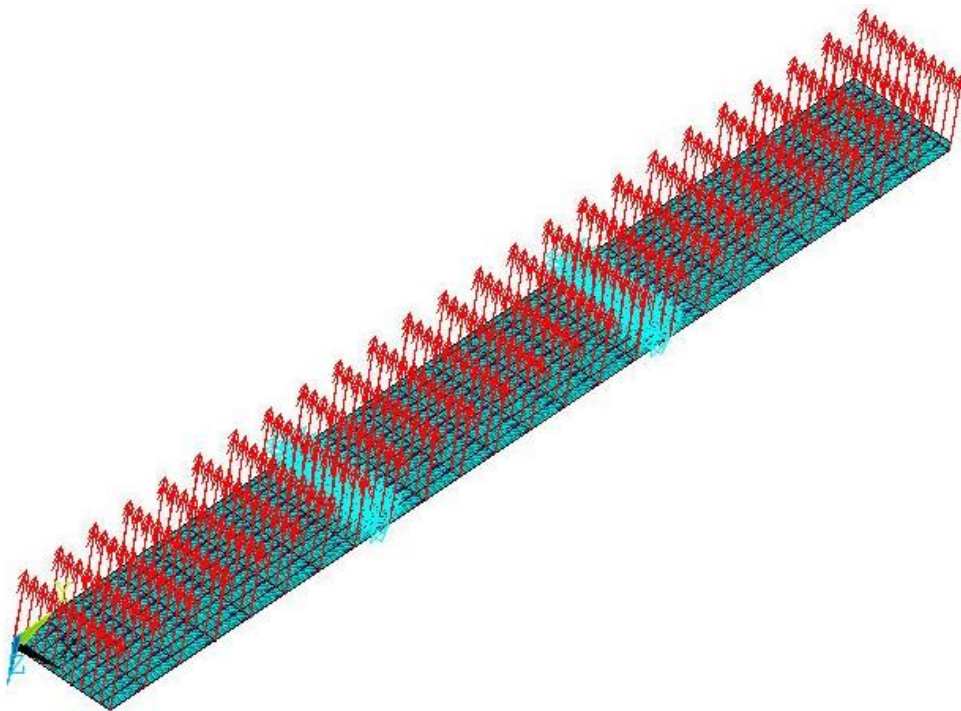


Figure 3. 24 Diagrammatic sketch of external loads (red arrow) and constrains (cyan arrow) conditions at each cell for ANSYS structural solver.

PART II: Bio-inspired Active Flow Control for Renewable Turbine

Chapter 4: Bio-inspired Active Flow Control for Vertical Axis

Turbine by Oscillating Flap

4.1 Introduction

The present study is focused on an H-shaped lift force driven VAT. In comparison with the HAT and drag force driven VAT, H-shaped VAT has many advantages, such as the simple blade design, capable to work in all current flow directions and non-sensitive to water depth. However, the efficiency of existing H-shaped VAT is still relatively low as compared to the HAT as mentioned in Section 1.1. It is thus necessary and valuable to carry on a deep research in order to enhance VAT efficiency via various mechanical and control methods (Gretton et al., 2009; Gretton, 2009).

Inspired by the vortex control mechanism, utilized by some aero-/aqua- animals to improve their propulsion performance via their fins or tails flapping motion (Xiao and Liao, 2010; Xiao et al., 2012), turbine blade with oscillating flap is developed and investigated in the present study. The oscillating flap is designed to move periodically around a pitching axis as shown in Fig. 4.1.

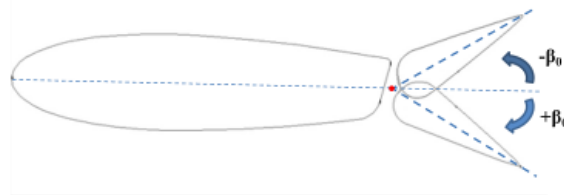


Figure 4. 1 The active oscillating turbine blade in the present study.

Distinct from a fixed flap, the use of an oscillating flap not only controls the near boundary layer fluid flow, but also regulates the vortex interaction in the wake

between each blade. For multiple-blade turbine as studied in this chapter, the flow analysis focusing on the blade wake vortex interference is therefore crucial for enhancing the overall turbine performance.

In this chapter, a numerical investigation is carried out with the main objective to explore the potential for enhancing VAT energy extraction efficiency by using an oscillating flap blade.

4.2 Description of problem

The simulated turbine model, plotted in Fig. 4.2, is based on a real marine current turbine, currently operates at the WANXIANG II station in China (Sun et al., 2009). Detailed geometry parameters and operating conditions are summarized in Table 4.1. To simplify the problem, the blade is assumed infinitely long in span-wise direction, therefore two-dimensional modelling is conducted. The Reynolds number used in the present simulation is set as 4.7×10^5 which is identical to real operating condition. The turbine azimuthal angle (θ_t) is defined as the angle which sweeps from the positive x axis to the line connecting the origin to the blade mass centre as shown in Fig. 4.2.

The active oscillating turbine blade is investigated as shown in Fig. 4.1. The angle between the flap centre line and the main part centre line is defined as flap angle β_0 . For the oscillating flap, the flap rotates with its axis at the centre of the gap between main and flap parts with the following specified motion equation:

$$\omega_f = \beta_0 \sin\left(n_t \omega t + \frac{\pi}{2}\right), \quad (4.1)$$

where β_0 represents the amplitude of the flap and ω_f is the rotational angular velocity of oscillating flap.

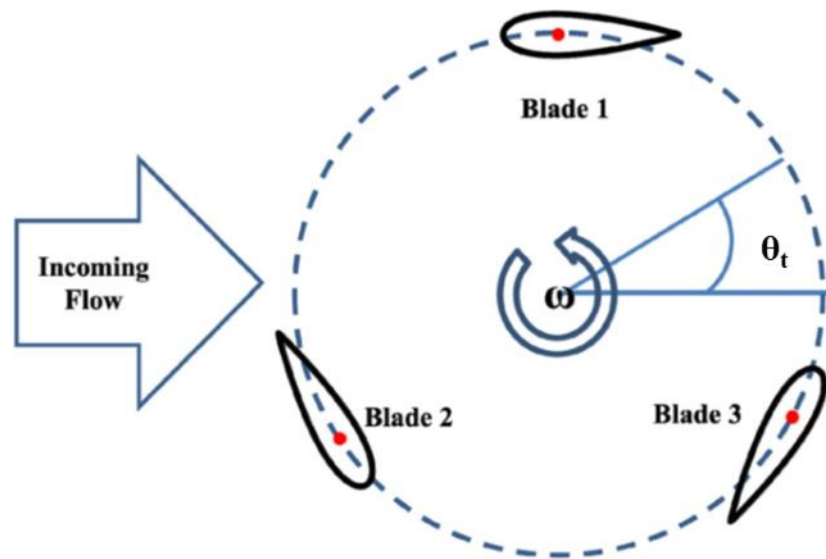


Figure 4. 2 Schematic diagram of flow configuration.

Table 4. 1 Operating conditions of WANXIANG II power station (From Sun, 2007).

Blade profile	NACA0018	
Rotor diameter	2.5	m
Number of blades	3	-
Blade length	5	m
Blade chord	0.3	m
Solidity	0.72	-
Rated power	40	kW
Stream speed	1.6	m/s
Rotational speed	1.2672	rad/s
Reynolds number	4.7×10^5	-

To quantify the oscillating flapping motion relative to the turbine rotational motion, one parameter ' n_f ' is introduced, which is defined as below:

$$n_t = T_{turb} / T_{flap}, \quad (4.2)$$

where T_{turb} is the turbine revolution period and T_{flap} is the flap revolution period.

4.3 Results and discussions

4.3.1 Mechanism of flow control by oscillating flap

Before a systematic parametric study is performed on a VAT with the oscillating flap blade, the study on a potential efficiency improvement of the properly controlled flow mechanism through the use of an oscillating flap is carefully conducted. A specific case, with the tip speed ratio $\lambda=1.572$, is selected to present the results below. Detailed discussion on the power coefficient, instantaneous momentum coefficient, lift coefficient and vortex contours are presented and compared between two different turbines, i.e. fixed flap turbine and oscillating flap turbine with oscillating amplitude of $\beta_0=30^\circ$ and $n_t=3.0$.

The time-mean power coefficient (c_{op}), maximum momentum coefficient (c_m), maximum lift coefficient (c_l) and blade surface flow separation point are summarized in Table 4.2 for the comparison between the two turbines tested. It is seen from this table that, the turbine with oscillating flap reaches a maximum time-mean power coefficient between two turbines, which is about as much as 1.22 times of the fixed flap blade. Examinations on the instantaneous c_m and c_l variation in one revolution (shown in Fig. 4.3 and 4.4) indicate that this is attributed to the increased c_m and c_l peak values at the instantaneous time of $0.5T_{turb}$. Obviously, for a lift-driven turbine, increasing the blade lift force can lead to the enhancement of overall turbine torque and energy extraction.

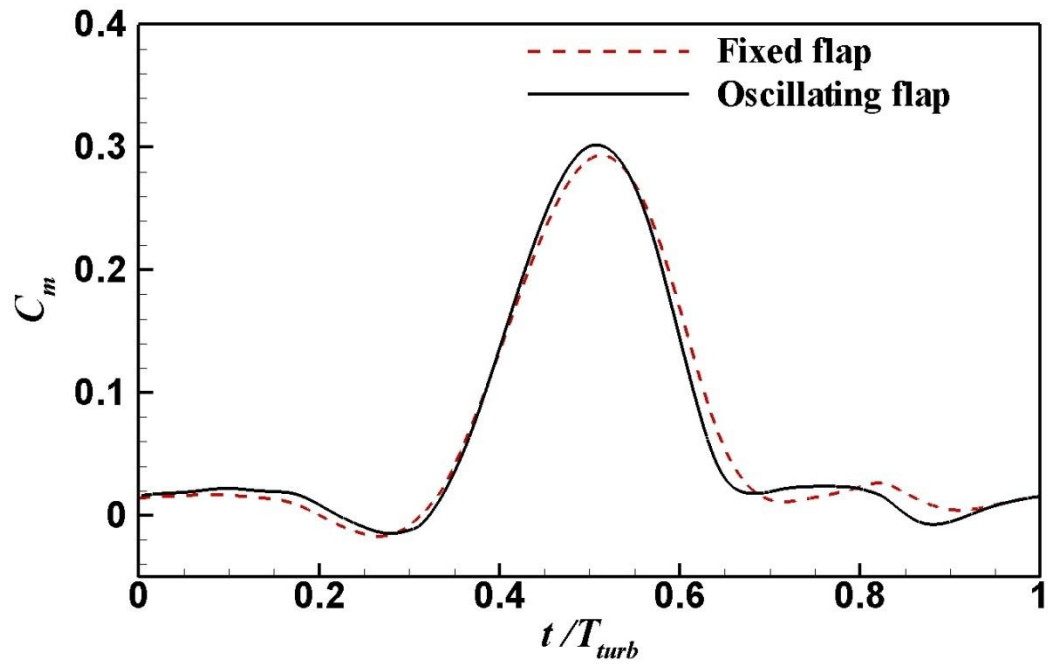


Figure 4. 3 Comparison of instantaneous blade moment coefficient against time for two different blade turbines ($\lambda=1.572$). For oscillating blade, $\beta_0=30^\circ$; $n_t=3.0$.

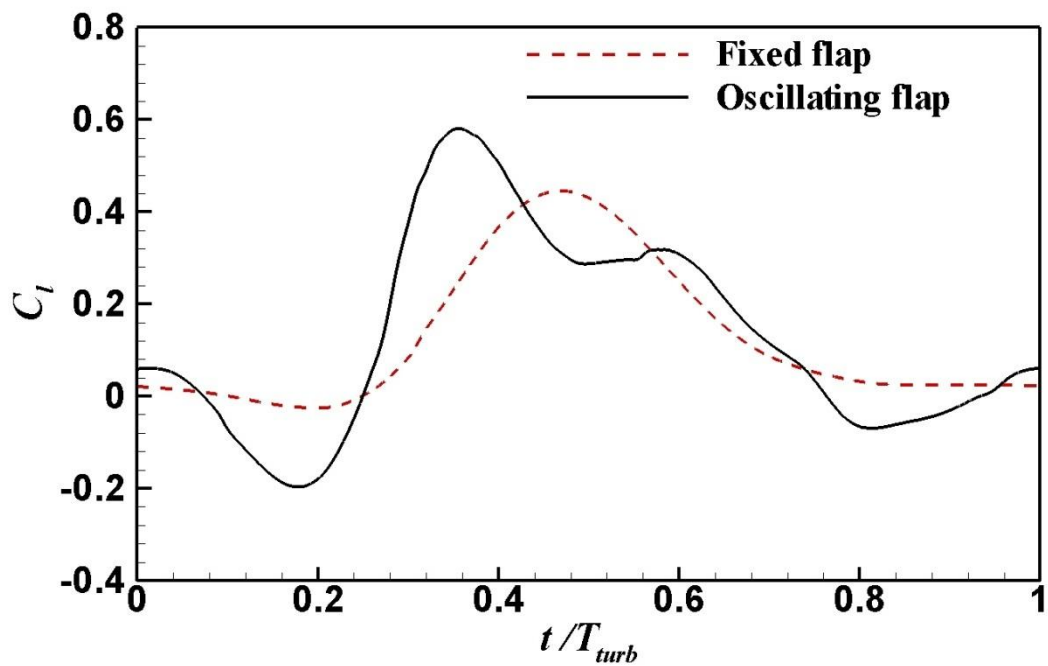


Figure 4. 4 Comparison of instantaneous blade lift coefficient against time for two different blade turbines ($\lambda=1.572$). For oscillating blade, $\beta_0=30^\circ$; $n_t=3.0$.

A further investigation on the difference between a fixed flap and oscillating flap is carried out. The time-mean power coefficient shown in Table 4.2 indicates an improved energy extraction performance by using an oscillating flap. The increased instantaneous peak lift and momentum coefficients presented in Table 4.2 could be the reason for such enhancement. Apart from this, further examination on the snapshots of instantaneous vortex contours within one revolution in Fig. 4.5 reveals some specific flow features.

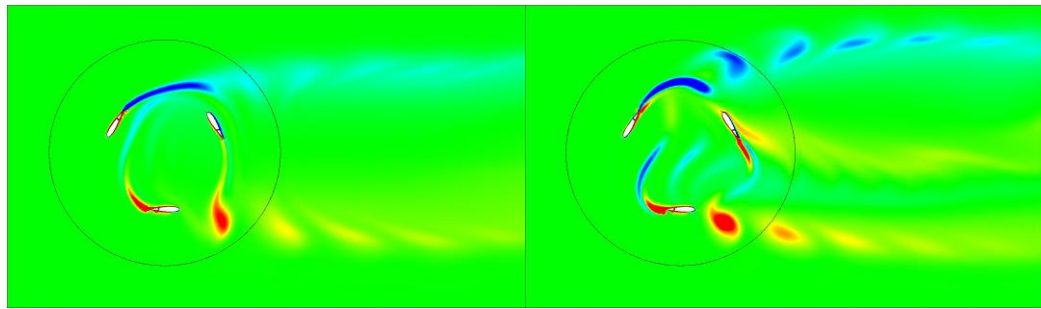
Table 4. 2 Comparison of key performance parameters for two different turbines ($\lambda=1.572$; oscillating flap amplitude: $\beta_0=30^\circ$; $n_t=3.0$).

Turbine type	Time-mean c_{op}	Max. c_m	Max. c_l	Separation point
Turbine blade with fixed flap	0.421	0.293	0.445	0.967c
Turbine blade with oscillating flap	0.514	0.380	0.580	0.950c

Fig. 4.5 (a) to (f) compare the vortex contour for the turbines with a fixed and oscillating flap at three different azimuthal angles. It can be seen that, with a fixed flap, a long wake tail characterizing with a Karman vortex generates as the blades rotate, which results in a strong vortex interaction between two adjacent blades. This becomes more obvious when the blade is located at the azimuthal angle of 90° . The turbine blade wake, where many vortices appear, is turbulent region due to the blade motions. When the turbine blade goes through these vortices, the pressure difference between inner and outer surface of the blade drops due to turbulence flow field. This phenomenon results in a lift force decrease of the turbine blade. As a lift driven VAT, the decrease of the lift forces could lead to a decrease of the power coefficient or energy extraction efficiency.

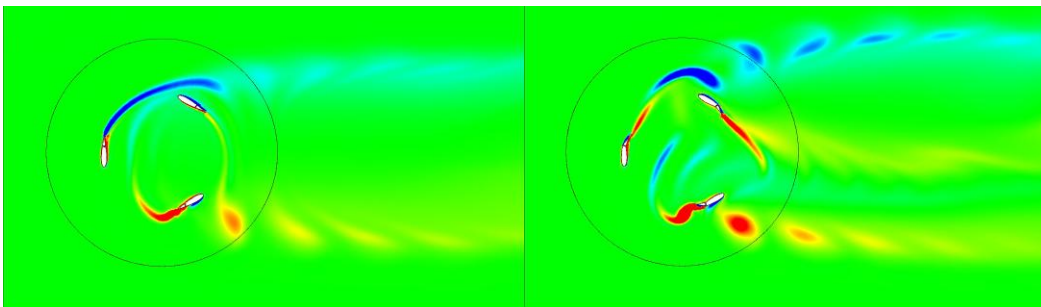


Z Vorticity: -30 -24 -18 -12 -6 0 6 12 18 24 30



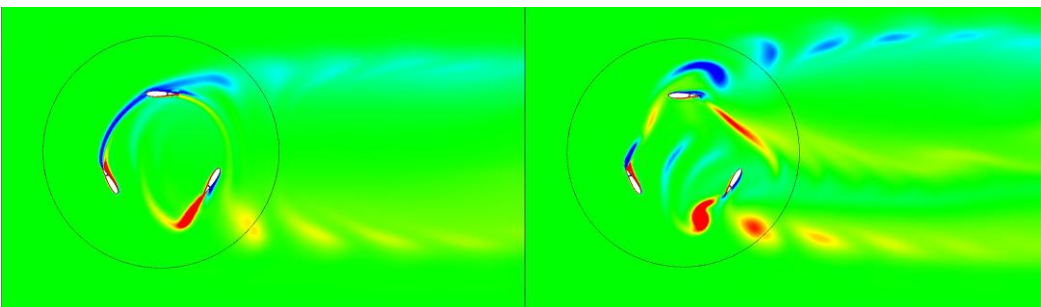
(a) $t/T_{turb}=5/12$, fixed flap

(d) $t/T_{turb}=5/12$, oscillating flap



(b) $t/T_{turb}=6/12$, fixed flap

(e) $t/T_{turb}=6/12$, oscillating flap



(c) $t/T_{turb}=7/12$, fixed flap

(f) $t/T_{turb}=7/12$, oscillating flap

Figure 4. 5 Comparison of vortex contour within one revolution for fixed and oscillating flap turbine at $\lambda=1.572$. (a) $t/T_{turb}=5/12$, fixed flap; (b) $t/T_{turb}=6/12$ fixed flap (c) $t/T_{turb}=7/12$, fixed flap; (d) $t/T_{turb}=5/12$, oscillating flap; (e) $t/T_{turb}=6/12$, oscillating flap; (f) $t/T_{turb}=7/12$, oscillating flap. For oscillating flap, $\beta_0=30^\circ$; $n_t=3.0$.

However, with an oscillating blade as shown in Fig. 4.5 (d) to (f), the long wake tail is broken down by the periodic motion of oscillating flap, and vortex shedding from the upstream blade is quickly “thrown” away from wake leading to the weak vortex-

blade interaction. This phenomenon is believed to suppress the top and bottom blade wall pressure difference declining trend, and ensure the blade lift force at a large level.

Based on above preliminary study of the flow control mechanism from one specific case study, a systematic parametric study is further carried out with a series of variations on oscillating flap parameters. Computed results are presented in Section 4.3.2.

4.3.2 Oscillating flap parameters

Table 4. 3 Summary of numerical cases for oscillating flap.

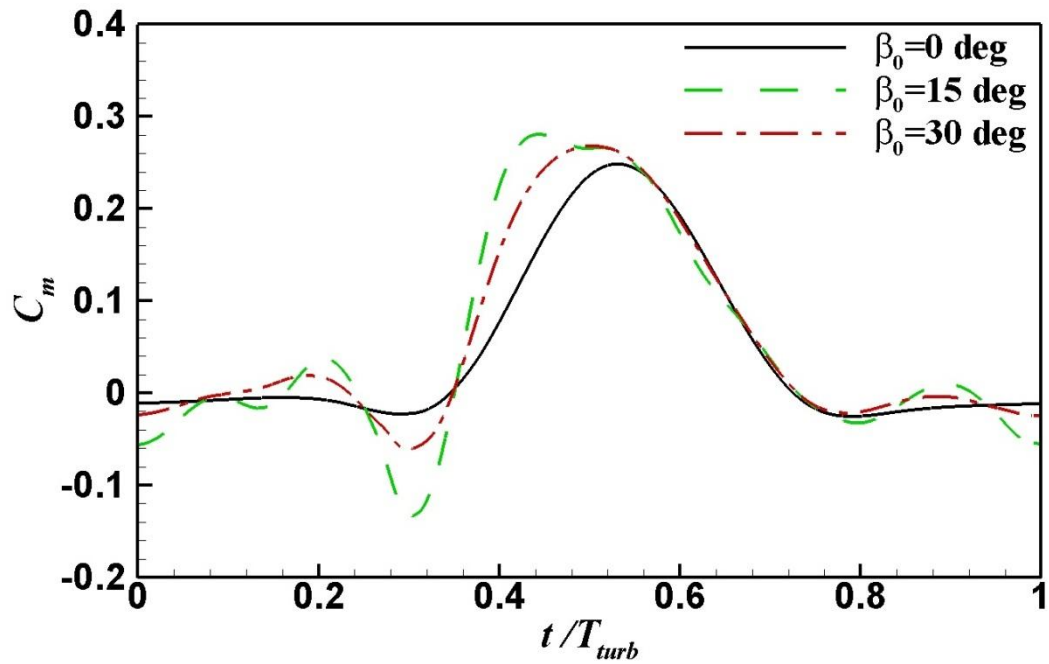
Turbine type	Oscillating amplitude β_0 (deg)	Revolution ratio n_t (-)
Oscillating flap amplitude effect	0	3
	15	
	30	
Revolution ratio effect	15	1
		1.5
		3

The investigation of an oscillating flap influence on the turbine power performance is presented in this section. The motion of the flap is defined as Eq. 4.1 and Eq. 4.2 in Section 4.2. As seen from the flap motion equations, there are three parameters which influence the oscillating flap motion, i.e. the flap size, the amplitude β_0 and the oscillating frequency, the last parameter is determined by the revolution ratio n_t . The

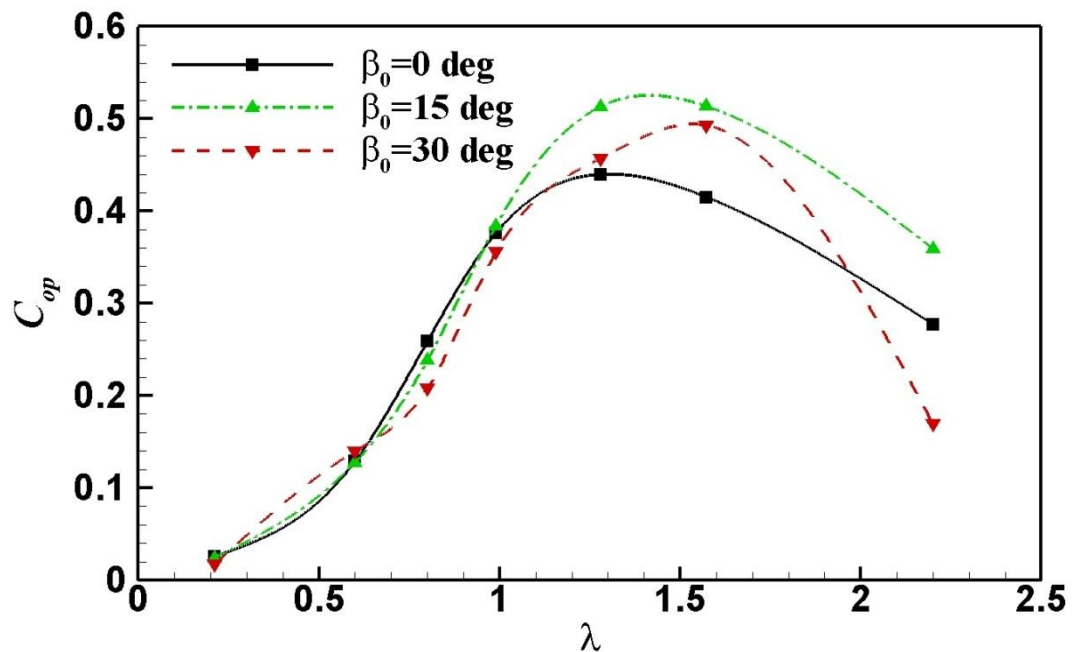
study of the influence of flap motion on power extraction is therefore concentrated on the amplitude β_0 and the oscillating frequency of the flap with a fixed flap size of $c/4$. Detailed information for various cases tested is summarized in Table 4.3.

4.3.2.1 Oscillating amplitude

The effect of oscillating amplitude on the instantaneous moment coefficient and time-mean power coefficient is shown in Fig. 4.6 (a) and (b) for a comparison between the fixed flap blade ($\beta_0=0^\circ$) and an oscillating flap blade ($\beta_0 \neq 0^\circ$). The instantaneous results, such as in Fig. 4.6 (a), provide the detail information of the force or moment of the blade at different time instants, while the time-averaged results, such as in Fig. 4.6 (b), give the overall level of the performance of the energy turbine at different working conditions. Obviously, an oscillating flap enhances the turbine performance as compared to a fixed flap blade turbine. It can also be seen that the blade with the amplitude of 15° displays the widest large c_m region which covers the azimuthal angle from 145° to 200° . The high moment coefficient region becomes smaller when the flap oscillating amplitude increases from 15° to 30° . The maximum c_m of 0.28 is also achieved for a blade with the amplitude of 15° , which is about 12.98% times that of a blade with fixed flap. With regard to the time-mean power coefficient shown in Fig. 4.6 (b), an increase of 23.72% c_{op} at $\lambda=1.572$, as compared to fixed flap, is achievable with oscillating flap at 15° amplitude.



(a) Instantaneous blade moment coefficient against time at $\lambda=2.2$. (Various flap amplitude)



(b) Time-averaged power coefficient against tip speed ratio. (Various flap amplitude)

Figure 4. 6 Oscillating flap amplitude effect on the instantaneous blade momentum coefficient and time-averaged power coefficient. ($n_t=3$) (a) Instantaneous blade moment coefficient against time; (b) Time-averaged power coefficient against tip speed ratio.

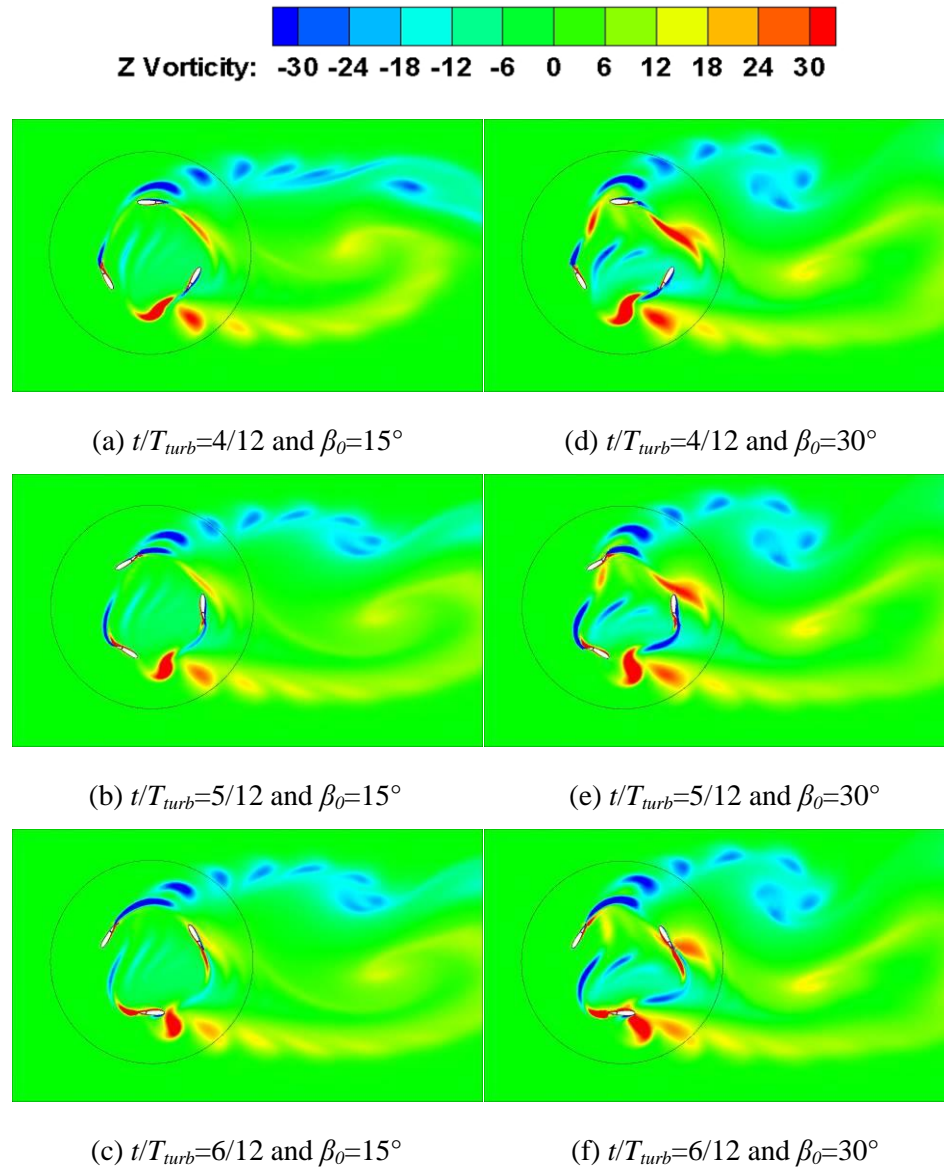
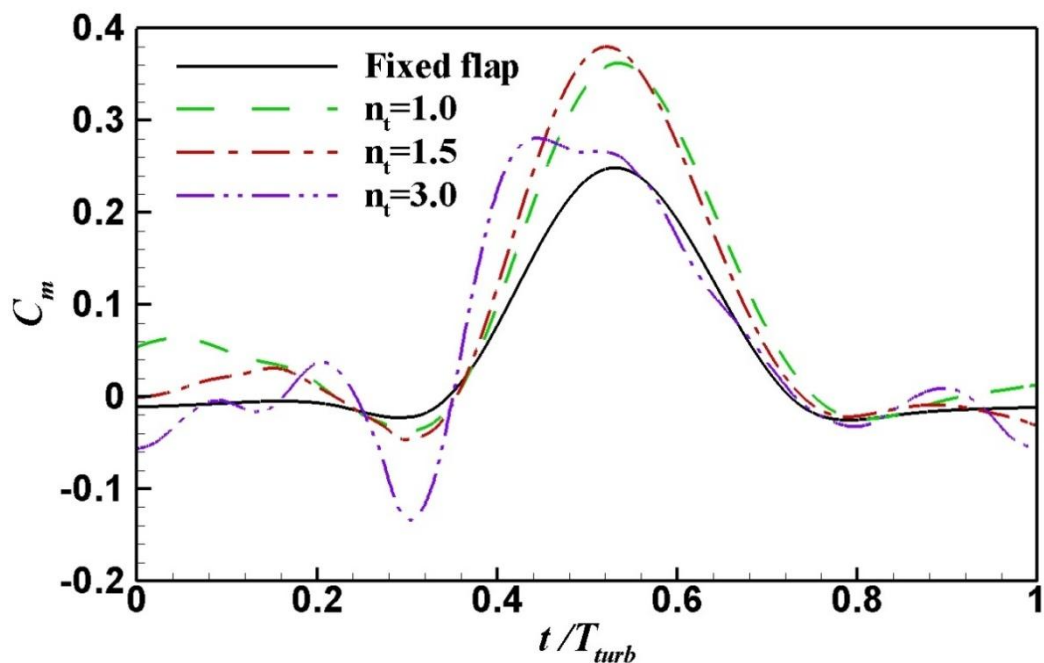


Figure 4. 7 Comparison of vortex contour for an oscillating flap blade with oscillating amplitude of $\beta_0=15^\circ$ and $\beta_0=30^\circ$ ($\lambda=2.2$; $n_t=3$) (a) $t/T_{turb}=4/12$ and $\beta_0=15^\circ$; (b) $t/T_{turb}=5/12$ and $\beta_0=15^\circ$; (c) $t/T_{turb}=6/12$ and $\beta_0=15^\circ$; (d) $t/T_{turb}=4/12$ and $\beta_0=30^\circ$; (e) $t/T_{turb}=5/12$ and $\beta_0=30^\circ$; (f) $t/T_{turb}=6/12$ and $\beta_0=30^\circ$.

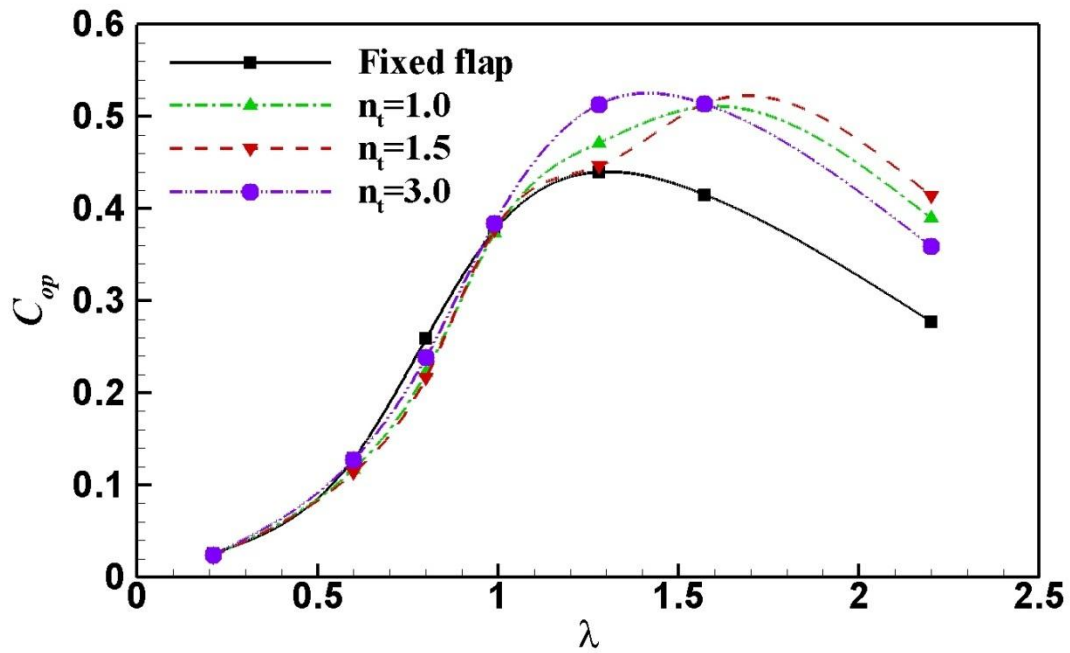
As it is mentioned in Section 4.3.1, the flow control mechanism associated with an oscillating flap is related to the breakdown of vortex tail in the downstream wake of rotating blade. In addition, it should also be noted that changing actual blade streamline via the use of a fixed flap with non-zero flap angle is not beneficial to the boundary layer separation control (Xiao et al., 2013). Using an oscillating flap is

resembled to adopting a flap with non-zero flap angle in terms of varying the actual blade streamlines with a periodic motion. Therefore, to achieve a better performance, optimal oscillating amplitude is desired with which the vortex wake is properly broken down while the blade streamline is not significantly altered. A comparison on the vortex contour for the oscillating flaps with amplitude of 15° and 30° are shown in Fig. 4.7 (a) to (f). Clearly revealed from these figures, the vortex interaction between two rotating blades becomes more chaotic and complicated with increasing oscillating amplitude from 15° to 30° , which is not attractive for a better performance of the turbine. With a flap oscillating amplitude of 30° , extra pairs of vortices generate (as shown in the Fig. 4.7). Some of the vortices stay at the blade rotational disk and hit the downstream blade during the turbine rotation. It results in a lift drop of the turbine blade and a decrease of the power coefficient.

4.3.2.2 Oscillating frequency



(a) Instantaneous blade moment coefficient against time at $\lambda=2.2$.
(Various flap oscillating frequency)



(b) Time-averaged power coefficient against tip speed ratio.

(Various flap oscillating frequency)

Figure 4. 8 Oscillating flap frequency effect on the instantaneous blade momentum coefficient and time-averaged power coefficient. ($\beta_0=15^\circ$) (a) Instantaneous blade moment coefficient against time; (b) Time-averaged power coefficient against tip speed ratio.

The frequency of oscillating flap is another key parameter for the turbine with an oscillating flap blade. Based on Eq. 4.1 in Section 4.2, the frequency is controlled by the revolution ratio n_t .

There are three different revolution ratios tested in the present study which are 1.0, 1.5 and 3.0. Fig. 4.8 (a) illustrates the instantaneous moment coefficient, which shows the differentiation on peak c_m for various oscillating frequencies. The maximum c_m of 0.36 is observed when the flap oscillates at the same speed as that of blade rotating speed ($n_t=1.0$). Increasing the flap revolution ratio from 1.0 to 1.5, the peak c_m and the width of the high c_m region remain the same but have a phase lag. Further increasing the flap revolution ratio from 1.5 to 3.0, the peak c_m drops while a

slightly increased high c_m region is observable. By increasing the revolution ratio from 1.5 to 3.0, extra vortices generate by the high frequency oscillating motion and stay at the rotational disk. The interaction between vortices and blade due to these high frequency vortices reduces the power coefficient of the turbine. In general, the effect of the revolution ratio (n_t) on the c_m distribution and magnitude could be ignored at $\lambda < 1.0$. This is also indicated from Fig. 4.8 (b) where the time-mean power coefficients are compared for fixed flap, oscillating flap with varying n_t .

4.4. Summary

In this study, a new concept via the use of an oscillating flap to moderate the traditional H-shaped VAT blade is proposed. By a systematic numerical modelling investigation, the potential benefit to improve the VAT energy extraction efficiency is explored. 2×10^6 CPU seconds calculated on HPC high performance computing facilities of University of Strathclyde are needed for a typical case in this chapter. Simulation results indicate that an oscillating flap presents a better performance than that of a fixed flap. The parametric study performed provides the optimal geometry parameters under the real operating conditions. With an oscillating flap, parameters include the oscillating amplitude of 15° and the revolution ratio of 3.0. With the above parameters, the peak power coefficient (c_{op}) rises about 23.72% relative to the fixed flap blade turbine at $\lambda = 1.572$. With an oscillating flap, it provides the influence on reducing the blade wake vortex interaction. The above factor is beneficial in order to increase the blade lift coefficient, momentum coefficient and thus the overall efficiency of the turbine. The lift and drag forces of the entire turbine system are necessary to be calculated in the future work.

Chapter 5: Bio-inspired Active Flow Control for Oscillating Foil

Turbine by Flexible Blade

5.1 Introduction

Currently, existing work on the oscillating foil turbine mainly focuses on the investigation of a rigid foil, which is only sensible under the normal weather and sea conditions, where the deformation of a foil blade can be ignored. However, under some extreme flow conditions, a large-scale blade may experience a huge unsteady loading, resulting in a potential blade deformation in chordwise and spanwise directions. Studies that are restricted to rigid blades have severe limitations in their practical application.

Inspired by the advantages of a flexible wing over a rigid wing in flapping propulsion, this study investigates whether the flexible structure influence is also beneficial to a flapping wing energy device. To the best of the author's knowledge, no relevant work has been performed in this area, although a small number of studies have been done on the potential distortion of a wind turbine blade under extreme high wind speed conditions (Lachenal et al., 2013; Turnock et al., 2009). To this end, this study will begin the investigation by comparing the power efficiency of two flexible models, emulating the hawkmoth wing (trailing edge control (TEC)) and the trout ray fin (leading edge control (LEC)) model against that of a rigid wing. Subsequently, this study seeks to develop a new preferred wing using the insights gained from the above two models. Since the simulation will be based on a two-dimensional simulation model, only chord-wise flexibility will be taken into account. In this chapter, a priori structural result that will determine the prescribed wing

deformation will use, which means this computational fluid dynamic study is decoupled from structural analysis. Apart from a single flexible wing study, the present study will further include a flexible twin-wing system mimicking the fish swimming in schools and the birds flying in flocks to preserve their flow energy between neighbours.

The outline of the rest of the paper is as follows. This study begins by describing the problem with relevant flexible models and parameters that control the flapping wing kinematics and power generation features in Section 5.2. In Section 5.3, a systematic presentation of the predicted results is included. It starts with an examination of the efficiency of the flexible wing enhancing device via a detailed analysis of the wake structure and various instantaneous parameters and local effective AOA, followed by a discussion of the results with a systematic parametric study that is pertinent to global and local flexibility. Unlike the other existing works of Kinsey and Dumas (2008, 2012a, 2012b), this study particular interest focuses on the flexible wing's influence by comparing the rigid and flexible data in a turbulent flow regime to emphasize the distinction between them.

5.2 Description of problem

The configuration of the current problem is shown in Fig. 5.1, where an oscillating NACA0012 hydrofoil is immersed in a uniform viscous water flow. Practically, the device is forced to pitch/rotate on a fixed axis, so the generated unsteady hydrodynamic force around the foil and water surrounding it activates the foil's up and down heave motion. The kinematic energy of the water current is converted to the mechanical energy associated with the heave motion via a damper, and then

transformed into electricity by a generator as discussed in Section 2.2. In the present study, the foil pitches at $c_{pit} = 1/3$ chord length from its leading edge.

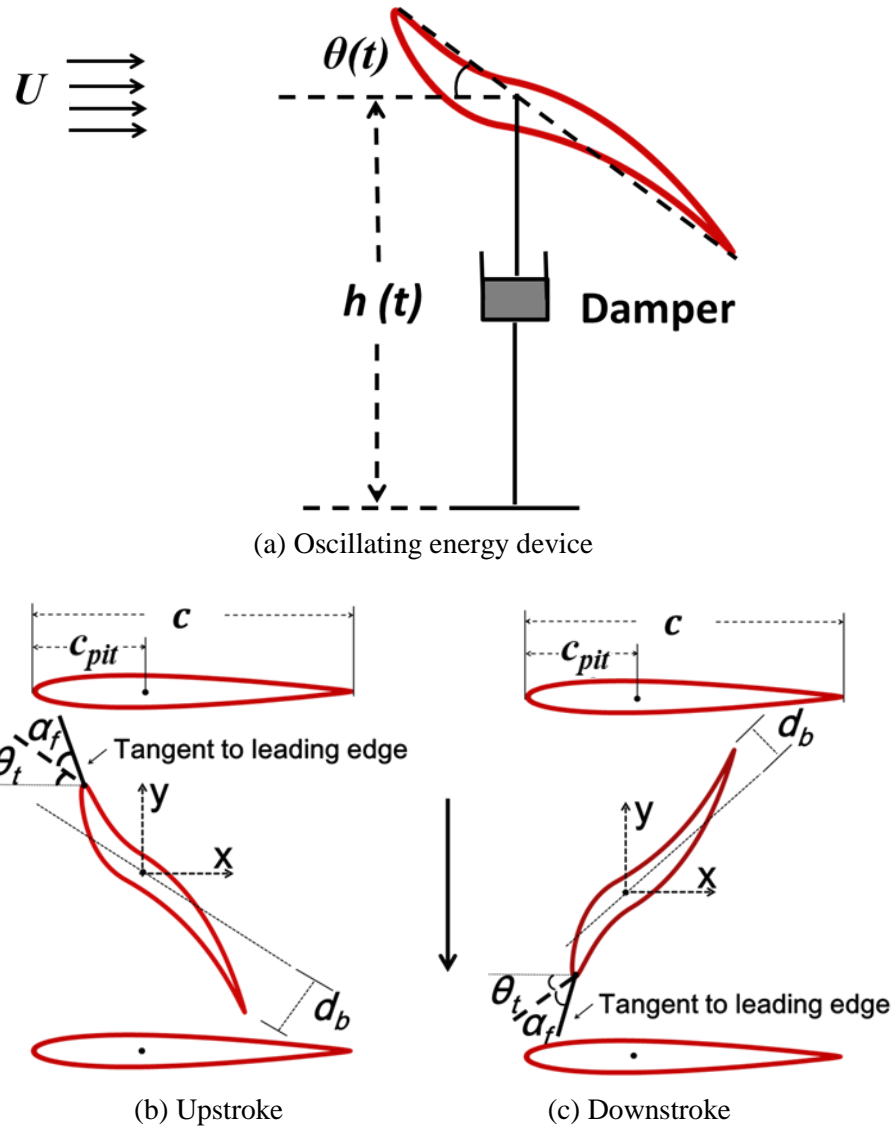


Figure 5. 1 Schematic diagram for (a) oscillating energy device (b) upstroke (c) downstroke.

To examine the bio-inspired animal flexible structural impact on the oscillating wing device's performance, the flexible deformation of foil is specified as a function of instantaneous time, wing chord-length and flapping frequency. The instantaneous lateral excursion of the foil ($y(x_f, t)$) is defined as based on a body-fixed coordinate system:

$$y(x_f, t) = \alpha_t(x_f) \sin\left(\omega t - \frac{\pi}{2}\right), \quad (5.1)$$

where x_f is the local coordinate of foil relative to the pitching axis, $\alpha_t(x_f)$ is the lateral amplitude defined as a piecewise function as:

$$\alpha_t(x_f) = \begin{cases} -c_{pit} \times \left(\frac{x_f}{c_{pit}}\right)^n \times \sin \alpha_f(t) & x_f < 0 \\ (c - c_{pit}) \times \left(\frac{x_f}{c - c_{pit}}\right)^n \times d_b & x_f \geq 0 \end{cases}, \quad (5.2)$$

where α_f is the local Angle of Attack (AOA) near the leading edge in a body-fixed coordinate system and d_b is the foil displacement at the trailing edge, as shown in Fig. 5.1 (b) and (c). These equations are defined by the author based on sinusoidal functions and taking the parameters of pitch location and trailing edge displacement into account.

The following four different wing models are studied depending on their specific blade flexibility.

- a) *Rigid model.* ($\alpha_f=0^\circ$, $d_b/c=0$) This is a conventional model that is utilized by the oscillating wing device. It is commonly used in industrial application and relevant research. Here it is used as a benchmark case to evaluate the device's capability in comparison to other flexible wings. By switching off the blade flexibility (i.e. setting $\alpha_f=0^\circ$ and $d_b/c=0$), the motion equation is simplified to

$$\begin{cases} h(t) = h_0 \sin(\omega t) \\ \theta(t) = \theta_0 \sin\left(\omega t - \frac{\pi}{2}\right). \\ y(x_f, t) = 0 \end{cases} \quad (5.3)$$

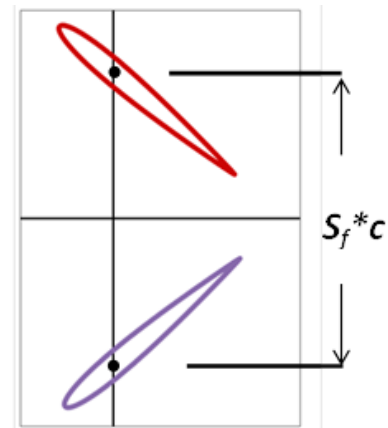
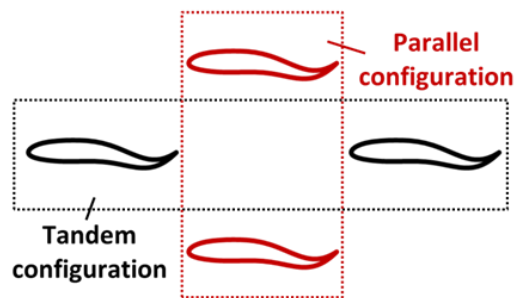
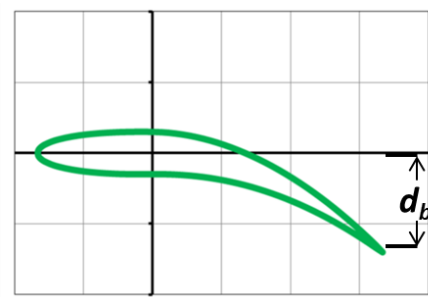
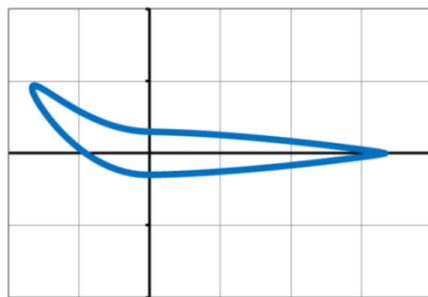
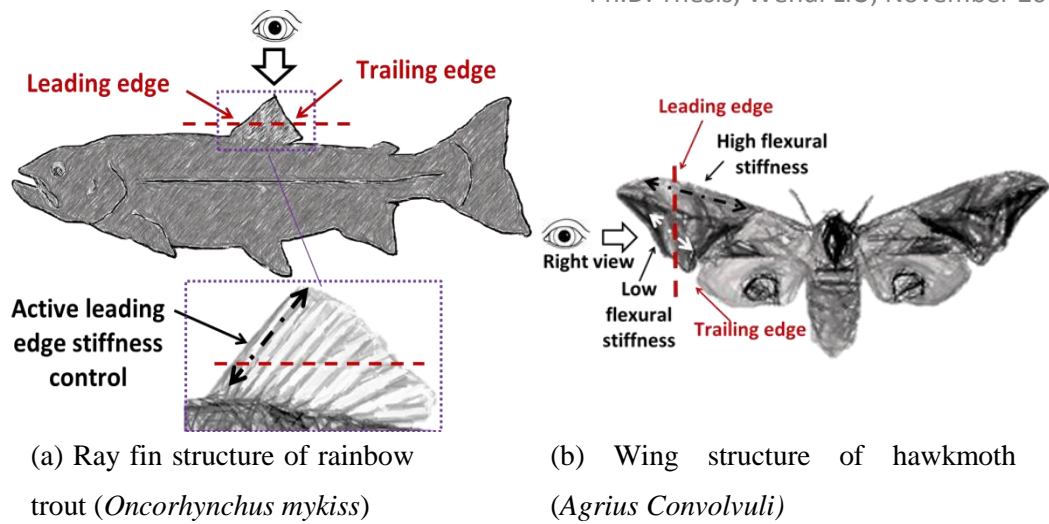


Figure 5. 2 Structure of (a) rainbow trout fin, (b) hawkmoth wing, (c) two-dimensional model of leading edge control model (top view from Fig. 2 (a)), (d) two-dimensional model of trailing edge control model (right view from Fig. 2 (b)), (e) Schematic illustrating fish swimming in group, (f) Two-dimensional twin-wing parallel configuration.

b) *Leading edge control (LEC) model.* ($\alpha_f \neq 0^\circ$, $d_b/c=0$) This imitates the ray fin of a rainbow trout, as shown in Fig. 5.2 (a) and (c). Rainbow trout use their undulating ray fin as an auxiliary thrust producer. The fin-rays are connected by a flexible membrane that is external to the thrust body and joined with the trout's back muscles internally so that the locomotion and stiffness of each fin-ray can be actively controlled by the trout (Sfakiotakis et al., 1999). A previous study by Shoele and Zhu (2012) showed that trout propels itself by flapping its flexible fin at a relative *low* frequency. The active control of the stiffness (strengthen) at the fin leading edge generated a large thrust force which is attributed to the Leading Edge Vortex (LEV) shedding. Shoele and Zhu's research shows the significant influence of the leading edge feature on the LEV. Efficient domination of the leading edge feature could achieve the goal of manipulating the LEV. To apply this biomimetic concept to the oscillating wing energy device, this study varies the local AOA (α_f) at the leading edge from 7.5° to 30° , using the suggestions from Shoele and Zhu (2012). With $d_b/c=0$, the motion profile becomes:

$$\left\{ \begin{array}{l} h(t) = h_0 \sin(\omega t) \\ \theta(t) = \theta_0 \sin\left(\omega t - \frac{\pi}{2}\right) \\ y(x_f, t) = \alpha_t(x_f) \sin\left(\omega t - \frac{\pi}{2}\right) \\ \alpha_t(x_f) = \begin{cases} -c_{pit} \times \left(\frac{x_f}{l_c}\right)^n \times \sin \alpha_f(t) & x_f < 0 \\ 0 & x_f \geq 0 \end{cases} \end{array} \right. \quad (5.4)$$

c) *Trailing edge control (TEC) model.* ($\alpha_f=0^\circ$, $d_b/c \neq 0$) The model is inspired by the flapping insect wing, particularly the hawkmoth wing shown in Fig.

5.2 (b) and (d). A numerical investigation by Nakata and Liu (2012) and experiments from Combes and Daniel (2003a and 2003b) indicated that the hawkmoth wing has the lowest stiffness at its trailing edge and deforms profoundly when the wing flaps at *high* frequency, where a large loading is produced. To represent the foil flexible effect associated with the hawkmoth wing, the trailing edge deformation (d_b/c) is varied from 0.05 to 0.15, as recommended by Combes and Daniel (2003a and 2003b). The motion equation is thus written as:

$$\left\{ \begin{array}{l} h(t) = h_0 \sin(\omega t) \\ \theta(t) = \theta_0 \sin\left(\omega t - \frac{\pi}{2}\right) \\ y(x_f, t) = \alpha_t(x_f) \sin\left(\omega t - \frac{\pi}{2}\right) \\ \alpha_t(x_f) = \begin{cases} 0 & x_f < 0 \\ (c - c_{pit}) \times \left(\frac{x_f}{c - c_{pit}}\right)^n \times d_b & x_f \geq 0 \end{cases} \end{array} \right. \quad (5.5)$$

d) *Integrated model.* ($\alpha_f \neq 0^\circ$, $d_b/c \neq 0$) The new concept proposed here is initiated by combining the propulsion enhancement benefits from the LEC at a low flapping frequency with the TEC at high frequency. Since both α_f at leading edge and displacement d_b/c at trailing edge are not zero, the description of the overall motion equations are the first four equations in this chapter.

The snapshots of the above four models are plotted in Fig. 5.3 over one flapping cycle. The detailed parameter matrix in the present study is summarized in Table 5.1. The heave amplitude (h_0/c) is given as 0.5 and 1.0, which are the widely adopted parameters in industry and research.

Flexible coefficient (n), the index in the lateral amplitude equation, is a means to quantify the flexibility or flexural stiffness of wing material. Obviously, a large n represents a more flexible structure in the chord-wise direction. To quantify a localized deformation in the proximity of leading and trailing edges, two additional parameters are introduced, i.e. local leading edge AOA (α_f) and trailing edge displacement (d_b/c).

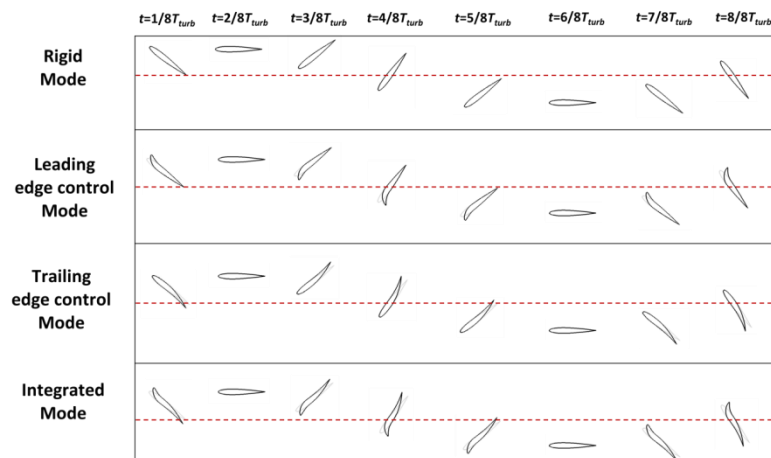


Figure 5. 3 Snapshots for four models over one flapping cycle.

The study by Kinsey and Dumas (2008) revealed that the optimal range of high efficiency existed between $f^* \approx 0.12$ to 0.18. Taking into account a moderate scale of device size, water current velocity (4 m/s in maximum), the oscillating reduced frequency in the present study varies from 0.05 to 0.25.

Apart from the above four single flexible/rigid models, attention is also focused on the twin-wing oscillating device, which is inspired by a group of flying or swimming animals to utilize energy which extracted from the vortex interaction between them (Liao, 2007) (Fig. 5.2 (e) and (f)). Though this biomimetic concept has been widely studied in terms of propulsion dominant flow, investigation into the field of energy extraction is limited.

Table 5. 1 Various parameters investigated in the present study.

Type	Number of wing	Heave amplitude (h_0/c)	Flexible coefficient (n)	Leading edge local AOA (α_f)	Trailing edge displacement (d_b/c)	Maximum (nominal) effective AOA (α_0)	Pitch axis (x_f/c)	Twin wing gap ratio (S_f)	Reduced frequency (f^*)
Rigid	1	0.5, 1.0	1	0°	0	0°, 5°, 10°	1/3	-	0.05-0.25
LEC	1	0.5	2, 3, 4	7.5°, 15°, 30°	0	10°	1/3	-	0.05-0.25
TEC	1	0.5	2, 5, 15	0°	0.05, 0.07, 0.15	10°	1/3	-	0.05-0.25
Integrated	1	0.5	Leading edge 3 Trailing edge 5	30°	0.15	0°, 5°, 10°	1/3	-	0.05-0.25
Rigid	2	0.5	1	0°	0	0°, 5°, 10°	1/3	2, 3	0.05-0.25
TEC	2	0.5	5	0°	0.05	0°, 5°, 10°	1/3	3	0.05-0.25

The current research will focus on the parallel twin-wing configuration for both rigid and TEC models and the interaction between two wings will be studied. The description of the kinematic motions of twin-wings is presented as:

$$\mathbf{Foil\ 1:} \left\{ \begin{array}{l} h(t) = h_0 \sin(\omega t + \pi) + \frac{S_f \times c}{2} \\ \theta(t) = \theta_0 \sin\left(\omega t - \frac{3\pi}{2}\right) \\ y(x_f, t) = \alpha_t(x_f) \sin\left(\omega t - \frac{3\pi}{2}\right) \\ \alpha_t(x_f) = \begin{cases} 0 & x_f < 0 \\ (c - c_{pit}) \times \left(\frac{x_f}{c - c_{pit}}\right)^n \times d_b & x_f \geq 0 \end{cases} \end{array} \right. , \quad (5.6)$$

$$\mathbf{Foil\ 2:} \left\{ \begin{array}{l} h(t) = h_0 \sin(\omega t) - \frac{S_f \times c}{2} \\ \theta(t) = \theta_0 \sin\left(\omega t - \frac{\pi}{2}\right) \\ y(x_f, t) = \alpha_t(x_f) \sin\left(\omega t - \frac{\pi}{2}\right) \\ \alpha_t(x_f) = \begin{cases} 0 & x_f < 0 \\ (c - c_{pit}) \times \left(\frac{x_f}{c - c_{pit}}\right)^n \times d_b & x_f \geq 0 \end{cases} \end{array} \right. . \quad (5.7)$$

As can be seen, these two wings perform an anti-phase heave and pitch motion. Given the average gap ratio S_f of 2.0, defined as the vertical gap between two wings divided by the chord length as shown in Fig. 5.2 (f), the actual distance between the two wings is $1.0c$ and $3.0c$ when they reach the nearest and distant positions, respectively.

In order to account for both the wing's chord-wise local flexure effect and the pitch angle, an equivalent local effective AOA is defined as

$$a_l(t, x) = \theta_l(t, x) - \arctan\left(\frac{h(\dot{t})}{U_\infty}\right), \quad (5.8)$$

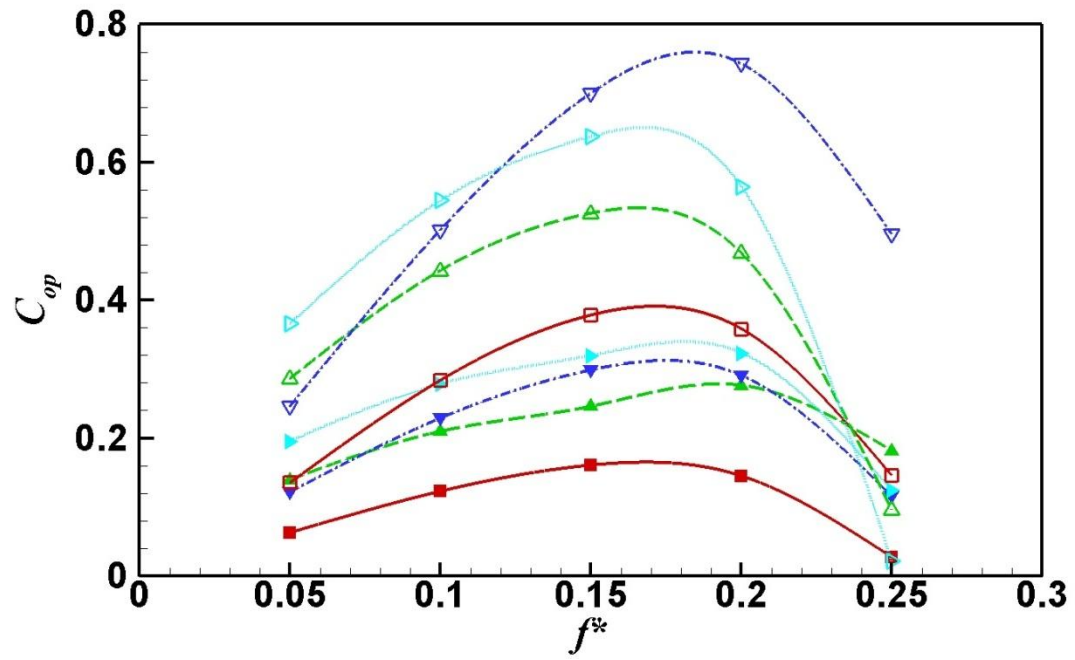
where $\theta_l(t, x)$ is a local pitch angle, defined as the angle of the local tangential line relative to a global x coordinate.

5.3 Results and discussions

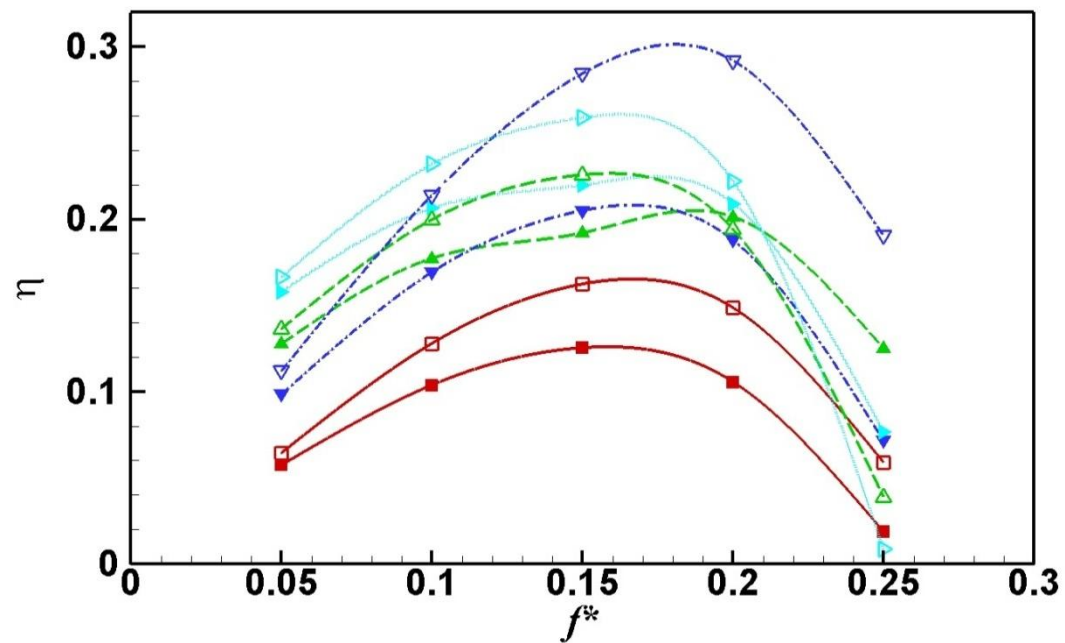
5.3.1 Mechanism of various bio-inspired flexible shapes for a single wing

It is generally accepted that a flapping wing with some degree of flexibility can potentially provide an improved propulsion performance that is otherwise impossible for a rigid wing. The fundamental mechanisms behind this may be attributed to (a) the change of the local effective angle of attack due to the flexible deformation of the wing shape; and (b) the enhanced stability of leading edge vortex shedding (Zhu, 2007; Nakata and Liu, 2012). The present study will show that a flexible wing can generate much more power than a rigid wing even when the wing is merely flapping for energy extraction. The local effective angle of attack and the stability of the Leading Edge Vortex (LEV) also influence the efficiency of the energy extraction situation, the mechanism of which is more or less similar to the propulsion situations.

Fig. 5.4 (a) and (b) display the mean power coefficient and efficiency for four models at two heave amplitudes (h_0/c) of 0.5 and 1.0 with nominal effective AOA of 10° . As can be clearly seen from the figures, within the f^* from 0.05 to 0.25, all flexible flapping wings generate larger efficiency than the rigid wing. Given $f^*=0.15$, the efficiency is increased from 12.5% (rigid) to 21.9% (integrated model) for $h_0/c=0.5$ and from 16.2% (rigid) to 28.4% (TEC) for $h_0/c=1.0$ respectively.



(a) Power coefficient



(b) Efficiency

Figure 5. 4 Comparison of (a) power coefficient and (b) efficiency among various flexible/rigid modes with nominal effective AOA of 10° . ($h_o/c=0.5$ ■: rigid, ▲: LEC, ▼: TEC and ►: Integrated) and ($h_o/c=1.0$ □: rigid, △: LEC, ▽: TEC and ▷: Integrated); $\alpha_f=30^\circ$ (LEC) and $d_b/c=0.15$ (TEC) and $\alpha_f=30^\circ$ plus $d_b/c=0.15$ (integrated model).

The improvement is especially profound when the wing flaps at small heave amplitude. However, the best flexible morphography is reliant on the particular flapping parameters, such as flapping frequency, pitch and heave amplitude, flexible coefficient, local leading/trailing edge displacement, or more specifically the nominal and local effective AOA a_0 and $(a_l(t, x))$, which will discuss shortly.

In order to examine the influence of wing flexibility on its performance, the investigation begins on the behaviour of a rigid wing. The evolution of LEV is depicted in Fig. 5.5 over half a cycle. It can be seen that at instantaneous time $t/T_{urb}=1/8$ the LEV starts to generate and further develops at $t/T_{urb}=2/8$. At $t/T_{urb}=3/8$, the wing undergoes its downstroke motion, the LEV sheds from the leading edge, convects to the wing trailing edge and eventually sheds into wake, leaving behind a shear layer near its trailing edge at $t/T_{urb}=4/8$. The above general observation is consistent with some earlier investigation (Xiao et al., 2012), Kinsey and Dumas (2008) and the results of Peng and Zhu (2009). Previous studies on the rigid wing device indicated that the LEV plays a leading role in the device power generation enhanced by increasing the instantaneous lifting force and moment coefficient (Peng and Zhu, 2009; Xiao et al., 2012). Flapping wing devices could generate and maintain LEV because of the pressure gradient and non-inertial forces during their downstroke motion. The LEV could generate a low pressure region compared with the surrounding fluid field. Such a low pressure region produces a suction effect on the upper surface of the flapping wing which could enlarge the pressure difference between the upper and lower surface and result in an enhancement on the lift amplitude during the flapping period (Shyy and Liu, 2007). The LEV could be attached to the wing surface during the whole downstroke motion

which acts like an energy resource to provide extra lift to the device continuously. A high efficiency is obtained when the energy of LEV is “recovered” by the wing. This is also well manifested by the instantaneous c_l and c_m plot in Fig. 5.6. As LEV starts to generate and develop, the peak lift force (c_l) increases and the moment (c_m) remains at a high value. Once the LEV fully develops and sheds from the leading edge, the c_l reaches its highest value, and both c_l and c_m decrease afterwards.

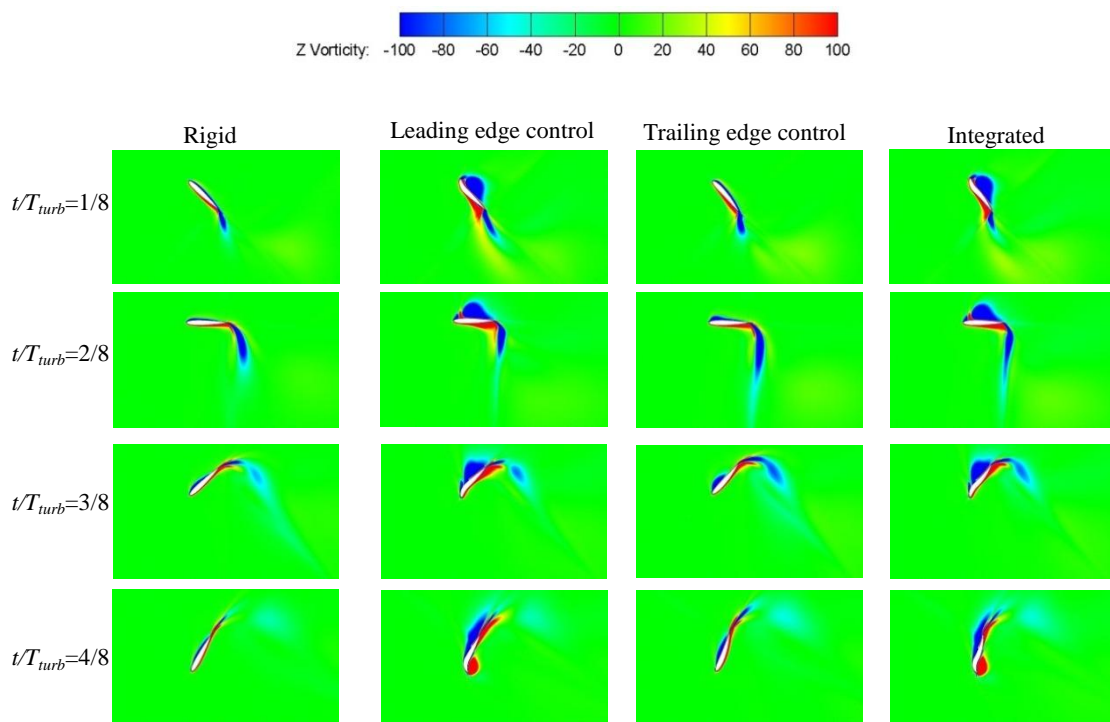
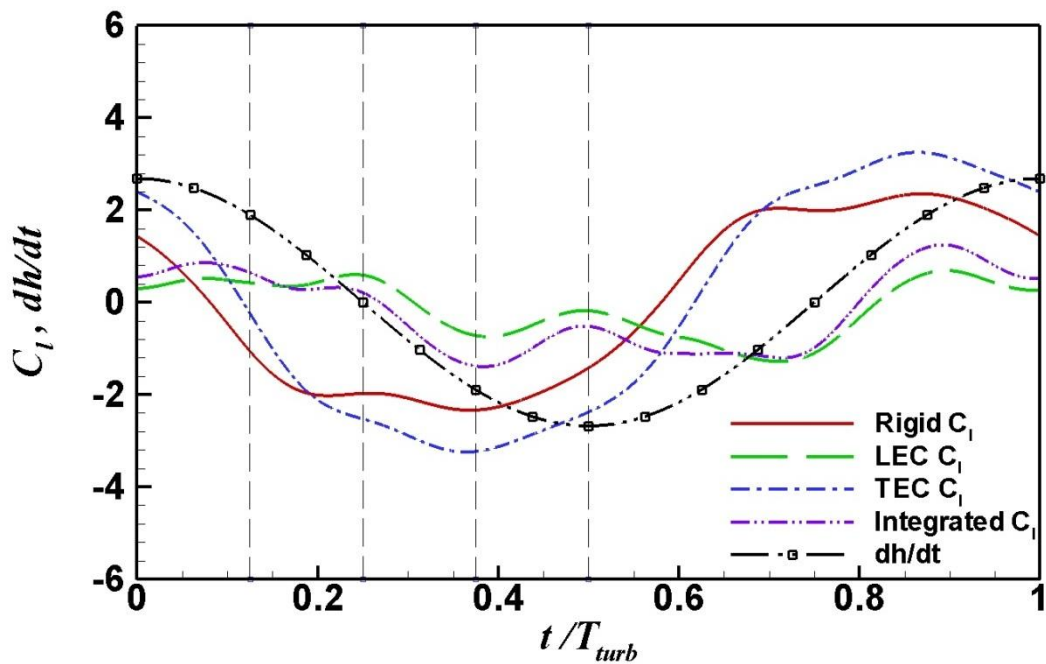


Figure 5. 5 Instantaneous vortex contours over half a cycle for various flexible/rigid wings $h_0/c=1.0$; $f^*=0.2$; nominal effective AOA of 10° ; $\alpha_f=30^\circ$ (LEC) and $d_b/c =0.15$ (TEC) and $\alpha_f=30^\circ$ plus $d_b/c =0.15$ (integrated model).

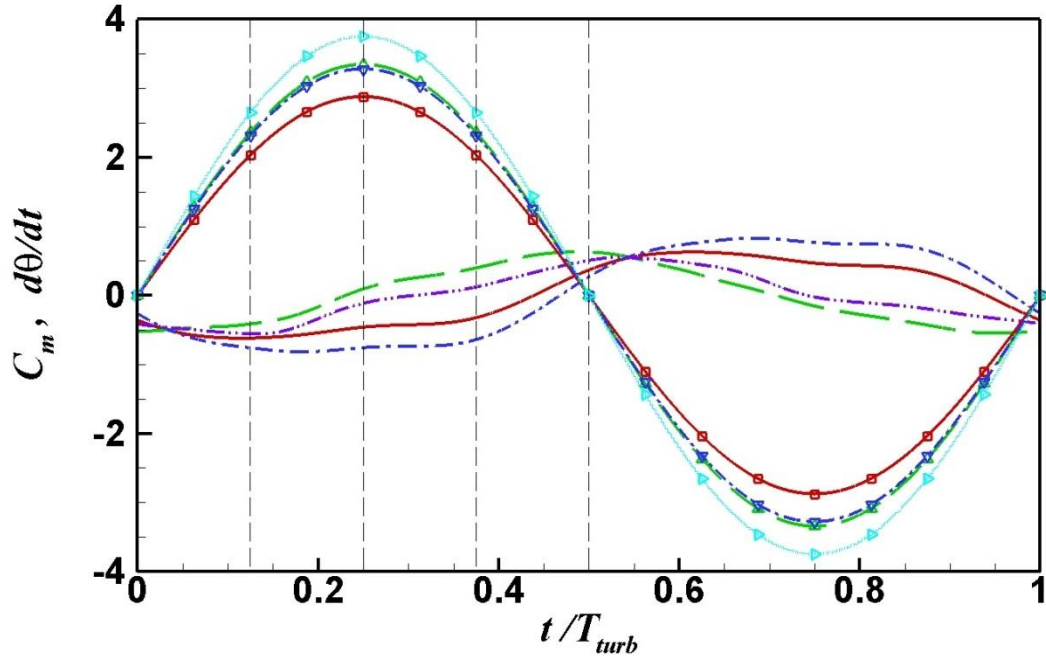
Apart from the instantaneous magnitude of c_l and c_m , with regards to device power or efficiency (as depicted by the power and efficiency equations in this chapter), it is also influenced by the phase shift between c_l and heaving velocity (dh/dt) as well as c_m and pitching angular velocity ($d\theta/dt$) (Xiao et al., 2012; Kinsey and Dumas, 2008). Since the power is the product of force multiplied by the displacement velocity, to

achieve high power efficiency, both c_m and $d\theta/dt$ are expected to co-exist in the same sign over one cycle.

Fig. 5.6 (a) and (b) show the comparison of time distribution of c_l , dh/dt , c_m and $d\theta/dt$ for four models. Given a rigid wing, a near-sinusoidal profile presents for the above four parameters, which further leads to a similar trend of instantaneous c_{op} , as shown in Fig. 5.7. The phase shift between c_l and dh/dt is $\pi/3$ approximately, which allows the c_l and dh/dt to have the same sign over more than half of the cycle, leading to a positive contribution from $c_l \times dh/dt$ to the mean power output. However, the phase shift between c_m and $d\theta/dt$ is nearly π , as displayed in Fig. 5.6 (b), and thus in this case they will result in opposite signs, giving a negative contribution from $c_m \times d\theta/dt$ to the mean power.



(a) Lift coefficient



(b) Moment coefficient

Figure 5. 6 Instantaneous lift coefficient and moment coefficient (a) lift coefficient, (b) moment coefficient $h_0/c=1.0$; $f^*=0.2$; nominal effective AOA of 10° ; $\alpha_f=30^\circ$ (LEC) and $d_b/c =0.15$ (TEC) and $\alpha_f=30^\circ$ plus $d_b/c =0.15$ (integrated model). In (b), solid line: rigid c_m , dashed line: LEC c_m , dash dot line: TEC c_m , dash double dot line: integrated c_m , ■: rigid $d\theta/dt$, △: LEC $d\theta/dt$, ▽: TEC $d\theta/dt$ and ▷: integrated $d\theta/dt$.

A different phase shift scenario appears when the wing is modelled with the LEC shape. As seen in Fig. 5.6 (a) and (b), for the majority of the time throughout a cycle, the c_l and dh/dt for the LEC model present the same sign. The phase shift between c_m and $d\theta/dt$ reduces to $\pi/2$, resulting in a positive contribution from $c_m \times d\theta/dt$ to the mean power output. The above force-velocity relation aligns with the different LEV interaction modes for rigid and LEC flapping wing, as depicted in Fig. 5.5. At $t/T_{turb}=1/8$, where the wing pitches to its maximum angle, the LEV of LEC fully develops and sheds from leading edge at $t/T_{turb}=2/8$, which is much earlier than for a rigid wing. In addition, the LEV of LEC is larger than that of a rigid wing, forming a large separation region near the trailing edge when the LEV reaches the wing trailing

edge. The peak values of the lift coefficient are influenced by both the size/strength of LEV at the leading edge and the flow separation region near the trailing edge. Recall that the mechanism of LEV provides a low pressure region to supply extra lift to the wing. A larger size/strength of LEV results in a large area/lower pressure in the low pressure region which could supply more lift to the wing. The superposition result of the above two effects can be seen in Fig. 5.6 and 5.7, where the lift coefficient distribution gives multiple peaks but a smaller amplitude, in comparison to its rigid wing counterpart.

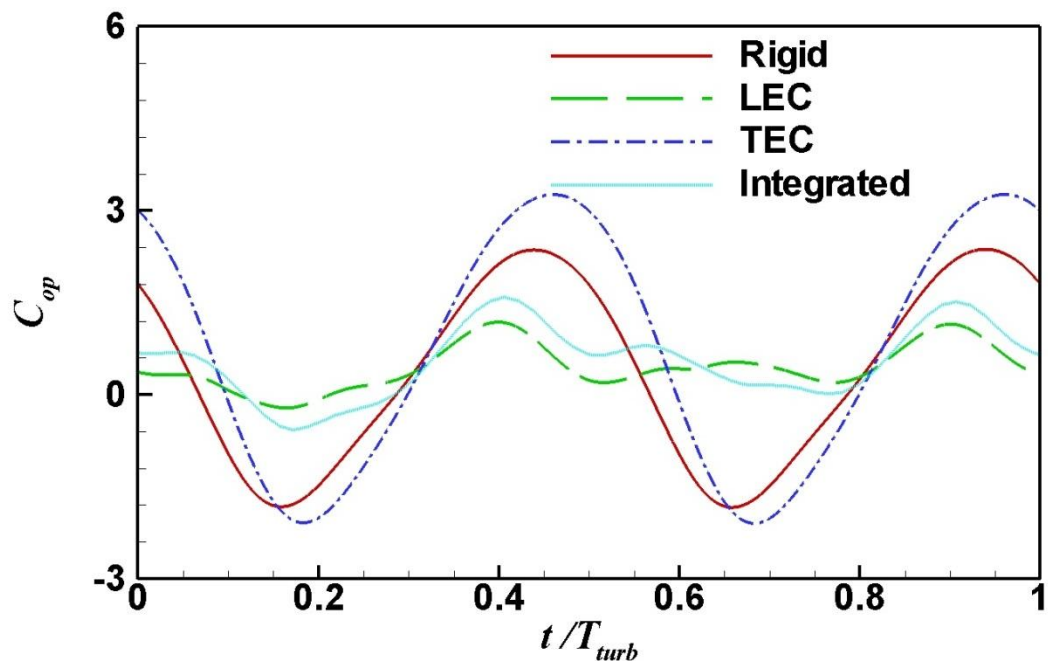


Figure 5. 7 Instantaneous power coefficient with nominal effective AOA of 10° and $h_0/c=1.0$; $f^*=0.2$. For a flexible wing $\alpha_f=30^\circ$ (LEC) and $d_b/c =0.15$ (TEC) and $\alpha_f=30^\circ$ plus $d_b/c =0.15$ (integrated model).

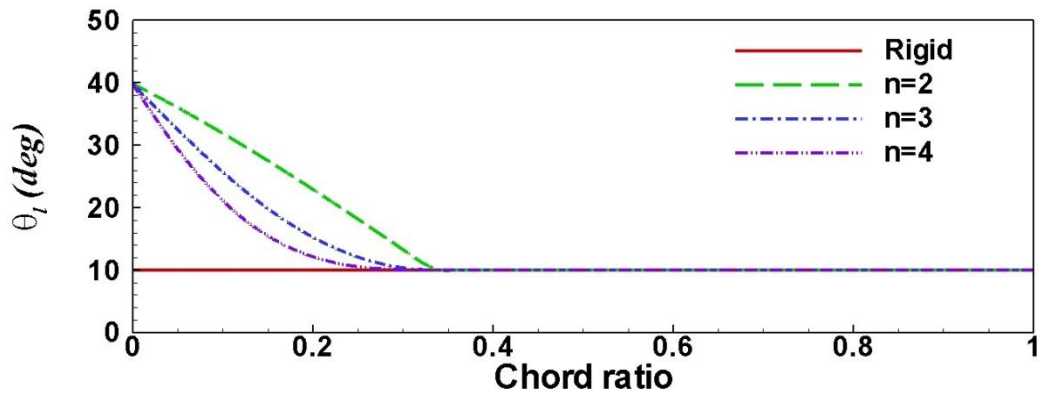
With the case of TEC, as displayed in Fig. 5.6 and 5.7, the trends of c_l , dh/dt , c_m , $d\theta/dt$ and c_{op} are essentially the same as those of a rigid wing. However, the peak values of the lift coefficient significantly increase from 2.35 of a rigid wing to 3.25 for TEC, and a remarkable increase in c_{op} can also be observed from Fig. 5.7, leading

to enhanced mean power efficiency. This is attributed to the enlarged LEV strength for TEC in comparison to a rigid wing, as depicted in Fig. 5.5.

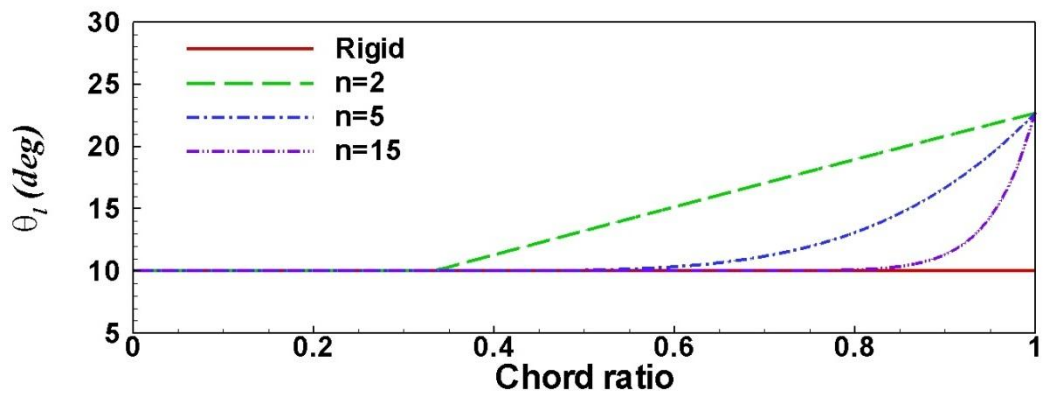
With the results presented above, the following general observations about a flexible wing with a LEC and TEC model can be made. Generally, a wing of LEC shape, where the wing deforms easily at the leading edge, can trigger the LEV to develop at an earlier stage than a rigid wing. As a consequence, the phase-shift between c_l and dh/dt and c_m and $d\theta/dt$ can present a favourable trend to enhance the cycle-mean power. On the other hand, a flexible wing of TEC shape, where the main deformation occurs near the trailing edge, can enhance the size and strength of LEV and thus increase the total power via increasing the peaks of lift and moment coefficients. It is expected that an even better performance can be achieved by employing both a flexible wing with an appropriately designed combination of LEC and TEC shapes. The results for an integrated model clearly prove the above hypothesis, as shown in Fig. 5.4 – 5.7.

Specific attention is drawn to the role of effective AOA on the power. Fig. 5.8 (a) to (c) shows the local AOA distribution along the chord-wise direction at an instantaneous time of $t/T_{turb}=1/8$, when the wing pitches to its maximum amplitude, i.e. $\theta_t(t)=\theta_0$. As can be clearly seen from the figures, although the nominal effective AOA $\alpha_0=10^\circ$ is identical for all four models, the local effective AOA ($\alpha_t(t,x)$) varies significantly with various models, as does the degree of the overall flexible deformation (represented by n), and local stiffness at leading and trailing edge (α_f and d_b). In particular, the flexible wing displays a large $\alpha_t(t,x)$ in comparison to a rigid

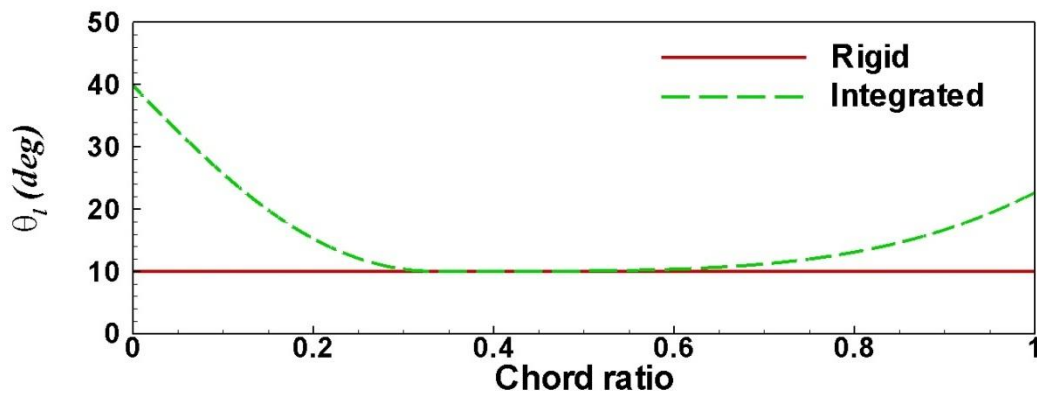
wing at the same chord-wise location, which as a consequence leads to the different behaviour of LEV, the lift and moment coefficient and then the efficiency.



(a) LEC



(b) TEC



(c) Integrated

Figure 5. 8 Foil local AOA along chord-wise direction at $\theta_i(t)=\theta_0$ for different flexible coefficients (n) at nominal effective AOA $\alpha_0=10^\circ$. (a) LEC, $\alpha_f=30^\circ$. (b) TEC, $d_b/c=0.15$. (c) Integrated model $\alpha_f=30^\circ$ and $d_b/c=0.15$.

In the following sections of investigations will be focused on a systematic parametric study to examine other relevant flexible influences on power efficiency.

5.3.2 Parametric study

5.3.2.1 Leading edge control model

The main cases simulated in this section are provided in Table 5.1. These include the effect of the flexible coefficient (n) and local leading edge AOA (α_f). As mentioned earlier, the flexible coefficient is an indication of wing flexibility along the chord-length direction. On the other hand, the local leading edge AOA (α_f) presents the potential for local deformation at the wing leading edge.

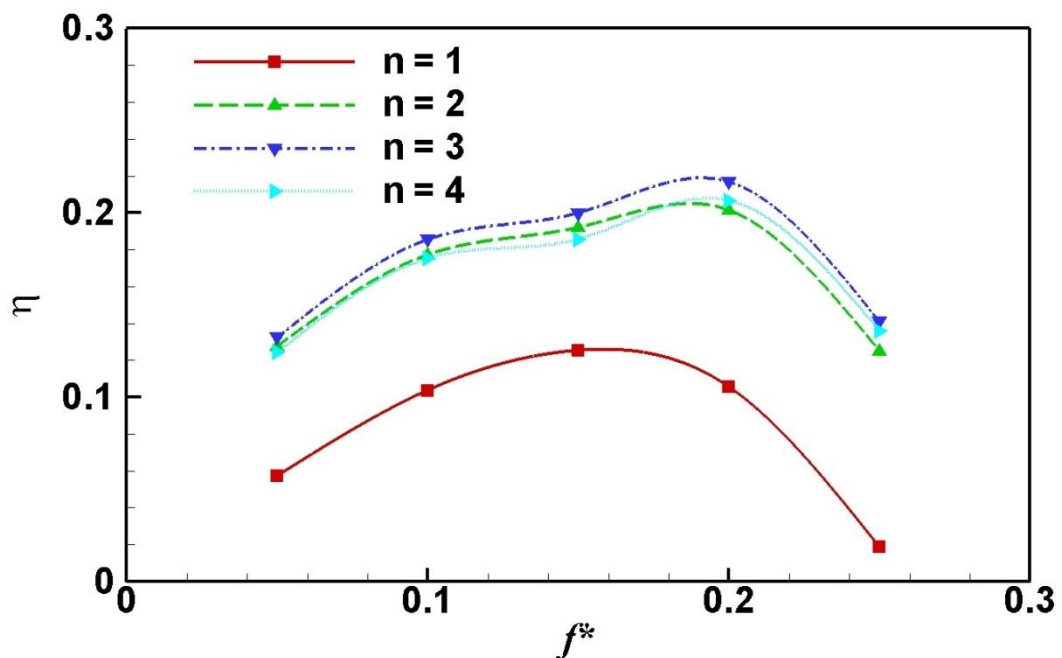
5.3.2.1.1 Flexible coefficient (n)

As shown in Fig. 5.8 (a)-(c) and Eq. 5.4 in Section 5.2, the flexible coefficient n determines the degree of flexibility of a wing in the chord-wise direction. The cases studied are associated with n of 1, 2, 3 and 4, where n equals to 1 indicating a rigid wing. The influence of the flexible coefficient on the cycle-mean efficiency is shown in Fig. 5.9 (a). For all cases studied here, though a flexible wing is better than a rigid wing, as was discussed in the last section, the best performance is achievable if the wing shape deforms moderately, particularly the case of n being 3.0. The instantaneous c_l and c_m distribution displayed in Fig. 5.10 (a) reveals that while the flexible coefficient has no impact on the phase shift of ($c_l \sim dh/dt$) and ($c_m \sim d\theta/dt$), it influences the peak values of c_l and c_m . Specifically, at a larger n , c_l amplitude increases while c_m decreases. Recall a negative effect from ($c_m \times d\theta/dt$) to mean power; a lessened peak c_m is beneficial to improve power.

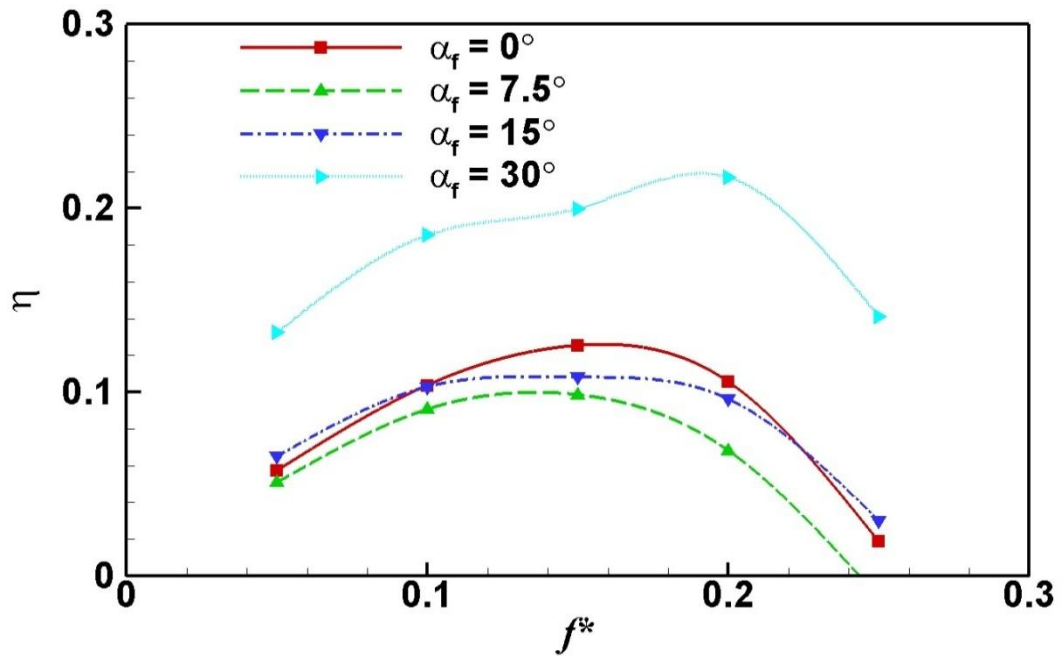
5.3.2.1.2 Local leading edge AOA (α_f)

The influence of local leading edge AOA has been investigated with α_f of 7.5° , 15° and 30° . As shown in Fig. 5.9 (b), where the time-mean efficiency is plotted for various local leading edge AOAs, a deteriorated effect on the power is depicted at low α_f . However, by increasing α_f to a large value, the efficiency is profoundly increased in comparison to a rigid wing ($\alpha_f = 0^\circ$). Fig. 5.10 (b) shows the instantaneous distribution of c_l and c_m for different α_f . The impact of α_f on power is established via its influence on peak values of c_l and c_m as well as the phase shifting between c_l and dh/dt , and c_m with $d\theta/dt$. Increasing α_f to a critical value ($\alpha_f \geq 15^\circ$) leads to a profoundly enlarged c_l , and a reduced phase shift between c_m and $d\theta/dt$, from π to $\pi/2$ corresponding to a rigid and LEC. This is consistent with the LEV effect associated with a flexible LEC, as discussed in the last section.

5.3.2.2 Trailing edge control model

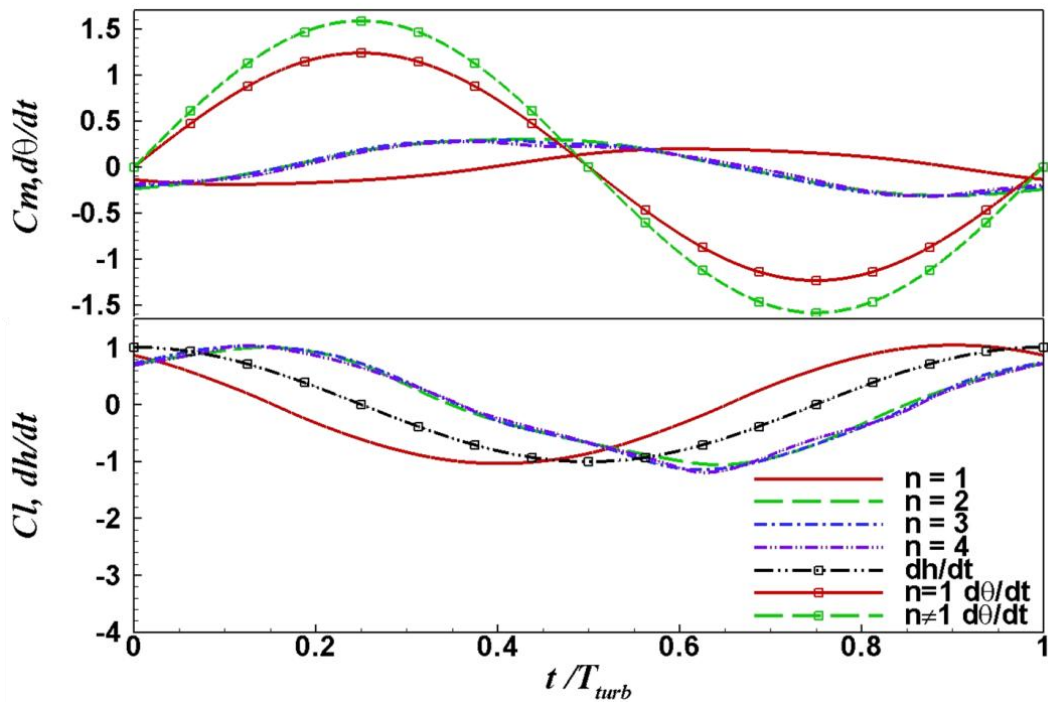


(a) Effect of the flexible coefficient (n), $n=1$ represents the rigid wing

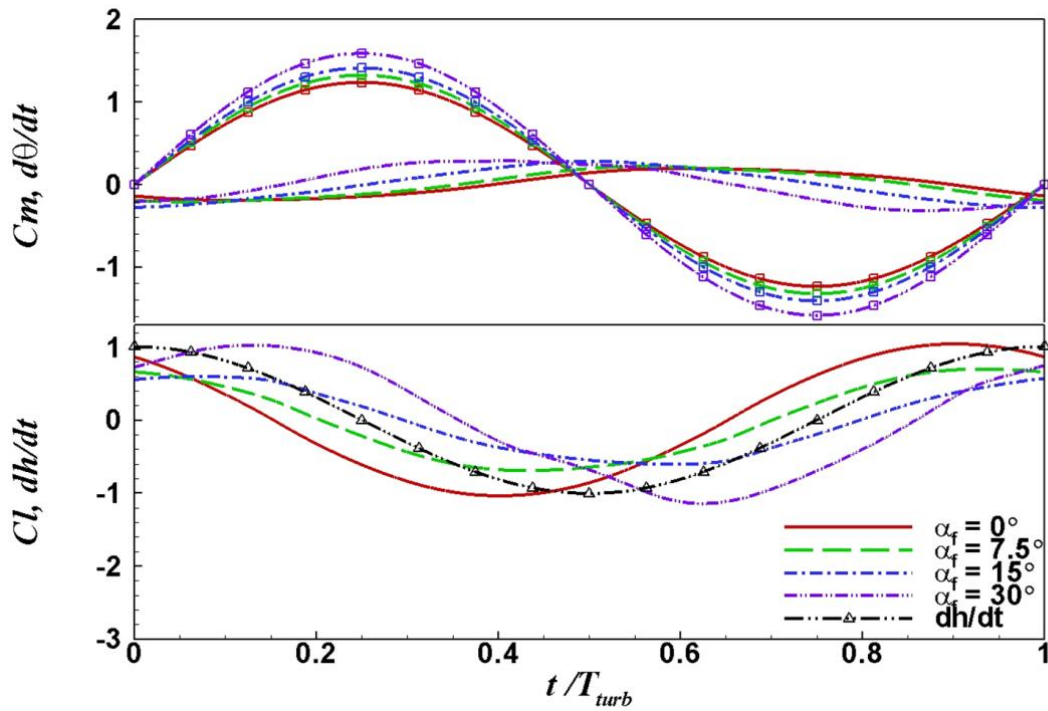


(b) Effect of leading edge local AOA (α_f)

Figure 5. 9 Various LEC parameters' effect on the cycle-mean efficiency at nominal effective AOA $\alpha_0=10^\circ$. (a) Flexible coefficient (n), (b) leading edge local AOA α_f . ($h_0/c=0.5$).



(a) n effect on c_l , dh/dt , c_m and $d\theta/dt$



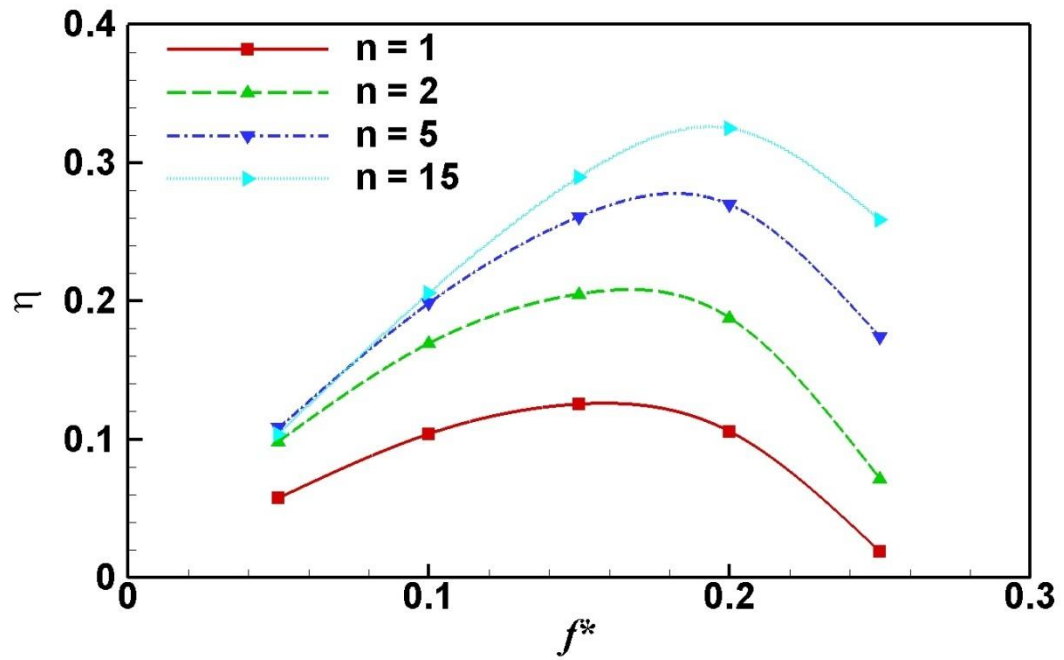
(b) α_f effect on c_l , dh/dt , c_m and $d\theta/dt$. \square with line: corresponding $d\theta/dt$.

Figure 5. 10 Instantaneous c_l , dh/dt , c_m and $d\theta/dt$ (LEC $h_0/c=0.5$; $f^*=0.15$) at nominal effective AOA $\alpha_0=10^\circ$. (a) Flexible coefficient effect and (b) α_f effect.

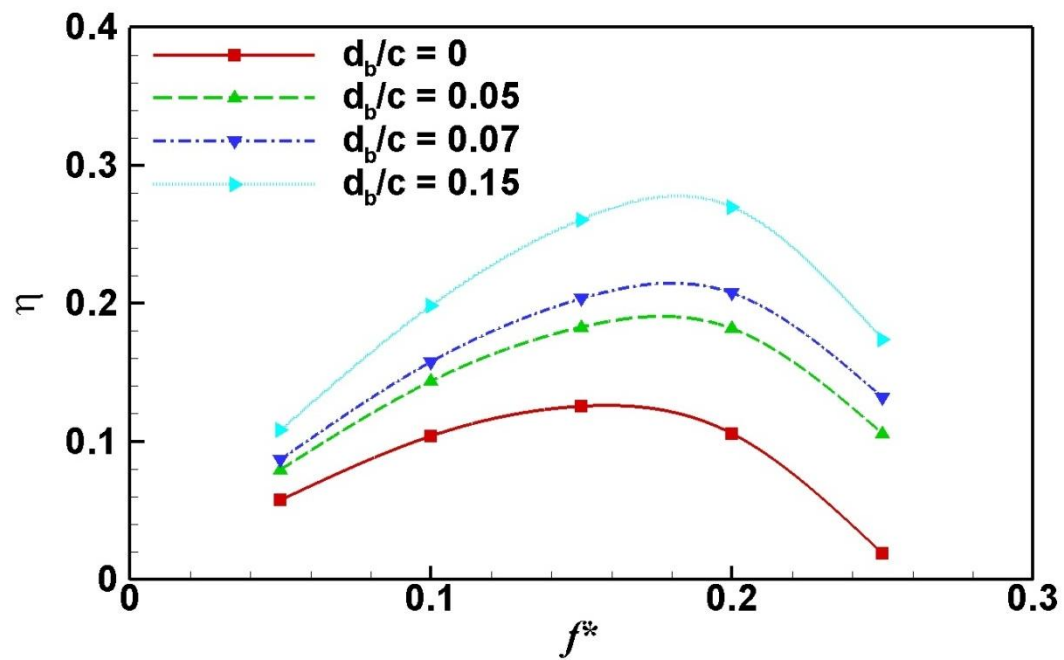
In this model, there are two parameters influencing the power, which are flexible coefficient (n) and trailing edge displacement (d_b), as defined as Eq. 5.5 in Section 5.2. In this section, the effects of these two parameters are investigated.

5.3.2.2.1 Flexible coefficient (n)

Three different flexible coefficients of 2, 5 and 15 are studied in this section. Distinguishing from the little n effect on an LEC model, it has a remarkable influence on the power efficiency of the TEC model, principally on the large flapping frequency. As can be seen from the cycle-mean efficiency in Fig. 5.11 (a), the addition of flexibility to a TEC monotonically improves the power with flexible coefficient n . Also, the peak efficiency even occurs at a larger f^* of 0.2, as compared to $f^*=0.15$ for a rigid wing.

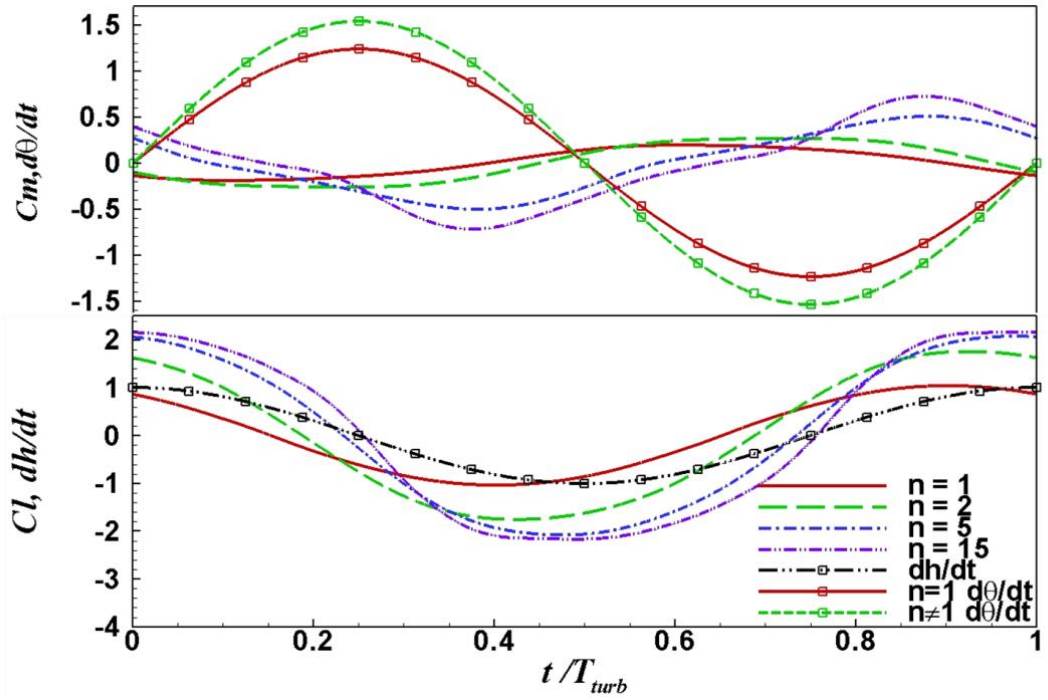


(a) Effect of flexible coefficient (n)

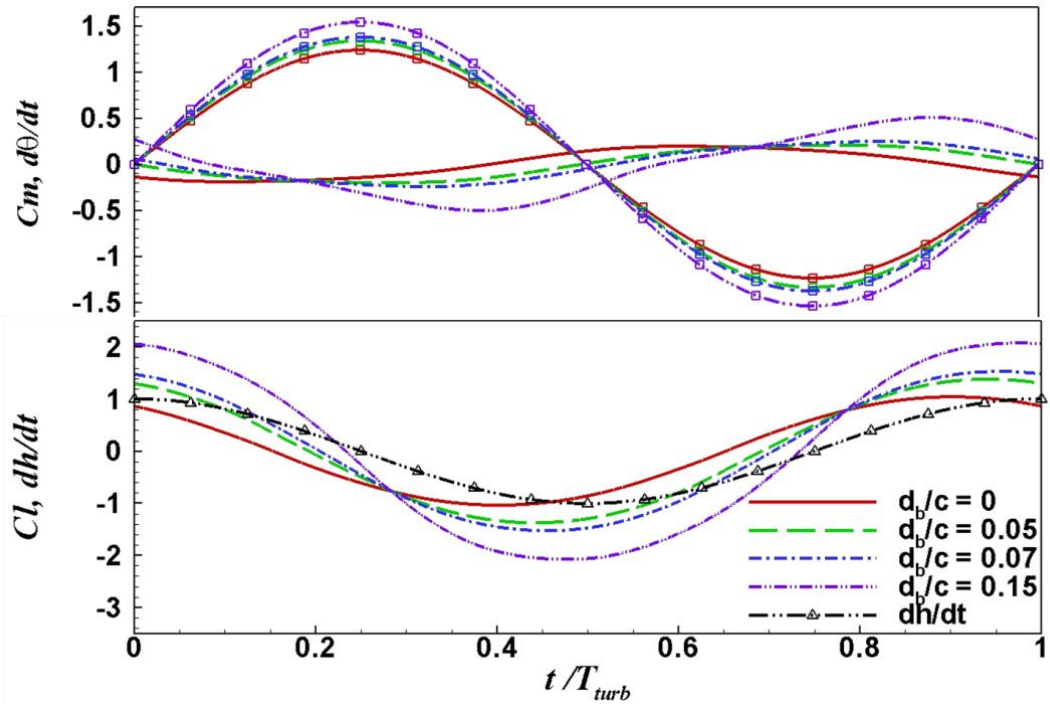


(b) Effect of trailing edge displacement d_b

Figure 5. 11 Effect of TEC parameters on the time-mean efficiency at nominal effective AOA $\alpha_0=10^\circ$. (a) Flexible coefficient (n) and (b) trailing edge displacement (d_b/c) ($h_0/c=0.5$).



(a) n effect on c_b , dh/dt , c_m and $d\theta/dt$



(b) d_b effect of c_l , dh/dt , c_m and $d\theta/dt$

Figure 5. 12 Instantaneous c_l , dh/dt , c_m and $d\theta/dt$ (TEC with $h_o/c=0.5$; $f^*=0.15$) at nominal effective AOA $\alpha_o=10^\circ$. (a) flexible coefficient effect and (b) trailing edge deformation effect. Open square with lines: $d\theta/dt$.

A detailed analysis of the instantaneous c_l and c_m plot is shown in Fig. 5.12 (a). As can be seen from the plot, a larger n is the greater of increase in c_l amplitude. A greater phase change of c_m is also observed with larger n . Although the higher efficiency can be achieved by increasing the flexible coefficient, considering a reasonable stiffness of biological animals in nature, the largest n of 15 in the present study is not recommended when this conceptual design is applied to the industry. Instead, a moderated n of 5 is highly recommended.

5.3.2.2.2 Trailing edge displacement (d_b/c)

Fig. 5.11 (b) shows the time-averaged efficiency for the trailing edge displacement effect on the TEC model. It is evident that a large displacement near the trailing edge can help to enhance the energy extraction in comparison to a rigid model with zero deformation at TE. A significant improvement can be seen in the frequency (f^*) between 0.1 - 0.2. The general trend of instantaneous c_l and c_m curve shown in Fig. 5.12 (b) is very similar to that of the flexible coefficient n effect. The peak values of c_l and c_m have been continually increasing with the increasing of trailing edge displacement. Moreover, although the pitching velocity ($d\theta/dt$) slightly increases at a large d_b/c , which is expected to detriment the mean-power by increasing the negative contribution from ($c_m \times d\theta/dt$), the improvement in the net cycle-mean power is still remarkable because of the profound increase of c_l . The phase between c_m and $d\theta/dt$ is also changed from π to $\pi/2$.

5.3.2.3 Integrated model

As mentioned earlier, an integrated flexible wing is expected to gain a larger efficiency than a LEC and TEC. The study of an integrated model is carried out with

three typical nominal effective AOA of 0° , 5° and 10° . The results of mean efficiency against flapping frequency are shown in Fig. 5.13. As can be seen clearly, with all three effective AOAs being examined, an enhanced efficiency is observable with the use of a flexible integrated model and this behaviour becomes more remarkable at low effective AOA. For example, at $\alpha_0=10^\circ$, the peak efficiency increases from 12.5% of the rigid wing to 22.1% of the flexible integrated wing, while at $\alpha_0=0^\circ$, η increases from 1.9% to 13.6%.

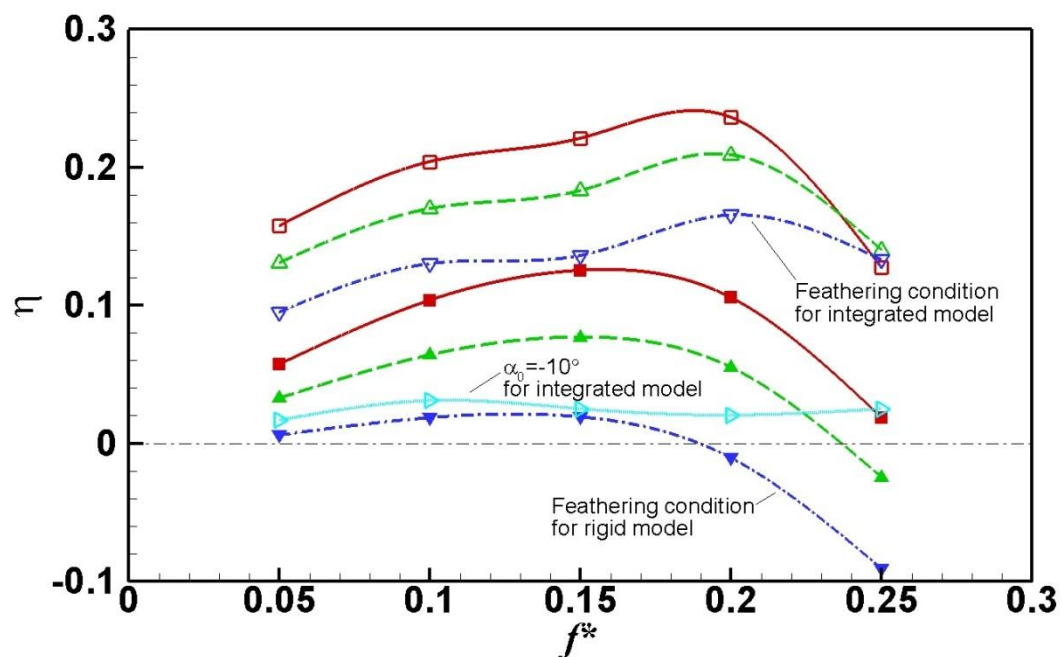


Figure 5. 13 Comparison of time-mean efficiency versus f^* between integrated flexible wing and a rigid wing for various α_0 (\blacksquare : rigid $\alpha_0=10^\circ$, \blacktriangle : rigid $\alpha_0=5^\circ$, \blacktriangledown : rigid $\alpha_0=0^\circ$, \square : integrated $\alpha_0=10^\circ$, \triangle : integrated $\alpha_0=5^\circ$, \triangledown : integrated $\alpha_0=0^\circ$ and \triangleright : integrated $\alpha_0=-10^\circ$) with $h_0/c=0.5$; $\alpha_f=30^\circ$; $d_b/c=0.15$; $n=3$ for leading edge and $n=5$ for trailing edge.

Special attention is paid to the case with a nominal effective AOA of zero ($\alpha_0=0^\circ$), i.e. the feathering condition. A totally diverse feathering behaviour is shown in Fig. 5.13 for a rigid and flexible wing. At $\alpha_0=0^\circ$, the efficiency of a rigid wing is more or less zero, which is consistent with the feathering definition (Kinsey and Dumas,

2008). However, with the use of a flexible integrated model, the wing operates in the power generation regime with the maximum efficiency of 10%. The actual feathering condition for a flexible integrated model, indicated by a zero mean efficiency, is reduced to a nominal effective AOA of -10° .

5.3.2.4 Parallel twin wing

The parallel twin-wing configuration is studied with the aim of examining whether a biomimetic concept of animals moving as a group can be similarly applied to energy devices. The study of rigid and TEC models is carried out with different gap ratios and nominal effective AOA of 0° , 5° and 10° .

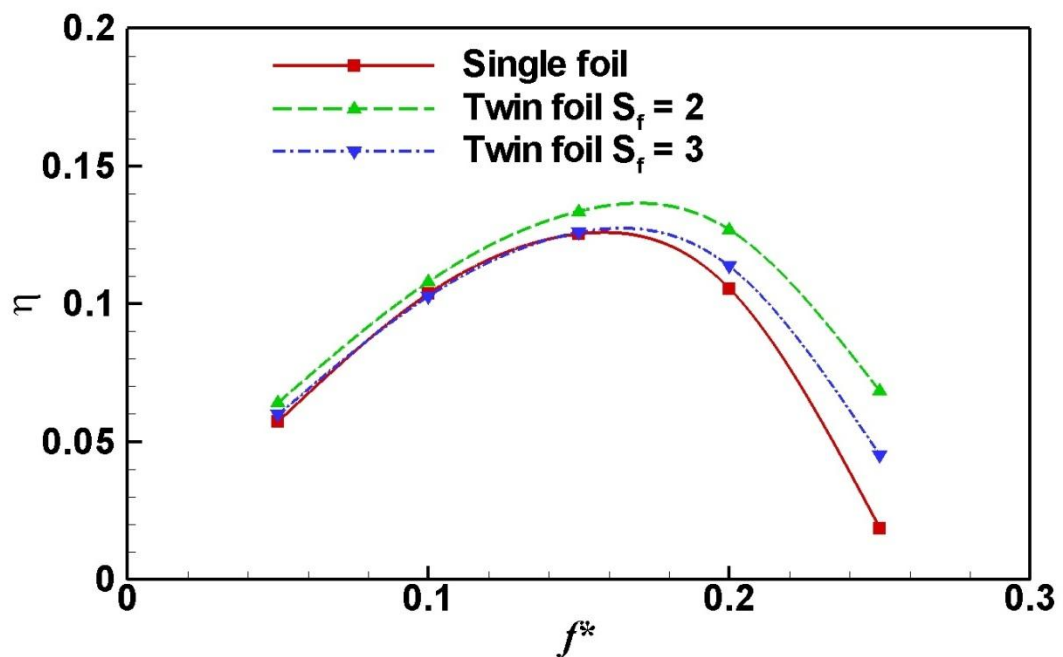


Figure 5. 14 Comparison of time-mean efficiency versus f^* under twin rigid foils configuration for different gap ratio with $h_0/c=0.5$ at nominal effective AOA $\alpha_0=10^\circ$.

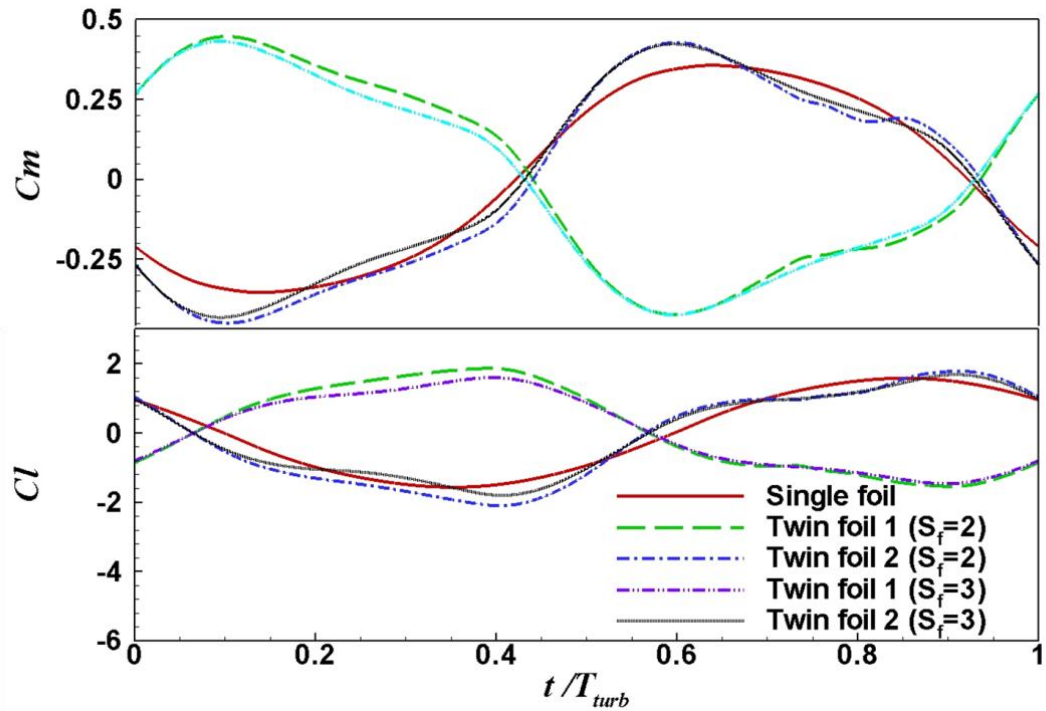


Figure 5. 15 Instantaneous lift coefficient and moment coefficient for rigid single and twin foil at nominal effective AOA $\alpha_0=10^\circ$ with $h_0/c=0.5$ and $f^*=0.2$.

5.3.2.4.1 Gap ratio (S_f)

The comparison between a rigid single wing and parallel twin-wings is shown in Fig. 5.14 with heaving amplitude h_0 of $0.5c$ and α_0 equals to 10° . Generally, a parallel twin-foil configuration improves the efficiency in comparison to a single wing, especially at a large flapping frequency. A small gap between the two wings is beneficial to enhance the overall efficiency. The instantaneous distribution of lift and moment coefficients displayed in Fig. 5.15 at $f^*=0.2$ reveals a slightly enlarged amplitude of c_l and c_m . With the analysis of the comparison of a single and twin-wings for instantaneous vortex contour, as shown in Fig. 5.16, a stronger vortex interaction is observed around twin-wings than a single wing, which is believed to be the cause of the improved power. The behaviour observed here very much resembles the schooling fish and flying insects in nature, when they move from one place to

another in order to preserve their propulsion energy. The present results also indicate that a parallel arranged twin-wing can generate more power than a single wing with a similar biological mechanism.

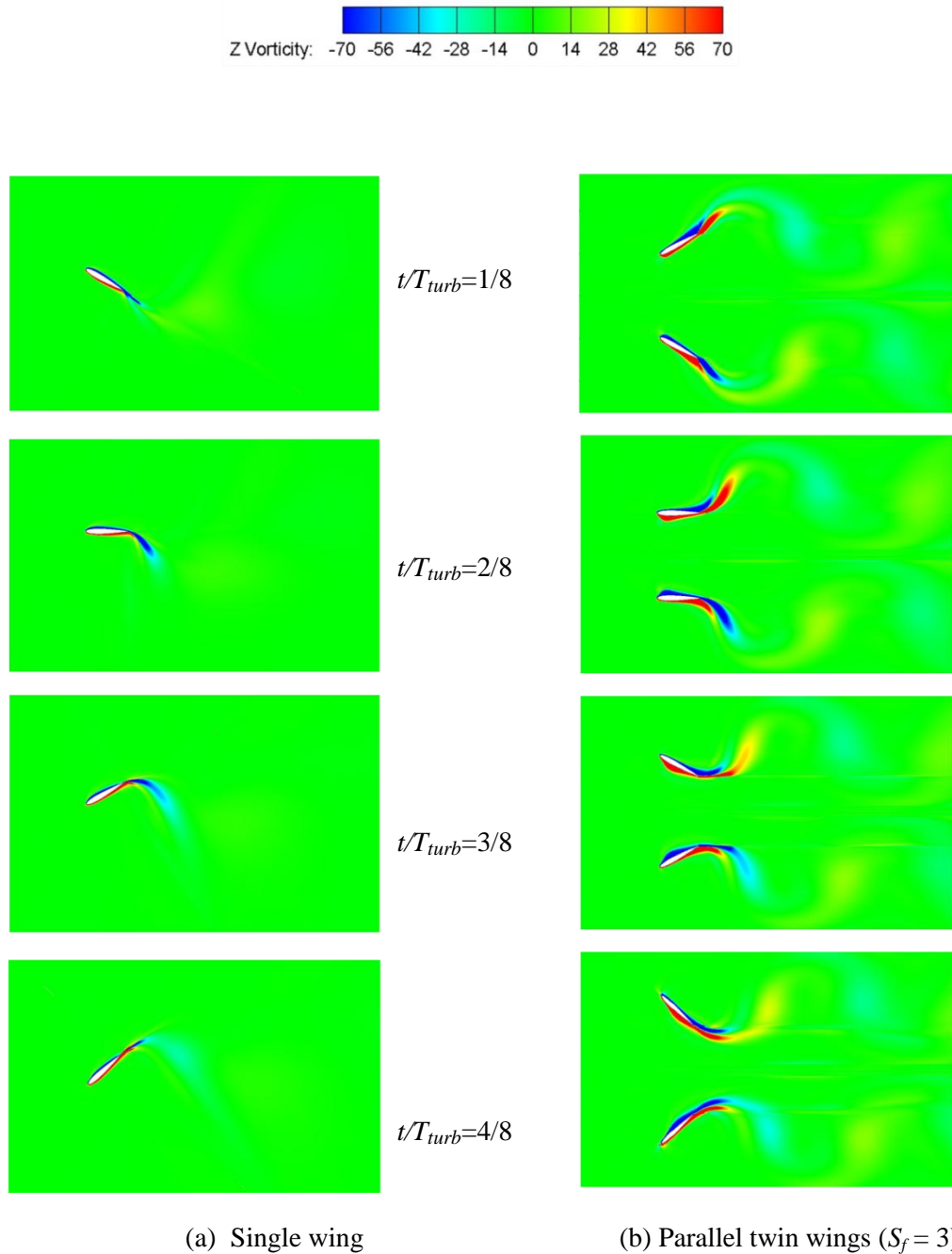


Figure 5. 16 Comparison of instantaneous vortex contours at nominal effective AOA $\alpha_0=10^\circ$ for (a) single rigid wing and (b) parallel rigid twin-wings ($S_f = 3$) with $h_0/c=0.5$; $\alpha_0=10^\circ$ and $f^*=0.2$

5.3.2.4.2 Nominal effective AOA (α_0)

The time-mean efficiency against the flapping frequency with different α_0 is shown in Fig. 5.17. A similar phenomenon can be found when a single flexible wing model is observed, e.g. by applying a flexible TEC with a small α_0 ($\alpha_0=0^\circ$ and 5°), a larger efficiency is achieved especially at a large flapping frequency. However, the efficiency reduces with $\alpha_0=10^\circ$ at a large flapping frequency. An examination of the detailed flow structure shows that too large an angle of attack destroys the benefits from a favourable vortex interaction between twin-wings.

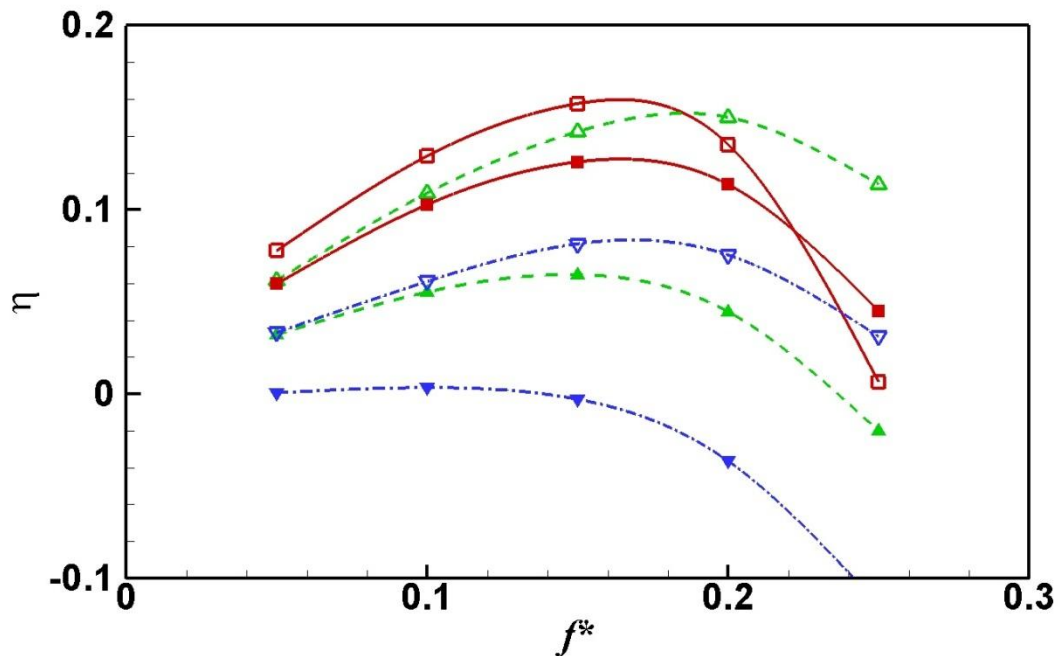


Figure 5. 17 Comparison of time-mean efficiency versus f^* under twin wing configuration (TEC model ($d_b/c=0.05$) vs. rigid model with $h_0/c=0.5$ and $S_f=3$). ■: rigid, $\alpha_0=10^\circ$, ▲: rigid, $\alpha_0=5^\circ$, ▼: rigid, $\alpha_0=0^\circ$; □: TEC, $\alpha_0=10^\circ$, △: TEC, $\alpha_0=5^\circ$, ▽: TEC, $\alpha_0=0^\circ$.

5.4. Summary

A turbulent Computational Fluid Dynamics (CFD) simulation of an ocean energy extraction device consisting of an oscillating/flapping flexible single and twin-wing

have performed. The concept is inspired by the flexible wings of natural flying insects/birds and swimming fish. Particularly, the LEC, TEC, and a further developed integrated model combining the best features of the above two models. 10^6 CPU seconds calculated on ARCHIE-WeST high performance computing facilities of University of Strathclyde are needed for a typical case in this chapter. The simulation shows that the chord-wise deformation causes a remarkable increase in the local angle of attack, leading to the enhanced power efficiency of a flexible wing device compared to a rigid wing. The hydrodynamic performance of the wing is affected not only by the increased instantaneous lift and moment amplitude due to the deformation, but also by the phase shift among lift and heaving-velocity and moment and pitching-velocity, by initiating an earlier development of leading edge vortex. The contribution from the peak force and phase shift to the overall cycle-mean power efficiency very much depends on the specific models, i.e. whether the deformation mainly occurs in the vicinity of the trailing edge like a hawkmoth wing or near the leading edge as with a trout ray fin, as well as the degree of flexibility. The systematic simulation results find that, with the new proposed integrated model, the power efficiency reaches a 7.68% enhancement relative to a rigid wing, which is associated with a nominal effective AOA of 10° at $f^*=0.15$. A dramatic increase of efficiency (about six times that of a rigid wing) is obtained for a nominal effective AOA at zero degree. One striking finding is that, with such a flexible wing, the pitching amplitude can be profoundly reduced when the wing operates at a feathering condition.

Studies on a parallel-arranged twin-wing configuration for various nominal effective AOAs show that twin-wings generate much more power than a single wing. A

relatively small gap between the two wings ($S_f=2.0$) enriches the vortex interaction between the gap, and thus improves the energy extraction ability.

Finally, in the present study the flexible structure of wings is pre-determined (active controlled). In reality, insects and fish with different wing/fin stiffness and mass ratios could achieve their best performance by passive deformation. Performing a fully coupled fluid-structure interaction analysis to account for wing passive torsion and bending will be in the Chapter 7 in the present research.

PART III: Bio-inspired Passive Flow Control for Renewable Turbine

Chapter 6: Bio-inspired Passive Flow Control for Vertical Axis

Turbine by Oscillating Flap and Passive Flexible Blade

6.1 Bio-inspired Passive Flow Control for VAT by Oscillating Flap

6.1.1 Introduction

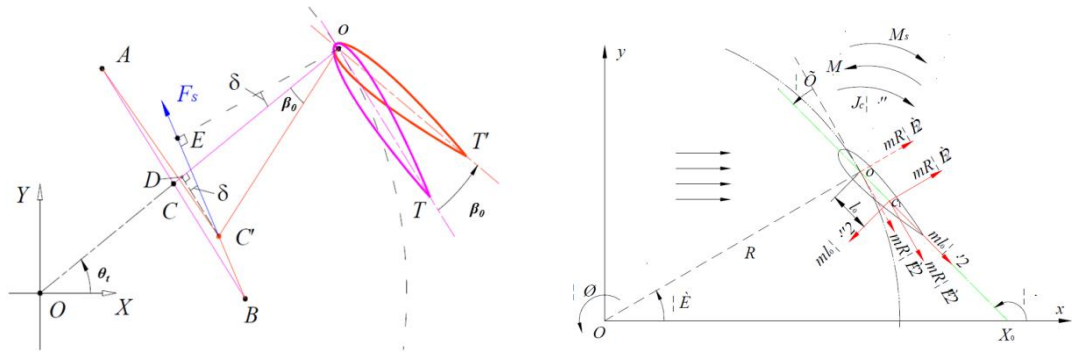
The wings of an insects and fins of a fish could be deformed passively in nature and there are many benefits of using a passive control system instead of an active control system in both nature and the industrial field. In Section 6.1, as a continuing study of Chapter 4, a numerical investigation is carried out with the main objective of exploring the potential for enhancing VAT energy extraction efficiency by using a passive oscillating flap blade.

6.1.2 Description of problem

The simulated turbine model is the same as in Chapter 4. All the basic turbine parameters and working conditions are shown in Table 4.1. Instead of the prescribed flap oscillating motion, a passive flap oscillating motion using the Spring Restoring Moment Theory adopted from Sun et al. (2009) and Sun (2007) is used for the oscillating flap in Section 6.1. This theory is first used for the passive control of the pitch angle for the turbine blade as shown in Fig. 2.7. In this study, this theory is used for the control of the flap motion. Based on the investigation and derivation from Sun et al. (2009) and Sun (2007), the following equation is used to define the spring restoring moment M_s :

$$M_s = K \cdot (l_1 - l \sin \beta_0) \cdot l \cos \beta_0, \quad (6.1)$$

where K is the stiffness of the spring, l_1 is the length of the spring slide bar (as shown in Fig. 6.1 (a) $l_1=AC=BC$), l is the length of the swing stem ($l=OC=OC'$ as shown in Fig. 6.1 (a)).



(a) Sketch of spring restoring moment principle

(b) Analysis of forces system on flap



(c) Sketch of vertical axis turbine blade with passive oscillation flap

Figure 6. 1 Sketches and principles for (a) and (b) spring controlled blade and spring restoring moment theory (Sun et al., 2009), (c) vertical axis turbine blade with passive oscillation flap.

The calculation of the spring restoring moment (M_s) is shown in the equations below and is based on Sun et al. (2009) and Sun (2007):

$$M_0 = (J_c + ml_o^2)\beta_0'' - mR\omega^2l_o \cos \beta_0 + M_s, \quad (6.2)$$

where M_0 is the moment of the flap generated by the fluid field, J_c is the moment of inertia of the flap, m is the mass of the flap, and l_o is the length from the rotational centre to the mass centre of the flap as shown in Fig. 6.1 (b).

By using the above equations, the flap could be passively oscillating during the turbine rotation as shown in Fig. 6.1 (c). The spring stiffness K is set as 1099.76 N/m, l_f is 0.0399 m and l is 0.018 m (Sun et al., 2009). A pair of angle limits is also set for the present study as 29.3° and -26.5° as suggested by Sun et al. (2009).

6.1.3 Results and discussions

6.1.3.1 Energy extraction performance of passive oscillating flap turbine

The investigation results for the time-averaged power coefficient against the tip speed ratio among the fixed flap turbine, the active oscillating flap turbine and the passive oscillating flap turbine are shown in Fig. 6.2. It can be seen that the c_{op} for the passive oscillating flap turbine is smaller than that of the active oscillating flap turbine and the fixed flap turbine when the tip speed ratio is smaller than 1.28. During the range between $\lambda=1.28$ and $\lambda=1.572$, the c_{op} for the passive oscillating flap turbine still increases with the λ and the value is smaller than the active flap turbine but larger than the fixed flap turbine. When the tip speed ratio is larger than 1.572, the c_{op} for the passive oscillating flap turbine drops slowly compared with the active and fixed flap turbine. The c_{op} value for the passive oscillating flap turbine is the largest among these three types of turbine in the large tip speed ratio region. These

results indicate that the passive oscillating flap turbine has a better energy extraction performance in the large tip speed ratio region than others.

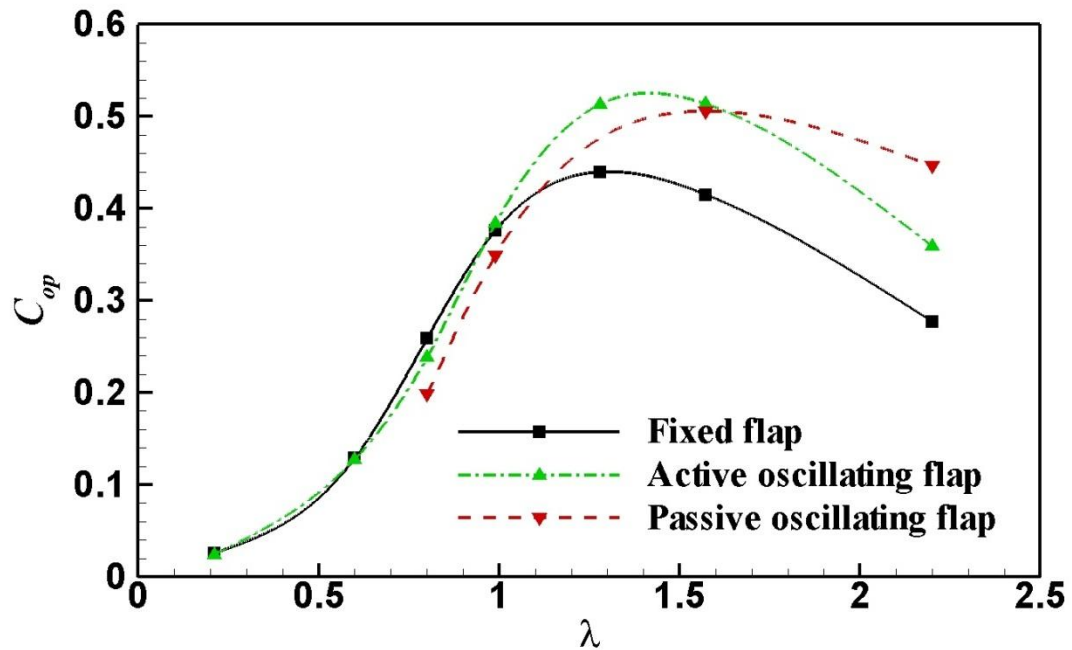


Figure 6. 2 Comparison of time-averaged power coefficient against tip speed ratio for fixed, active oscillating flap and passive oscillating flap turbine. For the active oscillating flap turbine, $\beta_0=15^\circ$ and $n_t=3$.

6.1.3.2 Flap oscillating characteristics of passive oscillating flap turbine

The positive direction of the flap angle β_0 is defined as the downward motion of trailing edge as shown in Fig. 4.1. The instantaneous flap angle variation for the passive flap oscillating turbine during one period is shown in Fig. 6.3 with a different tip speed ratio. The instantaneous flap angle variation for the active flap oscillating turbine with $\beta_0=15^\circ$, $n_t=3$ (the optimized condition as discussed in Chapter 4) and $\lambda=2.2$ is also included in Fig. 6.3 for reference. Generally, the flap angle variation with time for a passive flap is different than that of the active flap. The flap angle motion is not a sinusoidal function as prescribed in Chapter 4. For a passive flap, the

range and configuration of angle β_0 is also different with a different tip speed ratio. It is observed that the amplitude of angle β_0 has a negative correlation with the value of tip speed ratio λ . For $\lambda=0.8$ and $\lambda=0.99$, the amplitude of the passive flap approach to the angle limit during the period. When $\lambda=1.572$, the passive flap has a positive flap angle β_0 during $t/T_{turb}=0.8$ and $t/T_{turb}=0.9$ ($\theta_t=288^\circ$ to $\theta_t=324^\circ$). The passive flap has a negative flap angle β_0 during the entire period with the tip speed ratio $\lambda=2.2$. The flap angle β_0 for the passive flap reach to the maximum value in the negative direction at $t/T_{turb} = 0.6$ ($\theta_t=216^\circ$) and then reach to the maximum value in the positive direction at $t/T_{turb} = 0.85$ ($\theta_t=306^\circ$) suddenly for all the tip speed ratio conditions.

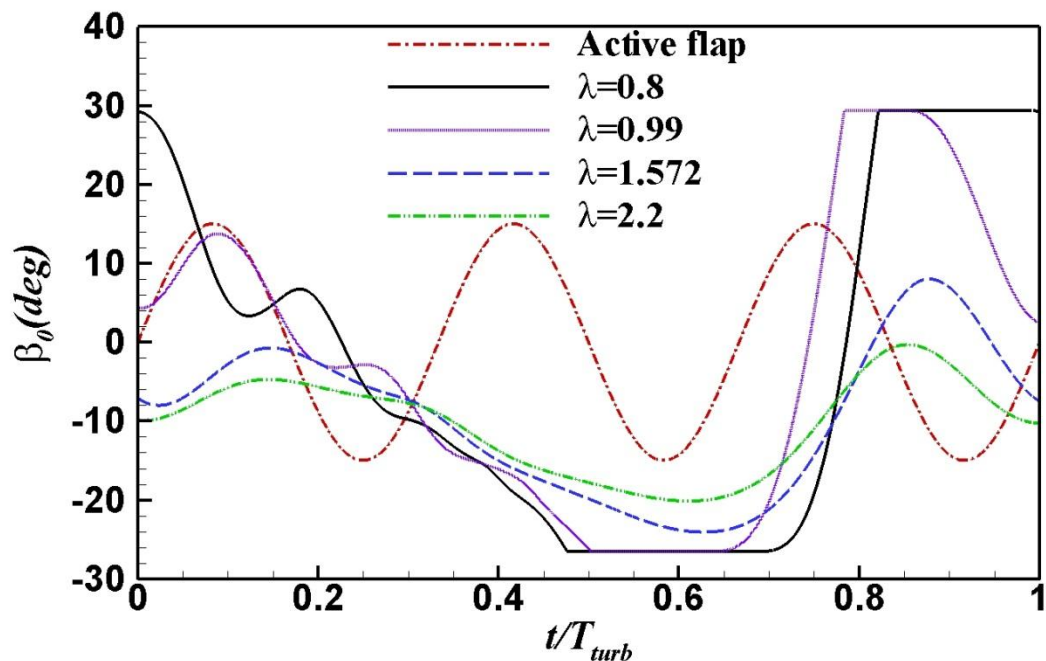


Figure 6. 3 Instantaneous active and passive flap angle during one period for tip speed ratio $\lambda=0.8, 0.99, 1.572$ and 2.2 . For active oscillating flap turbine, $\lambda=2.2$; $\beta_0=15^\circ$ and $n_t=3$.

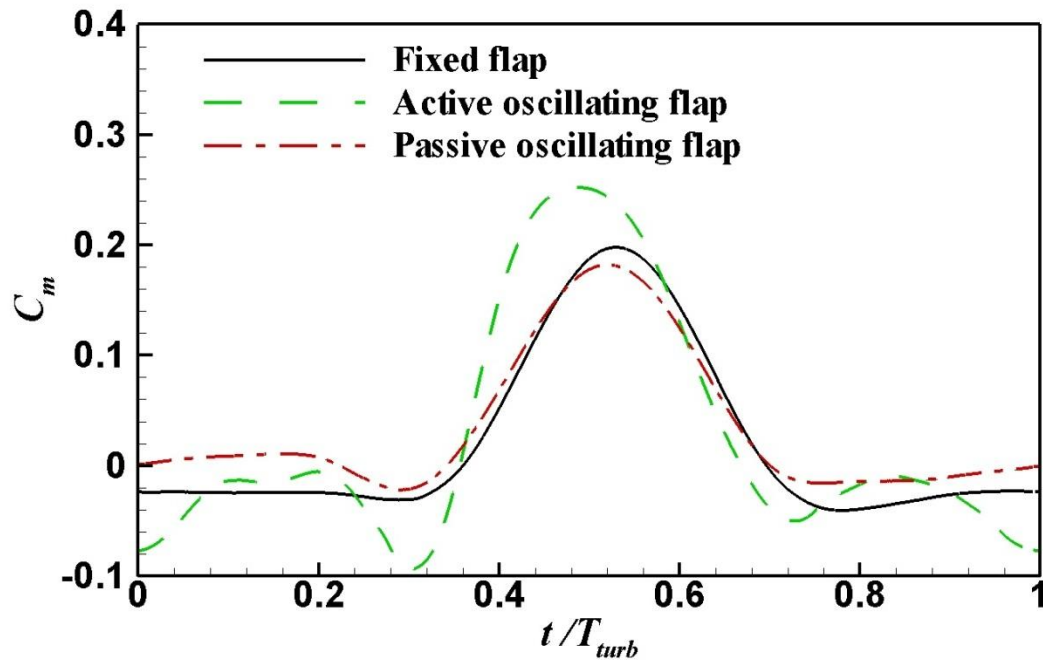


Figure 6. 4 Comparison of instantaneous blade moment coefficient against time for fixed, active oscillating flap and passive oscillating flap turbine with $\lambda=2.2$. For active oscillating flap turbine, $\beta_0=15^\circ$ and $n_r=3$.

6.1.3.3 Fluid field analysis for a passive oscillating flap turbine

The instantaneous moment coefficient plot among fixed, active and passive oscillating flaps with $\lambda=2.2$ is shown in Fig. 6.4. It can be seen that the peak value of c_m for a passive flap turbine blade is lower than that of a fixed and active flap turbine. The c_m for a fixed and active turbine blade is negative during $t/T_{turb}=0$ to $t/T_{turb}=0.3$ and $t/T_{turb}=0.7$ to $t/T_{turb}=1.0$. For the passive flap turbine blade, the moment coefficient c_m is positive during most of the above region except $t/T_{turb}=0.2$ to $t/T_{turb}=0.3$ and $t/T_{turb}=0.85$ to $t/T_{turb}=1.0$. As mentioned in Chapter 4, the vortex interaction between two rotating blades is an important effect which will influence the turbine's performance. As shown in Fig. 6.5, the vortex "thrown" effect is not remarkable for a passive flap turbine compared with the active one. However, the

fluid field region which is subject to large stress vortices is much less than the active one, i.e. the vortex stress for the passive flap blade is small. Thus, the effect of the vortex blade interaction could be reduced by replacing the active flap blade with the passive one at $\lambda=2.2$ under present working condition.

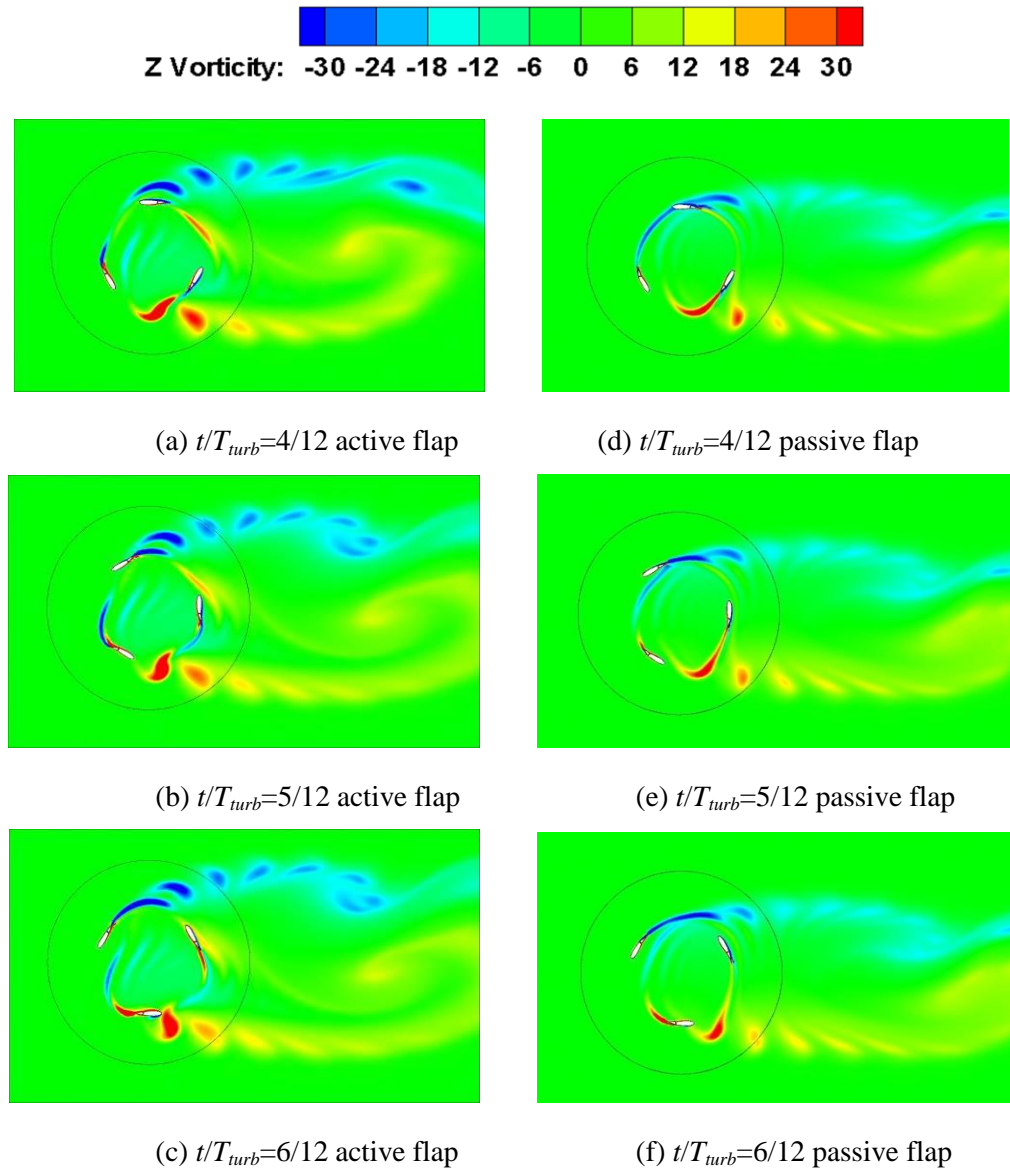


Figure 6. 5 Comparison of vortex contour within one revolution for active and passive oscillating flap turbines at $\lambda=2.2$. For active oscillating flap turbines, $\beta_0=15^\circ$ $n_t=3$ (a) $t/T_{turb}=4/12$ and active flap; (b) $t/T_{turb}=5/12$ and active flap; (c) $t/T_{turb}=6/12$ and active flap; (d) $t/T_{turb}=4/12$ and passive flap; (e) $t/T_{turb}=5/12$ and passive flap; (f) $t/T_{turb}=6/12$ and passive flap.

6.1.4 Summary of Section 6.1

In this study, a further investigation via the use of an oscillating flap to modify the traditional H-shaped VAT blade through the passive control method is proposed. By using a passive control flap, the energy extraction efficiency of the turbine at a high tip speed ratio is enhanced compared with the fixed and active controlled oscillating flap turbine. 4×10^6 CPU seconds calculated on ARCHIE-WeST high performance computing facilities of University of Strathclyde are needed for a typical case in this section. A complicated oscillating motion of the flap is also observed and the angle range has a negative correlation with the tip speed ratio of the turbine. After a fluid field analysis, the use of a passive controlled flap turbine could reduce the effect of the interaction between vortices and blades with a large tip speed ratio so that the negative torque region, as observed in fixed and active controlled flap blades, could be restrained and the energy extraction efficiency could be enhanced. A systematic investigation on the effect of the stiffness of the spring and the length of the spring slide bar need to be done in the future.

6.2 Investigation of VAT with Passive Flexible Blade

6.2.1 Introduction

In the present study, a three-dimensional vertical axis wind turbine with a flexible blade passively deformed in its span-wise direction has been numerically investigated. A realistic model of internal structures is used to obtain a certain degree of flexibility for the turbine blade. The main objective of the present study is to investigate the aerodynamic and structural behaviour of a VAWT with a flexible blade. The blade structural deflection associated with bending and twist is mainly

investigated in two flexibilities and strut locations. External fluid loads on the blade surface and the power performance of VAT are studied first, which is further extended to a blade stress analysis.

In the remainder of Section 6.2, the problem formulations are listed in Section 6.2.2. Section 6.2.3 first investigates the structural characteristics of the flexible turbine blade in Section 6.2.3.1, while the external loads on the flexible blade are studied in Section 6.2.3.2. The present study is further extended to a more flexible blade and the results are presented in Section 6.2.3.3. The impact of a different strut location on the flexible blade is examined in Section 6.2.3.4, which is followed by an analysis of the energy extraction performance of a flexible designed VAT in Section 6.2.3.5. Finally, a summary of this study is given in Section 6.2.4.

6.2.2 Description of problem

The present study considers a three-dimensional Darrieus type straight blade VAT with an NACA0012 cross-section blade and a passive bending and twist deflection in the blade spanwise direction. The pitch angle of the turbine blade is fixed as zero. A realistic internal structure is adopted from Heathcote et al. (2008), Chimakurthi et al. (2009) and Gordnier et al. (2010) to achieve the blade passive deformation. The chord radius ratio (\bar{c}) is 0.125 for the modelled turbine. The turbine, with a certain rotational speed, is immersed in air flow with a uniform speed of U . The Reynolds number based on the blade chord length is 10^5 . The Darrieus type straight blade VAT modelled by Hameed and Afaq (2013), shown in Fig. 6.6 (a) consists of one shaft, three blades and six radial arms. The radial arms connect the shaft at one end and the inner side of the turbine blade at the other end. In order to simplify the physical

model, only one blade is modelled in the present study. The aerodynamic impact from the shaft and radial arms is neglected, as shown in Fig. 6.6 (b). This study mainly focuses on the analysis of the structural characteristics of the flexible blade as well as the unsteady loads applied to the blade, which may cause the blade's structural deformation.



(a) Darrieus type straight blade VAT model in Hameed and Afaq (2013)

(b) VAT model in the present simulation

Figure 6. 6 3D VAT model for (a) Hameed and Afaq (2013) and (b) in the present simulation.

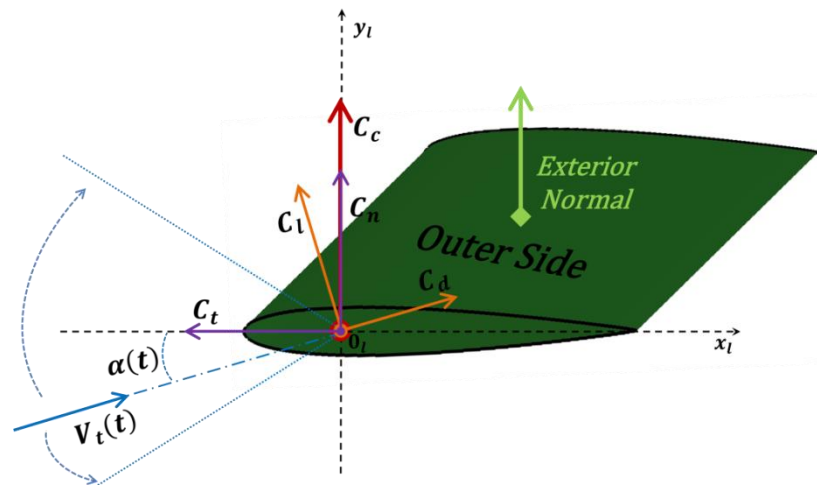


Figure 6. 7 Sketch of turbine blade forces, resultant velocity and angle of attack under local body fitted coordinate x_l, y_l .

6.2.2.1 Kinematics for a vertical axis turbine

As shown in Fig. 6.6 (b), the turbine is rotating with an angular velocity ω in the incoming flow. As mentioned in Section 1.2.1, the present study focus on the steady

state of the turbine. Thus, the angular velocity ω is independent of time but varies under different tip speed ratios.

In the present study, λ is changed in the range of 2.50-7.50 by varying the turbine rotational speed. Fig. 6.7 shows the blade local body fitted coordinate $x_l O_l y_l$ and the force applied to the blade, the resultant velocity and the angle of attack of the blade. The origin of this local coordinate is fixed to the blade centre line and $\frac{1}{4}$ of chord length from the leading edge. The body fitted coordinate is attached to the turbine blade with rotating motions under the global coordinate. At $t/T_{turb}=0$, the direction of the incoming flow velocity is the same as the positive y_l axis under the body fitted coordinate. The magnitude of blade instantaneous resultant fluid velocity $V_l(t)$ and its direction (i.e. the blade instantaneous angle of attack $\alpha(t)$) both vary with time as a sinusoidal function as shown in Fig. 1.6 (b) and as discussed in Section 1.2.3. The total fluid forces could be decomposed as the drag force and lift force or the thrust force and normal force relative to instantaneous velocity or body fitted coordinate, respectively. Since the local coordinate is a non-inertia reference frame, it encounters an inertia force which is the centrifugal force in the present case. The non-dimensionalized centrifugal force is defined as:

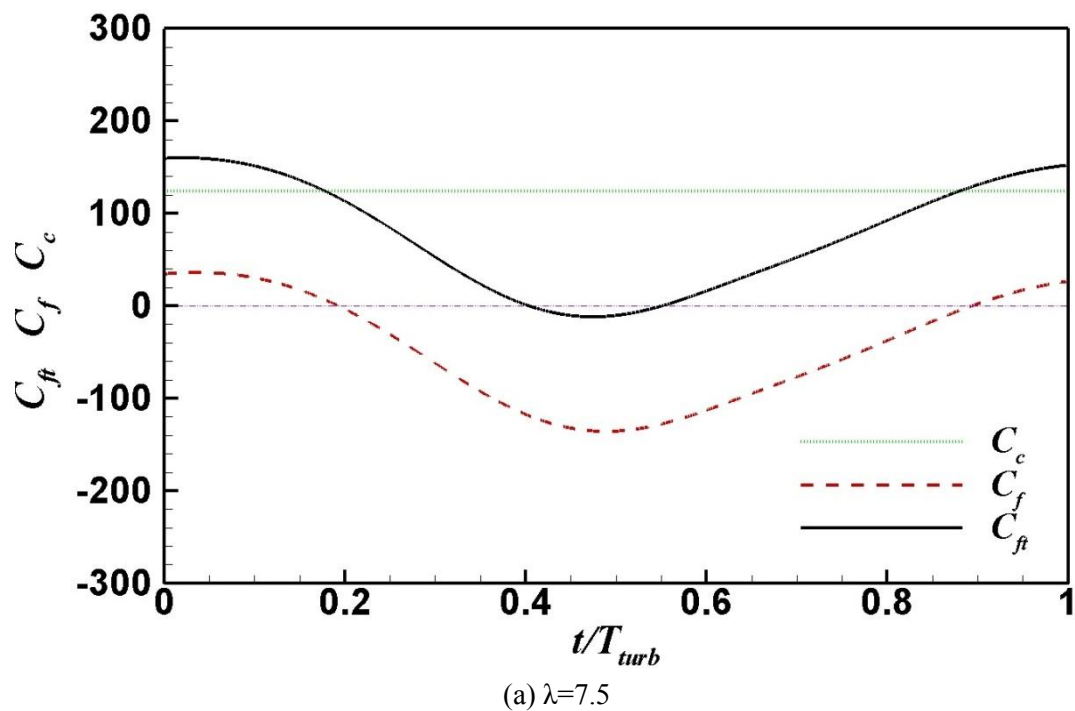
$$c_c = \frac{F_c}{\frac{1}{2} \rho_f U^2 c H}, \quad (6.3)$$

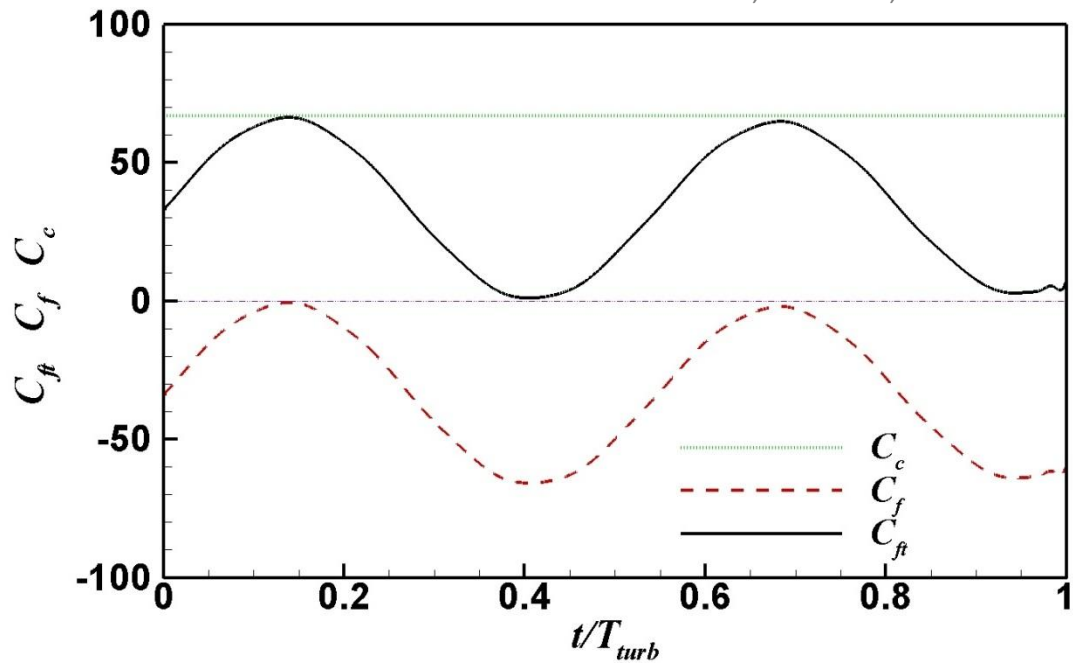
where F_c is the centrifugal force of the turbine blade, ρ_f is the density of the fluid, c is the chord length of the blade and H is the span length of the blade. The detailed comparison of the centrifugal force and fluid force is listed in Table 6.1. Examples of the comparison between the centrifugal force coefficient c_c , the total fluid force coefficient c_f and the total force coefficient c_{ft} , which take both fluid force and

centrifugal force into account during one turbine rotating cycle, can be found in Fig. 6.8 (the magnitude of the centrifugal forces is also depend on the blade material, such as density, etc.).

6.2.2.2 Structural design of turbine blade

The present study adopts the same concepts based on a study of the flexible effect on the propulsion performance of a flapping wing from Heathcote et al. (2008), Gordnier et al. (2010) and Chimakurthi et al. (2009), and further applies this flexible structure in the vertical axis wind turbine. The cross-section of the blade is displayed in Fig. 6.9 (a). The flexible blade is constructed by polydimethylsiloxane (PDMS) rubber outside to form the NACA0012 shape with a metal stiffener located inside. Aluminium is selected as the material of the metal stiffener. Based on Chimakurthi et al. (2009), only metal stiffener is considered in the structural dynamic analysis and the structural dynamic characteristics of the PDMS rubber are neglected in the present study (Liu et al., In Press).





(b) $\lambda=5.5$

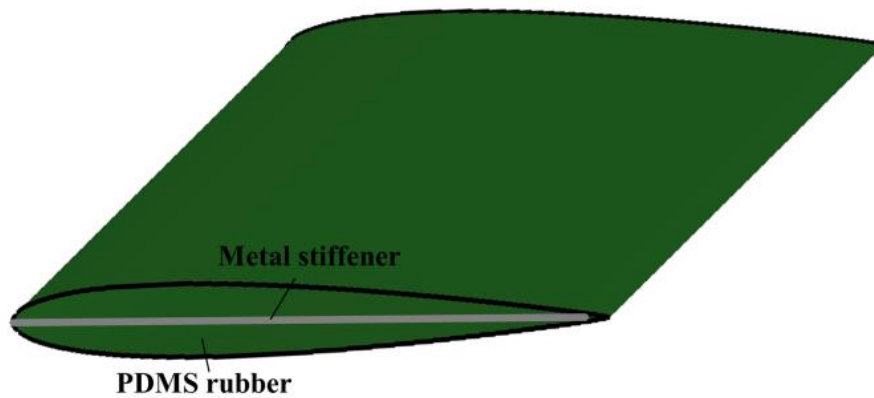
Figure 6. 8 Examples of comparison between blade total force coefficient and blade centrifugal force coefficient with $l_{st}/c=10/3$, $\Pi=3.19 \times 10^3$.

Fig. 6.9 (b) shows the main blade parameters with different strut locations. The span length H of the turbine blade is ten times blade chord length c . The parameter l_{st} is defined as the length from the strut location to its nearest blade tip. In the present study, two different l_{st} , i.e. $10c/3$ and 0 , are studied. For $l_{st}=10c/3$, three different regions, i.e. region a, region b and region c which are separated by two struts are shown in Fig. 6.9 (b).

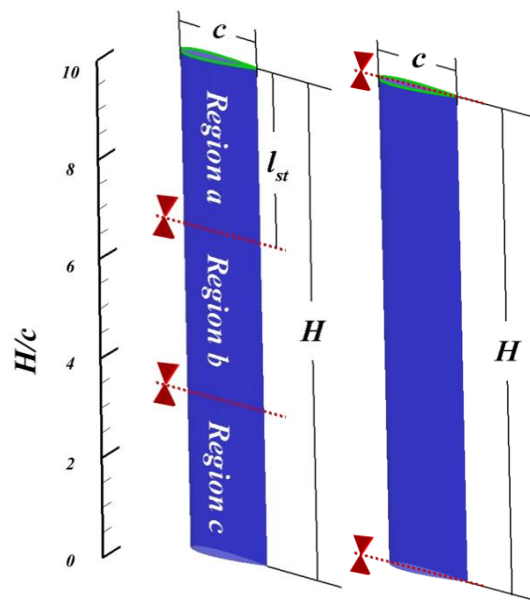
It notes that the stiffness of the structure is often characterized by the effective stiffness Π (Shyy et al., 2010). This parameter describes the elastic bending forces relative to the fluid dynamic forces as:

$$\Pi = \frac{ET_{sf}^3}{12(1 - \nu^2)\rho_f U^2 c^3} \quad (6.4)$$

where ν is the Poisson ratio of the stiffener and c is the chord length of the foil. The effective stiffness Π is widely tested by the experiments of Heathcote and Gursul (2007) and Heathcote et al. (2008) and numerical simulations from Chimakurthi et al. (2009) and Gordnier et al. (2013).



(a) VAT blade inner structure (adopted from Heathcote et al., 2008)



(b) Different strut locations of VAT blade. $l_{st}/c=10/3$ (left); $l_{st}/c=0$ (right)

Figure 6. 9 VAT blade design for the present simulation.

Table 6. 1 Past relevant research on flexible blade and the parameters used in the present research.

Data source	Device type	Π	Max. c_f	c_c	Max. D_{is}/c_{eff}
Heathcote et al. (2008) and Shyy et al. (2010)	Plunging foil (spanwise flexibility)	2.14×10^2	4.76×10^0	-	1.23×10^{-1}
Butbul et al. (2015)	Vertical axis turbine (chordwise flexibility)	3.18×10^0	3.53×10^0	7.10×10^0	1.71×10^{-1}
Hameed and Afaq (2013)	Vertical axis turbine (spanwise flexibility)	2.81×10^5	8.55×10^1	4.31×10^2	3.58×10^{-2}
The present research	Vertical axis turbine (spanwise flexibility)	3.19×10^3	1.42×10^2	1.24×10^2	1.53×10^0

In the studies of Heathcote et al. (2008) and Shyy et al. (2010), Π is selected around 10^2 for their flexible wing under propulsion conditions. This value of Π allowed their wing to reach a maximum non-dimensionalized displacement D_{is}/c as 1.23×10^{-1} . However, it is necessary to recall that the blades of VAT have an extra inertia centrifugal force because of the rotating motion around the centre shaft. Moreover, the total fluid force coefficient acting on the VAT blade is around 10^2 which is much larger than that of the propulsion flexible wing. Thus, adopting the same magnitude of Π as in the study of Heather et al. (2008) may lead to an unacceptable large blade

displacement for a VAT. In the study of Butbul et al. (2015), a chordwise flexible blade is considered which is different to the design of a spanwise flexible blade as discussed in Shyy et al. (2010). In addition, the turbine they studied was small in scale (as can be seen in Table 6.1, i.e. that both the maximum c_f and c_c are no more than 10^1). Thus, the II selected by Butbul et al. (2015) may not be suitable for the present study. In the study of Hameed and Afaq (2013) for the bending motion of a blade of VAT, a much stiffer blade is investigated with II of 10^5 , which caused a relatively small D_{is}/c of 3.58×10^{-2} . In the present study, in order to observe a distinct influence by the flexible VAT blade, an effective stiffness (II) is chosen around 10^3 , as shown in Table 6.1. The maximum non-dimensionalized displacement D_{is}/c under $II=3.19 \times 10^3$ and $\lambda=5.5$ (i.e. the turbine reaches its maximum energy extraction condition) is 7.26×10^{-1} , which is in the same order as that studied by Heathcote et al. (2008) and Shyy et al. (2010). The maximum D_{is}/c could approach 1.53×10^0 with $II=3.19 \times 10^3$ and $\lambda=7.5$ as depicted in Table 6.1. A smaller effective stiffness $II=9.37 \times 10^2$ is also investigated in the present research.

Apart from the coupled fluid structure interaction modelling, the flexible blade stress calculation using the commercial software ANSYS is also performed. This is used to estimate the maximum displacement and stress distribution when the maximum fluid load is applied to the blade. The results are compared with those obtained from the in-house code as a part of the CFD verification and are summarised in Table 6.3. A diagrammatic sketch of fluid loads and structural constraints in each cell using the ANSYS solver is shown in Fig. 3.24. As it is seen, uniformly distributed external loads are applied to each structural cell with red arrows. Different constrains which represent the strut locations are indicated as cyan arrows. Hameed and Afaq (2013)

tested the effect of the element type on the prediction of maximum stress and deflection of a vertical axis turbine blade. They found that “*The solid45 element type can approximate the large distortion in the shape of the blade*” (Hameed and Afaq, 2013). As this study adopt a similar turbine blade model and strut locations to that of Hameed and Afaq’s work, SOLID45 element is selected for present Finite Element Analysis.

In order to compare the stress among different types of marine devices, non-dimensionalized stress c_{st} is used and is defined as follows:

$$c_{st} = \frac{\sigma}{\frac{1}{2}\rho_f U^2}. \quad (6.5)$$

6.2.3 Results and discussions

As stated in Section 6.2.1, the investigation was started on a flexible blade of an effective stiffness $II=3.19\times 10^3$ and strut location $l_{st}/c=10/3$. The predicted blade structural characteristics (blade deformation and structure stress) and external loads are examined and compared with a rigid blade in Sections 6.2.3.1 and 6.2.3.2. Sections 6.2.3.3, 6.2.3.4 and 6.2.3.5 are the flexibility effect, strut effect and energy extraction performance of the turbine, respectively. A summary of relevant cases is listed in Table 6.2. For a rigid blade, it is assumed to have an infinitely large stiffness. To carry out an FSI study, the modal analysis method is used. The first ten natural vibrational modes are applied to estimate the blade deflections. The first four mode shapes and their frequency ratios for $l_{st}/c=10/3$ and $II=3.19\times 10^3$ are shown in Fig. 6.10 as an example. These four modes are identified as the first bending mode for regions a and c ($1/T_{m1}$), the second bending mode for regions a and c ($1/T_{m7}$), the

first torsion mode for regions a and c ($1/T_{m3}$) and the first bending mode for region b ($1/T_{m2}$) (see Fig. 6.9 (b) for the definitions of regions a to c). The generalized displacement q_j (as indicated in Eq. 3.18 in Section 3.3.2) variation for the first ten modes at $\lambda=5.5$ during one revolution is shown in Fig. 6.11. Clearly seen in this figure is that the first mode plays a leading role in the blade structural deformation behaviour.

Table 6. 2 Case summary for present simulation.

Case group	Π	l_{st}/c	λ
Rigid	∞	-	3.50-7.50
Flexible blade with middle strut	3.19×10^3	$10/3$	3.50-7.50
High flexibility blade with middle strut	9.37×10^2	$10/3$	3.50-7.50
Flexible blade with tip strut	3.19×10^3	0	3.50-7.50

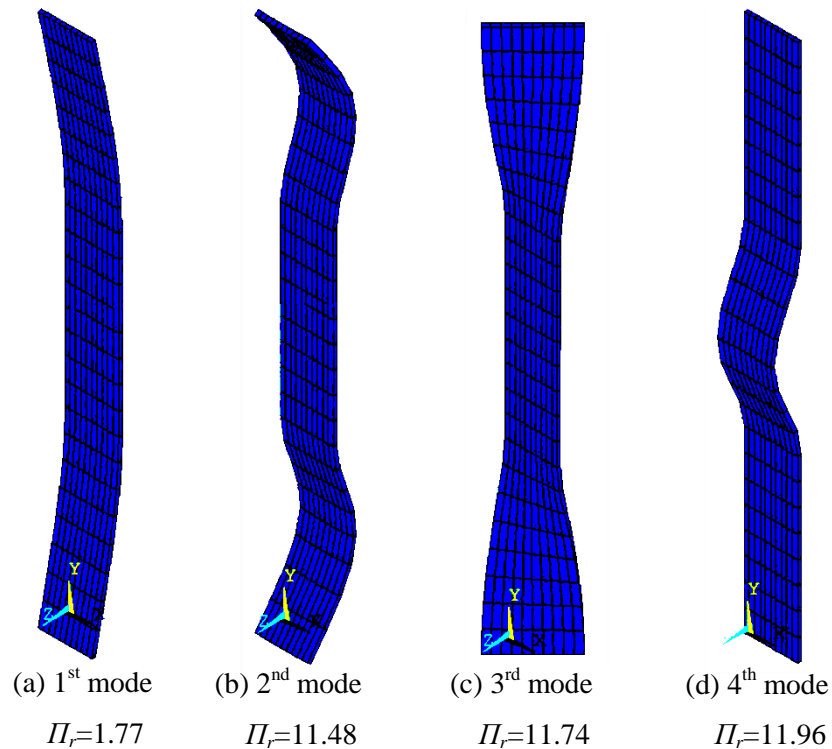


Figure 6. 10 First four mode shapes with $l_{st}/c=10/3$, $\Pi=3.19 \times 10^3$.

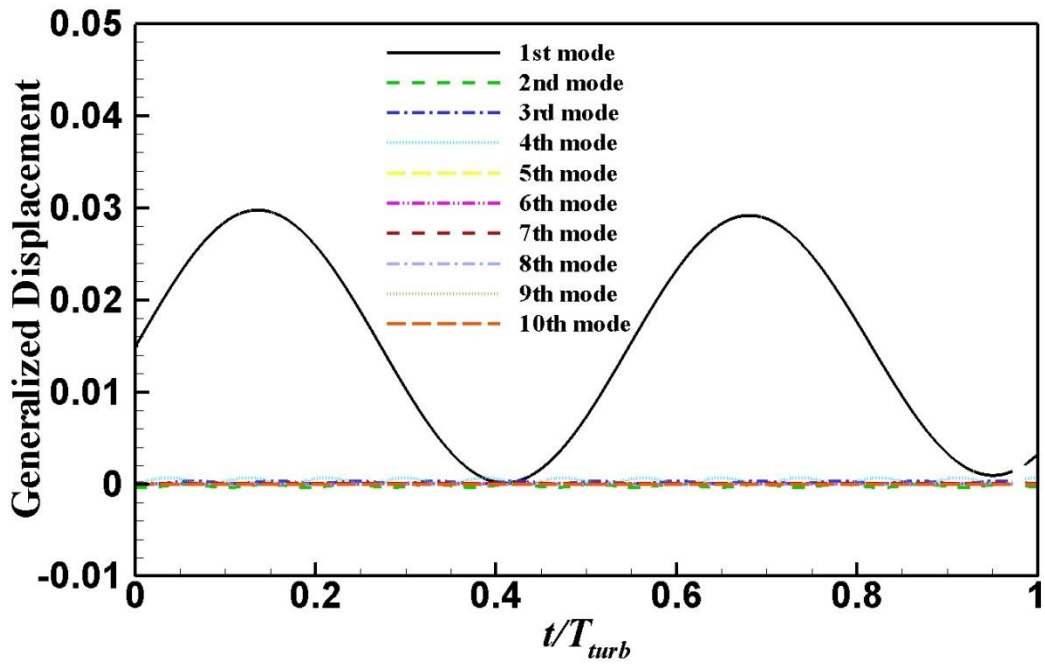


Figure 6.11 Time histories of the generalized displacements of the first ten modes with $l_{st}/c=10/3$, $\Pi=3.19 \times 10^3$ and $\lambda=5.5$.

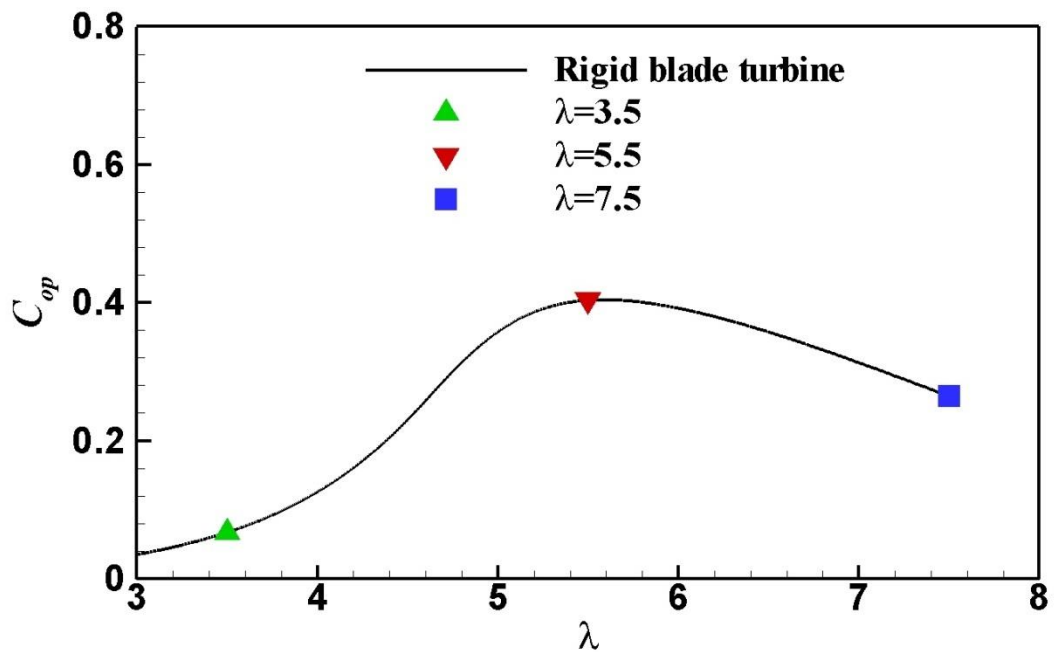


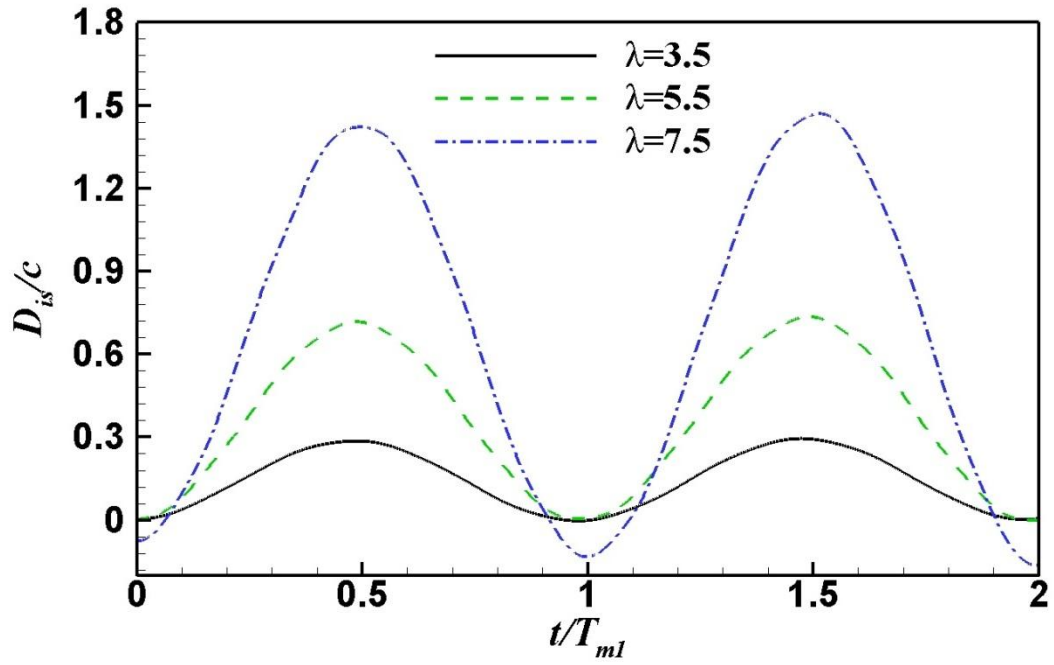
Figure 6.12 Power coefficient vs. tip speed ratio for rigid blade turbine and c_{op} value for $\lambda=3.5$, 5.5 and 7.5 .

6.2.3.1. Structure characteristics

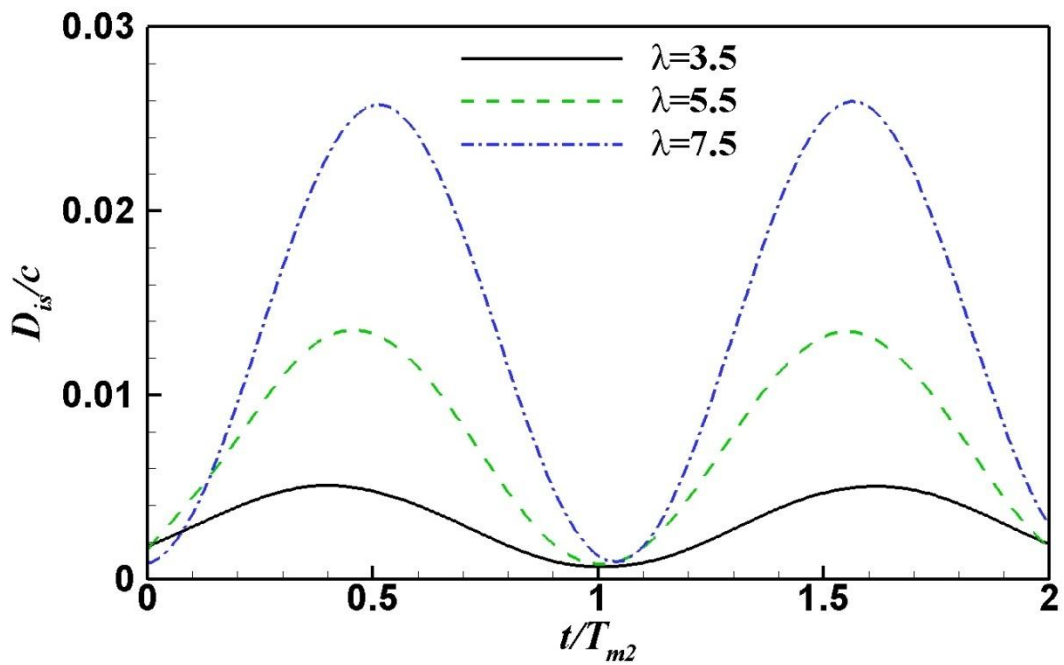
In this section, the study is focus on three typical tip speed ratios, i.e. $\lambda=3.5$, 5.5 and 7.5. They are selected to represent three statuses for power coefficient c_{op} vs. λ , i.e. climbing up ($\lambda=3.5$), peak c_{op} ($\lambda=5.5$) and drop down ($\lambda=7.5$), as indicated in Fig. 6.12.

Fig. 6.13 shows the instantaneous non-dimensionalized bending displacement D_{is}/c for different tip speed ratios λ with $l_{st}/c=10/3$ and $\Pi=3.19\times 10^3$ at the blade tip ($H/c=0$) and centre (i.e. $H/c=5$). Two time periods are used to non-dimensionalize the time, i.e. the turbine revolution period (T_{turb}) for Fig. 6.13 (c) and (d) and the 1st mode shape period of regions a (or region c) and b (T_{m1} and T_{m2}) for Fig. 6.13 (a) and (b). The positive direction of the displacement D_{is}/c is aligned with the positive y_l axis at the local body fitted coordinate (see Fig. 6.7). Based on these results, it is obvious that the flexible blade deforms periodically with one dominant frequency under various tip speed ratios λ and at different H/c . Given a large λ condition, the blade displacement gets larger because of the increased centrifugal force at a high rotating speed. In addition, the flexible blade always shows a larger deformation at the tip ($H/c=0$) than at its centre ($H/c=5$) for this middle strut support (see Figure 6.9 (b)). For example, at $\lambda=5.5$, the displacement of the blade tip is 7.26×10^{-1} which is 55.85 times larger than that at the blade centre. A further examination of these plots shows that all deformations display a positive magnitude, pointing to the positive y_l . Thus, it is inferred that the flexible deformation is mainly induced by the large magnitude of centrifugal force (c_c) rather than the fluid forces, as shown in Fig. 6.8 (b). A careful look at Figs. 6.13 (a) and (b), where the time history of deformation is represented against the instantaneous time relative to the 1st bending mode period of regions a

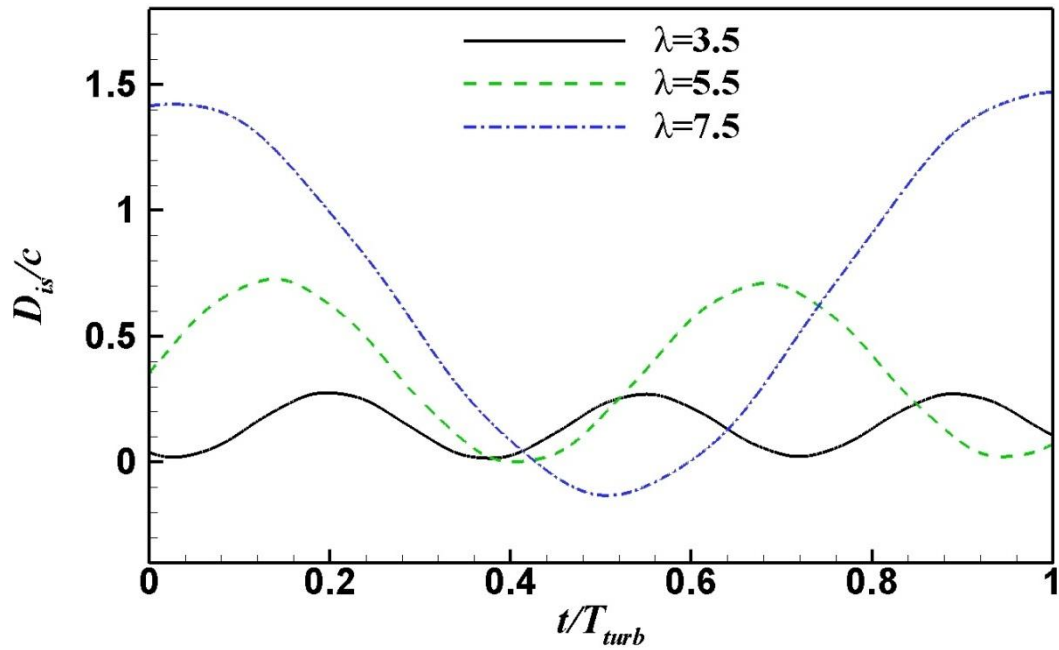
($\Pi_r=1.77$) and b ($\Pi_r=11.96$) indicates that the structural deformation frequency matches the system natural frequency exactly.



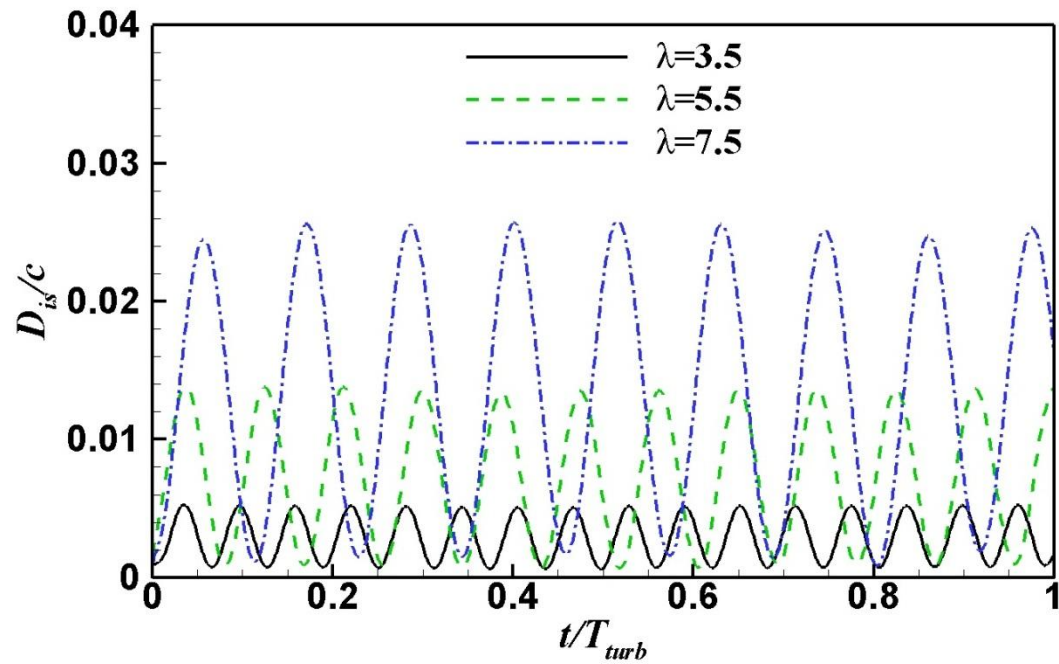
(a) $H/c=0$



(b) $H/c=5$

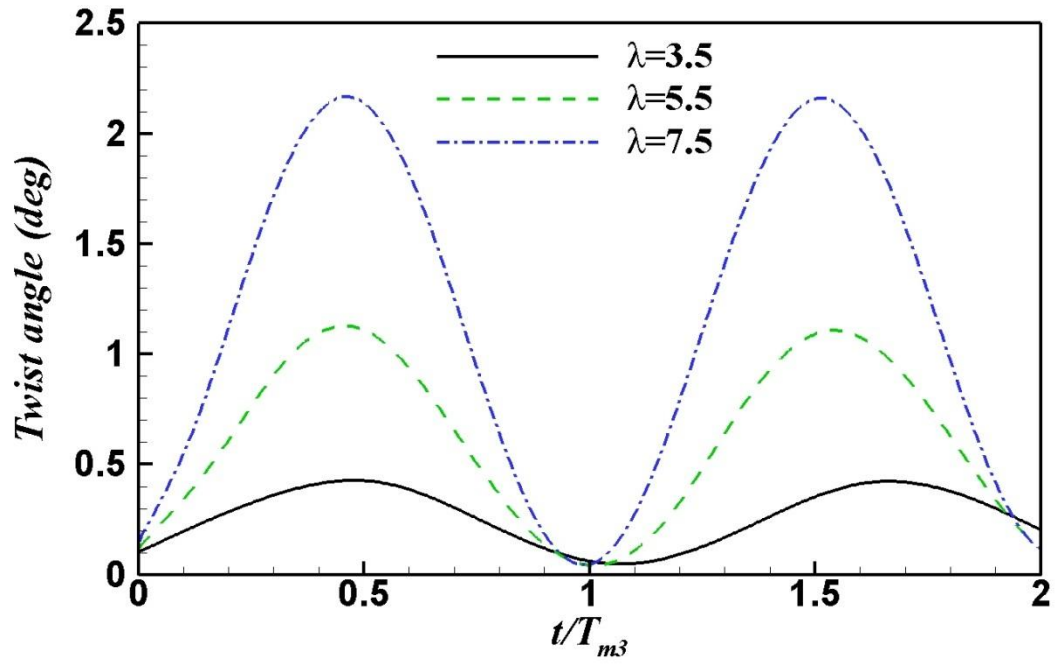


(c) $H/c=0$

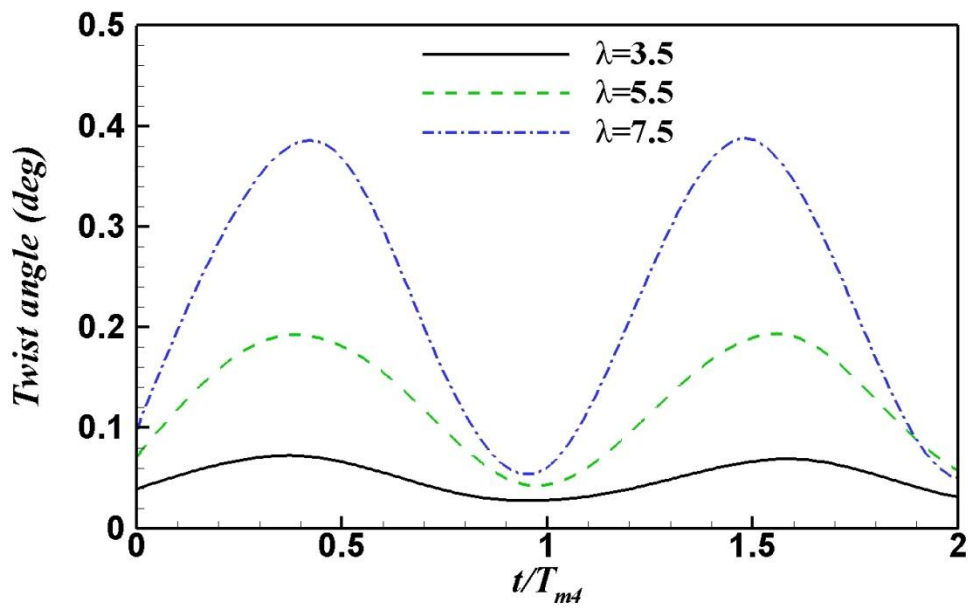


(d) $H/c=5$

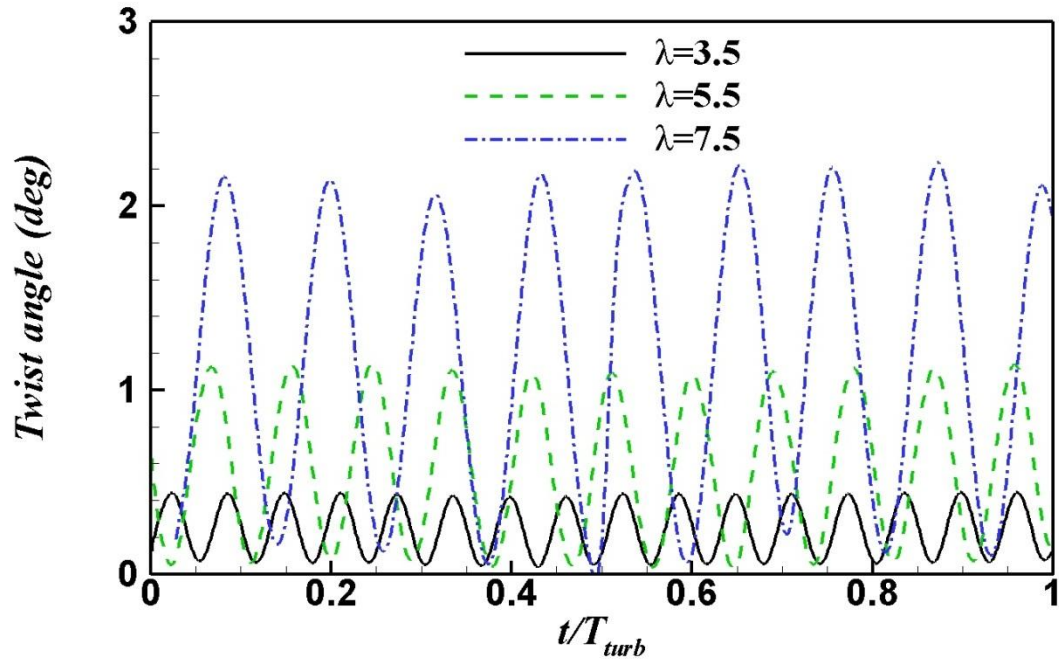
Figure 6. 13 Instantaneous non-dimensionalized displacement at (a) and (c) $H/c=0$ and (b) and (d) $H/c=5$ for different tip speed ratios with $l_{st}/c=10/3$, $\Pi=3.19 \times 10^3$. (a) and (b) time is non-dimensionalized by blade mode cycles and (c) and (d) time is non-dimensionalized by turbine revolution.



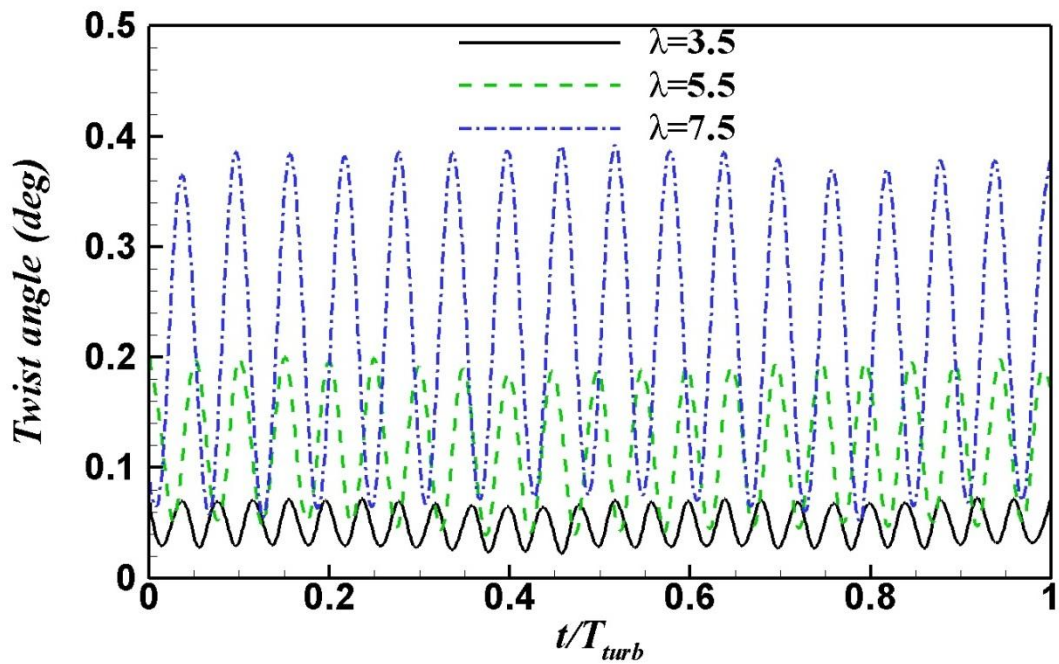
(a) $H/c=0$



(b) $H/c=5$



(c) $H/c=0$



(d) $H/c=5$

Figure 6. 14 Instantaneous twist angle at (a) $H/c=0$ and (b) $H/c=5$ for different tip speed ratios with $l_{st}/c=10/3$, $\Pi=3.19 \times 10^3$. (a) and (b) time is non-dimensionalized by blade mode cycles and (c) and (d) time is non-dimensionalized by turbine revolution.

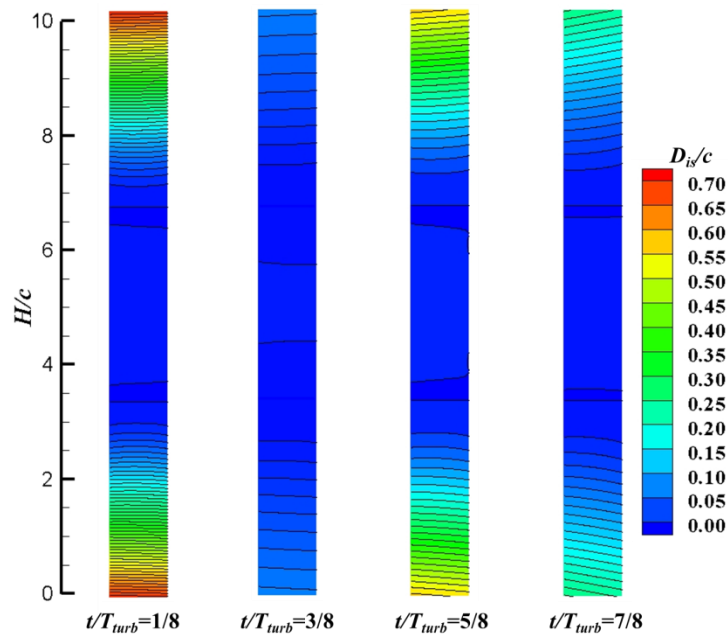


Figure 6. 15 Non-dimensionalized bending and twist displacement contour with $l_{st}/c=10/3$, $\Pi=3.19\times 10^3$ and $\lambda=5.5$ viewing from the inner side of the blade.

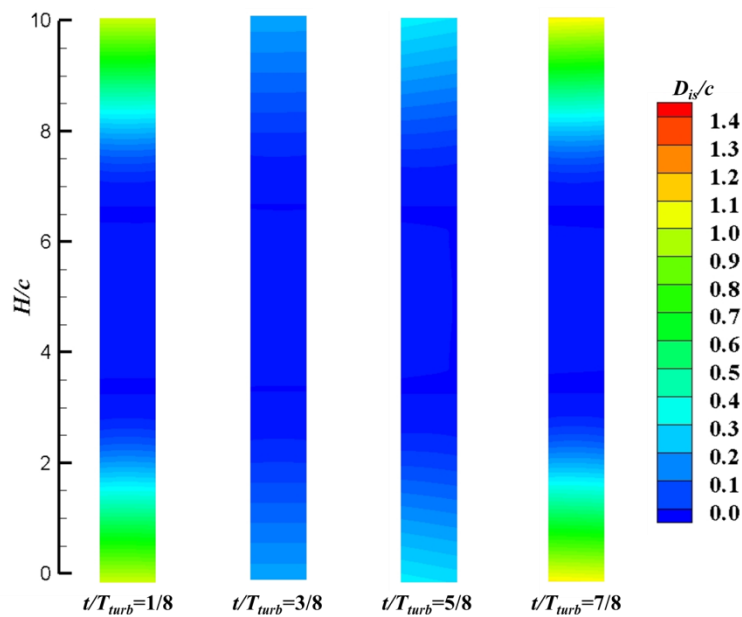


Figure 6. 16 Non-dimensionalized bending and twist displacement contour with $l_{st}/c=10/3$, $\Pi=3.19\times 10^3$ and $\lambda=7.5$ viewing from the inner side of the blade.

Fig. 6.14 (a) - (d) plots the instantaneous blade twist angle at the tip and the centre of the blade for different tip speed ratios λ . The blade twist angle is defined as the nose up positive. A similar behaviour as the bending effect discussed above is observed.

In fact the twist angles tend to behave like a sinusoidal motion under different λ and H/c conditions with positive values. The increase in the tip speed ratio results in an increase in the twist angle at both the blade tip and centre. The maximum twist angle in the blade tip is no more than 2.23° , while in the blade centre it is less than 0.40° . The mechanism associated with twist motion will be discussed in Sec. 6.2.3.2.

To further analyse the structural deformation along the blade span-wise direction, Fig. 6.15 plots the bending and twist displacement contour under $l_{st}/c=10/3$, $\Pi=3.19\times 10^3$ and $\lambda=5.5$ conditions at four different time instants during one cycle. It is apparent that the large bending occurs near the vicinity of the blade free ends, i.e. in H/c between 0 and 0.5 and in H/c between 9.5 and 10. Because of the support of two struts, the central part of region b has the minimum deformation compared to regions a and c. This trend is observed during the whole cycle. The twist behaviour could also be observed at time instant $t/T_{turb}=7/8$ at regions a, b and c in Fig. 6.15, (as indicated by the inclined contour lines). An increase in the tip speed ratio leads to increased deformation as shown in Fig. 6.16 for $\lambda=7.5$ due to centrifugal force.

In order to further analyse the flexible blade structural stress, the ANSYS structural solver is adopted (as mentioned in Section 3.4 and Section 6.2.2.2) to estimate the deflections and stresses under the extreme condition, where the flexible blade endures the maximum external loads. The results are summarised in Table 6.3 along with the data from Hameed and Afaq (2013). By comparing the results obtained using various methods, it is observed that the prediction of maximum displacement from the ANSYS solver has a slight discrepancy from the results estimated by the present in-house code. One possible explanation may be due to the simplified models

that are used in ANSYS structural solver, such as a uniformly distributed load applied to the blade without taking twist motion into account which will lead to a less deformation of the blade. The general trend of maximum displacement and stress variation with the tip speed ratio is consistent, i.e. both increase with the growth of λ . The stress distribution contours from the ANSYS solver at $\lambda=5.5$ and $\lambda=7.5$ are plotted in Fig. 6.17. It is clearly shown that regions a and c endure more stress than region b. The maximum stress appears near the strut location.

Table 6. 3 Comparison of the maximum displacement ratio and stress coefficient.

Data source	Case type			Max. D_{is}/c		Max. c_{st}
	l_{st}/c	Π	λ	In-house FSI solver	ANSYS	ANSYS
Hameed and Afaq (2013)	0.217	2.81×10^5	4.1	-	3.85×10^{-2}	2.87×10^6
The present research	10/3	3.19×10^3	5.5	7.26×10^{-1}	6.63×10^{-1}	1.48×10^6
			6.5	1.15×10^0	9.77×10^{-1}	2.18×10^6
			7.5	1.53×10^0	1.33×10^0	2.96×10^6
		9.37×10^2	5.5	1.76×10^0	1.74×10^0	2.57×10^6
	0	3.19×10^3	5.5	6.17×10^{-1}	6.20×10^{-1}	1.30×10^6

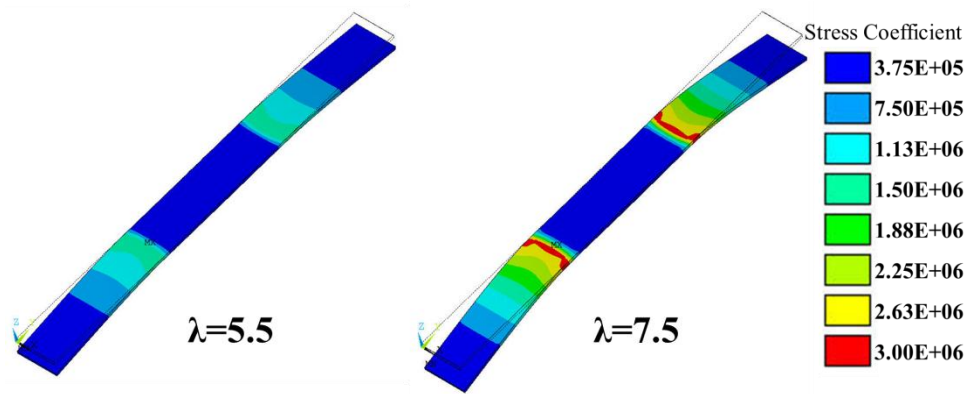


Figure 6.17 Contour of stress distribution over the blade under the largest external load condition for the flexible blade for different tip speed ratios with $l_{st}/c=10/3$ and $\Gamma=3.19 \times 10^3$ viewing from the inner side of the blade.

6.2.3.2 Fluid force and centrifugal force of turbine blade

In order to explain the structure characteristics observed in Section 6.2.3.1, an analysis of the fluid loads on the turbine blade is carried out in this section. Fig. 6.8 shows the time history of the forces applied to the blade during one cycle at two tip speed ratios, i.e. $\lambda=5.5$ and $\lambda=7.5$. As discussed in Section 6.2.2.1, the external loads acting on the blade (F_{ft}) can be decomposed into the centrifugal force (F_c) and fluid load (F_f), which can be non-dimensionalized and represented by the centrifugal force coefficient (c_c) and the fluid force coefficient (c_f), respectively. The dynamic displacement of the blade motion (bending or twist) is dictated by this net/resultant force ($c_{ft}=c_c+c_f$). During one revolution, apparently, the centrifugal force (c_c) does not change its magnitude and always points in the blade external normal direction (see Fig. 6.7). However, the fluid force (c_f), which mainly comes from the net pressure force acting on the blade, varies dramatically in its direction and magnitude within one cycle, as clearly depicted in Figs. 6.8 (a) and (b). In addition, the variation trend of c_f against time is also tip speed ratio dependent. Under various flow and structure conditions studied herein, it was found that the centrifugal force coefficient

(c_c) is always larger than the fluid force coefficient (c_f) at present working condition. At some time intervals within one cycle, they may point in the same direction (exterior normal), while at other intervals, they have opposite directions. With this in mind, it is obvious that the blade bending direction has always been outwards as displayed in Figs. 6.13 and 6.18. The dynamic behaviour of deflection is mainly determined by the fluid loads (c_f) or net pressure which will be discussed shortly.

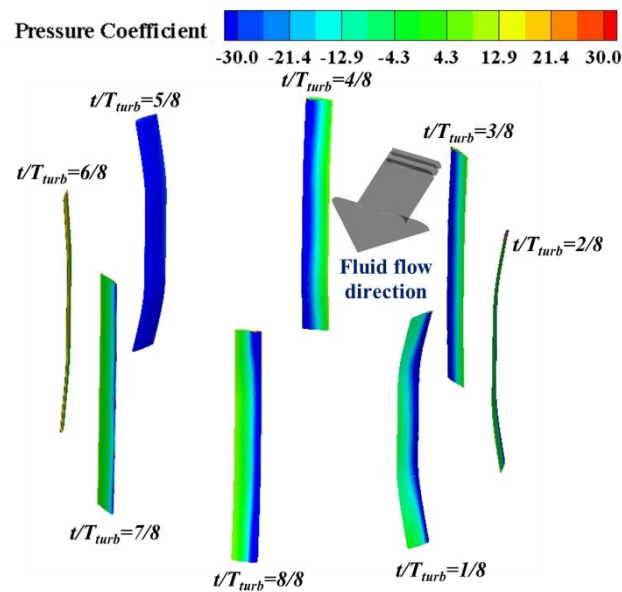
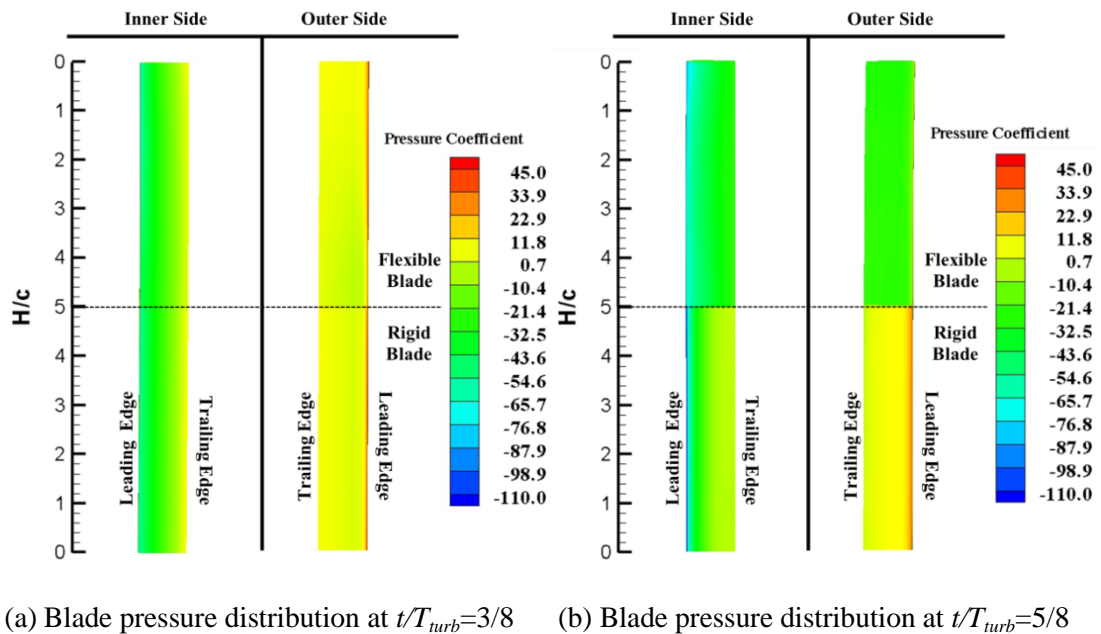
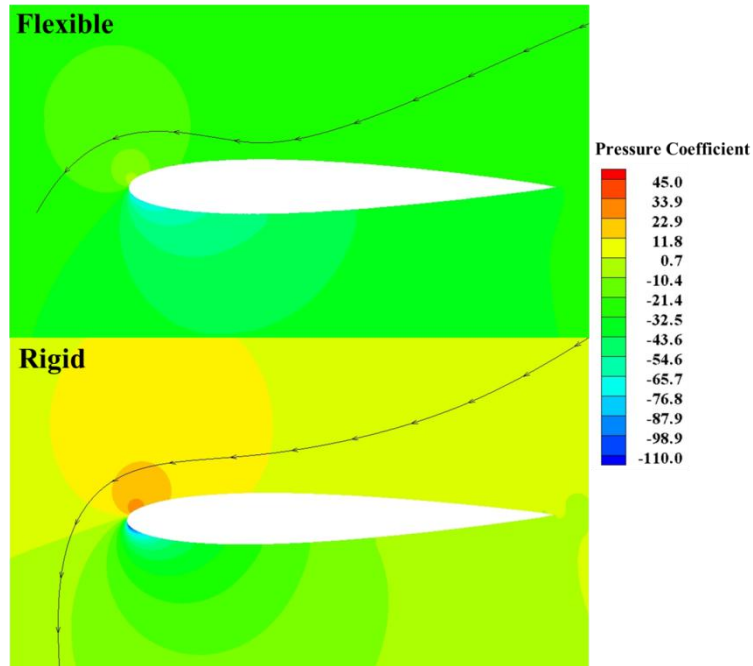


Figure 6. 18 Blade bending-twist motion and pressure distribution for different time instants with $l_{sp}/c=10/3$, $\Pi=3.19 \times 10^3$ and $\lambda=5.5$.

The pressure distribution on the blade is examined herein to aid the above force analysis. Fig. 6.18 plots the blade bending and twist motion contour and their pressure distribution at different time instants within one cycle. It is observed that the blade deflection becomes larger when the net pressure loads acting on the blade have a small value which is because c_c is outward and c_f is inward with large λ in air. Two time instants with a small and large deflection are selected for further analysis, as shown in Fig. 6.19, where a detailed comparison between the flexible and rigid blade

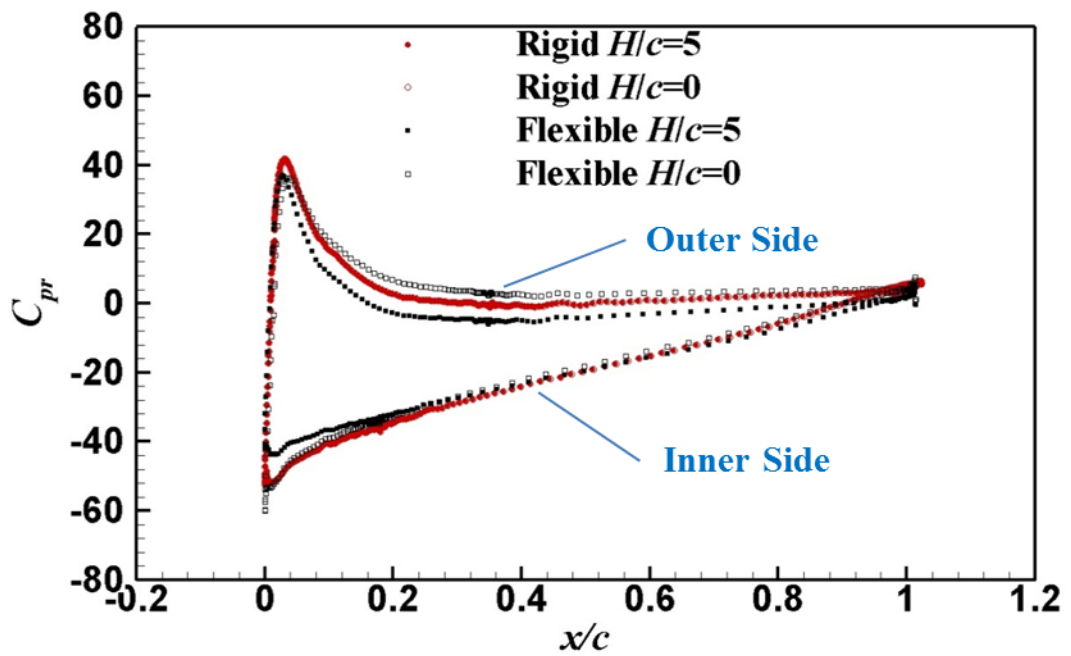
on both the inner and outer sides of the blade are presented. The pressure coefficient c_{pr} plot at $H/c=0$ and $H/c=5$ is displayed in Fig. 6.20. At $t/T_{turb}=3/8$ when the blade deflection is small, it is obvious that no apparent difference exists in pressure distribution for a flexible and rigid blade on both sides. In addition, the net pressure load is high compared to the time instant of $t/T_{turb}=5/8$, causing a small total force (c_{ft}) and thus a small blade deformation. However, at $t/T_{turb}=5/8$ when the flexible blade reaches a large deflection as shown in Fig. 6.19 (b), the pressure load acting on a flexible blade is lower than that of the rigid blade. From Fig. 6.20 (b) it can be seen that the c_{pr} has a significant decrease at both the inner and outer sides with a flexible blade. Moreover, the decrease of c_{pr} at the blade outer side is much larger than that of the inner side, leading to a decrease in the net pressure loads. Refer to Fig. 6.8 (b), Fig. 6.20 (a) and (b), since the net pressure loads are all negative at both $t/T_{turb}=3/8$ and $t/T_{turb}=5/8$, thus c_f and c_c counteract each other. Therefore, at $t/T_{turb}=5/8$, a larger total force c_{ft} and larger outward bending motion of the blade are observed.



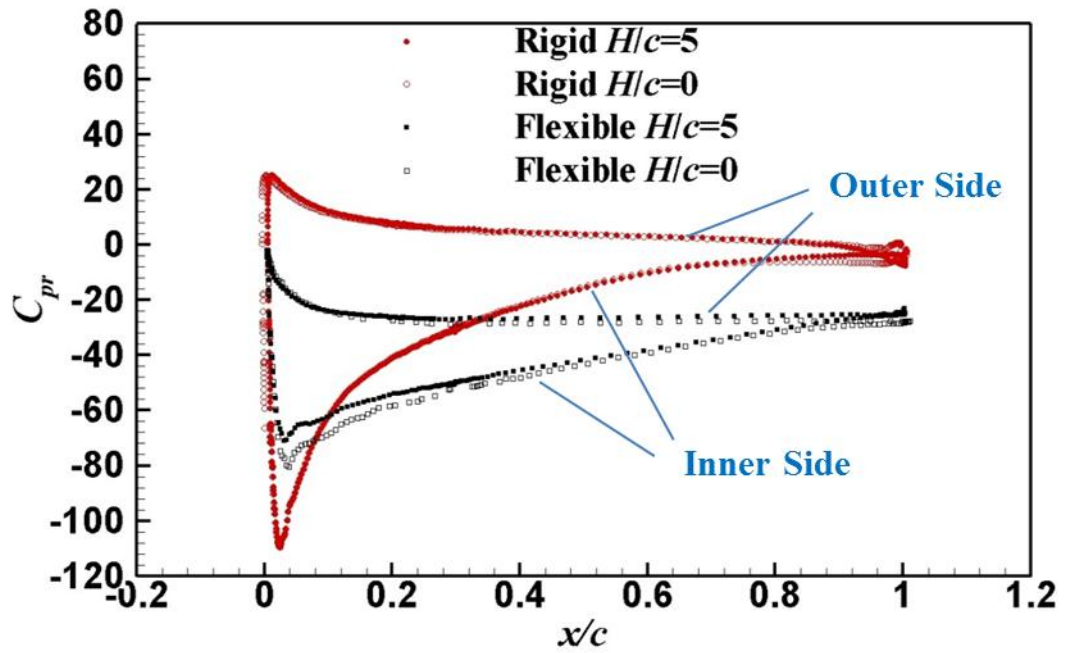


(c) Pressure distribution around blade at $t/T_{turb}=5/8$

Figure 6. 19 Pressure distribution with $l_{st}/c=10/3$, $\Pi = 3.19 \times 10^3$ and $\lambda=5.5$. (a) $t/T_{turb}=3/8$ and (b) and (c) $t/T_{turb}=5/8$



(a) $t/T_{turb}=3/8$



(b) $t/T_{turb}=5/8$

Figure 6. 20 Pressure coefficient distribution at (a) $t/T_{turb}=3/8$ and (b) $t/T_{turb}=5/8$ with $l_{st}/c=10/3$, $\Pi=3.19\times 10^3$ and $\lambda=5.5$.

The Leading Edge Suction (LES) effect is an important phenomena which influences the fluid flow field and the force generation for airfoil (DeLaurier and Harris, 1982; Chimakurthi et al., 2009). This phenomenon has also been observed in the present study, as indicated by the low pressure region of the blade leading edge (shown in Fig. 6.19 (b)) and the suction peak (shown in Fig. 6.20 (b)). For the flexible blade, the magnitude of the LES is lower than in the rigid blade, but the region which is affected by the LES effect is larger than that of the rigid blade (especially in the chord wise direction). Because of the existence of the LES effect, the foil leading edge experiences an additional suction force which generates an extra moment relative to its mass centre in the $x_lO_l y_l$ plane. This moment leads to a nose up position twist on the blades, which explains why the blade has the twist motion and the twist

angle is always positive, as shown in Fig. 6.14. The pressure contour plots around the blade section shown in Fig. 6.19 (c) coincide with the phenomenon described above.

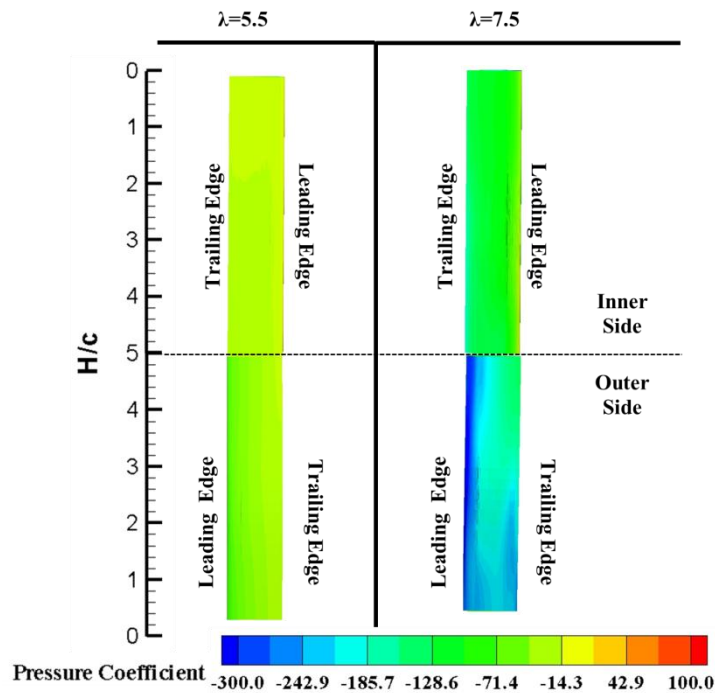


Figure 6. 21 Pressure distribution at $t/T_{turb}=5/8$ for different tip speed ratios with $l_{st}/c=10/3$ and $\Pi=3.19 \times 10^3$.

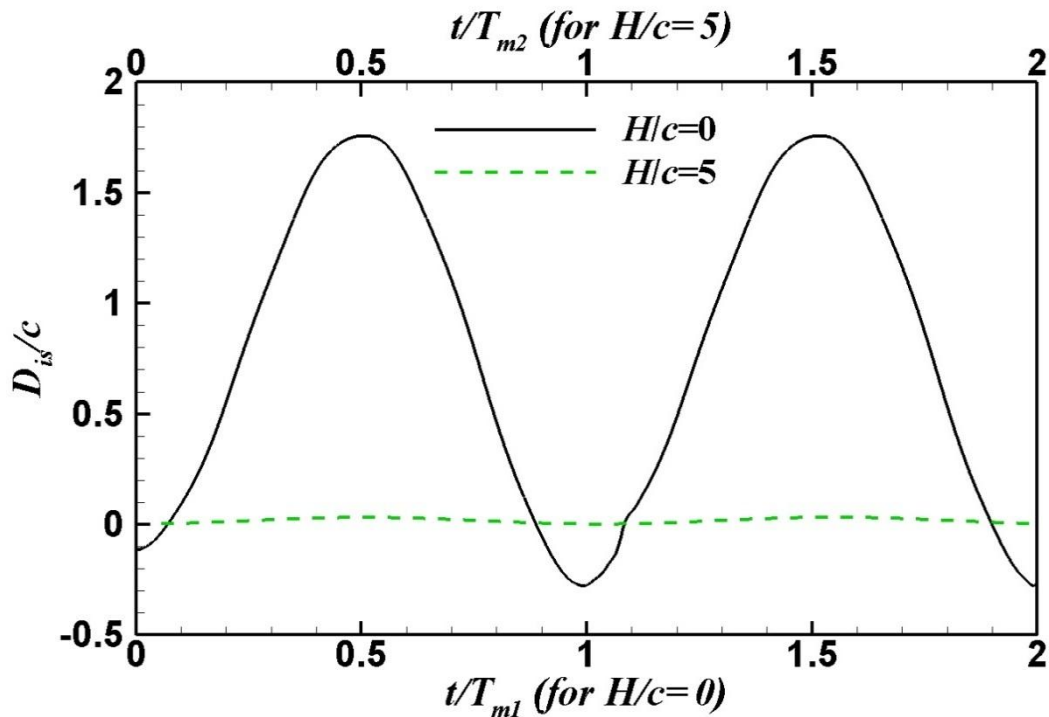
The λ effect on the pressure distribution is shown in Fig. 6.21 by comparing the flexible blade with $\lambda=5.5$ and $\lambda=7.5$ at the time instant of $t/T_{turb}=5/8$. A large pressure drop with an increase of λ is shown and the LES effect is pronounced at a larger λ .

6.2.3.3. Influence of flexible blade stiffness

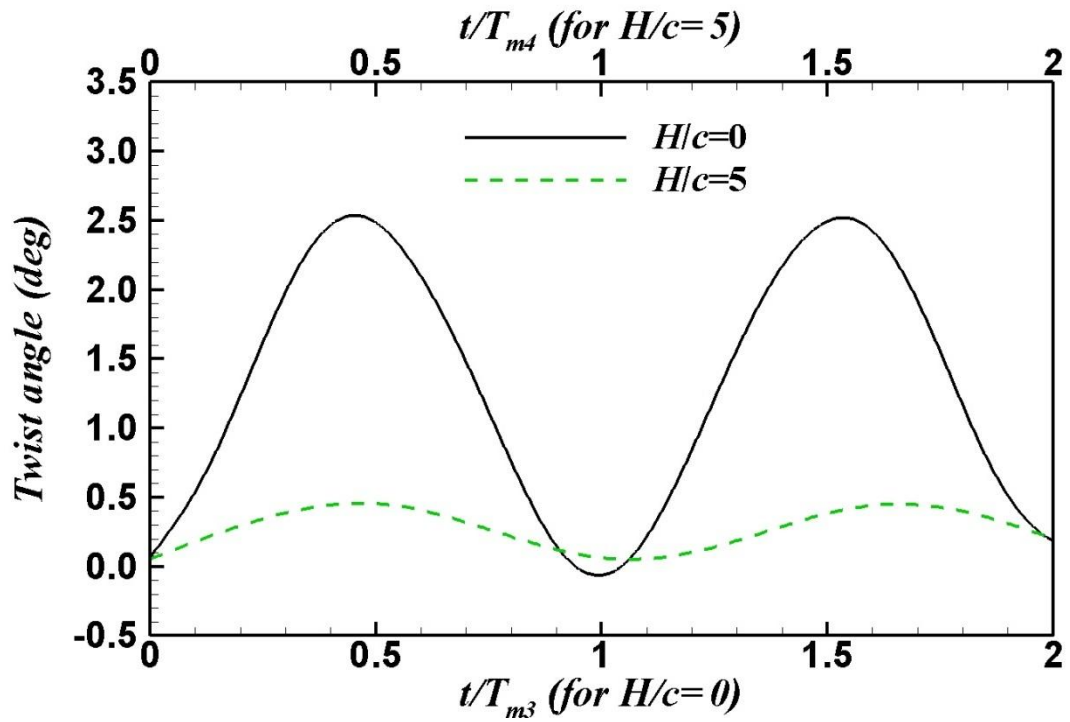
In this section, a flexible blade with different effective stiffness ($\Pi=9.37 \times 10^2$ and $\Pi=3.19 \times 10^3$) under $l_{st}/c=10/3$ condition is tested to study the effect of stiffness on the blade structural characteristics.

Figs. 6.22 and 6.23 show the bending and twist deflection of this flexible blade. As can be seen, by reducing the effective stiffness, the blade flexibility is increased, leading to a profound increase of the structural deformation compared to a less

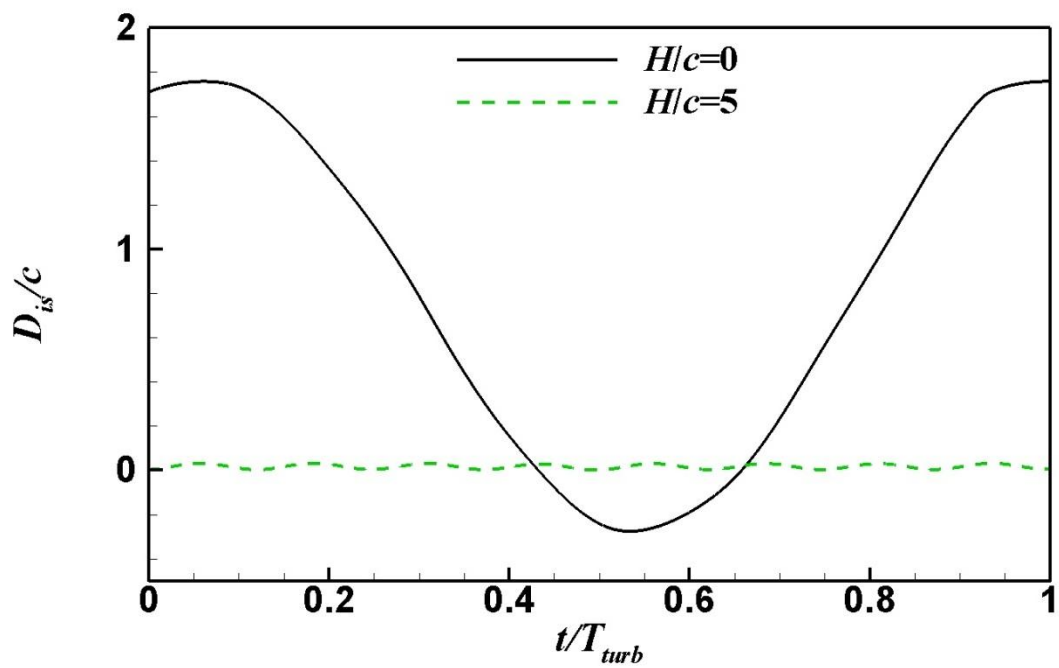
flexible blade in Figs. 6.13 and 6.14. In addition, the maximum stress coefficient (c_{st}) is also increased as summarized in Table 6.3. The stress coefficient contour shown in Fig. 6.24 indicates the occurrence of maximum stress around the strut, which is similar to the case of $\Pi=3.19 \times 10^3$. However, with this more flexible blade, the magnitude of stress is enlarged. The instantaneous blade bending-twist motions and the pressure distribution applied to the blade are shown in Fig. 6.25. Similar to a more rigid blade case, large blade deformation is caused by low pressure acting on the blade. This is well reflected by the pressure distribution plots at $t/T_{turb}=4/8$ and $t/T_{turb}=5/8$ in Fig. 6.26. In fact, the c_{pr} is around -100 in Fig. 6.26 (a) for the blade of $\Pi=9.37 \times 10^2$, which is 80 lower than that of the blade of $\Pi=3.19 \times 10^3$ at $t/T_{turb}=1/8$. However, at $t/T_{turb}=5/8$, as shown in Fig. 6.26 (b), the c_{pr} is around 40, which is 20 higher than that of the blade with $\Pi=3.19 \times 10^3$. Under this condition, the blade deforms oppositely with centrifugal force direction.



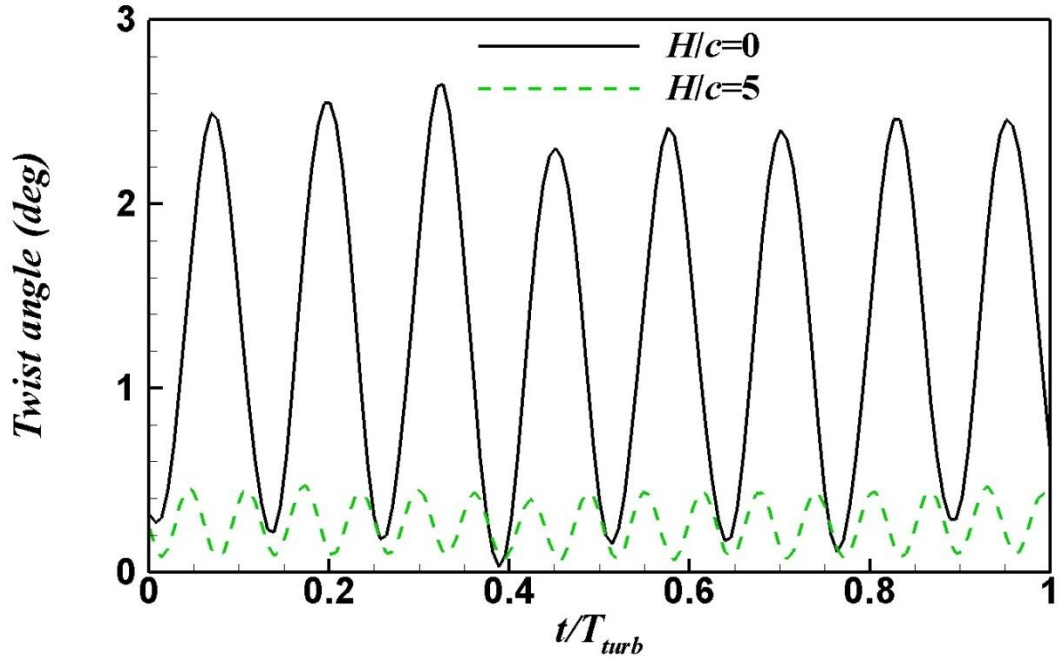
(a) Instantaneous non-dimensionalized displacement



(b) Instantaneous twist angle



(c) Instantaneous non-dimensionalized displacement



(d) Instantaneous twist angle

Figure 6. 22 Structure characteristics with $l_{st}/c=10/3$, $\Pi=9.37 \times 10^2$ and $\lambda=5.5$. (a) and (b) time is non-dimensionalized by blade mode periods and (c) and (d) time is non-dimensionalized by turbine period.

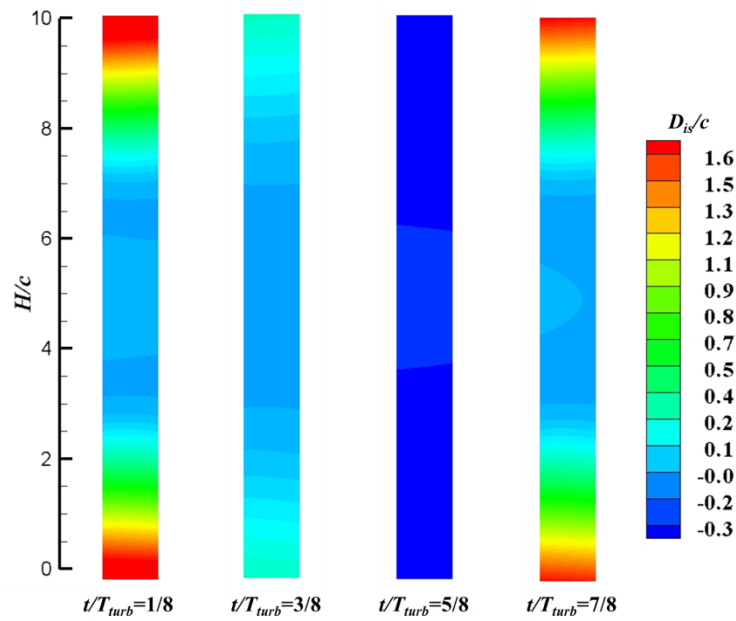


Figure 6. 23 Non-dimensionalized bending and twist displacement contour with $l_{st}/c=10/3$, $\Pi=9.37 \times 10^2$ and $\lambda=5.5$ viewing from the inner side of the blade.

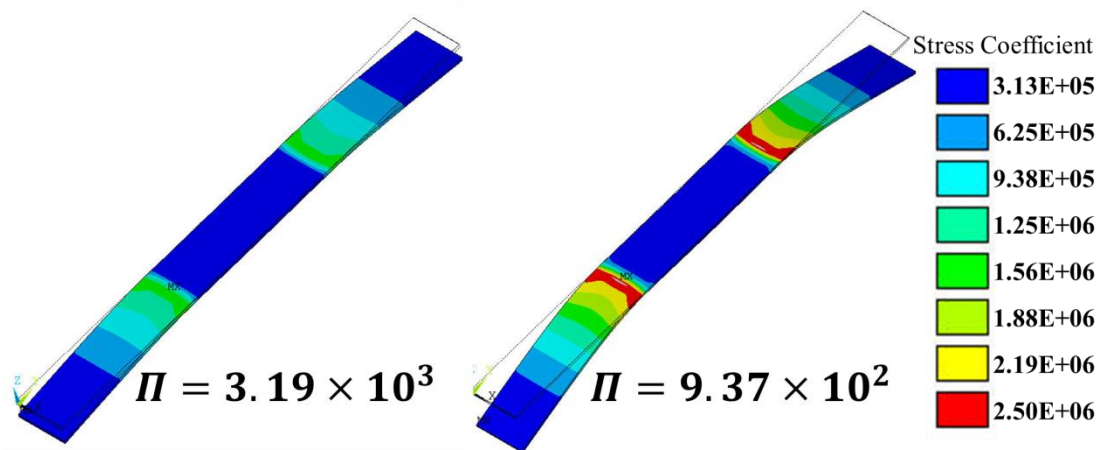


Figure 6. 24 Contour of stress distribution over the blade under the largest external load condition of the flexible blade with $l_{st}/c=10/3$, $\Pi=9.37\times 10^2$ and $\lambda=5.5$ viewing from the inner side of the blade.

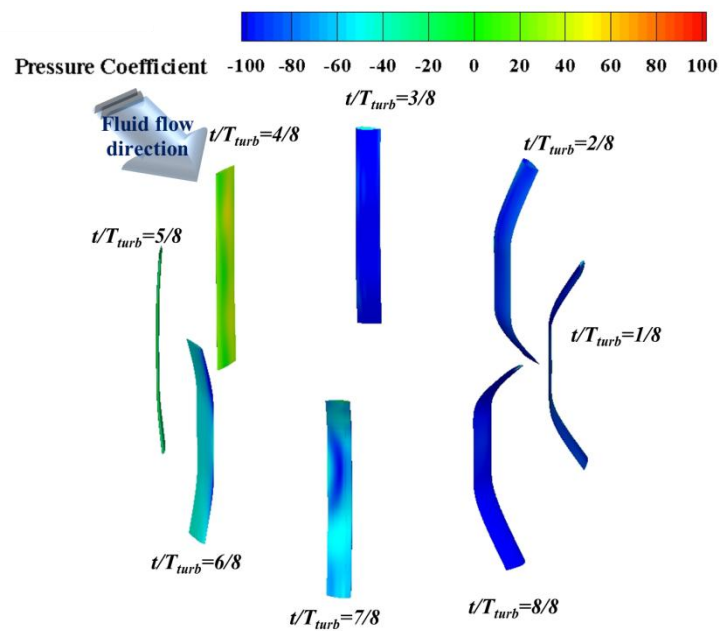


Figure 6. 25 Blade bending-twist motion and pressure distribution for different time instants with $l_{st}/c=10/3$, $\Pi=9.37\times 10^2$ and $\lambda=5.5$.

The LES phenomenon is not remarkable for both rigid and flexible blades with different Π because of the small blade instantaneous Angle of Attack (AOA) at these two time instants.

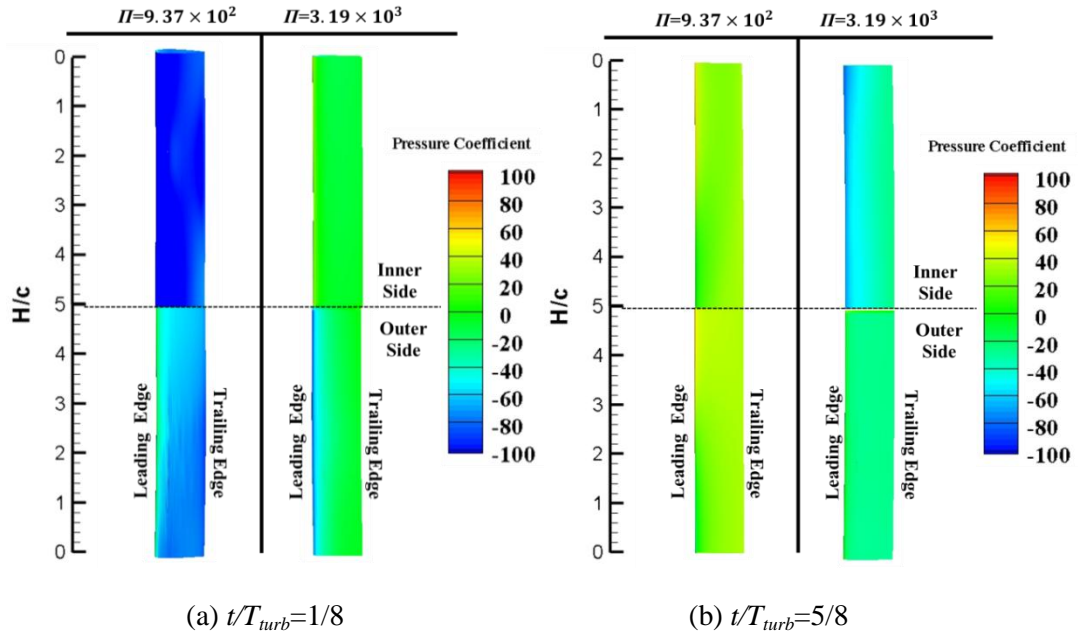


Figure 6. 26 Pressure distribution at (a) $t/T_{turb}=1/8$ and (b) $t/T_{turb}=5/8$ with $l_{st}/c=10/3$, $\lambda=5.5$ and $\Pi=9.37 \times 10^2$ compared with $\Pi=3.19 \times 10^3$.

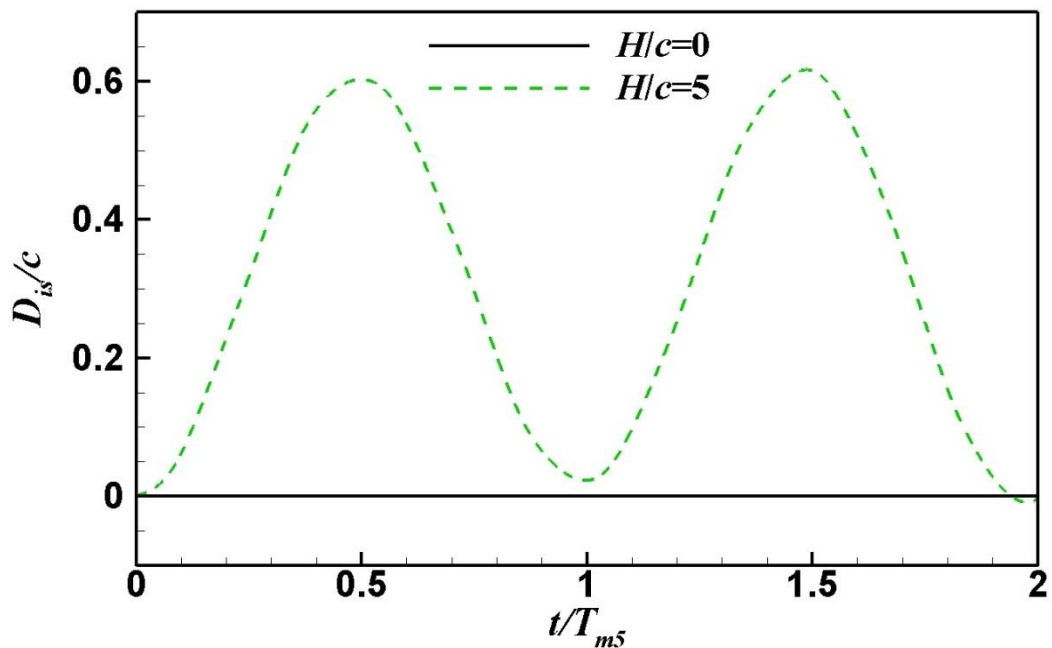
6.2.3.4. Influence of two different strut locations

In this section, two different strut locations which connects the flexible blade with radial arms at the blade tip (i.e. $l_{st}/c=0$) as seen from 6.9 (b) is studied to provide some preliminary information of the strut location effect. A flexible blade with $\Pi=3.19 \times 10^3$ is used in this study.

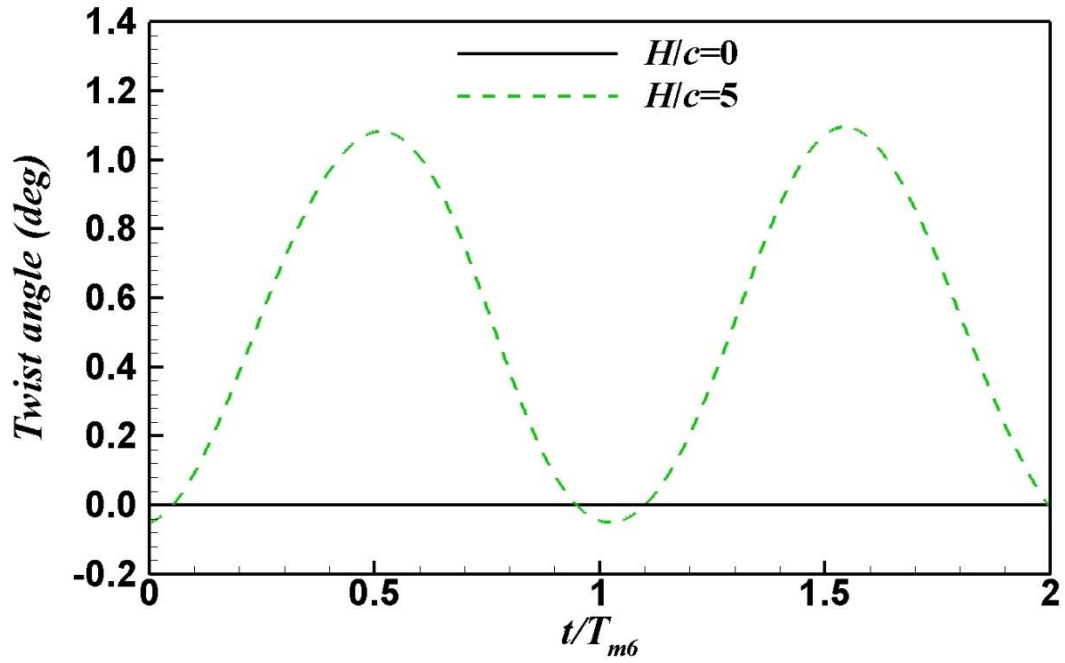
Fig. 6.27 shows the D_{is}/c and twist angle under $l_{st}/c=0$, $\Pi=3.19 \times 10^3$ and $\lambda=5.5$. Compared to the results with $l_{st}/c=10/3$, $\Pi=3.19 \times 10^3$ and $\lambda=5.5$, the maximum D_{is}/c are reduced, while the maximum twist angle remains the same. The displacement and twist angle at the blade tips are zero because of the struts, as shown in Fig. 6.27 and Fig. 6.28. The maximum displacement amplitude occurs at the blade

centre ($H/c=5$) as can be seen from Fig. 6.28. A detailed comparison between the condition of $l_{st}/c=0$ and the condition of $l_{st}/c=10/3$ is shown in Table 6.3. From the stress distribution contour under the largest external load condition in Fig. 6.29, the maximum stresses exist at the blade tips. Though the peak c_{st} has decreased by using the tip strut ($l_{st}/c=0$) instead of the middle strut ($l_{st}/c=10/3$), a large area with high stress is observed with c_{st} around 7.0×10^5 .

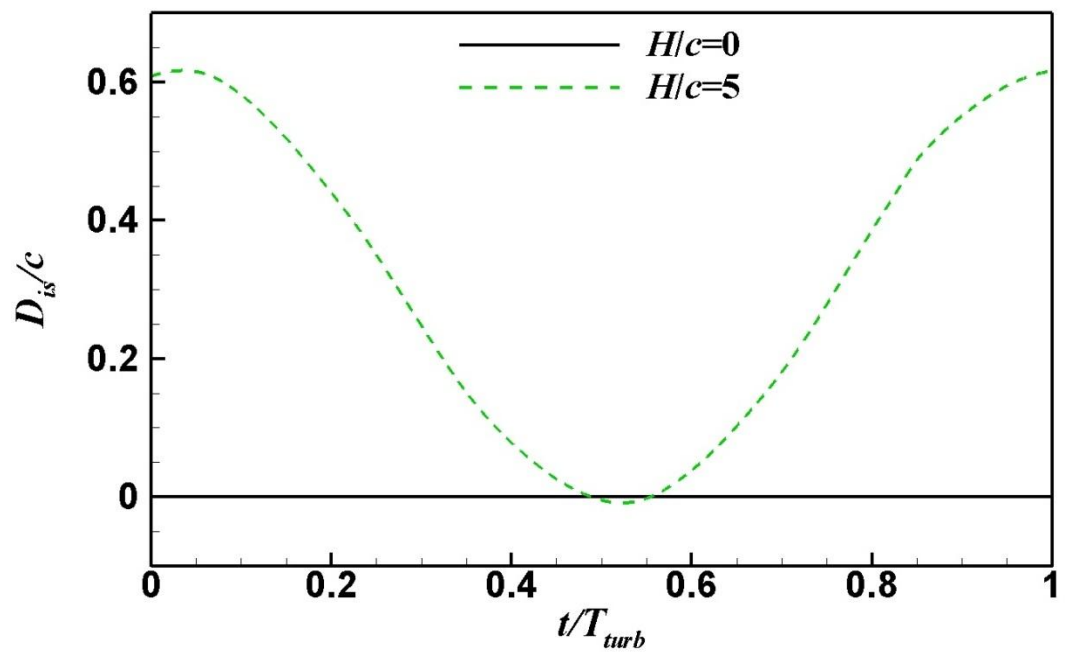
The blade bending and twist motion and pressure distribution at different time instants are shown in Fig. 6.30 which shows a similar observation as in the previous sections. Pressure distribution at $t/T_{turb}=1/8$ and $t/T_{turb}=4/8$ for both the inner side and the outer side compared with the middle strut blade is displayed in Fig. 6.31. The LES effect is quite obvious by using a tip strut flexible blade in these two plots. It results in large twist behaviour at $t/T_{turb}=1/8$ and $4/8$ as shown in Fig. 6.27 (b).



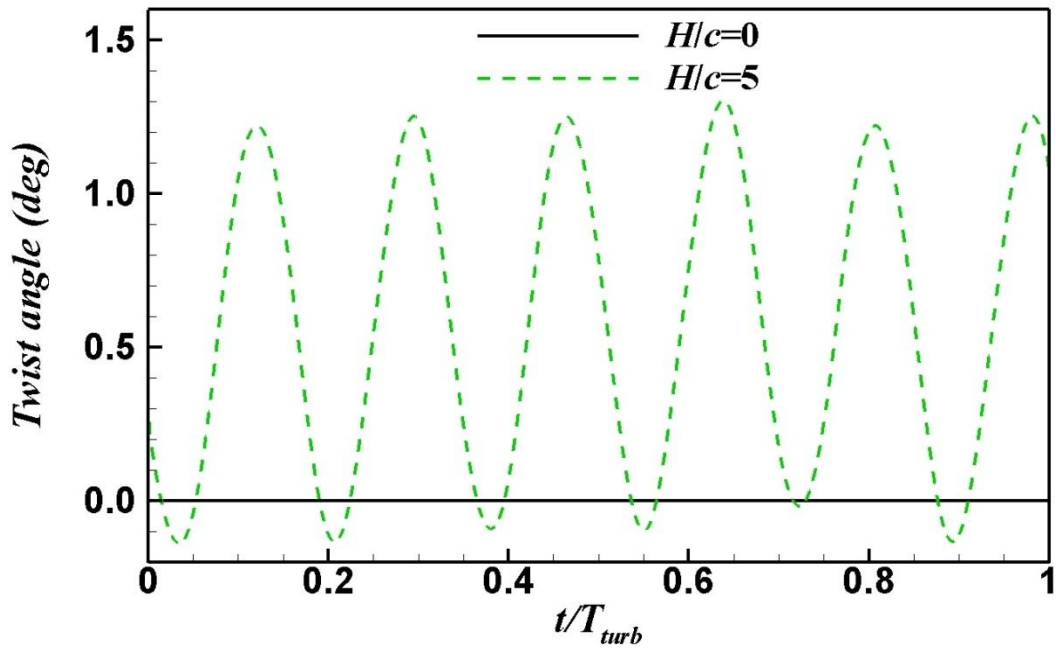
(a) Instantaneous non-dimensionalized displacement



(b) Instantaneous twist angle



(c) Instantaneous non-dimensionalized displacement



(d) Instantaneous twist angle

Figure 6. 27 Structure characteristics with $l_{st}/c=0$, $\Pi=3.19 \times 10^3$ and $\lambda=5.5$. (a) and (b) time is non-dimensionalized by blade mode periods and (c) and (d) time is non-dimensionalized by turbine revolution.

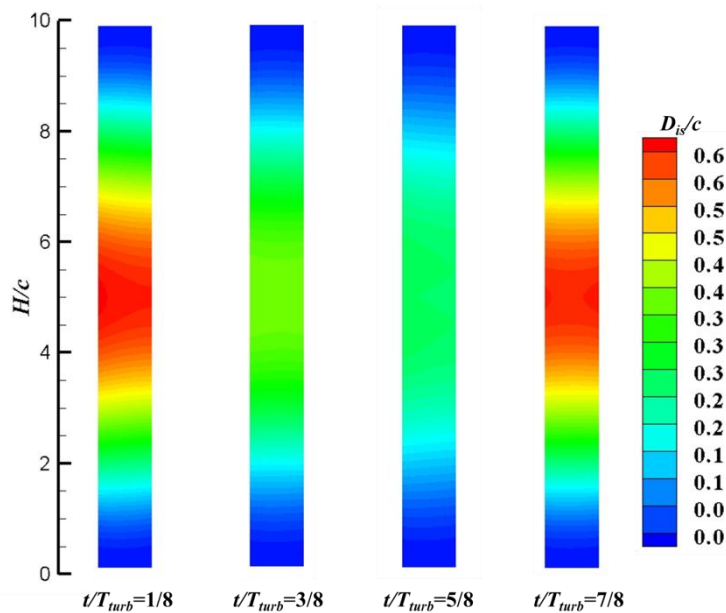


Figure 6. 28 Non-dimensionalized bending and twist displacement contour with $l_{st}/c=0$, $\Pi=3.19 \times 10^3$ and $\lambda=5.5$ viewing from the inner side of the blade.

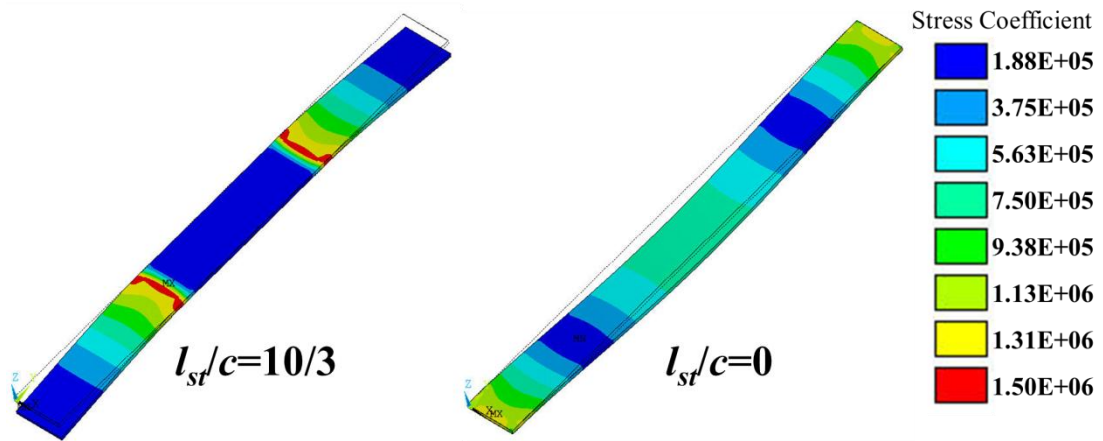


Figure 6. 29 Contour of stress distribution over the blade under the largest external load condition for the flexible blade turbine with $l_{st}/c=0$, $\Pi=3.19 \times 10^3$ and $\lambda=5.5$ viewing from the inner side of the blade.

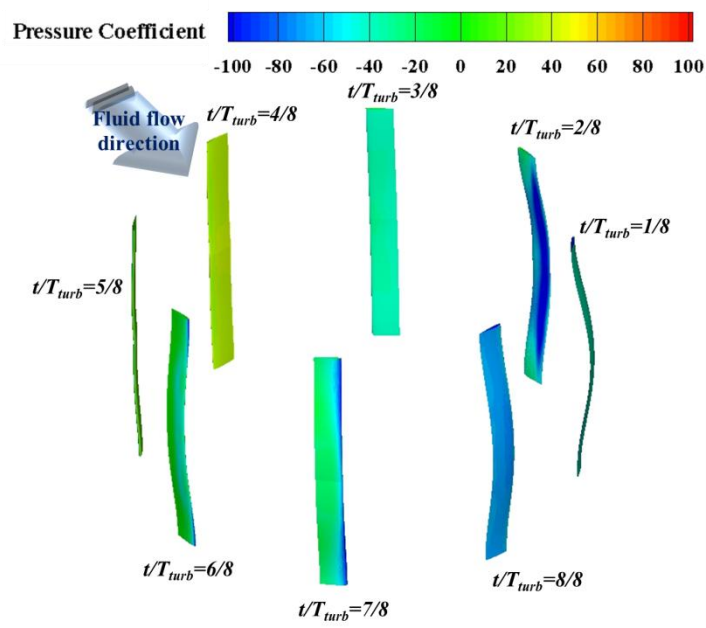


Figure 6. 30 Blade bending-twist motion and pressure distribution for different time instants with $l_{st}/c=0$, $\Pi=3.19 \times 10^3$ and $\lambda=5.5$.

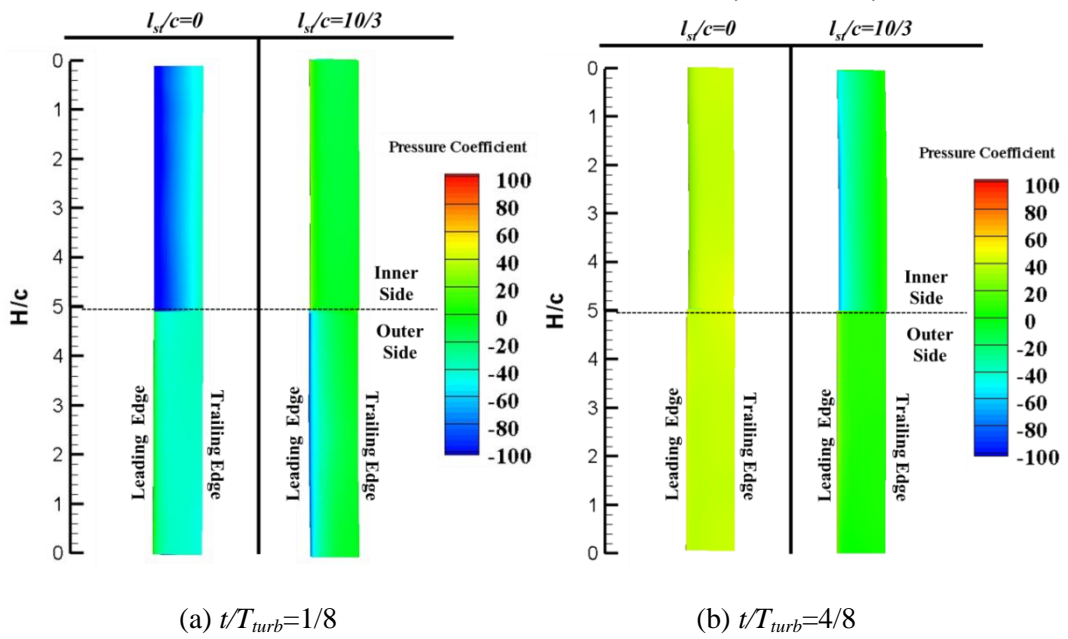


Figure 6.31 Pressure distribution at (a) $t/T_{turb}=1/8$ and (b) $t/T_{turb}=4/8$ with $\lambda=5.5$, $\Pi=3.19 \times 10^3$ and $l_{st}/c=0$ compared with $l_{st}/c=10/3$.

6.2.3.5. Energy extraction

As an energy extraction device, the vertical axis turbine with a flexible blade is also investigated in terms of its energy extraction performance in this section. Fig. 6.32 summarizes the instantaneous moment coefficient (c_m) under three different structural parameters discussed in the above sections along with the rigid blade results. It is seen that the peak c_m enlarges by using a flexible blade and high frequency fluctuations are observed during one revolution which indicates the appearance of flow field instability. Fig. 6.33 displays the vorticity field at $t/T_{turb}=5/8$ for a flexible blade under $l_{st}/c=0$, $\Pi=3.19 \times 10^3$ and $\lambda=5.5$ condition compared to a rigid one. A large flow separation is clearly associated with a flexible blade as observed in Fig. 6.32.

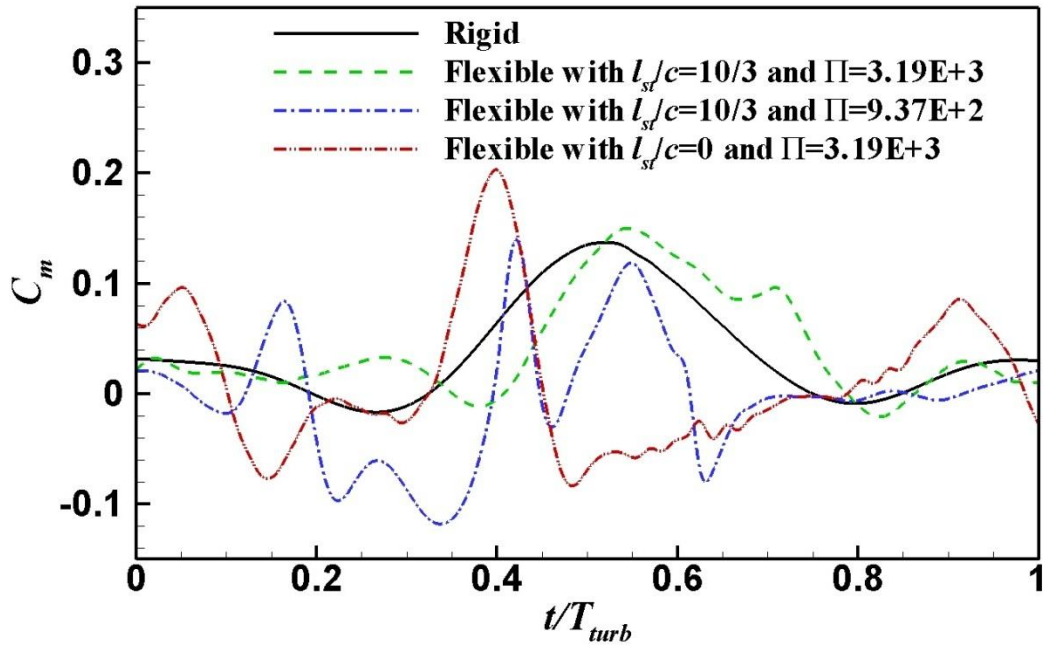


Figure 6.32 Instantaneous moment coefficient at $\lambda=5.5$.

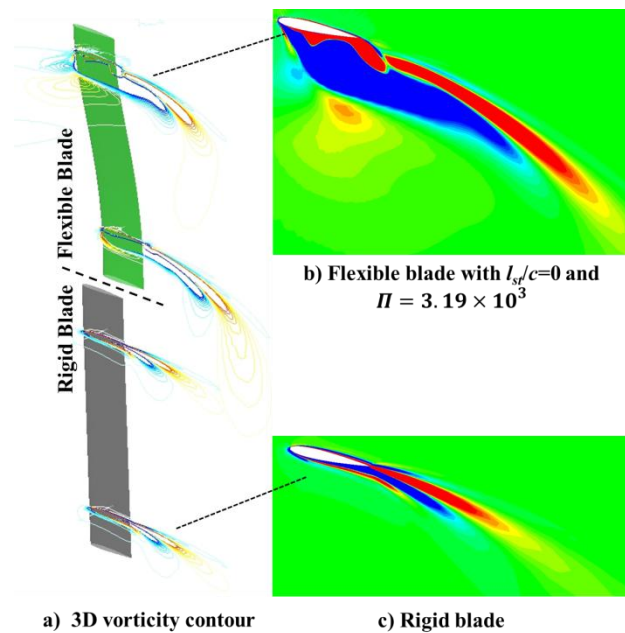


Figure 6.33 Vorticity contour at $t/T_{turb}=5/8$ and $\lambda=5.5$.

The time averaged power coefficient c_{op} variation with λ for both a rigid blade and a flexible blade turbine under three different conditions is shown in Fig. 6.34. Under the condition of $l_{st}/c=10/3$ and $\Pi=3.19 \times 10^3$ and when λ is smaller than 6.0, it is

observed that the flexible blade could enhance the overall energy performance compared with the rigid blade turbine. Up to an 8% enhancement of c_{op} is observed. The tip speed ratio λ , at which the peak c_{op} occurs, can move towards a smaller value. With a further increase of λ , the energy extraction performance for the flexible blade turbine drops suddenly compared to a rigid blade turbine. In addition, by reducing Π or moving the strut to the blade tip ($l_{st}/c=0$), the tip speed ratio (λ) associated with a peak c_{op} moves towards low λ and a smaller c_{op} . However, all of the above discrepancy in c_{op} nearly diminishes when λ is reduced to around 4.5. On the other hand, either a high flexible blade turbine or a turbine with struts at the blade tips is not as attractive as a rigid blade turbine in terms of energy extraction. This is an indication that very deformable blades are absolutely not efficient to use as an energy extraction device.

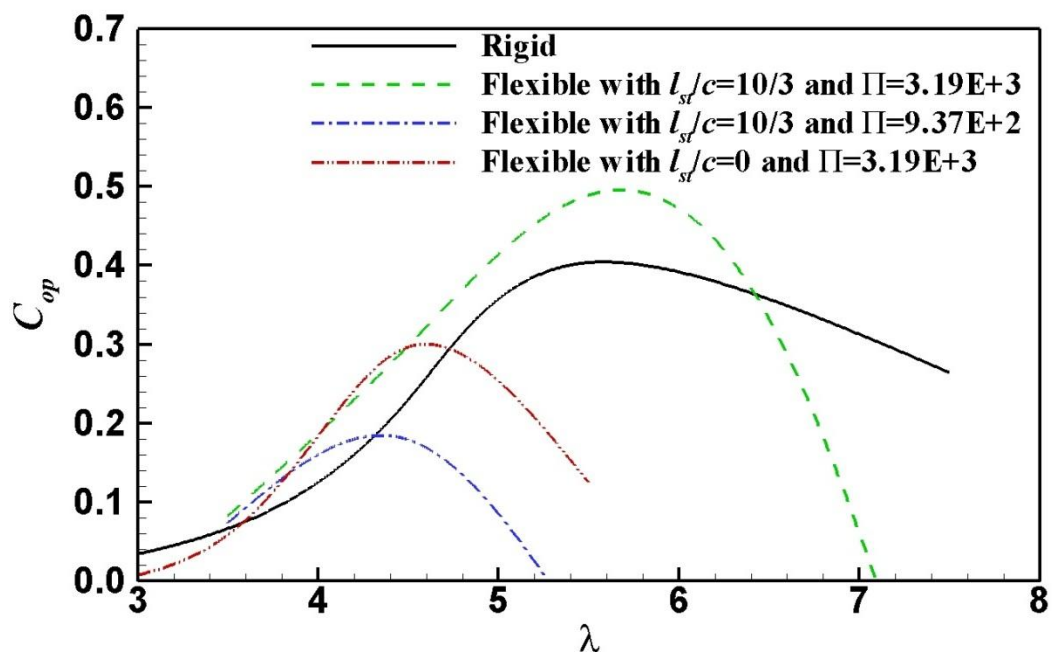


Figure 6. 34 Time averaged power coefficient.

6.2.4 Summary of Section 6.2

With the use of a fully-coupled Fluid-Structure-Interaction (FSI) method, a numerical investigation of the effect of the structural flexibility of a vertical axis wind turbine blade on its passive structure deformation, unsteady external loading, internal stress analysis and turbine energy extraction ability is carried out. For the flexible blade, two different values of effective stiffness are tested. With the real application in the VAT industry, the present study also studied cases with the blade support strut in two different locations. 10^8 CPU seconds calculated on ARCHIE-WeST high performance computing facilities of University of Strathclyde are needed for a typical case in this section.

The simulation shows that the blade bending and twist deformations vary with time periodically with one dominant frequency. Increasing the tip speed ratio leads to an increase in the peak values of bending and twist deformation. With the centrifugal force acting on the blade, the blade bending deflection always points in the positive centrifugal force direction. The blade internal stress contours under maximum external loads are provided in the present study, which is believed to be useful for further structure fatigue damage analysis in the industry.

The leading edge suction effect is observed in both rigid and flexible blade cases, which mainly leads to the twist motion of flexible blade, and thus enlarges the influence of LES. A large blade bending deflection with a small net pressure load on the blade surface is observed, which is induced by the opposite direction between the centrifugal force and net pressure forces applied on the flexible blade.

A larger bending and twist deflection occurs which is associated with a more flexible blade and results in higher stress caused by the flexible deflection. A blade with tip strut support shows a smaller bending deflection compared to its middle support method.

With a flexible blade, an unstable fluid field around the blade is observed which is associated with some small fluctuations in the instantaneous moment coefficient curve. With a small tip speed ratio, the energy extraction efficiency is enhanced with a flexible blade. However, it becomes worse than a rigid blade counterpart with relatively large tip speed ratios.

Lastly, in the present research, only one blade is modelled, which is simplified from real industry where three-bladed VATs are very commonly used to achieve a high level of energy. Therefore, performing a two-bladed or three-bladed VAT with a passively controlled bending and twist is required in future studies. Moreover, the present flexible blade deflection motion is actuated by air flow. It is believed that the blade bending/twist deflection should be different under different fluid mediums (such as water). Thus, a VAT with a passively deformed flexible blade under water conditions should be investigated in the near future.

Chapter 7: Bio-inspired Passive Flow Control for Oscillating Foil

Turbines by Flexible Material

7.1 Introduction

The present study examines the energy extraction of a passively flexible flapping foil through a fully-coupled fluid-structure interaction study. Unlike the simplified plate model with zero thickness (Tian et al., 2014), a more realistic NACA0012 foil shape is used in the present study. In addition, it takes into account the internal structure of the foil by using a stiffener to create the structural deformability. This makes the model closer to the real design. In this study, a finite volume method is used, which fully resolves the boundary layer so that it has better accuracy than the immersed-boundary method.

In the rest of this chapter, descriptions of the physical problem are listed in Section 7.2. In Section 7.3, it first considers cases with metal stiffener to examine whether structural flexibility has beneficial effect on energy extraction. The effects of Young's modulus and density ratio are then studied separately. Finally, a summary of these studies in this chapter is listed in Section 7.4.

7.2 Description of problem

7.2.1 Benchmark model

The present research considers a two-dimensional oscillating energy harvesting system based on a NACA0012 foil whose deformability is determined by a realistic internal structure. As shown in Fig. 7.1, the incoming flow is uniform with speed U . Similar to the study by Kinsey and Dumas (2008), the Reynolds number based on the

incoming flow speed and the chord length c of the foil in the present study is fixed as 10^3 so that a laminar flow assumption is used. In applications, there exists three types of design (Xiao and Zhu, 2014): systems with forced pitching and heaving motions, systems with forced pitching and induced heaving motions (semi-activated systems), and systems with self-sustained pitching and heaving motions (self-sustained systems). The present study concentrates on the first type, i.e. forced pitch and plunge motion (McKinney and DeLaurier, 1981; Kinsey and Dumas, 2008; Jones and Platzer, 1997; Jones et al., 2003; Kinsey and Dumas, 2012a; 2012b) and examines the effects of structural flexibility upon the energy harvesting performance.

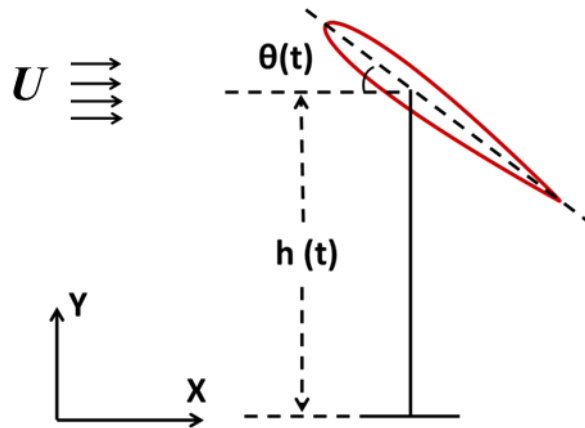


Figure 7. 1 Schematic diagram of oscillating energy device.

7.2.2 Structural design of flexible foils

To study the effect of structural deformability on the propulsion performance of a flapping wing, Heathcote and Gursul (2007) and Heathcote et al. (2008) developed chordwisely and spanwisely flexible wing models and performed experimental tests. Subsequently, relevant numerical simulations have also been carried out by Shyy et al. (2010), Gordnier et al. (2010) and Chimakurthi et al. (2009). The present study adopts similar internal designs from the above papers and creates a foil with

chordwise flexibility (Fig. 7.2 (a)). With a NACA0012 profile, the deformability of this foil is determined by a stiffener with thickness T_{sf} and length c_{sf} . The surrounding material, made of polydimethylsiloxane rubber (PDMS) with Young's modulus of 250 kPa (Heathcote et al., 2008), contributes little to the overall structural dynamic properties (stiffness and inertia) of the foil (Chimakurthi et al., 2009). Thus, only the metal stiffener is considered to evaluate the flexible effect. In the present study, the stiffener thickness T_{sf} and length c_{sf} are fixed for all cases as $9 \times 10^{-3}c$ and $0.75c$, respectively. The present study assumes that the surrounding material is light and soft so that its inertia and stiffness are negligible. Indeed, by comparing experimental and numerical results, Gordnier et al. (2010, 2013) and Chimakurthi et al. (2009) concluded that the surrounding material (in their case it was polydimethylsiloxane rubber PDMS) with Young's modulus of 250 kPa (Heathcote et al., 2008)) contributes little to the overall structural behaviour of the foil. This is partly attributed to the fact that this material tapers off near the trailing edge, where the structural deformation is most pronounced, while the stiffener is uniformly distributed along the chord.

With the unsteady fluid loads acting on its surface, the flexible part of the foil deforms passively as shown in Fig. 7.2 (b). The instantaneous trailing edge bending angle relative to the local x coordinate (a local coordinate that coincides with the instantaneous chord of the foil if there is no deformation) is defined as β_0 , whose amplitude is defined as β_{0_amp} .

The Young's modulus coefficient E_c and the density ratio DR are the two key parameters to describe the structural property. Hereby they are defined as

$$\begin{cases} E_c = \frac{E}{\rho_f g c} \\ DR = \frac{\rho_s}{\rho_f} \end{cases} \quad (7.1)$$

where ρ_s is the density of the stiffener. The present study is focused on the flexible foil oscillating in water, thus the fluid density ρ_f in this study are aiming to simulate is 1000 kg/m^3 .

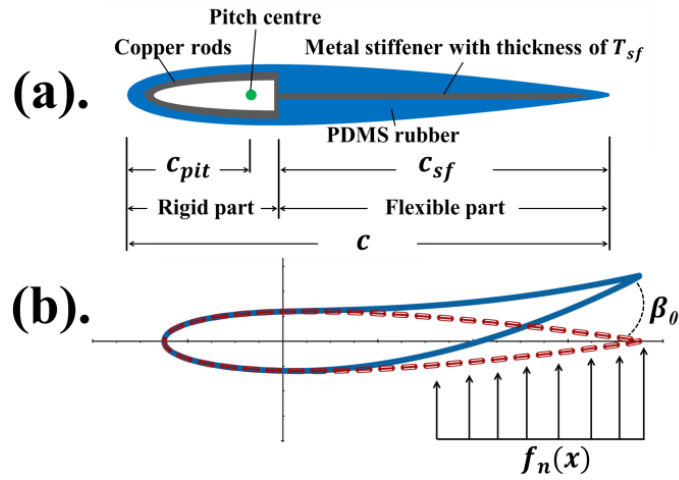


Figure 7. 2 (a) Inner structural design for trailing edge flexible foil and (b) flexible foil displacement.

Table 7. 1 Case summary for real materials.

Case	Material	Young's modulus coefficient E_c	Density ratio DR	Effective stiffness Π	Poisson ratio ν	Natural frequency ratio FR
1	Copper (Cu)	1.12×10^8	8.9	5.25×10^1	0.34	7.55
2	Tungsten Carbide (WC)	5.61×10^8	15.6	2.46×10^2	0.24	12.76

7.3 Results and discussions

This study starts the investigation by using real metal materials for the stiffener. Specifically, two types of material are used, *Copper (Cu)* and *Tungsten Carbide (WC)*. This is because copper is a common metal with relatively high flexibility. *Tungsten Carbide*, on the other hand, possesses large Young's modulus and density. The detailed parameters used in the present study are listed in Table 7.1. Numerical simulations are carried out for the above two stiffener materials and the results are compared with those with a rigid foil. Two pitching amplitudes, 60° and 75° , are applied. These are close to the pitching amplitudes with high efficiency energy harvesting (see, e.g. Kinsey and Dumas, 2008). The effective stiffness are 5.25×10^1 and 2.62×10^2 for Copper and Tungsten Carbide stiffener, respectively.

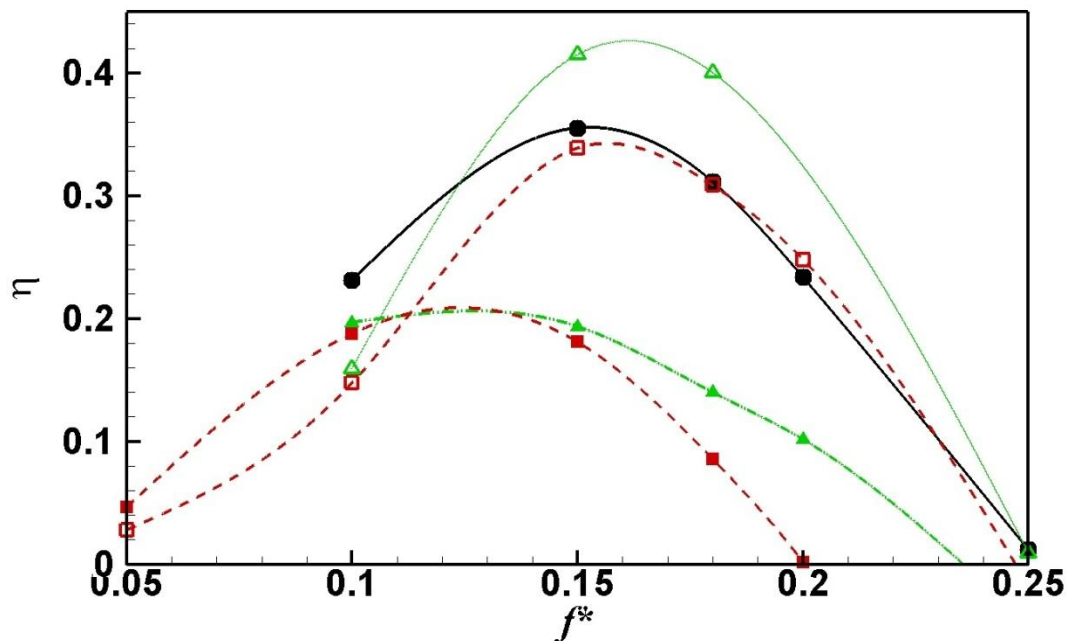
7.3.1 Energy harvesting performance with stiffeners of real materials

As shown as Eq. 1.17 in Section 1.2.2, the key parameter to quantify the energy extraction performance of an oscillating foil device is the efficiency η . Fig. 7.3 (a) compares the energy extraction efficiency of the copper stiffener foil (hereafter referred to as Cu), the tungsten carbide stiffener foil (referred to as WC) and the rigid foil at different reduced frequencies. Based on these results, flexible foils show a certain level of improved performance as compared to their rigid counterparts. For example, the peak efficiency of WC reaches 20% at the pitching angle of 60° and 43% at the pitching angle of 75° , while the corresponding results for the rigid foil are 19% and 35%, respectively. Cu also reaches 36% at 60° pitching angle. The efficiency enhancement of Cu (compared with the rigid foil) is 17.4% at a reduced frequency of 0.15 and 32.2% with $f^* = 0.25$. Since the structural model used herein is linear, which

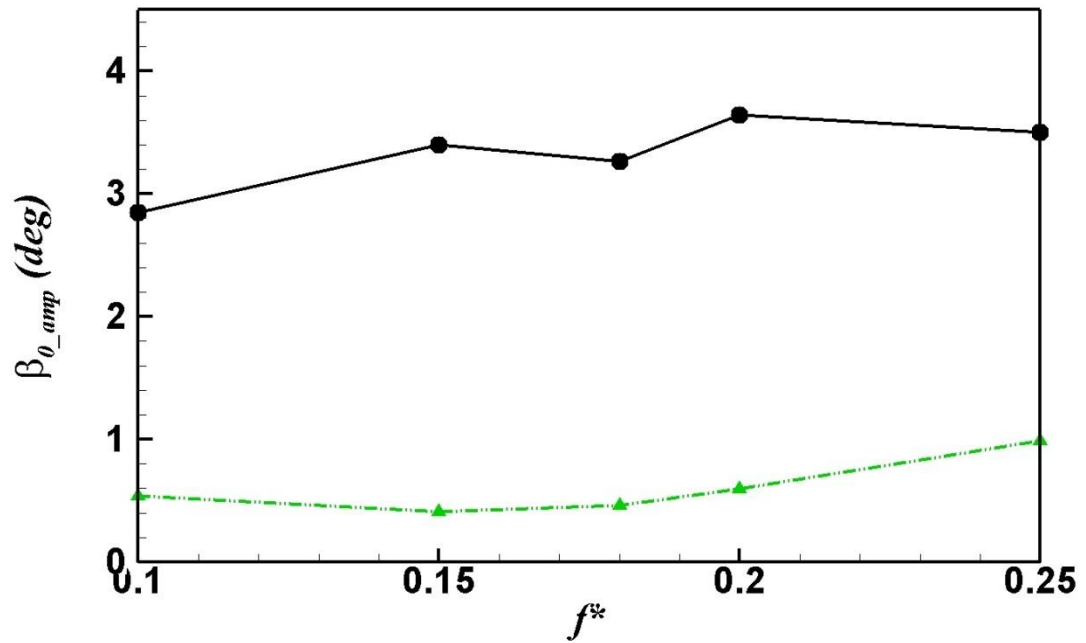
is not accurate in simulating large deformation, it is not used to study cases with low stiffness at high pitching angle.

Within the large reduced frequency region ($f^*=0.18-0.25$), where rigid foils usually present a decayed performance or even degrade to negative power extraction, both Cu and WC flexible foils still exhibit a positive energy extraction with the efficiency much higher than that of the rigid foil.

The trailing edge displacement amplitude β_{0_amp} shows different magnitudes and variation trends for the two flexible foils as displayed in Fig. 7.3 (b). Because of the small Young's modulus coefficient for Cu, the trailing edge displacement of Cu is larger than that of WC. For Cu, the maximum value of such displacement is around 3.64° .

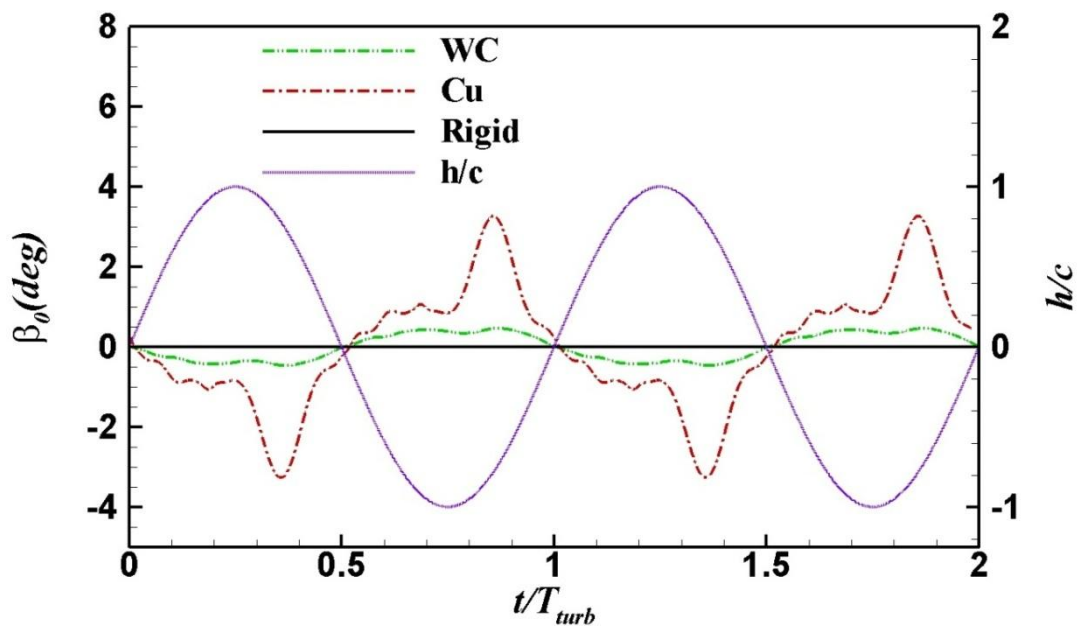


(a) Efficiency

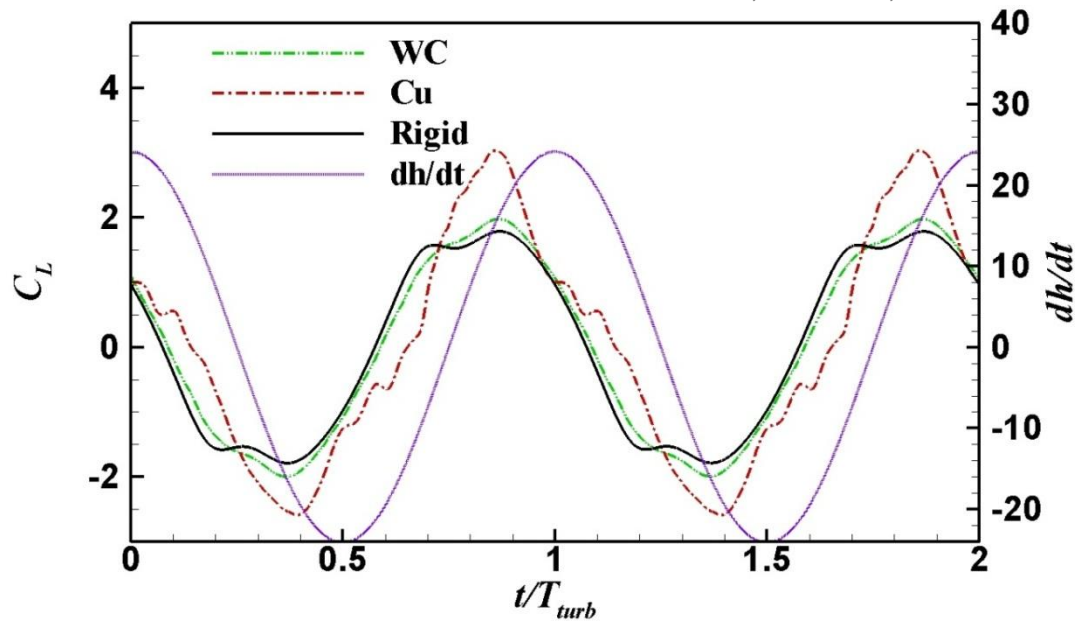


(b) Peak trailing edge displacement

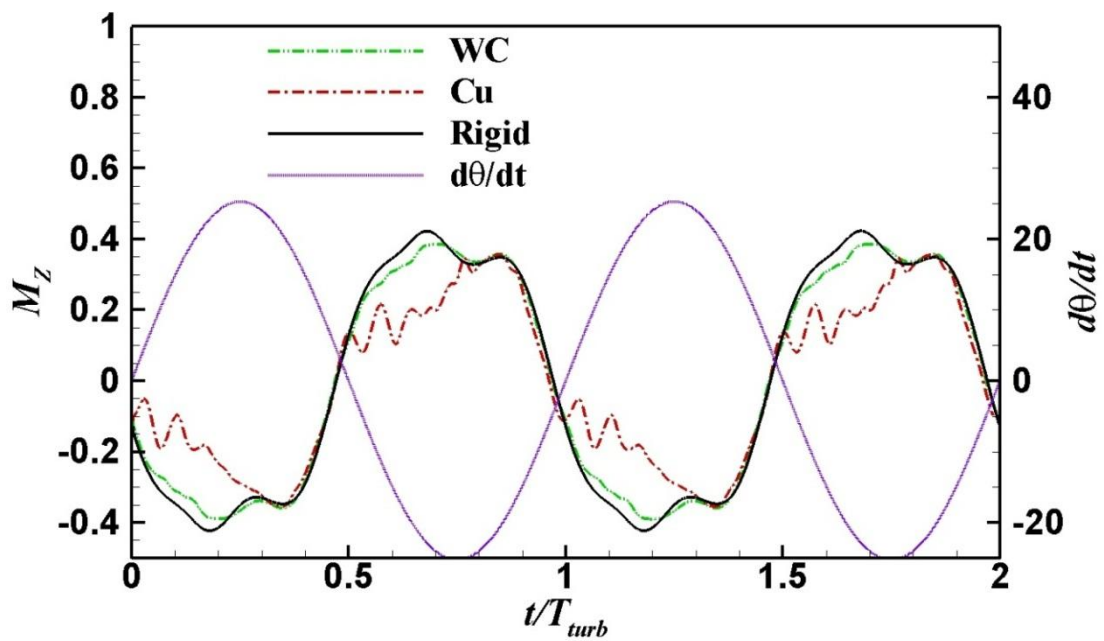
Figure 7. 3 The overall performance of a flexible oscillating foil device with $h_0/c=1.0$. ● Cu $\theta_0=60^\circ$; ▲ WC $\theta_0=60^\circ$; ■ Rigid $\theta_0=60^\circ$; □ Rigid $\theta_0=75^\circ$; △ WC $\theta_0=75^\circ$.



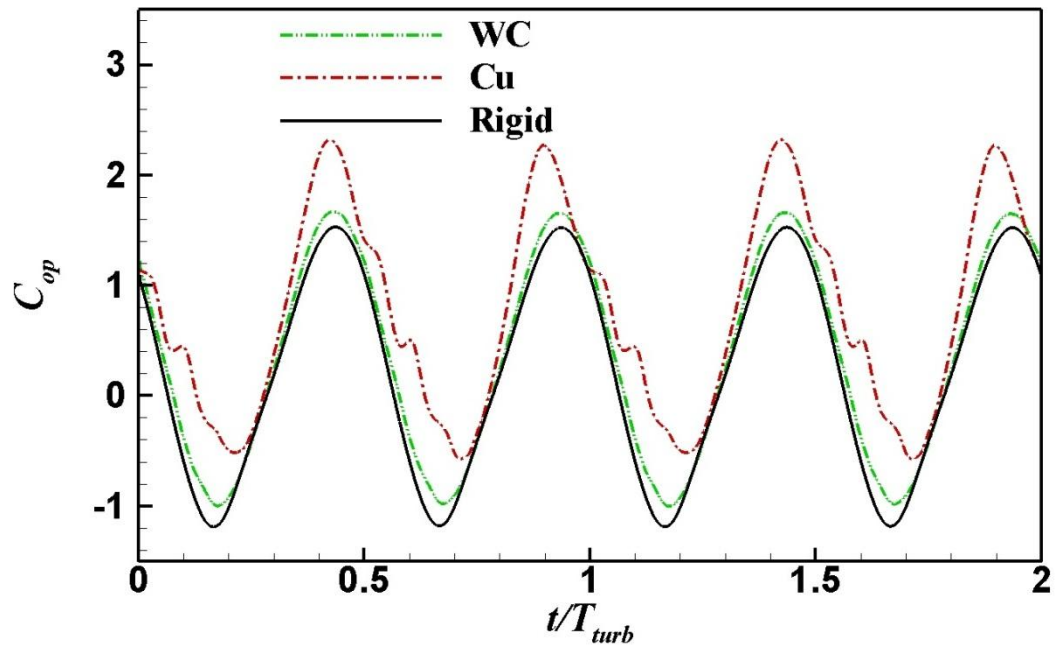
(a) Trailing edge displacement angle



(b) Lift coefficient and heaving velocity



(c) Moment coefficient and pitch velocity



(d) Power coefficient

Figure 7.4 Time histories for foils with Cu and WC stiffeners at $f^*=0.18$ and $\theta_0=60^\circ$.

Apart from the time-averaged results, the instantaneous displacement and force results at a reduced frequency of 0.18 are picked up for a detailed analysis.

The instantaneous trailing edge displacement angles for the two flexible foils and the rigid foil are plotted in Fig. 7.4 (a). It is clear that the peak value of 3.27° is reached at $t/T_{turb}=3/8$ for the Cu foil. Large trailing edge displacement angle is achieved during $t/T_{turb}=2/8$ and $3/8$ for the WC foil.

Fig. 7.4 (b) shows the lift coefficient along with the foil heaving velocity (dh/dt). It is observed that the structural flexibility significantly increases the peak lift coefficient (as shown in the curve of Cu). In addition, within the time frame from $t/T_{turb}=2/8$ to $4/8$, the flexible foils achieve higher c_l than the rigid foil. As concluded by Xiao et al. (2012), it has a positive contribution to the time-mean efficiency over

one cycle if the force or moment has the same sign as the heaving or pitching velocity. Therefore, an increased c_l in the above mentioned time frames contributes positively to the overall efficiency.

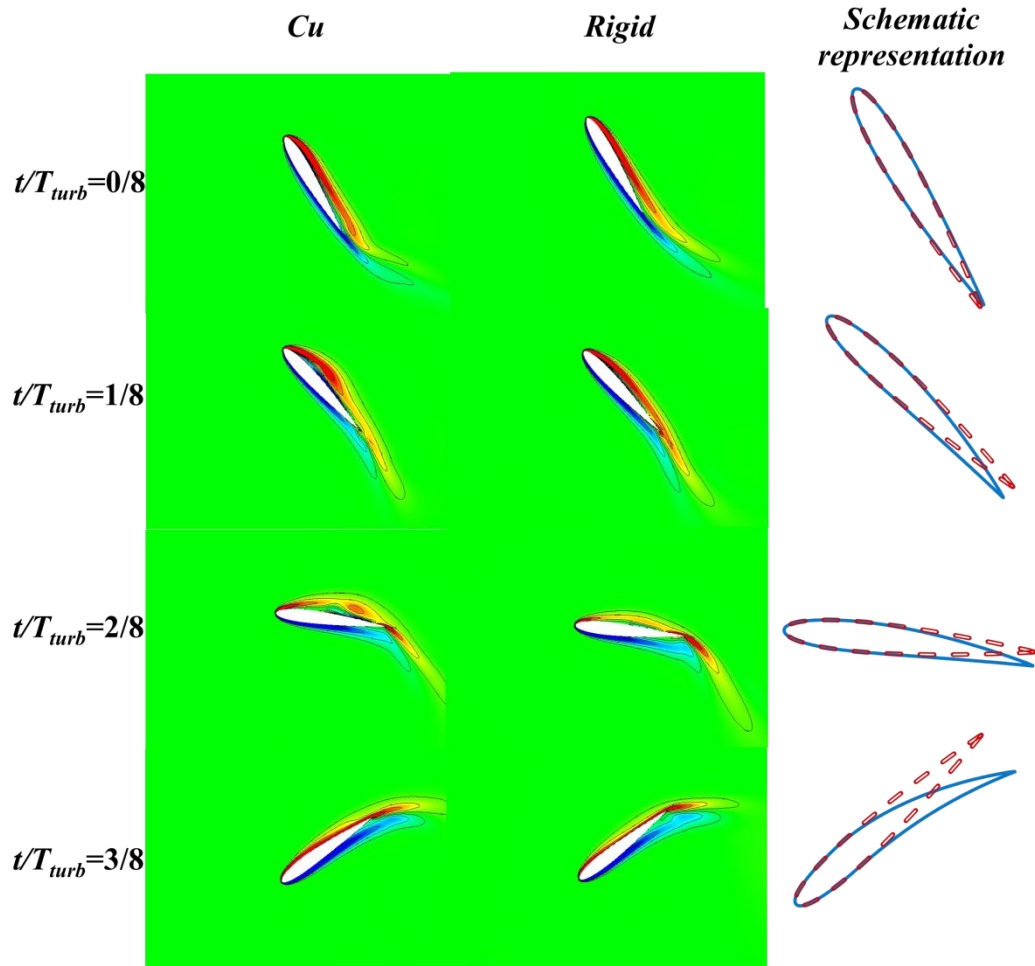


Figure 7. 5 Vorticity contours and schematic representation of foil kinematics for rigid and flexible foils at $f^*=0.18$; $\theta_0 = 60^\circ$ in half an oscillating period. In the schematic plot, the flexible foil is shown with blue solid lines, and the rigid foil is shown as red dashed lines.

The variations of the moment coefficient (Mz) and the pitch velocity ($d\theta/dt$) are presented in Fig.7.4 (c). A phase lag of 180° for Mz and $d\theta/dt$ is shown so that the pitching motion contributes negatively to the overall energy extraction. The flexibility of foil leads to a slight decrease in Mz during $t/T_{turb}=0/8$ and $3/8$, reduces

the power expenditure in pitching so that the overall energy harvesting performance is improved.

The instantaneous power coefficient is shown in Fig. 7.4 (d). It is clear that, with flexible foils, the positive instantaneous power is enhanced while the negative power is reduced.

Fig. 7.5 shows the vorticity contour for Cu, WC, and the rigid foil at $f^*=0.18$ and pitch amplitude of 60° within half an oscillating period. The most pronounced characteristic of the flexible foils compared to the rigid foil is the enhanced leading edge vortices. This is explained by the synchronization between the development of LEV and the foil deformation. As demonstrated in Fig. 7.5, at $t/T_{urb}=0$ the centre line of the foil is almost straight and the vorticity generated from the leading edge is attached to the upper surface of the foil. At $t/T_{urb}=1/8$ the hinder part of the foil starts bending downwards, making it hard for the leading edge vorticity to remain attached. This encourages the separation of the leading edge vorticity and the growth of the leading edge vortex. As indicated in Zhu (2011), the strength of leading edge vortices is closely associated with the energy harvesting performance. Enhanced leading edge separation and well-formed leading edge vortices usually lead to high efficiency (see Figs. 7 and 8 in Zhu, 2011). Based on this, a possible mechanism of performance improvement is the enhanced leading edge separation due to the structural deformations of the foil. With available results presented in this section, the flexible effect has little influence on the timing of LEV. As seen from Fig. 7.4 (b) and (c), the phase difference between a flexible blade and rigid blade for its lift and moment coefficients are not as remarkable as that of the amplitude difference. It can also be

confirmed by the contour plots in Fig. 7.5. It seems that the flexibility enlarges the leading edge flow separation and thus increases the LEV strength, leading to an increase of optimal f^* .

When studying the flexible wing or membrane problems, previous researchers (Heathcote et al., 2008; Gordnier et al., 2010; Chimakurthi et al., 2009) often used real materials with specific combinations of material properties (e.g. Young's modulus and density) as it did herein. On the other hand, several studies (Zhu, 2007; Chimakurthi et al., 2009) suggest that it is more interesting to decouple the Young's modulus coefficient and the density ratio and examine their effects independently. Hereby, it will study the effects of these two parameters separated by constructing some virtual materials with (a) a constant density ratio but variable Young's modulus coefficient and (b) a constant Young's modulus coefficient with different density ratios. In these cases, the foil oscillation reduced frequency is fixed as 0.18 and the pitching amplitude is set as 60° .

Table 7. 2 Case summary for virtual materials used to test Young's modulus effect. The Poisson ratio (ν) for all cases is 0.34.

Case	Young's modulus coefficient E_c	Effective stiffness Π	Natural frequency ratio FR
1	8.15×10^7	3.82×10^1	6.44
2	1.12×10^8	5.25×10^1	7.55
3	2.55×10^8	1.19×10^2	11.38
4	5.61×10^8	2.62×10^2	16.88
5	7.65×10^8	3.58×10^2	19.71
6	1.02×10^9	4.77×10^2	22.75

7.3.2 Young's modulus effect

In this part, six different Young's modulus coefficients ranging from 8.15×10^7 to 1.02×10^9 are investigated (further reduction of the Young's modulus coefficient leads to large foil deformations that are beyond the capacity of the linear structural model). The density ratio is set as 8.9. The effective stiffness for these cases varies from 3.82×10^1 to 4.77×10^2 , accordingly. The detailed parameters are summarized in Table 7.2.

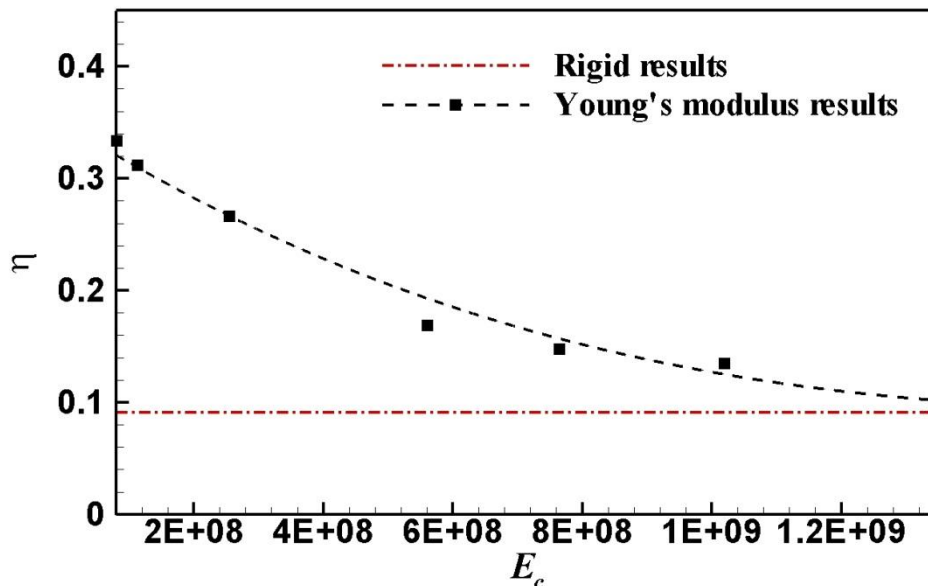
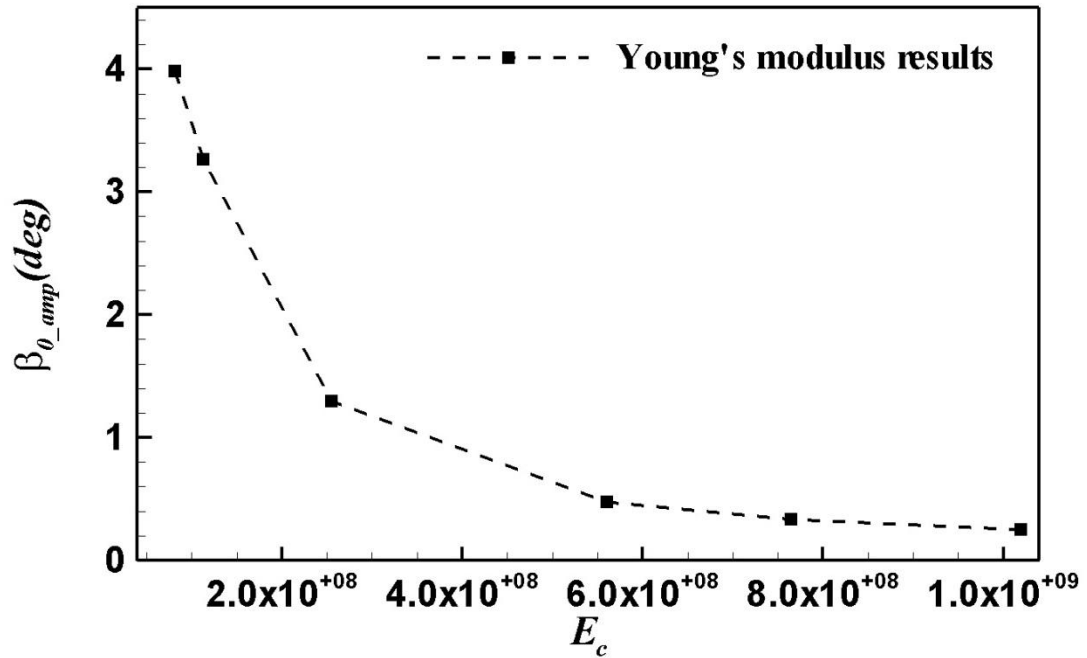


Figure 7. 6 Young's modulus effect on the efficiency of a flexible foil at $f^*=0.18$ and $\theta_0=60^\circ$.

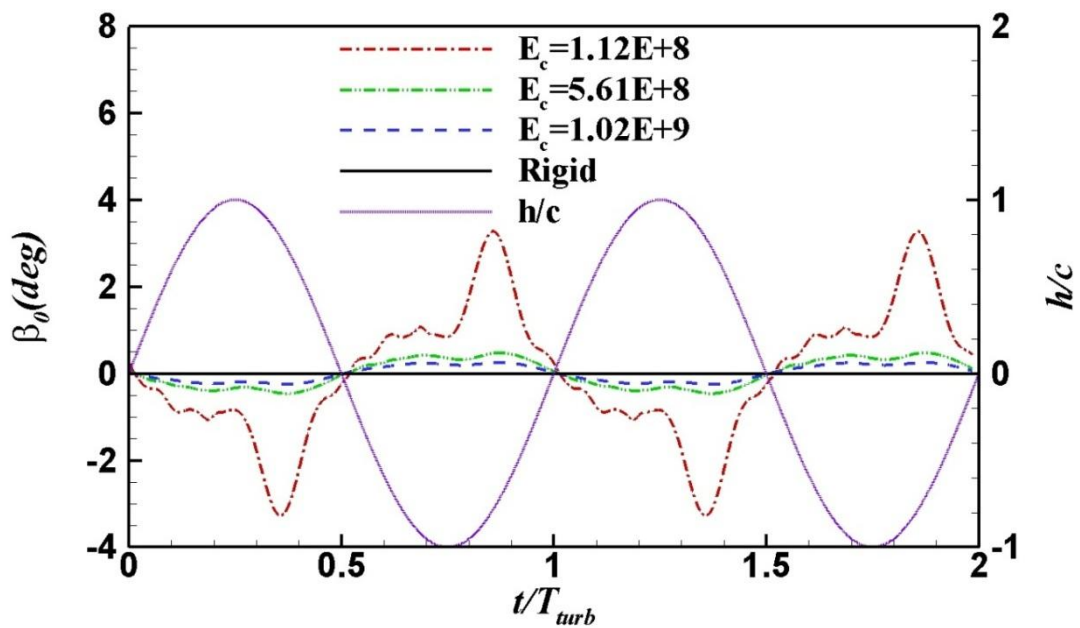
Fig. 7.6 shows the variation of the energy extraction efficiency with Young's modulus coefficient. With the increase of Young's modulus coefficient, the efficiency decreases and eventually approaches the rigid foil result. An empirical formulation is generated to quantify this curve and expressed (but only valid for present working condition, i.e. density ratio) as:

$$\eta = a_1 E_c^3 + a_2 E_c^2 + a_3 E_c + a_4, (8.15 \times 10^7 \leq E_c \leq 1.01 \times 10^9), \quad (7.2)$$

where $a_1 = -2 \times 10^{-29}$, $a_2 = 2 \times 10^{-19}$, $a_3 = -4 \times 10^{-10}$ and $a_4 = 0.3487$.

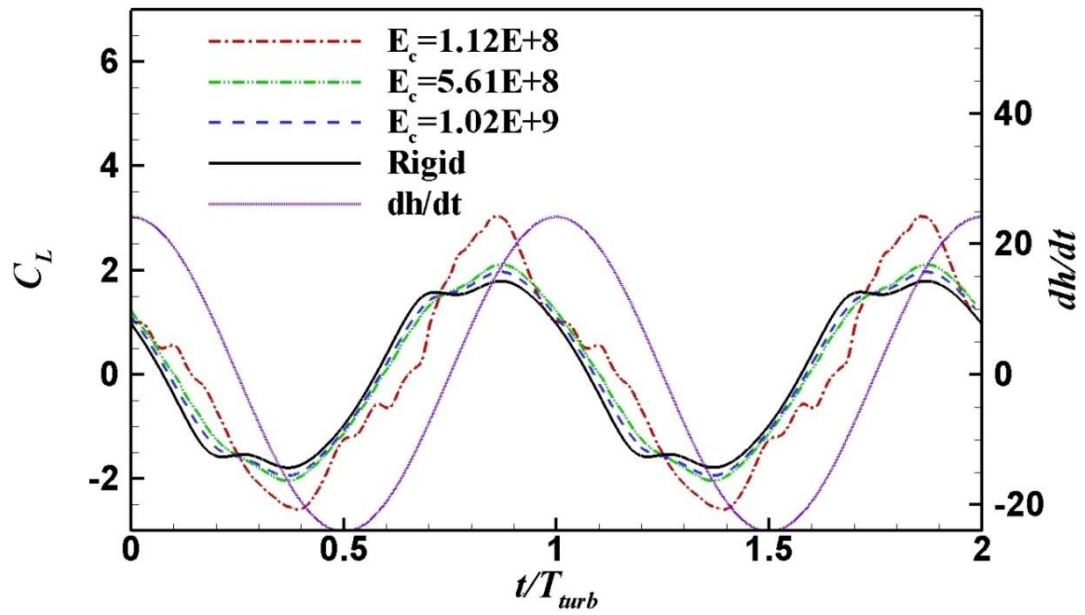


(a) Trailing edge displacement amplitude vs. Young's modulus coefficient

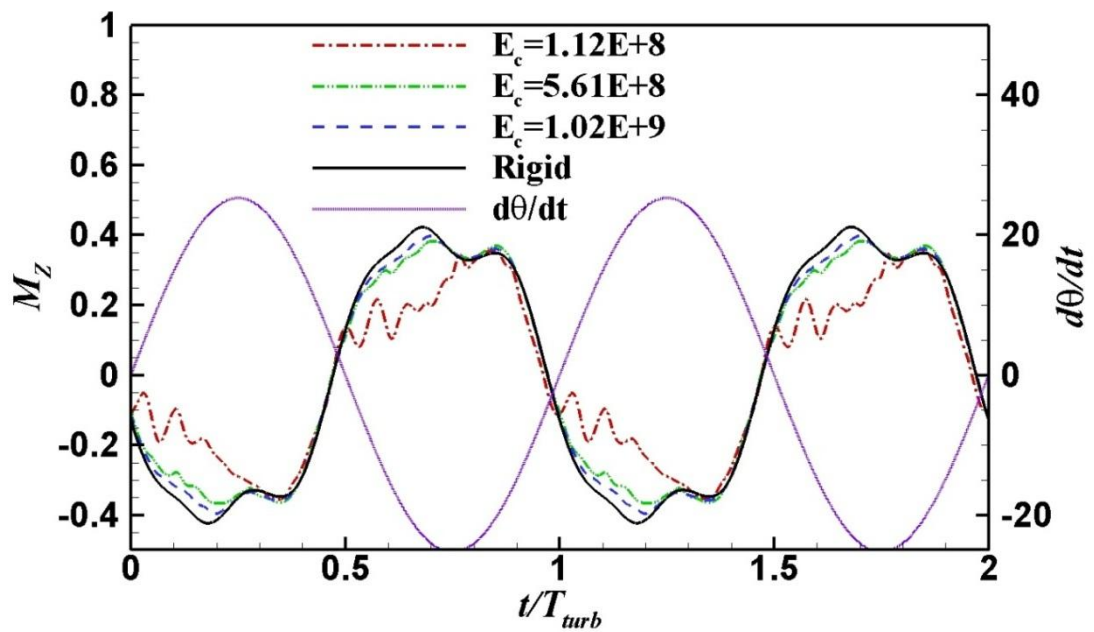


(b) Instantaneous trailing edge displacement

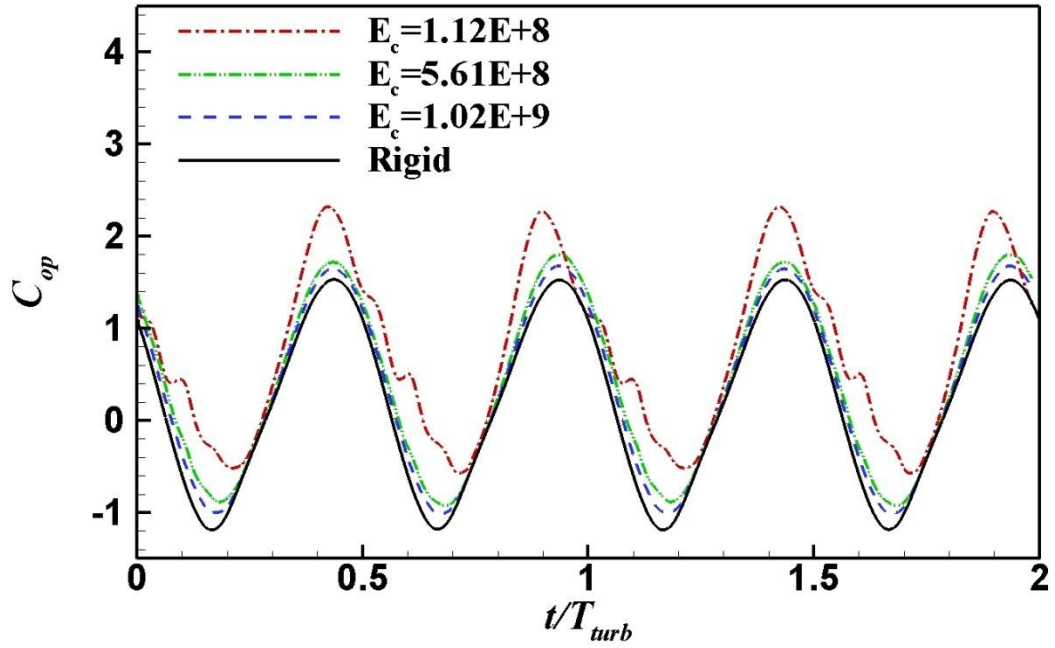
Figure 7.7 Trailing edge deformations of a flexible foil with different Young's modulus coefficient at $f^*=0.18$ and $\theta_0=60^\circ$.



(a) Lift coefficient and heaving velocity



(b) Moment coefficient and pitching velocity



(c) Power coefficient

Figure 7. 8 Time histories for Young’s modulus effect at $f^*=0.18$ and $\theta_0=60^\circ$.

Table 7. 3 Case summary for virtual materials used to test density ratio effect. The effective stiffness (II) and Poisson ratio (ν) for all cases are 5.25×10^1 and 0.34 respectively.

case	Density Ratio DR	Natural frequency ratio FR
1	7.0	8.54
2	8.9	7.55
3	12.0	6.53
4	15.6	5.72
5	20.0	5.05
6	30.0	4.13
7	70.0	2.70
8	700.0	0.85
9	1000.0	0.72
10	1200.0	0.65
11	1500.0	0.58

The peak trailing edge displacement at different values of Young's modulus coefficient is shown in Fig. 7.7 (a). Similar to the efficiency plot in Fig. 7.6, the displacement reduces rapidly with the increase of Young's modulus coefficient. This is well reflected by the profoundly smaller β_0 with larger E_c in Fig. 7.7 (b), where the instantaneous trailing displacement is shown within two oscillating periods.

The instantaneous lift coefficient (c_l), moment coefficient (M_z) and power coefficients (c_{op}) are analysed in Fig. 7.8. With the increase of Young's modulus coefficient, a drop of lift coefficient and moment coefficient can be seen in Fig. 7.8 (a) and (b). This leads to the drop of the instantaneous power Fig. 7.8 (c). It agrees well with the tendency of the time-mean energy efficiency as seen in Fig. 7.6.

7.3.3 Density ratio effect

In this part, nine density ratios ranging from 7 to 1500 are investigated with a fixed Young's modulus coefficient of 1.12×10^8 . The detailed parameters are listed in Table 7.3.

Fig. 7.9 shows the energy harvesting efficiency at various density ratios in a logarithmic graph. With the increase of the density ratio, the efficiency is dramatically decreased. As the density ratio is larger than 700, the foil switches from an energy extraction state (positive η) to an energy consumption state (negative η).

The variation of trailing edge displacement with density ratio is shown in Fig. 7.10 (a). The maximum displacement occurs at $DR=700$ with the magnitude of 13.45° , which actually is quite large compared with the pitching angle of 60° .

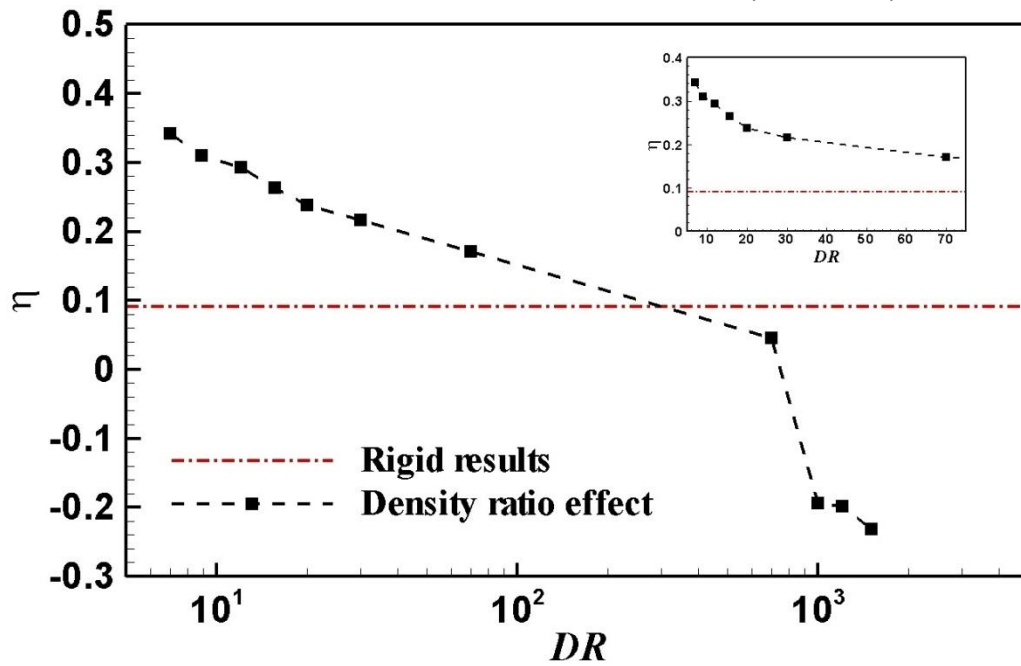
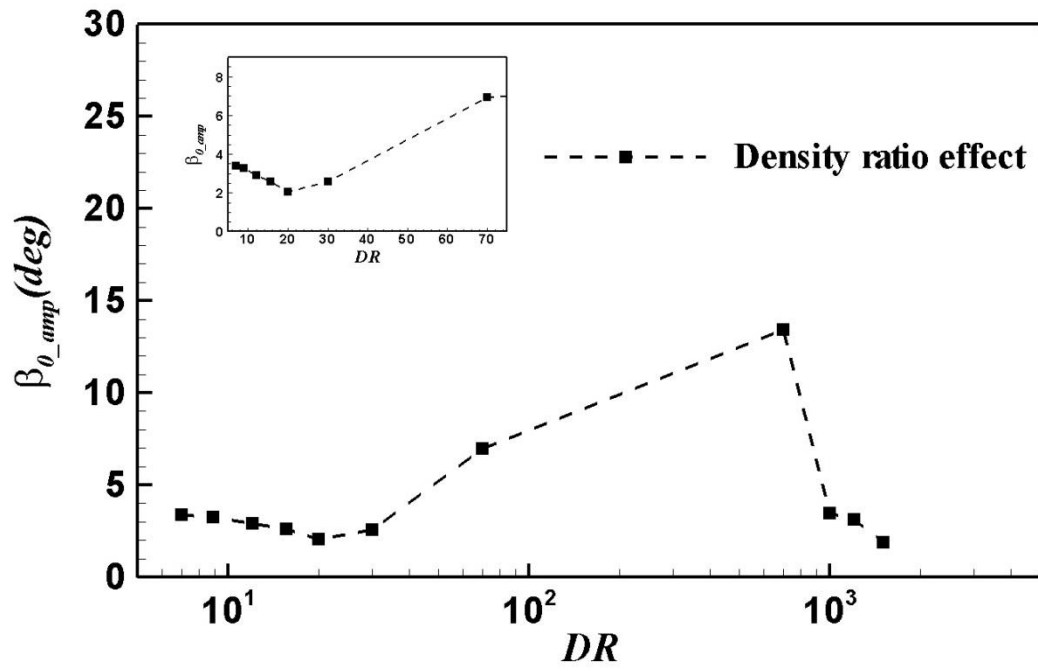
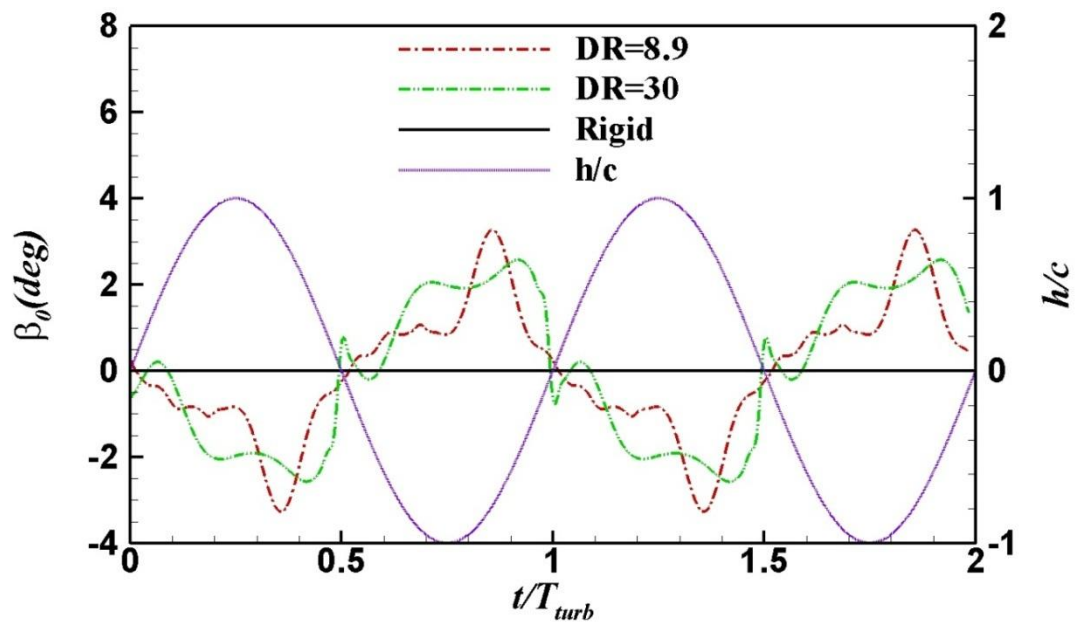


Figure 7. 9 Density ratio effect on the efficiency of a flexible foil at $f^*=0.18$ and $\theta_0=60^\circ$.

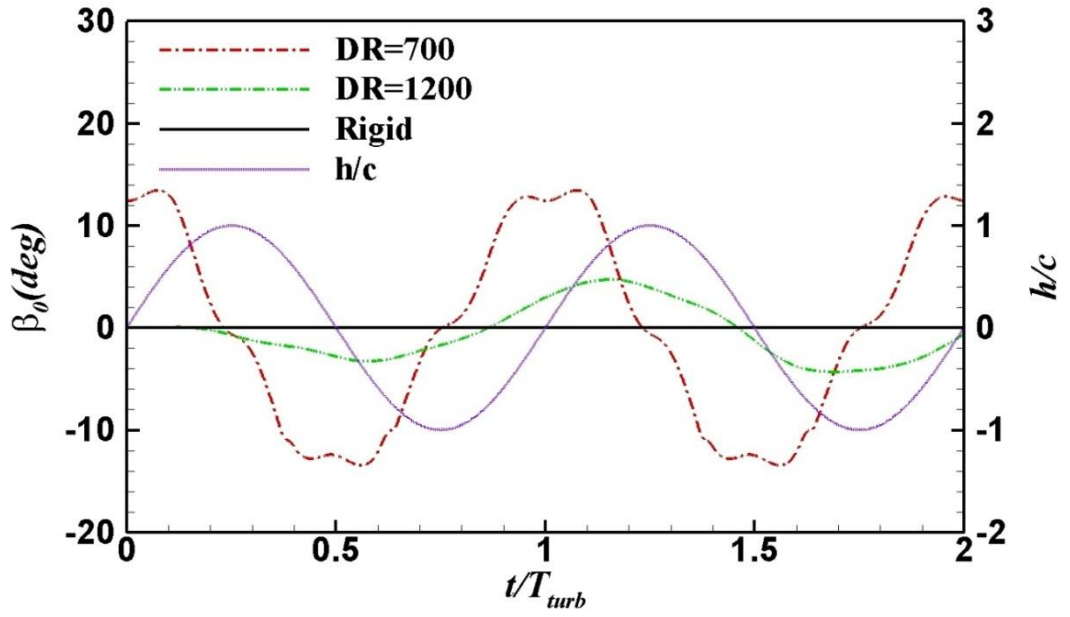
In Fig. 7.10 (b) and (c) the instantaneous trailing edge displacement with small density ratios ($DR=8.9$ and 30) and large DR s ($DR=700$, 1200 and rigid) are presented. Apart from the trend of peak beta variation with DR s, which is already shown in Fig. 7.10 (a), it is also noted that when the density ratio is near 700 , the instantaneous displacement profile presents a very regular sinusoid containing one dominant frequency. It is determined from the results that the phase difference between the trailing edge displacement angle and corresponding heave for small density ratios ($DR < 700$) is around 180° . However, when the density ratio has increased to 700 , the phase lag becomes 90° . This phase variation is consistent with the response of an oscillator around its natural frequency.



(a) Trailing edge displacement amplitude vs. density ratio

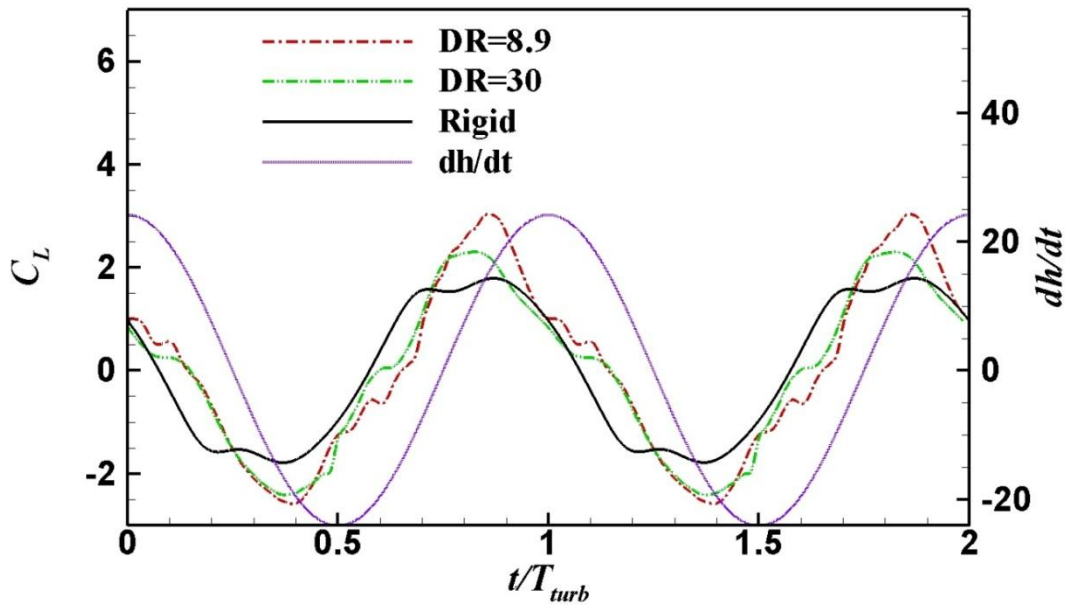


(b) Instantaneous trailing edge displacement ($DR=8.9$ and 30 , rigid foil)

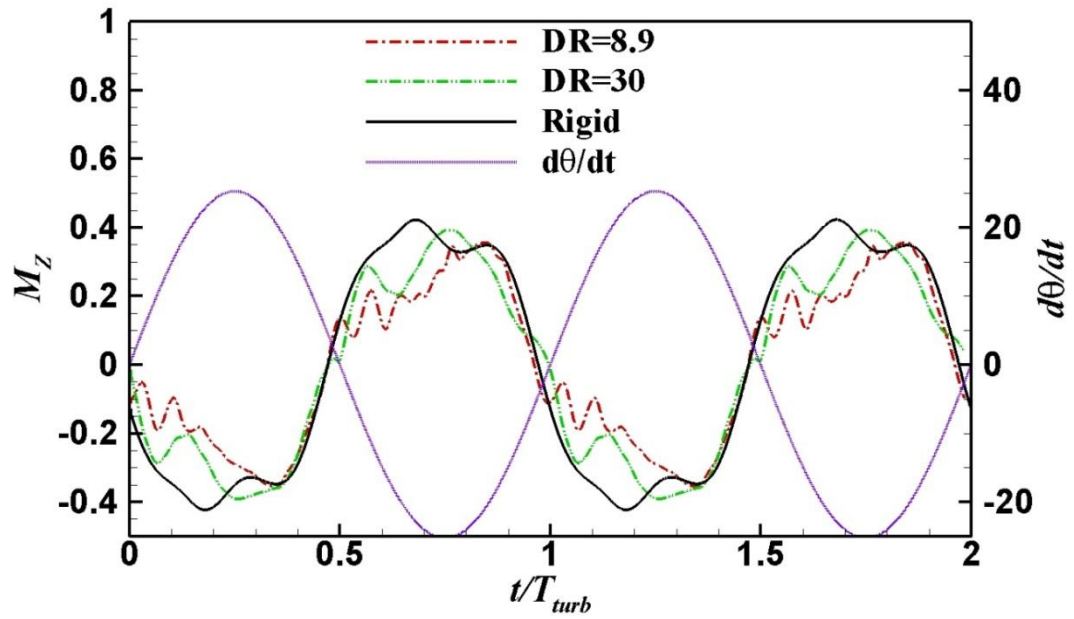


(c) Instantaneous trailing edge displacement ($DR=700$, 1200 and rigid foil)

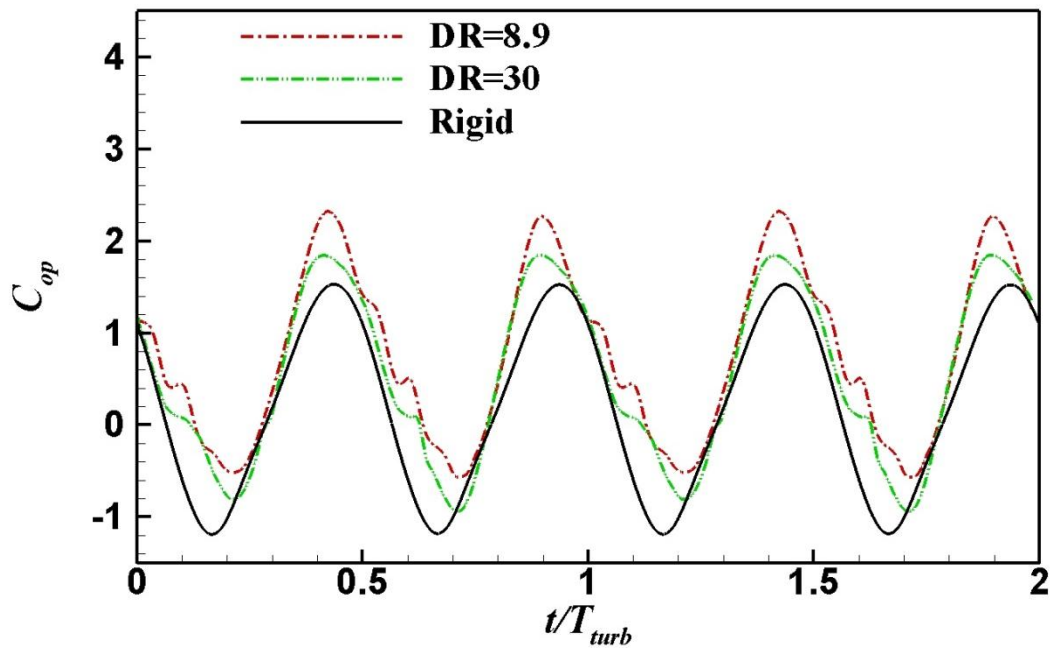
Figure 7. 10 Density ratio effect at $f^*=0.18$ and $\theta_0=60^\circ$.



(a) Lift coefficient and heaving velocity



(b) Moment coefficient and pitching velocity



(c) Power coefficient

Figure 7. 11 Time histories with low density ratios ($DR=8.9$ and 30) at $f^*=0.18$ and $\theta_0=60^\circ$.

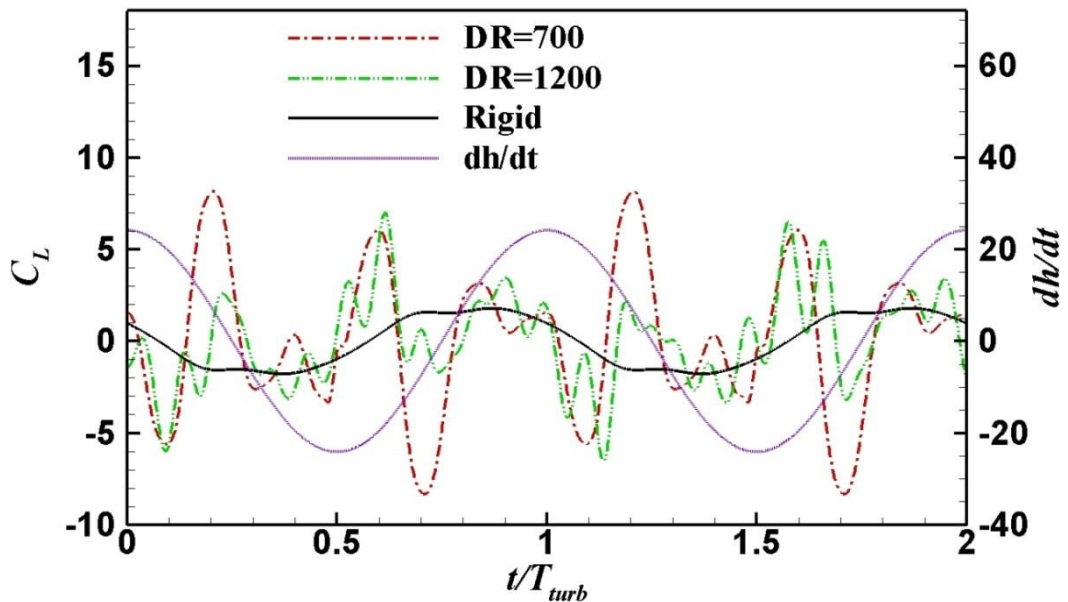
When DR is small, the foil deformation is mostly driven by the fluid forcing. For large values of DR , on the other hand, the effect of the inertia of the foil itself (herein

the inertia of the stiffener) becomes pronounced. To study the relative importance of these two effects, the present study considers the ratio between the mass of the stiffener and the added mass (which is a significant part of fluid forcing). In the heaving mode this ratio is estimated as:

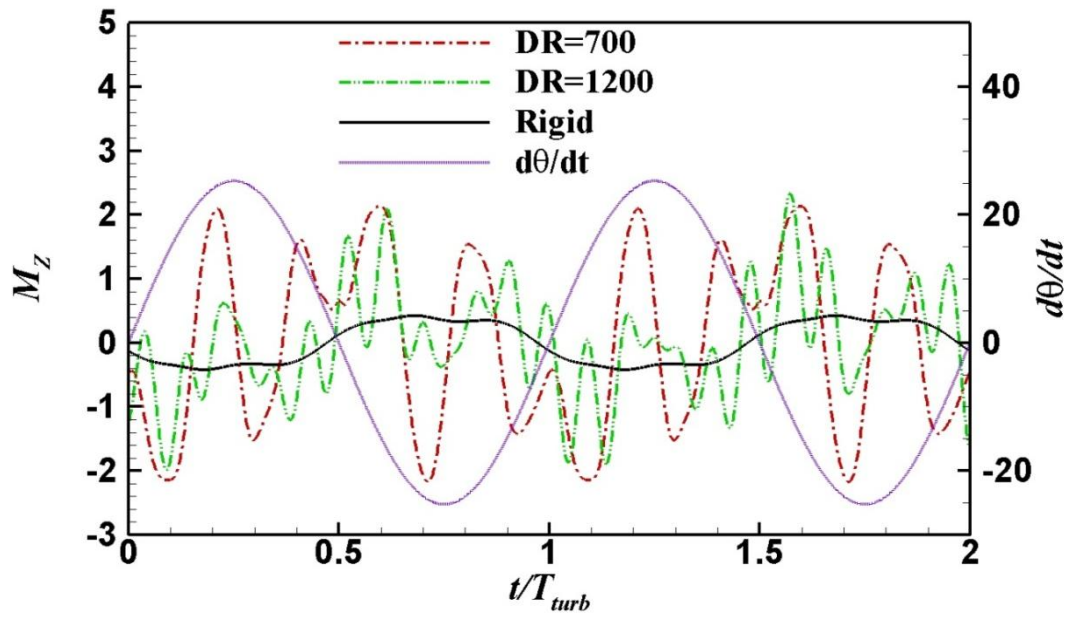
$$\frac{\rho_s c_{sf} T_{sf}}{\pi \rho_f \left(\frac{c}{2}\right)^2} = 8.6 \times 10^{-3} DR. \quad (7.3)$$

According to this parameter, the effect of the foil inertia surpasses the fluid forcing effect when the density ratio is higher than 116.

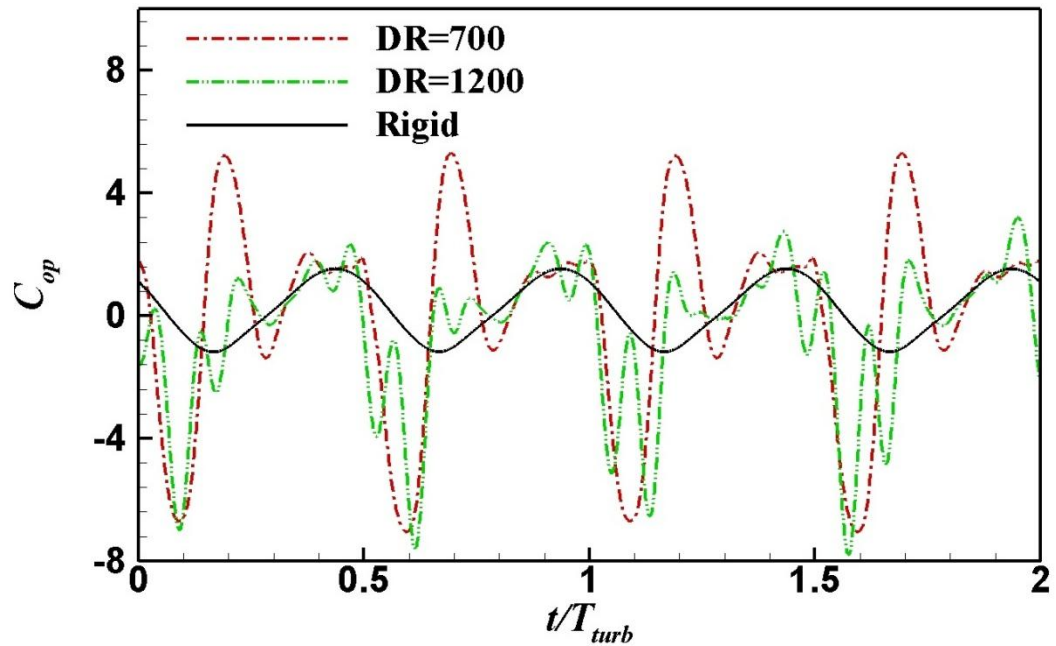
Fig. 7.11 (a) – (c) show the density ratio effect on the instantaneous lift, moment and power coefficients associated with low-density ratios ($DR=8.9$ and 30). It is clear that the difference of various density ratios mostly affects the peak lift coefficient, particularly within the time frames of $t/T_{turb}=2/8$ to $7/16$. In Fig. 7.12 (a)-(c), the instantaneous plots are shown at larger density ratios ($DR=700$ and 1200).



(a) Lift coefficient and heaving velocity



(b) Moment coefficient and pitching velocity



(c) Instantaneous power coefficient

Figure 7. 12 Time histories with large density ratios ($DR=700$ and 1200) at $f^*=0.18$ and $\theta_0=60^\circ$.

A large fluctuation occurs at $DR=700$, which is under a resonance condition. It is consist with the observation in Fig. 7.10 (a) that by increase the DR from 20, which is close to the resonance condition, the trailing edge displacement amplitude

increases, while by increase the DR from 700, which is far away from the resonance condition, the trailing edge displacement amplitude decreases.

From the vorticity plots in Fig. 7.13, it is seen that cases with smaller density ratio are characterized by enhanced development of LEV. An increased LEV generation, according to the discussion in Section 7.3.1, is beneficial to energy extraction. Moreover, within the time slot between $t/T_{turb}=2/8$ and $3/8$, the LEV re-attaches to the upper surface of the foil near the trailing edge, creating a counter-clockwise moment. It coincides with the pitching motion of the foil at that instant so that it provides an additional contribution to the energy harvesting. This beneficial effect is not achieved in cases with higher density ratio. In contrast, at these cases (e.g. $DR=700$ or 1200) during the counter-clockwise pitching motion of the foil there is significant vorticity attached to the lower surface of the foil near the trailing edge. The associated low pressure induces a clockwise moment so that there is a negative contribution to energy harvesting.

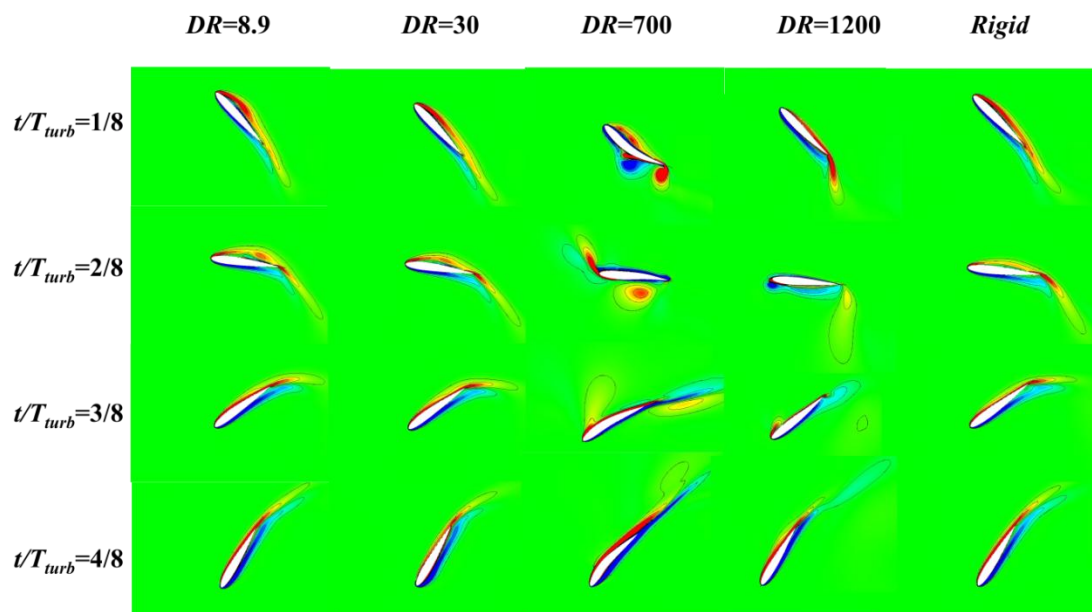


Figure 7. 13 Vorticity contours for density ratio effect at $f^*=0.18$ and $\theta_0 = 60^\circ$ in half an oscillating period.

A leading edge flexibility study, where a flexible internal structure is installed in the leading edge area, has also been performed. This structural design, however, leads to reduced efficiency according to the results (this is similar to the conclusion by Tian et al., 2014, in which it is suggested that passive deformability at the leading edge is not beneficial to energy harvesting). Specifically, the passively induced instantaneous leading edge deformation is 90° ahead of the foil heave displacement in phase. This leads to the decrease of the effective angle of attack at the leading edge and thus weakens the strength of LEV.

7.4 Summary

Using a fully-coupled FSI algorithm, this study numerically investigated the effect of structural flexibility upon the energy extraction capacity of an oscillating foil with realistic internal structure characterized by a stiffener near the trailing edge. The power generation predicted by the model is the net energy flux from the flow field to the foil. In a real system (such as the one proposed by Kinsey and Dumas (2012a, 2012b)), it is the extracted power minus the power input. For the stiffener, two types of real material (i.e. Copper and Tungsten Carbide) are tested with their different effective stiffness and density ratios. To distinguish the effects of Young's modulus coefficient and density ratio to the dynamic response and energy extraction efficiency, this study also studied cases with stiffener made of virtual materials with arbitrary Young's modulus and density. 5×10^7 CPU seconds calculated on ARCHIE-WeST high performance computing facilities of University of Strathclyde are needed for a typical case in this chapter.

The simulation shows that the passive structural flexibility in the vicinity of trailing edge is capable of enhancing the overall energy extraction performance. Up to 32.2% increase in the efficiency is achieved by using a foil with copper stiffener. This is attributed to the enhancement of leading edge vortices associated with the synchronization between vorticity generation/shedding and foil deformation. Within the range of parameters considered in this study, both Young's modulus and density ratio affect the amplitude as well as the phase lag between the deformation (characterized by the instantaneous trailing edge displacement angle) and heave displacements. At sufficiently large density ratios, such change causes the oscillating foil to switch from energy extraction into energy consumption. A resonance phenomenon is also observed when the natural frequency of the foil coincides with its heaving frequency.

The beneficial effect of structural flexibility in the energy extraction of a flapping foil is reminiscent of the similar performance enhancement of flapping foils propellers using deformable structures (see for example Zhu, 2011; Katz and Weihs, 1978; 1979). There are, however, fundamental differences between these two phenomena. According to Katz and Weihs (1978), the key mechanism of the propulsion efficiency increase in a chord-wisely flexible foil is that the overall fluid dynamic force is redirected more towards the front (see Fig. 6 in Zhu, 2011). Another mechanism is that in flexible propellers the leading edge separation is suppressed due to the reduction in the effective angle of attack at the leading edge. In contrast, the present research indicates that structural flexibility in an energy harvester actually encourages the development of LEV, leading to higher capacity in energy extraction.

Lastly, in the present study the flexible foil is modelled in two dimensions and thus only the bending motion is considered. In reality, a three-dimensional flexible wing may present a combined bending and twist motion under the external forces. Therefore, performing a fully three-dimensional fluid-structure interaction analysis to account for foil passive torsion and bending need to be studied and a more realistic device including electromechanical transducer, which in general requires a semi-passive or a fully passive device is necessary to be investigated in the future.

PART IV: Conclusions and Recommendations

Chapter 8: Conclusions and Recommendations

8.1 Conclusions

The main objective of the present research is to use bio-inspired flow control methods to enhance the efficiency of renewable turbines. The present studies focus on the Vertical Axis Turbine (VAT) and the Oscillating Foil Turbine (OFT) due to their low efficiency. Bio-inspired methods such as the fish tail active motion and the passive flexibility of butterfly wings are used to modify the traditional rigid turbine blade.

One of the studies in the present research aimed to explore the potential to improve Vertical Axis Turbine (VAT) energy harnessing efficiency by using modified blades with active and passive oscillating flaps. An oscillating flap is motivated by the relevant biomimetic studies on flapping wing propulsion or energy extraction. The present investigation concentrates on a VAT with a NACA0018 profile blade as its baseline turbine. Numerical simulations are carried out by solving incompressible unsteady Navier–Stokes equations in turbulence flow conditions. Computed results for the active oscillating flap show that under certain optimal flap geometry and flow conditions, the turbine power coefficient achieves 23.72% enhancement compared to the fixed blade turbine. A detailed analysis of the flow structure demonstrates that this is related to the vortex control by applying an oscillating flap. The results from the spring controlled passive oscillating flap turbine show an enhancement effect in terms of energy extraction efficiency at high tip speed ratios compared with the active oscillating flap turbine. A complicated oscillating motion of the flap is also observed and the angle range has a negative correlation with the tip speed ratio of the

turbine. After a fluid field analysis, the use of a passive controlled flap turbine could reduce the effect of the interaction between vortices and the blade at a large tip speed ratio, so that the negative torque region, as observed in the fixed and active controlled flap blade, could be restrained and the energy extraction efficiency could be enhanced.

Previous research on the flexible structure of flapping wings has shown an improved propulsion performance in comparison with rigid wings. However, not much is known about this function in terms of power efficiency modification for flapping wing energy devices. In order to study the role of the flexible wing deformation in the hydrodynamics of flapping wing energy devices, the two-dimensional flexible single and twin flapping wings in operation under the energy extraction conditions with a large Reynolds number of 10^6 has been computationally modelled. The blade flexibility for the study of a Bio-inspired Active Flow Control for Oscillating Foil Turbine by blade flexibility in the present research is predetermined based on a priori structural result which is different from a passive flexibility solution. Four different models are investigated with additional potential local distortions near the leading and trailing edges. The simulation results show that the flexible structure of a wing is beneficial for enhancing power efficiency by increasing the peaks of lift force over a flapping cycle, and tuning the phase shift between force and velocity to a favourable trend. Moreover, the impact of wing flexibility on efficiency is more profound at a low nominal effective angle of attack (AOA). At a typical flapping frequency $f^*=0.15$ and a nominal effective AOA of 10° , a flexible integrated wing generates 7.68% higher efficiency than a rigid wing. An even higher increase, around six times that of a rigid wing, is achievable if the nominal effective AOA is reduced to zero

degrees in feathering conditions. This is very attractive for a semi-actuated flapping energy system, where energy input is needed to activate the pitching motion. The results from the dual-wing study found that a parallel twin-wing device can produce more power compared to a single wing due to the strong flow interaction between the two wings.

A three-dimensional vertical axis wind turbine with fully passive flexible blades has also been numerically investigated in the present research. A realistic model of internal structures is used to obtain a certain degree of flexibility for the turbine blades. The blade structural deflection including bending and twisting is mainly investigated. External fluid pressure loads on to the blade surface and the energy extraction performance of the flexible blade turbine is also studied. A more flexible blade and a different strut method are also calculated to analyse the effective stiffness and the strut location effect. The simulation shows that the blade bending and twist motion all follow a sinusoidal function that varies with time. The bending and twist deflection amplitude is positively correlated with turbine tip speed ratio λ . The blade bending deflection is positive (i.e. has the same direction as the centrifugal force) in most of the conditions. This is because of the large magnitude of the centrifugal force acting on the vertical axis turbine blade with large tip speed ratio in air. Blade stress contours are also provided in the present study, which may benefit the structure industrial field. The blade maximum stress is around the strut location with middle strut. The Leading Edge Suction (LES) effect is observed in both rigid and flexible turbine blades which lead the blade to have a twist motion. An unstable of the fluid field and small fluctuations in the instantaneous moment coefficient curve are observed for the flexible blade. A larger bending and twist effect occurs for a more

flexible turbine blade. A flexible turbine blade with the tip strut method results in a decrease in the blade bending deflection compared with the middle strut method and most of the turbine blade region has large stress.

Following the work on an active controlled oscillating foil energy harvesting device with prescribed foil deformations, the fully-coupled dynamics of a flapping foil energy harvester with a passively deformable foil have also been investigated. To this end, the dynamics of a foil with a realistic internal structure (containing a rigid leading edge and a flexible trailing edge with a stiffener) in the energy harvesting regime through a Fluid Structure Interaction (FSI) scheme have been computationally studied. To examine the effect of different levels of flexibility, various materials (ranging from metals such as copper to virtual materials with arbitrary elasticity and density) for the stiffener have been tested. With the virtual materials, the effects of Young's modulus and density ratio have been studied. The simulation results show that flexibility around the trailing edge could enhance overall energy extraction performance. For example, with a copper stiffener, an increase of 32.2% in efficiency can be achieved at a high reduced frequency. The performance enhancement is mostly achieved in cases with a low Young's modulus and density ratio. A possible underlying mechanism is that the specific foil deformations in these cases encourage the generation and shedding of vortices from the foil leading edge, which is known to be beneficial to flow energy extraction.

8.2 Recommendations for future research

Due to the limited research period and limited calculation resources, the present studies cannot cover every relevant topic. There are also some assumptions and

simplifications in the present studies. Based on the results of the present studies, the following items have been pointed out as recommendations for future research.

- i. In the present studies, all of the governing functions of the active control motion for VAT and OFT are sinusoidal functions. It is believed that a non-sinusoidal function motion could achieve a better performance in some applications (Xiao et al., 2012). Thus, a non-sinusoidal function governed active control for VAT and OFT should be studied in the next stage.
- ii. A systematic investigation on the effect of the stiffness of the spring and the length of the spring slide bar of the passive flap controlled VAT need to be done in the future.
- iii. In the research on passive flow control for oscillating foil turbines by flexible material, the flexible foil is modelled in two dimensions and thus only the bending motion is considered. In reality, a three-dimensional flexible wing may present a combined bending and twist motion under the external forces. Therefore, performing a fully three-dimensional fluid-structure interaction analysis to account for foil passive torsion and bending should be the next task in the near future.
- iv. The research on the passive investigation of vertical axis turbines with flexible blades has only one blade. A vertical axis turbine usually has at least two blades to achieve a higher performance. Therefore, performing a fully two/three blades vertical axis turbine with passive bending and twist blade deflection needs to be studied in the next step.

- v. A more realistic device including an electromechanical transducer, which in general requires a semi-passive or a fully passive device, needs to be investigated in the future.
- vi. The research on the passive investigation of vertical axis turbines with a flexible blade uses air flow. It is believed that the blade bending and twist deflection motion should be different under different fluid mediums (such as water). Thus, the vertical axis turbine with a passive flexible blade under water should be investigated in the near future. A comprehensive study of the strut location impact will also be carried out in the next step.
- vii. The lift and drag forces of the entire VAT system and multi-blade OFT system are necessary to be calculated in the future work.

References

- Abiru, H., & Yoshitake, A. (2011). Study on a flapping wing hydroelectric power generation system. *Journal of Environment and Engineering*, 6(1), 178-186.
- Akgun, M. A., Kavukcuoglu, K., & Oktay, E. (2005). An Uncoupled Procedure For Wing Flutter Analysis. AIAC-2005-089, Ankara International Aerospace Conference.
- Almohammadi, K. M., Ingham, D. B., Ma, L., & Pourkashan, M. (2013). Computational fluid dynamics (CFD) mesh independency techniques for a straight blade vertical axis wind turbine. *Energy*, 58, 483-493.
- Alonso J. J., and Jameson, A. (1994) Fully-Implicit Time-Marching Aeroelastic Solutions. AIAA Paper 94-0056.
- Anderson, J. M., Streitlien, K., Barrett, D. S., & Triantafyllou, M. S. (1998). Oscillating foils of high propulsive efficiency. *Journal of Fluid Mechanics*, 360(1), 41-72.
- Barlas, T., van Wingerden, J. W., Hulskamp, A., & van Kuik, G. (2008). Closed-loop control wind tunnel tests on an adaptive wind turbine blade for load reduction. *Proceedings of the 46th AIAA/ASME*.
- Bazilevs, Y., Hsu, M. C., Kiendl, J., Wüchner, R., & Bletzinger, K. U. (2011). 3D simulation of wind turbine rotors at full scale. Part II: Fluid–structure interaction modeling with composite blades. *International Journal for Numerical Methods in Fluids*, 65(1 - 3), 236-253.
- Ben-Harav, A., & Greenblatt, D. (2014). Plasma - based feed - forward dynamic

stall control on a vertical axis wind turbine. *Wind Energy*.

Beri, H., & Yao, Y. (2011a). Effect of camber airfoil on self starting of vertical axis wind turbine. *Journal of Environmental Science and Technology*, 4(3), 302-312.

Beri, H., & Yao, Y. (2011b). Double multiple streamtube model and numerical analysis of vertical axis wind turbine. *Energy and Power Engineering*, 3(03), 262.

Bir, G. S., Lawson, M. J., & Li, Y. (2011). Structural design of a horizontal-axis tidal current turbine composite blade. In *ASME 2011 30th International Conference on Ocean, Offshore and Arctic Engineering* (pp.797-808). American Society of Mechanical Engineers.

Blackwell, B. F. (1974). Vertical-axis wind turbine: how it works. Sandia National Laboratory, Technical Report No. SLA-74-0160, Albuquerque, NM, USA.

Bohbot, D. D. (2001). Time domain analysis of two D.O.F. airfoil flutter using an Euler/Turbulent Navier-Stokes implicit solver. *International Forum on Aeroelasticity and Structural Dynamics*, Madrid, Spain.

Brøndsted, P., Lilholt, H., & Lystrup, A. (2005). Composite materials for wind power turbine blades. *Annu. Rev. Mater. Res.*, 35, 505-538.

Butbul, J., MacPhee, D., & Beyene, A. (2015). The impact of inertial forces on morphing wind turbine blade in vertical axis configuration. *Energy Conversion and Management*, 91, 54-62.

Campobasso, M. S., & Drofelnik, J. (2012). Compressible Navier–Stokes analysis of an oscillating wing in a power-extraction regime using efficient low-speed

preconditioning. *Computers & Fluids*, 67, 26-40.

Camporeale, S. M., & Magi, V. (2000). Streamtube model for analysis of vertical axis variable pitch turbine for marine currents energy conversion. *Energy Conversion and Management*, 41(16), 1811-1827.

Cardona, J. L. (1984). Flow curvature and dynamic stall simulated with an aerodynamic free-vortex model for VAWT. *Wind Engineering*, 8, 135-143.

Castelli, M. R., Dal Monte, A., Quaresimin, M., & Benini, E. (2013). Numerical evaluation of aerodynamic and inertial contributions to Darrieus wind turbine blade deformation. *Renewable Energy*, 51, 101-112.

Castelli, M. R., De Betta, S., & Benini, E. (2012b). Proposal of a means for reducing the torque variation on a vertical axis water turbine by increasing the blade number. *International Journal of Engineering and Applied Sciences*, 6, 221-227.

Castelli, M. R., De Betta, S., & Benini, E. (2012c). Numerical Analysis of the Performance of a Shrouded Vertical-Axis Water Turbine based on the NACA 0025 Blade Profile. In *Proceedings of World Academy of Science, Engineering and Technology* (No. 63). World Academy of Science, Engineering and Technology.

Castelli, M. R., Englaro, A., & Benini, E. (2011). The Darrieus wind turbine: Proposal for a new performance prediction model based on CFD. *Energy*, 36(8), 4919-4934.

Castelli, M. R., Simioni, G., & Benini, E. (2012a). Numerical Analysis of the Influence of Airfoil Asymmetry on VAWT Performance. *World Academy of Science, Engineering and Technology*, 61, 312-321.

Chenna, V. (2014). *Fatigue-Induced Failure in Horizontal-Axis Wind-Turbine (HAWT) Blades and HAWT Drivetrain Gears*. Master thesis, Thesis for MSc of Clemson University, USA.

Chimakurthi, S. K., Tang, J., Palacios, R., S. Cesnik, C. E., & Shyy, W. (2009). Computational aeroelasticity framework for analyzing flapping wing micro air vehicles. *AIAA Journal*, 47(8), 1865-1878.

Combes, S. A., & Daniel, T. L. (2003a). Flexural stiffness in insect wings I. Scaling and the influence of wing venation. *Journal of Experimental Biology*, 206(17), 2979-2987.

Combes, S. A., & Daniel, T. L. (2003b). Flexural stiffness in insect wings II. Spatial distribution and dynamic wing bending. *Journal of Experimental Biology*, 206(17), 2989-2997.

Danao, L. A., Edwards, J., Eboibi, O., & Howell, R. (2014). A numerical investigation into the influence of unsteady wind on the performance and aerodynamics of a vertical axis wind turbine. *Applied Energy*, 116, 111-124.

Daniel, T. L., & Combes, S. A. (2002). Flexible wings and fins: bending by inertial or fluid-dynamic forces? *Integrative and Comparative Biology*, 42(5), 1044-1049.

Darrieus, M. G. J. (1931). U.S. Patent No. 1,835,018. Washington, DC: U.S. Patent and Trademark Office.

Davids, S. T. (1999). *A computational and experimental investigation of a flutter generator*. Doctoral Dissertation, Monterey, California: Naval Postgraduate School.

Daynes, S., & Weaver, P. M. (2011). A shape adaptive airfoil for a wind turbine blade. In *SPIE Smart Structures and Materials+ Nondestructive Evaluation and Health Monitoring* (pp.79790H-79790H). International Society for Optics and Photonics.

Daynes, S., Weaver, P. M., & Potter, K. D. (2009). Aeroelastic study of bistable composite airfoils. *Journal of Aircraft*, 46(6), 2169-2174.

DeLaurier, J. D., & Harris, J. M. (1982). Experimental study of oscillating-wing propulsion. *Journal of Aircraft*, 19(5), 368-373.

Deng, J., Shao, X. M., & Yu, Z. S. (2007). Hydrodynamic studies on two traveling wavy foils in tandem arrangement. *Physics of Fluids*, 19, 113-104.

Deyuan, L., Zhiquan, Y., Yan, C., & Nengsheng, B. (2003). Load spectrum and fatigue life analysis of the blade of horizontal axis wind turbine. *Wind Engineering*, 27(6), 495-506.

Drees, H. M. (1978). The cycloturbine and its potential for broad application. In *Proceedings of 2nd International Symposium on Wind Energy Systems, Amsterdam, The Netherlands* (pp.3-6).

Drewry, M. A., & Georgiou, G. A. (2007). A review of NDT techniques for wind turbines. *Insight-Non-Destructive Testing and Condition Monitoring*, 49(3), 137-141.

Faure T. D., Pratt B. D. and Swan D. H. (1986). The Darrieus hydraulic turbine: model and field experiments. *Proceedings of the 4th ASME International Symposium for Hydro Power and Fluid Machinery, San Francisco*, 43, 123–129.

Feng, F., Li, S., Li, Y., & Tian, W. (2012). Numerical simulation on the aerodynamic effects of blade icing on small scale straight-bladed VAWT. *Physics Procedia*, 24, 774-780.

Fish, F. E. and Lauder G. V., (2006) Passive and active flow control by swimming fishes and mammals. *Annual Review of Fluid Mechanics*, 38, 193-224.

Gaden, D. L., & Bibeau, E. L. (2010). A numerical investigation into the effect of diffusers on the performance of hydro kinetic turbines using a validated momentum source turbine model. *Renewable Energy*, 35(6), 1152-1158.

Gao, C., Luo, S., Liu, F., & Schuster, D. M. (2005). Calculation of airfoil flutter by an Euler method with approximate boundary conditions. *AIAA Journal*, 43(2), 295-305.

Garrick, I. E. (1937). Propulsion of a flapping and oscillating airfoil. National Bureau of Standards, NACA-REPORT-567.

Ge, R., Wang, B., Mou, C., & Zhou, Y. (2010). Deformation characteristics of corrugated composites for morphing wings. *Frontiers of Mechanical Engineering in China*, 5(1), 73-78.

Georgescu, S. C., Georgescu, A. M., Cosoiu, C. I., & Costinas, S. (2013). Influence of duct geometry on Achard turbine efficiency. In *Advanced Topics in Electrical Engineering (ATEE)*, 2013 8th International Symposium on (pp.1-6). IEEE.

Gordnier, R. E., Attar, P. J., Chimakurthi, S. K., & Cesnik, C. E. (2010). Implicit LES simulations of a flexible flapping wing. *AIAA Paper*, 2960.

Gordnier, R. E., Chimakurthi, S. K., Cesnik, C. E., & Attar, P. J. (2013). High-fidelity aeroelastic computations of a flapping wing with spanwise flexibility. *Journal of Fluids and Structures*, 40, 86-104.

Greenblatt, D., Ben-Harav, A., & Mueller-Vahl, H. (2014). Dynamic stall control on a vertical-axis wind turbine using plasma actuators. *AIAA Journal*, 52(2), 456-462.

Greenblatt, D., Schulman, M., & Ben-Harav, A. (2012). Vertical axis wind turbine performance enhancement using plasma actuators. *Renewable Energy*, 37(1), 345-354.

Gretton, G. I. (2009). The hydrodynamic analysis of a vertical axis tidal current turbine. Ph.D. Thesis, University of Edinburgh.

Gretton, G. I., Bruce, T., & Ingram, D. M. (2009). Hydrodynamic modelling of a vertical axis tidal current turbine using CFD. In *Proceedings of the 8th European Wave and Tidal Energy Conference* (pp.468-476).

Griffin, O. M. (1971). The unsteady wake of an oscillating cylinder at low Reynolds number. *Journal of Applied Mechanics*, 38(4), 729-738.

Grylls, W., Dale, B., & Sarre, P. E. (1978). A theoretical and experimental investigation into the variable pitch vertical axis wind turbine. In *Proceedings of 2nd International Symposium on Wind Energy Systems*, Amsterdam, The Netherlands (pp.3-6).

Haar, J. (2011). U.S. Patent No. 7,988,413. Washington, DC: U.S. Patent and Trademark Office.

Hameed, M. S., and Afaq, S. K. (2013). Design and analysis of a straight bladed vertical axis wind turbine blade using analytical and numerical techniques. *Ocean Engineering*, 57, 248-255.

Hansen, M. O. (2013). *Aerodynamics of wind turbines*. Routledge.

Harper, P. W., & Hallett, S. R. (2015). Advanced numerical modelling techniques for the structural design of composite tidal turbine blades. *Ocean Engineering*, 96, 272-283.

Hau, E., & Von Renouard, H. (2013). *Wind turbines: fundamentals, technologies, application, economics*. Springer Science & Business Media.

Heathcote, S., & Gursul, I. (2007). Flexible flapping airfoil propulsion at low Reynolds numbers. *AIAA Journal*, 45(5), 1066-1079.

Heathcote, S., Wang, Z., & Gursul, I. (2008). Effect of spanwise flexibility on flapping wing propulsion. *Journal of Fluids and Structures*, 24(2), 183-199.

Helen. A. N. (2008). *The Application of CFD in the Analysis of Vortex Induced Vibration on a Riser*. MSc Thesis, Cranfield University.

Hirsch, H., & Mandal, A. C. (1987). A cascade theory for the aerodynamic performance of Darrieus wind turbines. *Wind Engineering*, 11(3), 164-175.

Holme, O. (1977). A contribution to the aerodynamic theory of the vertical-axis wind turbine. In *International Symposium on Wind Energy Systems* (Vol. 1, p.4).

Huxham, G. H., Cochard, S., & Patterson, J. (2012). Experimental parametric investigation of an oscillating hydrofoil tidal stream energy converter. In *Proceedings*

Hwang, I. S., Lee, Y. H., & Kim, S. J. (2009). Optimization of cycloidal water turbine and the performance improvement by individual blade control. *Applied Energy*, 86(9), 1532-1540.

Hwang, I. S., Min, S. Y., Jeong, I. O., Lee, Y. H., & Kim, S. J. (2006). Efficiency improvement of a new vertical axis wind turbine by individual active control of blade motion. In *Smart Structures and Materials* (pp.617311-617311). International Society for Optics and Photonics.

Islam, M., Ting, D. S. K., & Fartaj, A. (2008). Aerodynamic models for Darrieus-type straight-bladed vertical axis wind turbines. *Renewable and Sustainable Energy Reviews*, 12(4), 1087-1109.

Islam, M., Ting, D. S., & Fartaj, A. (2007a). Desirable airfoil features for smaller-capacity straight-bladed VAWT. *Wind Engineering*, 31(3), 165-196.

Islam, M., Ting, D. S., & Fartaj, A. (2007b). Design of a special-purpose airfoil for smaller-capacity straight-bladed VAWT. *Wind Engineering*, 31(6), 401-424.

Isogai, K. (1979). On the transonic-dip mechanism of flutter of a sweptback wing. *AIAA Journal*, 17(7), 793-795.

Jameson, A., Schmidt, W., & Turkel, E. (1981). Numerical solutions of the Euler equations by finite volume methods using Runge-Kutta time-stepping schemes. *AIAA Paper*, 1259, 1981.

Jing, F., Sheng, Q., & Zhang, L. (2014). Experimental research on tidal current

vertical axis turbine with variable-pitch blades. *Ocean Engineering*, 88, 228-241.

Jones, K. D., & Platzer, M. F. (1997). Numerical computation of flapping-wing propulsion and power extraction. *AIAA Journal*, 97, 08-26.

Jones, K. D., Davids, S., & Platzer, M. F. (1999). Oscillating-wing power generator.

Jones, K. D., Lindsey, K., & Platzer, M. F. (2003). An investigation of the fluid-structure interaction in an oscillating-wing micro-hydropower generator. *Advances in Fluid Mechanics*, 36, 73-84.

Katz, J., & Weihs, D. (1978). Hydrodynamic propulsion by large amplitude oscillation of an airfoil with chordwise flexibility. *Journal of Fluid Mechanics*, 88(03), 485-497.

Katz, J., & Weihs, D. (1979). Large amplitude unsteady motion of a flexible slender propulsor. *Journal of Fluid Mechanics*, 90(04), 713-723.

Khalak, A., & Williamson, C. H. K. (1996). Dynamics of a hydroelastic cylinder with very low mass and damping. *Journal of Fluids and Structures*, 10(5), 455-472.

Khalak, A., & Williamson, C. H. K. (1999). Motions, forces and mode transitions in vortex-induced vibrations at low mass-damping. *Journal of Fluids and Structures*, 13(7), 813-851.

Khan, M. J., Bhuyan, G., Iqbal, M. T., & Quaicoe, J. E. (2009). Hydrokinetic energy conversion systems and assessment of horizontal and vertical axis turbines for river and tidal applications: A technology status review. *Applied Energy*, 86(10), 1823-1835.

Khan, M. J., Iqbal, M. T., & Quaicoe, J. E. (2006). A technology review and simulation based performance analysis of river current turbine systems. In *Electrical and Computer Engineering, 2006. CCECE'06. Canadian Conference on* (pp.2288-2293). IEEE.

Kiho, S., Shiono, M., & Suzuki, K. (1996). The power generation from tidal currents by Darrieus turbine. *Renewable Energy*, 9(1), 1242-1245.

Kinsey, T., & Dumas, G. (2008). Parametric study of an oscillating airfoil in a power-extraction regime. *AIAA Journal*, 46(6), 1318-1330.

Kinsey, T., & Dumas, G. (2012a). Computational Fluid Dynamics Analysis of a Hydrokinetic Turbine Based on Oscillating Hydrofoils. *Journal of Fluids Engineering*, 134(2), 021104.

Kinsey, T., & Dumas, G. (2012b). Optimal Tandem Configuration for Oscillating-Foils Hydrokinetic Turbine. *Journal of Fluids Engineering*, 134(3), 031103.

Kinsey, T., & Dumas, G. (2012c). Three-dimensional effects on an oscillating-foil hydrokinetic turbine. *Journal of Fluids Engineering*, 134(7), 071105.

Kinsey, T., & Dumas, G. (2014). Optimal operating parameters for an oscillating foil turbine at Reynolds number 500,000. *AIAA Journal*, 52(9), 1885-1895.

Kinsey, T., Dumas, G., Lalande, G., Ruel, J., Mehut, A., Viarouge, P., Lemay, J., and Jean, Y. (2011). Prototype testing of a hydrokinetic turbine based on oscillating hydrofoils. *Renewable Energy*, 36(6), 1710-1718.

Kirke, B. (2006). Developments in ducted water current turbines. *Tidal Paper*, (25-

04).

Kiwata, T., Yamada, T., Kita, T., Takata, S., Komatsu, N., & Kimura, S. (2010). Performance of a vertical axis wind turbine with variable-pitch straight blades utilizing a linkage mechanism. *Journal of Environment and Engineering*, 5(1), 213-225.

Klimas, P. C. (1982). Darrieus rotor aerodynamics. *ASME, Transactions, Journal of Solar Energy Engineering*, 104, 102-105.

Kolonay, R. M. (2001). Computational aeroelasticity. RTA-NATO, The Applied Vehicle Technology Panel, General Electric Corporate Research & Development Center Ankara, Turkey.

Kong, C., Bang, J., & Sugiyama, Y. (2005). Structural investigation of composite wind turbine blade considering various load cases and fatigue life. *Energy*, 30(11), 2101-2114.

Labbé, D. F. L., & Wilson, P. A. (2007). A numerical investigation of the effects of the spanwise length on the 3-D wake of a circular cylinder. *Journal of Fluids and Structures*, 23(8), 1168-1188.

Lachenal, X., Daynes, S., & Weaver, P. M. (2013). Review of morphing concepts and materials for wind turbine blade applications. *Wind Energy*, 16(2), 283-307.

Larsen, H. C. (1975). Summary of a vortex theory for the cyclogiro. In *Proceedings of the 2nd US National conference on Wind Engineering Research*.(1975-8), Colorado State University (Vol. 8, p.1).

Le, T. Q., & Ko, J. H. (2015). Effect of hydrofoil flexibility on the power extraction of a flapping tidal generator via two-and three-dimensional flow simulations. *Renewable Energy*, 80, 275-285.

Le, T. Q., Ko, J. H., & Byun, D. (2013). Morphological effect of a scallop shell on a flapping-type tidal stream generator. *Bioinspiration & Biomimetics*, 8(3), 036009.

Li, Z. (2002). Parallel Computations Of 3d Unsteady Compressible Euler Equations With Structural Coupling. Master's Candidate July, 19.

Liao, J. C (2007). A review of fish swimming mechanics and behaviour in altered flows. *Philosophical Transactions of the Royal Society B: Biological Sciences*, 362(1487), 1973-1993.

Lifante, C., Frank, T., & Kuntz, M. (2007). Extension and Validation of the CFX Cavitation Model for Sheet and Tip Vortex Cavitation on Hydrofoils. "In 5th Joint FZR & ANSYS Workshop" Multiphase Flows: Simulation, Experiment and Application.

Lindsey, K. (2002). A feasibility study of oscillating-wing power generators. MSc. Thesis, Naval Postgraduate School Monterey Ca.

Liu, F. (1991) Numerical Calculation of Turbomachinery Cascade Flows. Ph.D. thesis, Princeton University, May.

Liu, F., & Ji, S. (1996). Unsteady flow calculations with a multigrid Navier-Stokes method. *AIAA Journal*, 34(10), 2047-2053.

Liu, H. (2005). Simulation-based biological fluid dynamics in animal locomotion.

Applied Mechanics Reviews, 58, 269-282.

Liu, J. (2011). Experimental Study and Numerical Simulation of Passive Variable-Pitch Vertical Axis Turbine. MEng dissertation, Harbin Engineering University, Harbin, China.

Liu, W., Xiao, Q., & Cheng, F. (2013). A bio-inspired study on tidal energy extraction with flexible flapping wings. *Bioinspiration & Biomimetics*, 8(3), 036011.

Liu, W., Xiao, Q., & Zhu, Q. (In Press). A coupled fluid-structure study of the passive flexibility effect on oscillating foil energy harvester. *AIAA Journal*.

Mandal, A. C., & Burton, J. D. (1994). Effects of dynamic stall and flow curvature on the aerodynamics of Darrieus turbines applying the cascade model. *Wind Engineering*, 18(6), 267-282.

Manual F. (2009). Manual and user guide of Fluent Software. Fluent Inc.

McKinney, W., & DeLaurier, J. (1981). The wingmill: An oscillating-wing windmill. *Journal of Energy*, 5(2), 109-115.

Micallef, D., Farrugia, R., Sant, T., & Mollicone, P. (2014). An aerodynamic study on flexed blades for VAWT applications. In *Journal of Physics: Conference Series*, Vol. 555, No. 1, p. 012073, IOP Publishing.

Michael, V., Altman, A., Eldredge, J. D., Garmann, D. J., & Lian, Y. (2010). Résumé of the AIAA FDTC Low Reynolds Number Discussion Group's Canonical Cases.

Mohamed, M. H. (2012). Performance investigation of H-rotor Darrieus turbine with new airfoil shapes. *Energy*, 47(1), 522-530.

Mohamed, M. H. (2014). Aero-acoustics noise evaluation of H-rotor Darrieus wind turbines. *Energy*, 65, 596-604.

Muraca, R. J., Stephens, M. V., & Dagenhart, J. R. (1975). Theoretical performance of cross-wind axis turbines with results for a catenary vertical axis configuration. USA:NASA, TMX-72662.

Nakata, T., & Liu, H. (2012). Aerodynamic performance of a hovering hawkmoth with flexible wings: a computational approach. *Proceedings of the Royal Society B: Biological Sciences*, 279(1729), 722-731.

Nemec, O. (2001). U.S. Patent No. 6,320,273. Washington, DC: U.S. Patent and Trademark Office.

Nicholls-Lee, R. F., Turnock, S. R., & Boyd, S. W. (2008). Simulation based optimisation of marine current turbine blades.

Nicolato, P. C., & Moreira, R. M. (2009). Numerical Modeling of Water Wave Impact on Reservoirs. In *Proceedings of the 20th International Congress of Mechanical Engineering*. Gramado (pp.1-9).

Paluszek, M. A., & Bhatta, P. (2012). U.S. Patent No. 8,193,657. Washington, DC: U.S. Patent and Trademark Office.

Papamoschou, D., & Liu, F. (2008). Aerodynamics of Fan Flow Deflectors for Jet Noise Suppression. *Journal of Propulsion and Power*, 24(3), 437-445.

Paraschivoiu, I. (1988). Double-multiple streamtube model for studying vertical-axis wind turbines. *Journal of propulsion and power*, 4(4), 370-377.

- Pawsey, N. C. K. (2002). Development and evaluation of passive variable-pitch vertical axis wind turbines. University of New South Wales.
- Pawsey, N. C. K., & Barratt, A. J. (1999). Evaluation of a Variable-Pitch Vertical Axis Wind Turbine. *Wind Engineering*, 23(1), 23-30.
- Peel, L. D., & Jensen, D. W. (2001). The response of fiber-reinforced elastomers under simple tension. *Journal of Composite Materials*, 35(2), 96-137.
- Peel, L. D., Jensen, D. W., & Suzumori, K. (1998). Batch fabrication of fiber-reinforced elastomer prepreg. *Journal of Advanced Materials*, 30(3), 3-10.
- Peng, Z., & Zhu, Q. (2009). Energy harvesting through flow-induced oscillations of a foil. *Physics of Fluids*, 21, 123602.
- Phillips, D. G., Richards, P. J., & Flay, R. G. J. (2002). CFD modelling and the development of the diffuser augmented wind turbine. *Wind and Structures*, 5(2_3_4), 267-276.
- Ponta, F. L., & Jacovkis, P. M. (2001). A vortex model for Darrieus turbine using finite element techniques. *Renewable Energy*, 24(1), 1-18.
- Pryor, D. H. (1983). U.S. Patent No. 4,383,801. Washington, DC: U.S. Patent and Trademark Office.
- Read, S., & Sharpe, D. J. (1980). An extended multiple streamtube theory for vertical axis wind turbines. In *Wind Energy Workshop* (Vol. 1, pp.65-72).
- Roa, A. M., Aumelas, V., Maître, T., & Pellone, C. (2010). Numerical and experimental analysis of a Darrieus-type cross flow water turbine in bare and

shrouded configurations. In IOP Conference Series: Earth and Environmental Science (Vol. 12, No. 1, p.012113). IOP Publishing.

Rossetti, A., & Pavesi, G. (2013). Comparison of different numerical approaches to the study of the H-Darrieus turbines start-up. *Renewable Energy*, 50, 7-19.

Sadeghi, M. (2004). Parallel computation of three-dimensional aeroelastic fluid-structure interaction. Doctoral Dissertation, University of California Irvine.

Sadeghi, M., Liu, F., Lai, K. L., & Tsai, H. M. (2004). Application of three-dimensional interfaces for data transfer in aeroelastic computations. AIAA Paper, 5376, 2004.

Savonius, S. J. (1931). The S-rotor and its applications. *Mech. Eng*, 53, 333-338.

Scheurich, F., & Brown, R. E. (2013). Modelling the aerodynamics of vertical axis wind turbines in unsteady wind conditions. *Wind Energy*, 16(1), 91-107.

Schönborn, A., & Chantzidakis, M. (2007). Development of a hydraulic control mechanism for cyclic pitch marine current turbines. *Renewable Energy*, 32(4), 662-679.

Scott, D., Sabourin, M., Beaulieu, S., Papillon, B., & Ellis, C. (2014). CFD model of an aerating hydrofoil. In IOP Conference Series: Earth and Environmental Science (Vol. 22, No. 6, p.062008). IOP Publishing.

Semler, C. S. (2010). Experimental investigation of an oscillating flow generator (Doctoral dissertation, Monterey, California. Naval Postgraduate School).

Sfakiotakis, M., Lane, D. M., & Davies, J. B. C. (1999). Review of fish swimming

modes for aquatic locomotion. *IEEE Journal of Oceanic Engineering*, 24(2), 237-252.

Sharpe, D. J. (1977). A theoretical and experimental study of the Darrieus vertical axis wind turbine. Polytechnic School of Mechanical, Aeronautical and Production Engineering. Kingston Polytechnic. Research report; October, 1977.

Shoele, K., & Zhu, Q. (2012). Leading edge strengthening and the propulsion performance of flexible ray fins. *Journal of Fluid Mechanics*, 693, 402-432.

Shoele, K., & Zhu, Q. (2013). Performance of a wing with nonuniform flexibility in hovering flight. *Physics of Fluids (1994-present)*, 25(4), 041901.

Shokrieh, M. M., & Rafiee, R. (2006). Simulation of fatigue failure in a full composite wind turbine blade. *Composite Structures*, 74(3), 332-342.

Shyy, W., & Liu, H. (2007). Flapping wings and aerodynamic lift: the role of leading-edge vortices. *AIAA Journal*, 45(12), 2817-2819.

Shyy, W., Aono, H., Chimakurthi, S. K., Trizila, P., Kang, C. K., Cesnik, C. E., & Liu, H. (2010). Recent progress in flapping wing aerodynamics and aeroelasticity. *Progress in Aerospace Sciences*, 46(7), 284-327.

Sneeringer, C. P. (2009). U.S. Patent Application 12/545,929.

South, P., & Rangi, R. (1973). performance and economics of the vertical-axis wind turbine developed at the National Research Council, Ottawa, Canada.

Stephens, T. G., & Else, S. C. (2011). U.S. Patent No. 7,911,076. Washington, DC: U.S. Patent and Trademark Office.

Stephens, T. G., Brantley, B. D., Cormey, J. D., Vance, R. C., & Skarzenski, P. C.

(2009). U.S. Patent Application 12/614,232.

Strickland, J. H. (1975). The Darrieus turbine: a performance prediction model using multiple streamtube. SAND75-0431.

Strickland, J. H., Webster, B. T., & Nguyen, T. (1979). A vortex model of the Darrieus turbine: an analytical and experimental study. *Journal of Fluids Engineering*, 101(4), 500-505.

Strickland, J. H., Webster, B. T., & Nguyen, T. (1980). Vortex model of the darrieus turbine: an analytical and experimental study. NASA STI/Recon Technical Report N, 80, 25887.

Sun, K. (2007). Numerical simulation on fluid dynamic performance of H-shaped vertical axis turbine and duct. Doctoral Dissertation, Harbin Engineering University, China.

Sun, K., Zhang, L., Shao, W., & Zhou, P. (2009). Numerical simulating method for passive control vertical turbine in marine stream energy. In *Greentech-International Conference on Marine Science & Technology for Green Shipping*.

Takamatsu, Y., Furukawa, A., Okuma, K., & Shimogawa, Y. (1985). Study on Hydrodynamic Performance of Darrieus-type Cross-flow Water Turbine. *Bulletin of JSME*, 28(240), 1119-1127.

Templin, R. J. (1974). Aerodynamic performance theory for the NRC vertical-axis wind turbine (No. N-76-16618; LTR-LA-160). National Aeronautical Establishment, Ottawa, Ontario (Canada).

Tian, F. B., Young, J., & Lai, J. C. (2014). Improving power-extraction efficiency of a flapping plate: From passive deformation to active control. *Journal of Fluids and Structures*, 51, 384-392.

Triantafyllou, M. S., Techet, A. H., & Hover, F. S. (2004). Review of experimental work in biomimetic foils. *IEEE Journal of Oceanic Engineering*, 29(3), 585-594.

Trivellato, F., & Castelli, M. R. (2014). On the Courant–Friedrichs–Lewy criterion of rotating grids in 2D vertical-axis wind turbine analysis. *Renewable Energy*, 62, 53-62.

Turnock, S. R., Keane, A. J., Bressloff, N. W., Nicholls-Lee, R. F., & Boyd, S. W. (2009). Morphing of ‘flying’ shapes for autonomous underwater and aerial vehicles. *NATO-RTO Modelling & Simulation Conference 2009*, 23-25 June, Lisbon, Portugal, 1-19.

Wang, L. (2005). Theoretical and experimental study on hydrodynamic performances of vertical-axis tidal turbine. *Doctoral Dissertation*, Harbin Engineering University, China.

Wang, L. B., Zhang, L., & Zeng, N. D. (2007). A potential flow 2-D vortex panel model: Applications to vertical axis straight blade tidal turbine. *Energy Conversion and Management*, 48(2), 454-461.

Wang, S., Ingham, D. B., Ma, L., Pourkashanian, M., & Tao, Z. (2010). Numerical investigations on dynamic stall of low Reynolds number flow around oscillating airfoils. *Computers & Fluids*, 39(9), 1529-1541.

Wenlong, T., Baowei, S., & Zhaoyong, M. (2013). Conceptual design and numerical

simulations of a vertical axis water turbine used for underwater mooring platforms.

International Journal of Naval Architecture and Ocean Engineering, 5(4), 625-634.

Williamson, C. H. K. (1989). Oblique and parallel modes of vortex shedding in the wake of a circular cylinder at low Reynolds numbers. *Journal of Fluid Mechanics*, 206, 579-627.

Wilson, R. E. (1978). Vortex sheet analysis of the Giromill. *Journal of Fluids Engineering*, 100(3), 340-342.

Wilson, R. E., & Lissaman, P. B. (1974). *Applied aerodynamics of wind power machines*. Oregon State University, Corvallis, USA, PB-238595.

Wootton, R. J. (1990). The mechanical design of insect wings. *Scientific American*, 263, 114-120.

Wu, W. (2011). Two-dimensional RANS Simulation of Flow Induced Motion of Circular Cylinder with Passive Turbulence Control. Doctoral Dissertation, The University of Michigan.

Xiao Q, Liao W. (2009) Numerical study of asymmetric effect on a pitching foil. *International Journal of Modern Physics C*, 20(10), 1663-1680.

Xiao Q, Liao W. (2010) Numerical investigation of angle of attack profile on propulsion performance of an oscillating foil. *Computers and Fluids*, 39:1366-1380.

Xiao, Q., & Zhu, Q. (2014). A review on flow energy harvesters based on flapping foils. *Journal of Fluids and Structures*, 46, 174-191.

Xiao, Q., Liao, W., Yang, S., & Peng, Y. (2012). How motion trajectory affects

energy extraction performance of a biomimic energy generator with an oscillating foil? *Renewable Energy*, 37(1), 61-75.

Xiao, Q., Liu, W., & Incecik, A. (2013). Flow control for VATT by fixed and oscillating flap. *Renewable Energy*, 51, 141-152.

Xiao, Q., Tsai, H. M., & Papamoschou, D. (2007). Numerical investigation of supersonic nozzle flow separation. *AIAA Journal*, 45(3), 532.

Yang, S., Liu, F., Luo, S., Tsai, H. M., Schuster, D. M., & by Institutions, F. (2004). Three-dimensional aeroelastic computation based on stationary body-conforming grids with small perturbation boundary conditions. In *Proceedings of the 34th AIAA Fluid Dynamics Conference and Exhibit*, Paper No. AIAA-2004-2235.

Yates Jr, E. C. (1988). AGARD standard aeroelastic configurations for dynamic response I-wing 445.6 (No. AGARD-R-765). Advisory Group for Aerospace Research and Development Neuilly-Sur-Seine, France.

Yin, B., & Luo, H. (2010). Effect of wing inertia on hovering performance of flexible flapping wings. *Physics of Fluids (1994-present)*, 22(11), 111902.

Young, J. (2005). Numerical simulation of the unsteady aerodynamics of flapping airfoils. University of New South Wales, Australian Defence Force Academy, School of Aerospace, Civil and Mechanical Engineering.

Young, J., Ashraf, M. A., Lai, J. C., & Platzer, M. F. (2013). Numerical simulation of fully passive flapping foil power generation. *AIAA Journal*, 51(11), 2727-2739.

Young, J., Lai, J. C., & Platzer, M. F. (2014). A review of progress and challenges in

flapping foil power generation. *Progress in Aerospace Sciences*, 67, 2-28.

Zhang, Z., Yang, S., Liu, F., & Schuster, D. M. (2005). Prediction of flutter and LCO by an Euler method on non-moving cartesian grids with boundary-layer corrections. In 43rd AIAA Aerospace Sciences Meeting and Exhibit (pp.10-13).

Zhao, Y. (2012). Sina Blog. 05 July 2012. Yanchun Zhao's Blog. Available from: <http://blog.sina.com.cn/s/blog_698085bf0102e2kq.html/>. [24 June 2015].

Zheng, Z. C., & Zhang, N. (2008). Frequency effects on lift and drag for flow past an oscillating cylinder. *Journal of Fluids and Structures*, 24(3), 382-399.

Zhu, Q. (2007). Numerical simulation of a flapping foil with chordwise or spanwise flexibility. *AIAA Journal*, 45(10), 2448-2457.

Zhu, Q. (2011). Optimal frequency for flow energy harvesting of a flapping foil. *Journal of Fluid Mechanics*, 675, 495-517.

Zhu, Q. (2012). Energy harvesting by a purely passive flapping foil from shear flows. *Journal of Fluids and Structures*, 34, 157-169.

Zhu, Q., & Peng, Z. (2009). Mode coupling and flow energy harvesting by a flapping foil. *Physics of Fluids*, 21(3), 033601-033601.

Zhu, Q., Haase, M., & Wu, C. H. (2009). Modeling the capacity of a novel flow-energy harvester. *Applied Mathematical Modelling*, 33(5), 2207-2217.

Appendix I: MathCAD Calculation Process for Structural Parameters of 2D Free Oscillating Cylinder

Solving process for eigenvector " Φ (phi)"

Step 1: Define mass matrix as
$$\begin{pmatrix} 1 & xa \\ xa & ra^2 \end{pmatrix}$$

where : xa is the distance between the centre of rotation and centre of gravity; ra is the radius of gyration. Both of them have been non-dimensionalized by the semi-chord "b".

For **2D cylinder cases**, xa sets as zero since the translation/rotation centre and the gravitation centre are both located in the cylinder centre; ra sets as one since the radius of gyration and the semi-chord "b" are both equals to the radius of the cylinder.

$$xa \equiv 1.8 \quad ra \equiv 1.86$$

$$M11 := 1 \quad M12 := xa \quad M21 := xa \quad M22 := ra^2$$

Step 2: Give an initial number for phi matrix
$$\begin{pmatrix} x & y \\ z & w \end{pmatrix}$$

$$x := 3.7743 \quad y := 0.50444 \quad z := -2.0232 \quad w := 0.27041$$

Calculate the approximate result by using GIVEN-FIND function

Given

$$x^2 \cdot M11 + xz \cdot M21 + xz \cdot M12 + z^2 \cdot M22 = 1$$

$$xy \cdot M11 + zy \cdot M21 + xw \cdot M12 + zw \cdot M22 = 0$$

$$xy \cdot M11 + xw \cdot M21 + yz \cdot M12 + zw \cdot M22 = 0$$

$$y^2 \cdot M11 + yw \cdot M21 + yw \cdot M12 + w^2 \cdot M22 = 1$$

$$\text{Find}(x, y, z, w)^T = (3.78764 \ 0.50438 \ -2.0309 \ 0.27048)$$

Step 3: Collect the result from the "Find(x,y,z,w)" statement. Go back to Step 2 and re-insert these values into the initialization part until the final results do not change. (Man-made explicit iteration)

Step 4: Collect the final results and insert it into the matrix below to check if it can reach to an acceptable result or not. (NOTE: the result of the second matrix equation should approach to the identity matrix)

$$\begin{pmatrix} \text{phicsd11} & \text{phicsd12} \\ \text{phicsd21} & \text{phicsd22} \end{pmatrix} := \begin{pmatrix} 3.78764 & 0.50438 \\ -2.0309 & 0.27048 \end{pmatrix} \quad \begin{pmatrix} M11 & M12 \\ M21 & M22 \end{pmatrix} = \begin{pmatrix} 1 & 1.8 \\ 1.8 & 3.478 \end{pmatrix}$$

$$\begin{pmatrix} \text{phicsd11} & \text{phicsd12} \\ \text{phicsd21} & \text{phicsd22} \end{pmatrix}^T \cdot \begin{pmatrix} M11 & M12 \\ M21 & M22 \end{pmatrix} \cdot \begin{pmatrix} \text{phicsd11} & \text{phicsd12} \\ \text{phicsd21} & \text{phicsd22} \end{pmatrix} = \begin{pmatrix} 1 & 2.792 \times 10^{-6} \\ 2.792 \times 10^{-6} & 1 \end{pmatrix}$$

Appendix II: MathCAD Calculation Process for Structural Parameters of 2D Free Oscillating Isogai Airfoil

Solving process for eigenvalue " λ " and eigenfrequency " ω "

Step 1: Define stiffness matrix as

$$\begin{bmatrix} \left(\frac{\omega h}{\alpha a}\right)^2 & 0 \\ 0 & r a^2 \end{bmatrix}$$

where : ωh is the eigenfrequency of heaving corresponding to h/b ; $\omega \alpha$ is the eigenfrequency of rotation corresponding to α

For **2D cylinder cases**, assume $\omega h = \omega \alpha = \omega n$, which ωn is the natural oscillation frequency of the cylinder.

$$\begin{aligned} \omega h &\equiv 1 & \omega \alpha &\equiv 1 \\ K_{11} &:= \left(\frac{\omega h}{\alpha a}\right)^2 & K_{12} &:= 0 & K_{21} &:= 0 & K_{22} &:= r a^2 \end{aligned}$$

Step 2: Calculae eigenvalue:

$$\begin{pmatrix} K_{11} & K_{12} \\ K_{21} & K_{22} \end{pmatrix} = \begin{pmatrix} 1 & 0 \\ 0 & 3.478 \end{pmatrix}$$

$$\begin{pmatrix} \text{phicsd11} & \text{phicsd12} \\ \text{phicsd21} & \text{phicsd22} \end{pmatrix}^T \cdot \begin{pmatrix} K_{11} & K_{12} \\ K_{21} & K_{22} \end{pmatrix} \cdot \begin{pmatrix} \text{phicsd11} & \text{phicsd12} \\ \text{phicsd21} & \text{phicsd22} \end{pmatrix} = \begin{pmatrix} 28.692 & -2.412 \times 10^{-4} \\ -2.412 \times 10^{-4} & 0.509 \end{pmatrix}$$

$$\begin{pmatrix} \text{phicsd11} \\ \text{phicsd21} \end{pmatrix}^T \cdot \begin{pmatrix} K_{11} & K_{12} \\ K_{21} & K_{22} \end{pmatrix} \cdot \begin{pmatrix} \text{phicsd11} \\ \text{phicsd21} \end{pmatrix} = 28.692$$

$$\begin{pmatrix} \text{phicsd12} \\ \text{phicsd22} \end{pmatrix}^T \cdot \begin{pmatrix} K_{11} & K_{12} \\ K_{21} & K_{22} \end{pmatrix} \cdot \begin{pmatrix} \text{phicsd12} \\ \text{phicsd22} \end{pmatrix} = 0.509$$

Step 3: Collect the result of eigenvalue from the second matrix equation in step 2; Calculae eigenfrequency by insert the results from the third and fourth matrix equations in step 2 into the square root of ω_1 and ω_2 equations below respectively:

$$\omega_1 := \sqrt{28.692} \quad \omega_2 := \sqrt{0.509}$$

Step 4: Collect the final results for the eigenfrequency from the equations below:

$$\omega_1 = 5.356 \quad \omega_2 = 0.713$$

Appendix III: MathCAD Calculation Process for Structural Parameters of 3D AGARD Wing

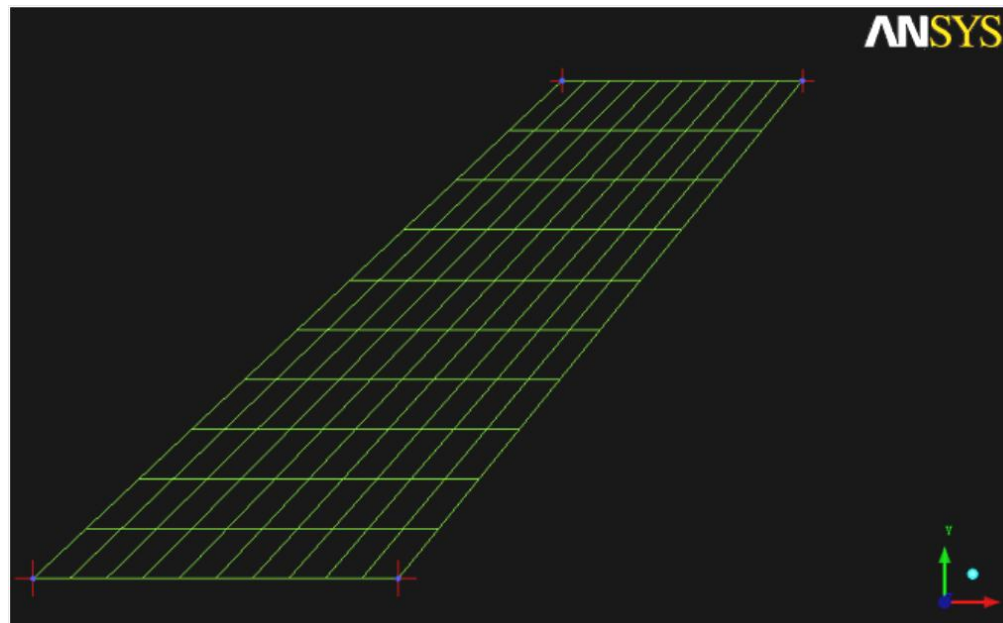
3-D AGARD Wing Structure Model Analysis

Wendi LIU

4th April 2013

ORIGIN=1

Note units m, newton, kg



1. Define nodes and coordinates

ctemp := Nchord := ctemp_{1,2} Nspan := ctemp_{1,3} Nthick := ctemp_{1,4} Nnod := Nchord · Nspan · Nthick ii := 1..3
{xxxx} in := 1..Nnod xc{in} := ctemp_{in+1,1} yc_{in} := ctemp_{in+1,2} zc_{in} := ctemp_{in+1,3} Node_{in,ii} := ctemp_{in+1,ii}

	1	2	3	4
1	"domain.1"	11	11	1
2	0	0	0	0
3	2.2	0	0	0
4	4.4	0	0	0
5	6.6	0	0	0
6	8.8	0	0	0
7	11	0	0	0
8	13.2	0	0	0
9	15.4	0	0	0
10	17.6	0	0	0
11	19.8	0	0	0
12	22	0	0	0
13	3.188	3	0	0
14	5.313	3	0	0
15	7.438	3	0	0
16	9.563	3	0	...

ctemp =

in =	xc _{in} =	yc _{in} =	zc _{in} =
1	0	0	0
2	2.2	0	0
3	4.4	0	0
4	6.6	0	0
5	8.8	0	0
6	11	0	0
7	13.2	0	0
8	15.4	0	0
9	17.6	0	0
10	19.8	0	0
11	22	0	0
12	3.188	3	0
13	5.313	3	0
14	7.438	3	0
15	9.563	3	0
...

2. Define elements' properties

$$\text{Nelem} := [\text{Nspan} \cdot (\text{Nchord} - 1)] + [\text{Nchord} \cdot (\text{Nspan} - 1)] \quad \text{ie} := 1.. \text{Nelem} \quad t_{ie} := 0.01 \quad \text{Nelem} = 220$$

Poisson's ratio $\mu := 0.31$ Youngs modulus: $E_{ie} := 0.4707210^6$ Shear Modulus $G_{ie} := \frac{E_{ie}}{2 \cdot (1 + \mu)}$

Define tubular member properties

Outer diameter Thickness Inner diameter Cross-section area

$$D_{ie} := 0.1 \quad T_{ie} := 0.024 \quad d_{ie} := D_{ie} - 2 \cdot T_{ie} \quad A_{ie} := \pi \cdot \left[\frac{(D_{ie})^2 - (d_{ie})^2}{4} \right] \quad I_{ie} := \frac{\pi \cdot [(D_{ie})^4 - (d_{ie})^4]}{64}$$

$d_{ie} =$	$A_{ie} =$	$I_{ie} =$
0.1	0.024	7.3631×10^{-5}
0.1	0.024	7.3631×10^{-5}
0.1	0.024	7.3631×10^{-5}
0.1	0.024	7.3631×10^{-5}
0.1	0.024	7.3631×10^{-5}
0.1	0.024	7.3631×10^{-5}
...

3a. Node end numbers 1 and 2

For each element:

$$i := 1..(Nchord - 1) \quad j := 1..Nspan \quad ie_{i,j} := (j - 1) \cdot Nchord + i - (j - 1)$$

$$n1_{(ie_{i,j})} := (j - 1) \cdot Nchord + i \quad n2_{(ie_{i,j})} := (j - 1) \cdot Nchord + i + 1$$

$$i := 1..Nchord \quad j := 1..(Nspan - 1) \quad ie_{i,j} := Nspan \cdot (Nchord - 1) + (j - 1) \cdot Nchord + i$$

$$n1_{(ie_{i,j})} := (j - 1) \cdot Nchord + i \quad n2_{(ie_{i,j})} := j \cdot Nchord + i$$

n1 =

	1
1	1
2	2
3	3
4	4
5	5
6	6
7	7
8	8
9	9
10	10
11	12
12	13
13	14
14	15
15	16
16	...

n2 =

	1
1	2
2	3
3	4
4	5
5	6
6	7
7	8
8	9
9	10
10	11
11	13
12	14
13	15
14	16
15	17
16	...

Define limits for plotting (to centre the figures in the plots and to provide an edge distance of approx 10)

$$\max x := \text{ceil}\left(\frac{\max(xc) + 2}{10}\right) \cdot 10 \quad \max x = 50 \quad \min x := \text{floor}\left(\frac{\min(xc) - 2}{10}\right) \cdot 10 \quad \min x = -10$$

$$\max y := \text{ceil}\left(\frac{\max(yc) + 2}{10}\right) \cdot 10 \quad \max y = 40 \quad \min y := \text{floor}\left(\frac{\min(yc) - 2}{10}\right) \cdot 10 \quad \min y = -10$$

$$\max z := \text{ceil}\left(\frac{\max(zc) + 2}{10}\right) \cdot 10 \quad \max z = 10 \quad \min z := \text{floor}\left(\frac{\min(zc) - 2}{10}\right) \cdot 10 \quad \min z = -10$$

3b. Plot shape of structure

$$iend := 1..2 \quad ie := 1..Nelem$$

$$Nelem = 220$$

Reorganise information

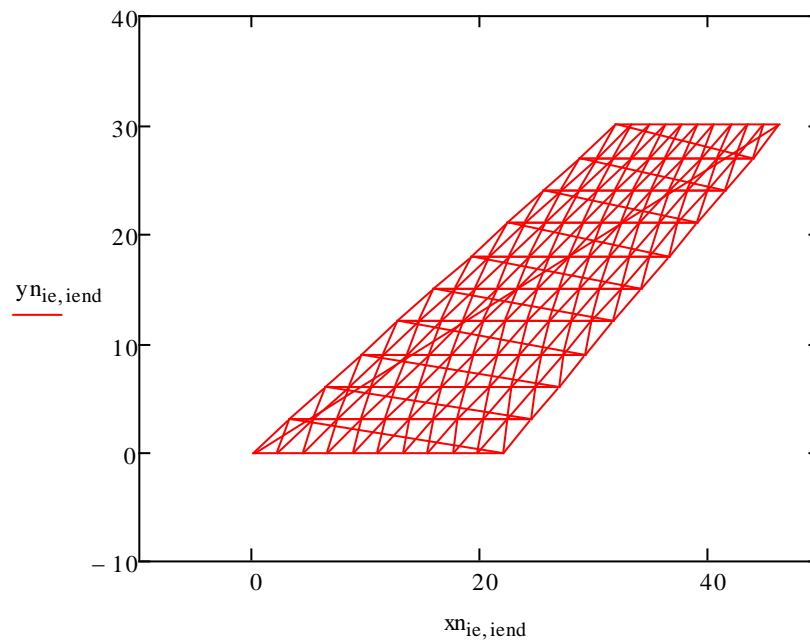
$$xn_{ie,1} := xc_{n1_{ie}} \quad xn_{ie,2} := xc_{n2_{ie}}$$

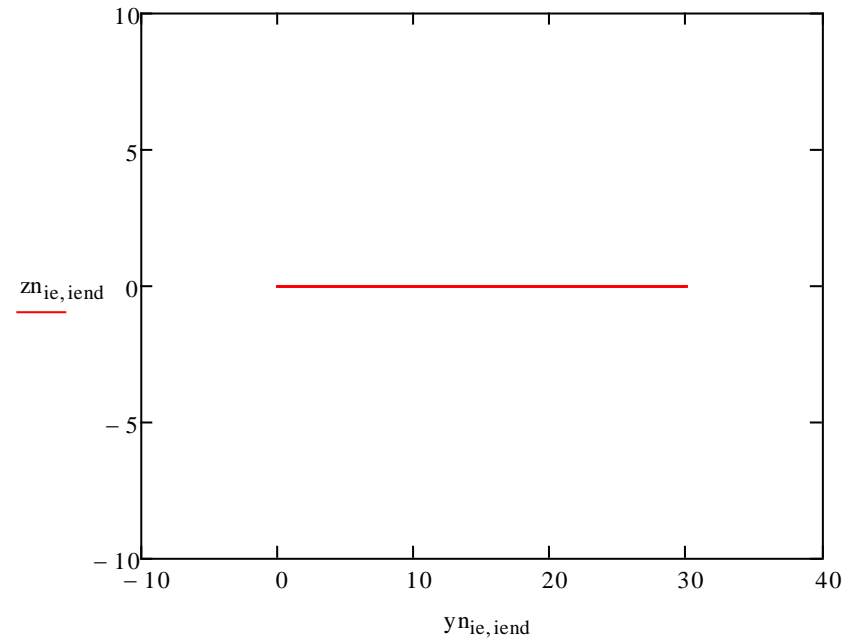
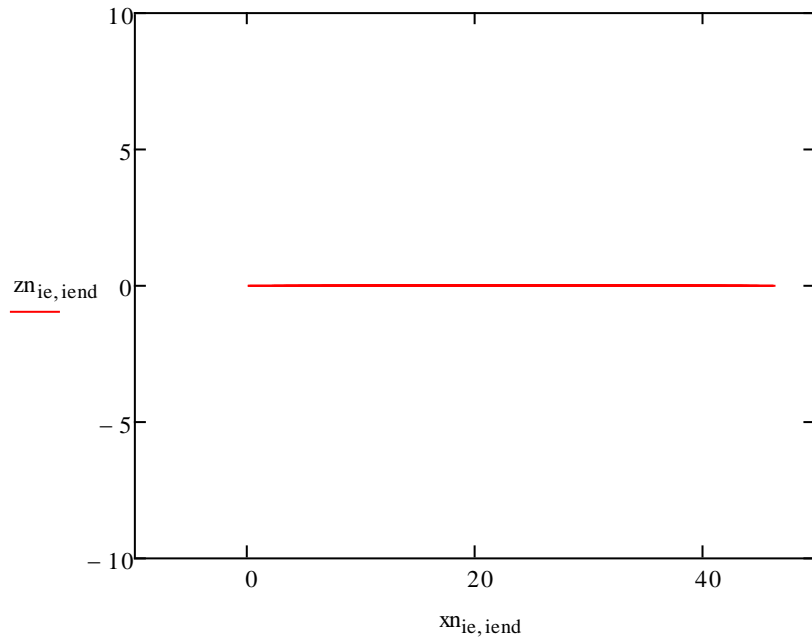
To suit Mathcad plotting routine

$$yn_{ie,1} := yc_{n1_{ie}} \quad yn_{ie,2} := yc_{n2_{ie}}$$

We need to plot member by member

$$zn_{ie,1} := zc_{n1_{ie}} \quad zn_{ie,2} := zc_{n2_{ie}}$$





5. Member lengths

Note member +ve x is from node 1 to node 2

$$L_{ie} := \sqrt{(x_{n2ie}^c - x_{n1ie}^c)^2 + (y_{n2ie}^c - y_{n1ie}^c)^2 + (z_{n2ie}^c - z_{n1ie}^c)^2}$$

$$\alpha_{ie} := \text{angle} \left[\left[x_{n2ie}^c - x_{n1ie}^c \right], \left[y_{n2ie}^c - y_{n1ie}^c \right] \right]$$

$L_{ie} =$	$\alpha_{ie} =$	$\frac{\alpha_{ie}}{\text{deg}} =$
2.2	0	0
2.2	0	0
2.2	0	0
2.2	0	0
2.2	0	0
2.2	0	0
2.2	0	0
2.2	0	0
2.2	0	0
2.2	0	0
2.2	0	0
2.125	0	0
2.125	0	0
2.125	0	0
2.125	0	0
2.125	0	0
...

6a. Define submatrix partition functions

Degrees of freedom per node Ndof := 3

$$K11(A, I, L, E) := \begin{pmatrix} \frac{E \cdot A}{L} & 0 & 0 \\ 0 & \frac{12 \cdot E \cdot I}{L^3} & \frac{6 \cdot E \cdot I}{L^2} \\ 0 & \frac{6 \cdot E \cdot I}{L^2} & \frac{4 \cdot E \cdot I}{L} \end{pmatrix} \quad K12(A, I, L, E) := \begin{bmatrix} -\left(\frac{E \cdot A}{L}\right) & 0 & 0 \\ 0 & -\left(\frac{12 \cdot E \cdot I}{L^3}\right) & \frac{6 \cdot E \cdot I}{L^2} \\ 0 & -\left(\frac{6 \cdot E \cdot I}{L^2}\right) & \frac{2 \cdot E \cdot I}{L} \end{bmatrix}$$

Note: $K21 = K12^T$

$$K21(A, I, L, E) := K12(A, I, L, E)^T \quad K22(A, I, L, E) := \begin{bmatrix} \frac{E \cdot A}{L} & 0 & 0 \\ 0 & \frac{12 \cdot E \cdot I}{L^3} & -\left(\frac{6 \cdot E \cdot I}{L^2}\right) \\ 0 & -\left(\frac{6 \cdot E \cdot I}{L^2}\right) & \frac{4 \cdot E \cdot I}{L} \end{bmatrix}$$

6b. Calculate element stiffness matrices

$r := 1..Ndof \cdot Nnod$ $c_{\alpha\alpha} := 1..Ndof \cdot Nnod$ $KG_{r,c} := 0$

$$K11S_{ie} := K11(A_{ie}, I_{ie}, L_{ie}, E_{ie}) \quad K12S_{ie} := K12(A_{ie}, I_{ie}, L_{ie}, E_{ie})$$

$$K21S_{ie} := K21(A_{ie}, I_{ie}, L_{ie}, E_{ie}) \quad K22S_{ie} := K22(A_{ie}, I_{ie}, L_{ie}, E_{ie})$$

7. Transform each partition into global coordinates

Note I have defined this matrix using the same convention as in your notes

$$T(\alpha) := \begin{pmatrix} \cos(\alpha) & -\sin(\alpha) & 0 \\ \sin(\alpha) & \cos(\alpha) & 0 \\ 0 & 0 & 1 \end{pmatrix} \quad T(0) = \begin{pmatrix} 1 & 0 & 0 \\ 0 & 1 & 0 \\ 0 & 0 & 1 \end{pmatrix} \quad T\left(\frac{\pi}{2}\right) = \begin{pmatrix} 0 & -1 & 0 \\ 1 & 0 & 0 \\ 0 & 0 & 1 \end{pmatrix}$$

α is the angle from global to local axes

$$x_{\text{global}} = T x_{\text{local}}$$

Transform to global axes

$$TM(\alpha) := \begin{pmatrix} \cos(\alpha) & -\sin(\alpha) & 0 \\ \sin(\alpha) & \cos(\alpha) & 0 \\ 0 & 0 & 1 \end{pmatrix}$$

$$K11T_{ie} := TM(\alpha_{ie}) \cdot K11S_{ie} \cdot TM(\alpha_{ie})^T \quad K12T_{ie} := TM(\alpha_{ie}) \cdot K12S_{ie} \cdot TM(\alpha_{ie})^T$$

$$K21T_{ie} := TM(\alpha_{ie}) \cdot K21S_{ie} \cdot TM(\alpha_{ie})^T \quad K22T_{ie} := TM(\alpha_{ie}) \cdot K22S_{ie} \cdot TM(\alpha_{ie})^T$$

$$K11S_1 = \begin{pmatrix} 5.041 \times 10^3 & 0 & 0 \\ 0 & 39.06 & 42.966 \\ 0 & 42.966 & 63.017 \end{pmatrix} \quad K11T_1 = \begin{pmatrix} 5.041 \times 10^3 & 0 & 0 \\ 0 & 39.06 & 42.966 \\ 0 & 42.966 & 63.017 \end{pmatrix}$$

8. Assemble the Global Stiffness Matrix

$$r := 1..3 \quad c := 1..3$$

First add in K11 matrix for element 1 - 3:

$$KG_{r+3 \cdot (n_{1e}-1), c+3 \cdot (n_{1e}-1)} := KG_{r+3 \cdot (n_{1e}-1), c+3 \cdot (n_{1e}-1)} + (K11T_{ie})_{r,c}$$

Then add in the other 3 partitions for each element

$$KG_{r+3 \cdot (n_{1e}-1), c+3 \cdot (n_{2e}-1)} := KG_{r+3 \cdot (n_{1e}-1), c+3 \cdot (n_{2e}-1)} + (K12T_{ie})_{r,c}$$

$$KG_{r+3 \cdot (n_{2e}-1), c+3 \cdot (n_{1e}-1)} := KG_{r+3 \cdot (n_{2e}-1), c+3 \cdot (n_{1e}-1)} + (K21T_{ie})_{r,c}$$

$$KG_{r+3 \cdot (n_{2e}-1), c+3 \cdot (n_{2e}-1)} := KG_{r+3 \cdot (n_{2e}-1), c+3 \cdot (n_{2e}-1)} + (K22T_{ie})_{r,c}$$

	1	2	3	4
1	6.387×10^3	1.262×10^3	-7.436	-5.041×10^3
2	1.262×10^3	1.231×10^3	50.869	0
3	-7.436	50.869	94.686	0
4	-5.041×10^3	0	0	1.142×10^4
5	0	-39.06	-42.966	1.279×10^3
6	0	42.966	31.509	-7.72
7	0	0	0	-5.041×10^3
8	0	0	0	0
9	0	0	0	0
10	0	0	0	...

KG =

9. Define and add in support stiffnesses

Support stiffness: $KS := 10^{19}$

Number of fixed Nodes: $N_{fn} := N_{chord}$

Number of fixed freedoms $N_f := N_{dof} \cdot N_{fn}$

$iff := 1..N_f$ $ifn := 1..N_{chord}$ $ifd := 1..N_{dof}$

$FixedNode_{ifn,ifd} := (ifn - 1) \cdot N_{dof} + ifd$

Location for support stiffness

$KG_{FixedNode_{ifn,ifd}, FixedNode_{ifn,ifd}} := KG_{FixedNode_{ifn,ifd}, FixedNode_{ifn,ifd}} + KS$

FixedNode =

	1	2	3
1	1	2	3
2	4	5	6
3	7	8	9
4	10	11	12
5	13	14	15
6	16	17	18
7	19	20	21
8	22	23	24
9	25	26	27
10	28	29	30
11	31	32	33

KG =

	1	2	3
1	1×10^{19}	1.262×10^3	-7.436
2	1.262×10^3	1×10^{19}	50.869
3	-7.436	50.869	1×10^{19}
4	-5.041×10^3	0	0
5	0	-39.06	-42.966
6	0	42.966	31.509
7	0	0	0
8	0	0	0
9	0	0	0
10	0	0	0
11	0	0	0
12	0	0	...

1a. Define submatrix partition functions

Structure mass $M_{total} := 0.1276$

$$ie := 1..Nnod \quad mnod_{ie} := \frac{M_{total}}{Nnod}$$

$$Mnod(ie) := \begin{pmatrix} mnod_{ie} & 0 & 0 \\ 0 & mnod_{ie} & 0 \\ 0 & 0 & mnod_{ie} \end{pmatrix}$$

3. Assemble the Global Stiffness Matrix

$r := 1..3 \quad c := 1..3$

$$M_{r+3 \cdot (ie-1), c+3 \cdot (ie-1)} := (Mnod(ie))_{r,c}$$

$$Mnod(1) = \begin{pmatrix} 1.055 \times 10^{-3} & 0 & 0 \\ 0 & 1.055 \times 10^{-3} & 0 \\ 0 & 0 & 1.055 \times 10^{-3} \end{pmatrix}$$

	1	2	3	4
1	1.055×10^{-3}	0	0	0
2	0	1.055×10^{-3}	0	0
3	0	0	1.055×10^{-3}	0
4	0	0	0	1.055×10^{-3}
5	0	0	0	0
6	0	0	0	0
7	0	0	0	0
8	0	0	0	0
9	0	0	0	0
10	0	0	0	0
11	0	0	0	0
12	0	0	0	...

M =

4. Nature Frequency

$$A := M^{-1} \cdot KC \quad \omega_2 := \text{eigenvals}(A) \quad X := \text{eigenvecs}(A) \quad \omega_c := \sqrt{\omega_2} \quad \omega := \text{Re}(\omega_c) \quad f := \frac{\omega}{2\pi} \quad fs := \begin{cases} f \leftarrow \text{sort}(f) \\ n \leftarrow \text{last}(f) \\ \text{for } i \in n, n-1..2 \\ f \leftarrow \text{trim}(f, i) \text{ if } f_i = f_{i-1} \\ f \end{cases}$$

$$\text{Mode}_i := fs_{i+1}$$

Mode

Mode =

	1
1	8.871
2	16.216
3	23.314
4	...

Appendix IV: Curriculum Vitae

Name

Wendi LIU

Education

Oct. 2011-Nov. 2015 Ph.D. Research Student, Department of Naval Architecture, Ocean & Marine Engineering, University of Strathclyde, Glasgow, UK.

Sep. 2009-Jul. 2011 BEng (Hons) Naval Architecture & Marine Engineering, Jointly with University of Glasgow and University of Strathclyde, Glasgow, UK.

Sep. 2007-Jul. 2011 BEng Naval Architecture & Ship Building, Harbin Engineering University, Harbin, China.

Employment History

Oct. 2014-Mar. 2016 Research Assistant (Part time), University of Strathclyde, UK.

Teaching Expertise

Tutor for Postgraduate course on Computational free-surface hydrodynamics – module on a variety of postgraduate courses on the Turbulence and Free-Surface modelling technique based on CFD method, 10 teaching hours per year, (2012-2015).

Tutor for Undergraduate course on Computational fluid dynamics – module on a variety of undergraduate courses on the basic fluid modelling technique based on CFD method, 18 teaching hours in 2012 and 3 teaching hours in 2015.

Co-supervision Postgraduate Students' Dissertation in the Following Topics:

1. Sukanda Bowonkanka, 'CFD Modelling on Offshore Floating Structure', Start date: November 2014; Degree awarded: MSc, November 2015.
2. Alexander Steinert, 'Heave and Pitch Motion of Anti-Roll Tank In Waves', Start date: November 2013; Degree awarded: MSc, November 2014.

Co-supervision Undergraduate Students' Thesis in the Following Topics:

1. Jordan McRuvie, 'Bio-Mimicry and the use of Shark-Skin Inspired Technology for the Reduction of Surface Resistance of Submarines and Other Underwater Craft', Start date: October 2014; Degree awarded: MEng, July 2016 (Expect).

2. Chang Xu, 'Prediction of Fluid Tank Roll Hydrodynamics',
Start date: October 2013; Degree awarded: BEng (Hons), July 2014.
3. Qiang Sun, 'Energy Extraction Performance on Oscillating Foil Turbine',
Start date: October 2012; Degree awarded: BEng (Hons), July 2013.
4. Sijia Zhao, 'A study on duct effect on VATT power performance',
Start date: October 2012; Degree awarded: BEng (Hons), July 2013.
5. Mengshi Sun, 'H-Shaped Vertical Current Turbine: The Physics of Self-Starting',
Start date: October 2011; Degree awarded: BEng (Hons), July 2012.

Research Experience

1. A Study of Bio-inspired Three-dimensional PASSIVELY Deformed Flexible Blade for Wind/Tidal Turbines [£ 21,579.30] (2015-2016).
 - Co-investigator
 - EPSRC funded project.
2. Tidal Stream RipRamp Generator System Project (2015-2016).
 - Supported by Technology Scotstream LTD.
3. CFD modelling of channel influence on Vertical Axis Tidal Turbine (2015-2016).
 - Joint research with the University of Edinburgh, Edinburgh, UK.
4. TLPWIND UK: "DRIVING DOWN THE COST OF OFFSHORE WIND IN UK WATERS" [£ 229,133.00] (2014-2016).
 - Supported by Innovate UK.
5. Fluid – structure interaction study of the passive flexible blade effect of the energy extraction turbine (2014-2015).
 - Joint research with University of California, USA and Chiba University, Japan.
 - The results have been published in J1 and J2
6. CFD analysis for Self-propelled Jellyfish Model (2013-2014).
 - Joint research with Department of Control and Industrial Engineering (DAP), École des Mines de Nantes.
7. Energy Harvesting Membrane behind a Square Cylinder (2013-2014).
 - Joint research with NanYang Technological University, Singapore.
8. The Male causeway tidal energy extraction turbine design (2013-2014).
 - Carried out for Hopewell LTD. Hong Kong.
9. The characteristics of surface arc plasma and its control effect on supersonic flow (2012-2014).
 - Joint research with Air Force Engineering University, China.
 - The results have been published in J3
10. Energy extraction by active flexible flapping wings [£ 6,000.00] (2012-2013).
 - Supported by Lloyd's Register LTD.

- The results have been published in J4
11. Mechanistic investigation and performance design for hydrofoils (2012-2013).
 - Joint research with ResHydro LTD.
 12. The Energy extraction enhancement of the vertical axis marine turbine (2011-2012).
 - Joint with Harbin Engineering University, China.
 - The results have been published in J5
 13. 4th year undergraduate individual research project–Fish motion simulation base on CFD theory, University of Glasgow and University of Strathclyde. (2010-2011)
 - The project presentation won 3rd awards in IMarEST 4th year project competition in NAME department
 - The results have been published in J6

Research Funding Application

1. Co-investigator: “A Study of Bio-inspired Three-dimensional PASSIVELY Deformed Flexible Blade for Wind/Tidal Turbines” [£ 21,579.30].
 - Funded by Engineering and Physical Sciences Research Council (EPSRC)
 - July 2015 - July 2016

Experiment Experience

I have been trained for experimental skills for marine engine experiment, flow pass a hydrofoil and wave modelling when I was at undergraduate studies. I was involved in the calibration and test stage of the experiment on floating vertical axis tidal turbine funded by EPSRC. I also joined the experiment of offshore floating TLP wind turbine, funded by Technology Strategy Board LTD in September 2015. In October 2015, I participated in the design and prototype test of the experiment of Vertical Axis Tidal Turbine with Flexible Blades and will contribute to the experiment when it begins.

Scholarships, Awards and Prizes

2012-2014	Research support by Lloyd’s Register Group Limited
2011-2013	Loyalty Ph.D. scholarship, funded by NA-ME department and Engineering Faculty, University of Strathclyde
2011	The 3rd awards on IMarEST 4th year project competition in NA-ME department
2008-2009	Third Academic Excellence Award from Harbin Engineering University

2007-2008 Secondary Academic Excellence Award from Harbin Engineering University

Certificates

Jun. /Jul. 2015 Certificate of 50 hours training on “Molecular Dynamics Theory and Applications”, Supporting team of ARCHIE-WeSt high performance computing, Glasgow, UK.

Apr. 2015 Gold level certificate of Strathclyde Enterprise Pathway on Enterprise Academy, Business School, University of Strathclyde.

Feb. 2015 Silver level certificate of Strathclyde Enterprise Pathway on Enterprise Academy, Business School, University of Strathclyde.

Other Academic Activities

Aug.2013 Participate in 2013’ International Summer School on Naval Architecture, Ocean Engineering and Mechanics in Shanghai Jiaotong University, China.

Jun.2012- Jun.2013 Student member of International Society of Offshore and Polar Engineers (ISOPE)

Jan.2012-June 2012 Member of organizing committee of University Research Day, University of Strathclyde

Publications

Journal Articles

- J1. Wendi Liu, Qing Xiao and Qiang Zhu. "A coupled fluid-structure study of the passive flexibility effect on oscillating foil energy harvester" AIAA Journal (In Press).
- J2. Wendi Liu and Qing Xiao. "Investigation on Darrieus Type Straight Blade Vertical Axis Wind Turbine with Flexible Blade" Ocean Engineering 110 A (2015): pp 339-356.
- J3. Sun, Quan, Yinghong Li, Bangqin Cheng, Wei Cui, Wendi Liu, and Qing Xiao. "The characteristics of surface arc plasma and its control effect on supersonic flow." Physics Letters A 378, no. 36 (2014): pp 2672-2682.
- J4. Wendi Liu, Qing Xiao and Fai Cheng. "A bio-inspired study on tidal energy extraction with flexible flapping wings" Bio-inspiration & Bio-mimetics 8 no. 036011 (2013): pp 1-16.

- J5. Qing Xiao, Wendi Liu and Atilla Incecik. "Flow control for VATT by fixed and oscillating flap." *Renewable Energy* 51 (2013): pp 141-152.
- J6. Qing Xiao, Wendi Liu and Jianxin Hu. "Parametric study on a cylinder drag reduction using downstream undulating foil." *European Journal of Mechanics-B/Fluids* 36 (2012): pp 48-62.

Conference Papers

- C1. Wendi Liu and Qing Xiao. "Bend and Twist Effect for Large-Scale Vertical Axis Turbine" 11th European Wave and Tidal Energy Conference Series (EWTEC), September 6th – 11th September 2015, Nantes, France, #607.
- C2. Wendi Liu and Qing Xiao. "A study on oscillating foil energy harvester with a passive flexible foil." Grand Renewable Energy (GRE) International Conference and Exhibition, 27th July – 1st August 2014, Tokyo, Japan.
- C3. Enhao Wang, Qing Xiao and Wendi Liu. "Numerical Simulation of Multi-Modal Vortex-Induced Vibration of a 3D Flexible Circular Cylinder." International Conference on Marine Technology (ICMT) 2014, 7th – 9th July 2014, Glasgow, UK, Session 6-1.
- C4. Enhao Wang, Qing Xiao and Wendi Liu. "System Damping Effect on VIV Energy Extraction Device." The 8th International Workshop on Ship Hydrodynamics (IWSH), 23rd – 25th September 2013, Seoul, Korea.
- C5. Wendi Liu and Qing Xiao. "Energy extraction by flexible flapping twin wing." 32nd International Conference on Ocean, Offshore and Arctic Engineering (OMAE), 9th–14th June 2013, Nantes, France, 2013-10233.
- C6. Wendi Liu and Qing Xiao. "Flow control for VATT by fixed and oscillating flap." 22nd International Offshore and Polar Engineering Conference (ISOPE) 17th–22nd June 2012, Rhodes, Greece, 1098-6189.
- C7. Qing Xiao, Wendi Liu and Jianxin Hu. "Parametric study on a cylinder drag reduction using downstream undulating foil." The 41st American Institute of Aeronautics and Astronautics (AIAA) Fluid Dynamics Conference and Exhibit, 27th – 30th June 2011, Honolulu, Hawaii, 2011-3896.

Abstracts

- A1. Wendi Liu and Qing Xiao. "Investigation on H-shape Vertical Axis Turbine with Flexible Blade." 4th Oxford Tidal Energy Workshop, 23rd–24th March 2015, Oxford, UK, PP 58-59.
- A2. Wendi Liu and Qing Xiao. "Energy Extraction by Flexible Flapping Foil." 3rd UK Marine Technology Postgraduate Conference (MTPC), 7th-8th June 2012, Glasgow, PP 39-39.
- A3. Qing Xiao, Wendi Liu and Atilla Incecik. "Flow control for VATT by fixed and oscillating flap" 25th Scottish Fluid Mechanics Meeting, 30th May 2012, Heriot-Watt University, PP 1-2.

Posters

- P1. Wendi Liu and Qing Xiao. "Bend and Twist Effect for Large-Scale Vertical Axis Turbine". Presented in:
- 11th European Wave and Tidal Energy Conference (EWTEC), September 6th – 11th September 2015, Nantes, France, 8P2 - 1.
- P2. Elif Oguz, Wendi Liu, Sandy Day, David Clelland and Atilla Incecik. "TLPWIND UK: Driving down the cost of offshore wind in UK Waters". Presented in:
- All Energy Exhibition and Conference, 6th-7th May 2015, Glasgow.
- P3. Wendi Liu, Qing Xiao and Atilla Incecik. "A bio-inspired study on tidal energy extraction with flexible flapping wings". Presented in:
- Faculty Research Presentation Day (RPD), 27th June 2013, University of Strathclyde, Glasgow.
 - Faculty of Engineering Exhibition to University Court, 30th April 2015, University of Strathclyde, Glasgow.
 - All Energy Exhibition and Conference, 6th-7th May 2015, Glasgow.
- P4. Wendi Liu, Qing Xiao and Atilla Incecik. "Flow control for VATT by fixed and oscillating flap". Presented in:
- Faculty Research Presentation Day (RPD), 21st February 2012, University of Strathclyde, Glasgow.
 - SJTU Summer School, 3rd–17th August 2013, Shanghai Jiaotong University, China.

Knowledge Exchange and Presentation at Conference Proceedings:

1. "Investigation on H-shape Vertical Axis Turbine with Flexible Blade." 4th Oxford Tidal Energy Workshop 23–24 March 2015.
2. "Flow control for VATT by fixed and oscillating flap." 22nd International Offshore and Polar Engineering Conference (ISOPE) 17–22 June 2012, Rhodes, Greece, 1098-6189.
3. "Energy extraction by flexible flapping foil." 3rd UK Marine Technology Postgraduate Conference 7–8 June 2012.
4. "Flow control for VATT by fixed and oscillating flap" 25th Scottish Fluid Mechanics Meeting, Heriot-Watt University, 30th May 2012.

